

Surface characterization of topological superconductor
materials using scanning tunneling microscopy and
spectroscopy

INAUGURAL-DISSERTATION
for
the purpose of
obtaining the degree of doctor
at Universität zu Köln

by
Mahasweta Bagchi
from Kolkata

Köln, 2023

This dissertation has been accepted by the Faculty of Mathematics and Natural Sciences
of the University of Cologne.

First examiner: Prof. Dr. Yoichi Ando
Second examiner: Prof. Dr. Thomas Michely
Assistant: Dr. Jens Brede
Chairperson: Prof. Dr. Stephen Schlemmer
Date of examination: 09.06.2023

Contents

Abstract	1
Introduction	3
1 Cu doped Bi₂Se₃: a quasi-2D TSC	9
1.1 Introduction	9
1.1.1 Crystal structure	11
1.1.2 Phase diagram of possible superconducting states	12
1.1.3 STM experiments	16
1.2 Sample growth and bulk characterization	16
1.3 Results from STM characterization	18
1.3.1 Zero-bias conductance peak on a side surface	20
1.3.2 Fitting of superconducting gap spectra	21
1.3.3 Structural defects: Non-QL step height and atomic defects	24
1.3.4 Measuring LDOS over a large bias range	26
1.4 Conclusion	28
2 Dopant position and absence of surface superconductivity in Sr doped Bi₂Se₃	29
2.1 Overview	29
2.2 Publication	33
3 Rotation of gap nodes in Cu doped (PbSe)₅(Bi₂Se₃)₆	47
3.1 Overview	47
3.2 Manuscript-main text	48
3.3 Manuscript-supplementary material	69
4 Pb(111) thin film on TlBiSe₂: a 2D TSC?	89
4.1 Motivation: topological proximity effect	89
4.2 TlBiSe ₂ : morphology	92
4.3 UHV growth of Pb thin film on TI	93
4.4 Characterization of the Pb film on TlBiSe ₂	94
4.5 Absence of Majorana modes in vortex cores	102
4.6 Additional experiments	104
4.6.1 Series of Pb thickness	104
4.6.2 Room temperature annealing and using a superconducting tip	108
4.6.3 Quality and role of the wetting layer	109

Contents

4.7	Discussion	110
4.8	Outlook	112
	Discussion	113
	Appendices	121
A.1	Scanning tunneling microscopy	121
A.2	Scanning tunneling spectroscopy	125
A.2.1	Normalization	128
A.3	Energy resolution and effective temperature	129
A.4	Superconducting density of states	130
A.4.1	Pairing symmetry	134
A.4.2	Fitting of superconducting gap spectra	137
A.5	Quasiparticle interference	139
A.6	Landau quantization	142
B.1	Additional data on CPSBS and PSBS	148
	Bibliography	165
	Acknowledgment	183
	Publications	185
	Erklärung zur Dissertation	186

Abstract

Realizing and understanding topological superconductors that can host exotic quasiparticles such as the Majorana fermions is currently an exciting challenge in condensed-matter physics. However, not many materials have been conclusively identified as topological superconductors. Here, we examine topological superconductivity in two different systems - the family of doped Bi_2Se_3 superconductors and in the heterostructure of a conventional superconductor [Pb(111) thin film] grown on a topological insulator (TlBiSe_2). We do so by using the surface-sensitive technique of scanning tunneling microscopy (STM) and spectroscopy (STS) under ultra high vacuum (UHV) and down to 350 mK.

We present the growth and characterization of three different members of the doped Bi_2Se_3 family [$\text{Cu}_x\text{Bi}_2\text{Se}_3$, $\text{Sr}_x\text{Bi}_2\text{Se}_3$, and $\text{Cu}_x(\text{PbSe})_5(\text{Bi}_2\text{Se}_3)_6$ (CPSBS)]. In this class of materials, bulk superconducting properties consistently show a peculiar twofold symmetry that is only compatible with a gap structure that has odd-parity and hence is considered to be topological. However, we find that superconductivity on the surface of these crystals is not robust and this constitutes a formidable challenge for our goal. Nevertheless, we have made several unexpected observations in each case.

On the superconducting area on the surface of $\text{Cu}_x\text{Bi}_2\text{Se}_3$, we measure a tunneling spectrum that suggests that the density of states around the Fermi energy is gapped but with a twofold anisotropy. This anisotropy also manifests in a 10% difference in the average superconducting gap measured as a function of the orientation of the in-plane magnetic field with respect to the crystal lattice. The minima in the gap structure is found to coincide with a crystallographic mirror plane. However, contrary to expectation that one should find a mirror-symmetry protected pair of point nodes, we find a minima and not a node in the gap structure since zero integrated density of states at the Fermi level is measured in the absence of a magnetic field.

For a superconducting region on CPSBS, we observe elliptical areas of enhanced quasi-particle density of states due to magnetic vortices penetrating the sample when the external magnetic field is applied normal to the sample plane. The anisotropy in the vortex profile is shown to be a consequence of the anisotropic gap structure. However, we discover that the orientation of the gap minima here is rotated by 60° compared to the point nodes in the bulk and that the expected gap nodes are most likely lifted in this case as well.

The above results are understood by employing a symmetry-based phenomenological analysis, work of A. Ramires. Her work shows that to find out the expected gap structure on the surface one must consider the effective symmetry, in particular the broken inversion symmetry at the surface as well as any other differences in crystal symmetry on the surface in comparison to the bulk. Any change in the effective symmetry on the surface will allow for a change in the superconducting gap structure. In this case the observed lifting of the

gap nodes and the rotation of the gap minima are consistent with the symmetry changes.

Among the three members of the doped Bi_2Se_3 family considered here, $\text{Sr}_x\text{Bi}_2\text{Se}_3$ is the only one to show a near 100% superconducting volume fraction in the bulk. However, on the surface of these crystals no gap in the density of states is observed around the Fermi energy, as long as clean metallic probe tips are used. Only when micron-sized flakes of the sample are transferred onto the STM probe tip during prolonged scanning a superconducting gap in the density of states appears. To rationalize this observation we have claimed that superconductivity in $\text{Sr}_x\text{Bi}_2\text{Se}_3$ crystals does not extend to the surface when the topological surface state (TSS) is intact. The existence of the TSS causes the charge distribution to be different near the surface compared to the bulk, leading to band bending and a consequential local electric field, which can kill superconductivity at the surface. Therefore, in micro-flakes, where the TSS is likely destroyed due to strain from the mechanical transfer, superconductivity can be observed on the surface.

The above hypothesis applies on the surface of $\text{Cu}_x\text{Bi}_2\text{Se}_3$ as well since no evidence for the TSS is found in the superconducting regions, hinting at the absence of any surface band bending or local electric field. Moreover, majority of the surface on $\text{Cu}_x\text{Bi}_2\text{Se}_3$ and CPSBS turned out to be nonsuperconducting, and for such areas we propose that band bending at the surface is tied to the suppression of the superconducting order parameter. Band bending and its impact on the superconducting properties have been discussed for cuprate superconductors where the relevant parameters of the Thomas-Fermi screening length (\sim nanometers) and carrier density ($\sim 10^{21} \text{ cm}^{-3}$) are similar to that of doped Bi_2Se_3 .

In parallel to our efforts on the doped Bi_2Se_3 superconductors, the heterostructure of Pb(111) thin film on TlBiSe_2 is also investigated for signatures of two-dimensional topological superconductivity. In particular, we searched for a localized Majorana mode inside vortex cores as well as a dispersive one-dimensional Majorana mode at the physical edge of the two-dimensional system. However, no signature of such modes is detected for this system.

Introduction

Topological superconductors (TSC) [1] can be imagined as superconducting analogues of topological insulators (TI) [2, 3]. Just like the non-trivial topology of the bulk gives birth to a surface state in a TI that lives inside the bulk band gap, a surface state¹ is expected to appear inside the superconducting (SC) gap of a TSC. This surface state, which has a Dirac-like dispersion, is special because its zero energy fermionic state is its own antiparticle and hence serves as the condensed-matter version of the Majorana fermion (MF)- spin-1/2 particle that Ettore Majorana proposed in his 1937 paper [4]. Common spin-1/2 particles such as electrons and holes are not Majorana fermions since they have opposite charge and therefore cannot be their own antiparticle. In recent years, theoretical prediction that localized zero-energy Majorana fermions [also referred to as Majorana zero mode (MZM)] can find potential application in quantum computing [5, 6] has lead to intense search for these quasiparticles in different condensed matter systems.

TSCs can host MFs due to the particle-hole symmetry inherent in a superconductor, i.e., quasiparticle excitations of a superconductor (known as Bogoliubov quasiparticles, see Appendix A.4 for its mathematical structure) are superpositions of electrons and holes. At Fermi energy (E_F) a Bogoliubov quasiparticle is described by an equal superposition of electron and hole-like states, meaning that it is equal to its own antiparticle and has a chance to be a Majorana state. Despite this, the Bogoliubov quasiparticles of a conventional s -wave superconductor are not exactly their own antiparticles since they do not have the same spin. The spin degree of freedom is eliminated by taking a *spinless* superconductor, i.e., a spin-triplet state where paired electrons have parallel spin. At the same time, having the same spin pairing (symmetric state) constrains the orbital part of the Cooper pair wavefunction since the total wavefunction must be anti-symmetric under interchange of the two electrons (fermionic). The simplest solution for the orbital part is found in a p -wave-like state for which the momentum dependent superconducting gap function $\Delta(\mathbf{k}) = -\Delta(-\mathbf{k})$. Such a *spinless, p-wave superconductor* can host MFs as excitations and is another way of describing a TSC. However, in the presence of spin-orbit interaction in the system separate classification of the spin and orbital part is not possible. In that case a TSC superconductor is identified by two other criteria [7]: (1) An inversion symmetric superconductor² can be a TSC if it has odd-parity pairing symmetry - this is possible when pairing takes place between different orbitals and the inversion operator (P) interchanges electrons from the two orbitals such that $P\Delta(\mathbf{k})P = -\Delta(-\mathbf{k})$ (see cartoon in Fig. 1); for a

¹For a three dimensional (3D) TSC this implies a two dimensional (2D) surface state. For different dimensionality of the TSC it may also be a 1D/0D state.

²Referring to centrosymmetric materials which have points of inversion symmetry in their unit cell such that every point (x, y, z) in the unit cell is indistinguishable from the point at $(-x, -y, -z)$.

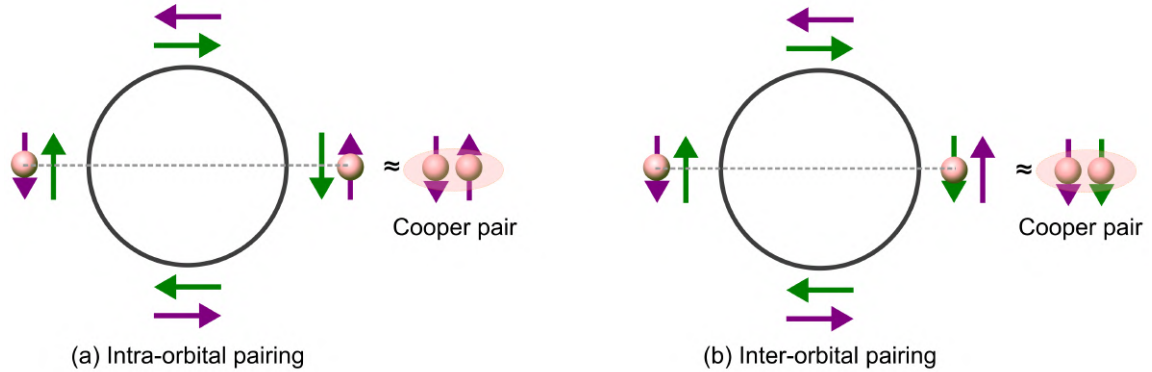


Figure 1: Pairing symmetry in superconducting topological insulators. Spin-orbit coupling in topological insulators leads to a helical spin structure for the Fermi surface. Further, due to inversion symmetry in the system, the two orbitals which make up the conduction band have opposite spin helicity as depicted above. Inter-orbital electron pairing leads to a spin-triplet like state for the Cooper pairs. Concept from Ref. [1].

single-orbital superconductor this condition is equivalent to spin-triplet pairing, and (2) the Fermi surface encloses an odd number of time reversal invariant momenta in the Brillouin zone.

To give examples, B -phase of superfluid Helium-3 with a spin-triplet, p -wave, odd-parity pairing is so far an undisputed TSC [8]. Other intrinsic TSC candidates include $\text{Cu}_x\text{Bi}_2\text{Se}_3$ [7], $\text{FeTe}_x\text{Se}_{1-x}$ [9, 10], and UTe_2 [11]. TSCs can also be engineered. A common approach, based on a theoretical proposal [12], is to induce s -wave superconductivity in nondegenerate spin states as found for the surface state of a TI [13] or a quantum anomalous hall insulator [14]. Pairing takes place on a spinless Fermi surface and therefore can be p -wave-like. The same idea can be applied to semiconducting materials with strong spin-orbit coupling (SOC) and a large g -factor [15]. Here, SOC helps to spin-split the surface state and then an external magnetic field opens a Zeeman gap at the crossing point of the bands. If the chemical potential lies inside the Zeeman gap then there is only one Fermi surface with the same spin polarization/helicity as that of a TI, i.e., one is back to the spinless regime. This approach is also applicable for the superconductor-semiconductor nanowire experiments [16–18] which realizes a 1D TSC. Also, instead of having to apply an external magnetic field one may simply start with an intrinsic ferromagnetic material as done in Refs. [19–21]. Interestingly, Refs. [20, 21] have addressed topological superconductivity in van der Waals (vdW) heterostructures.

Since the MZMs localize at appropriate boundaries of the TSC, it is desirable that they are probed using a local spectroscopic technique such as scanning tunneling microscopy (STM). The first STM observation of topological superconductivity and MZMs was made by Nadj-Perge *et al.* [22] who grew ferromagnetic iron (Fe) atomic chains on the surface of superconducting lead (Pb) with spin-orbit coupling. p -wave superconductivity was

expected in the odd number of spin-polarized Fe d -bands crossing E_F and localized zero-bias conductance peaks (ZBCP) at the ends of the chain were identified as signatures of Majorana quasiparticles. Since the Fe chains in this case were obtained via self-assembly of Fe on the Pb surface, there was no control over the length of the chain, the latter being a relevant parameter for obtaining MZMs in the topological phase that are non-interacting. More recently, a modified and well-controlled version of this experiment was realized by Schneider *et al.* [23, 24]: chains of Mn atoms were built on a Nb(110) substrate in an atom-by-atom fashion using STM-tip-assisted atom manipulation. Here, the low-energy bands are formed from hybridizing Yu-Shiba-Rusinov (YSR) states that arise from the interaction of the magnetic atom (Mn) with the superconductor (Nb). For a chain length of 35 nm (corresponding to 70 atoms in this case), a topological gap of $50 \mu\text{eV}$ is expected with MZMs localized at both ends of the chain³. The longest chain the authors managed to create consisted of 45 atoms. This chain did show localized states at both ends and were rationalized to be precursors of MZMs due to possible coupling between the modes at both ends. Key advantages of this experimental approach was the defect-free, perfect geometry of the atoms chains which made it possible to observe the ZBCP from the MZM for both ends of the chain, in contrast to the Fe chains on Pb where the ZBCP was observed at only one end. Moreover, after manipulating only one end of the chain (by placing or removing an atom), both end states were equally affected which proved that the states were a product of the entire 1D structure and not a spurious observation.

In practice, the different routes to topological superconductivity outlined above still suffer from different material complications and are under active research. Both theoretical and experimental work are required to understand if and how the MZMs found in some of the platforms can be adequately manipulated in a device geometry and thereby store information.

In this work, we have examined the intrinsic TSC candidate doped Bi_2Se_3 , in particular $\text{Cu}_x\text{Bi}_2\text{Se}_3$ (Chapter 1), $\text{Sr}_x\text{Bi}_2\text{Se}_3$ (Chapter 2) and $\text{Cu}_x(\text{PbSe})_5(\text{Bi}_2\text{Se}_3)_6$ (Chapter 3), with an aim towards addressing existing open questions and conflicting experimental reports. Early experiments on $\text{Cu}_x\text{Bi}_2\text{Se}_3$ were controversial and contradicted each other. Several experiments indicated topological superconductivity in the material, for example, point-contact spectroscopy [26] found a ZBCP on the surface which was attributed to the topologically protected MZMs and upper critical field measurements [27] showed absence of Pauli limiting behavior which suggested spin-triplet superconductivity. More recently, nuclear magnetic resonance (NMR) measurements [28] confirmed a spin-triplet bulk superconducting state due to an unchanged Knight shift (K_s) across the SC transition temperature for magnetic field applied perpendicular to the (001) sample plane. On the other hand, scanning tunneling spectroscopy (STS) [29] data pointed to an s -wave-like trivial SC gap in the material and Andreev reflection spectroscopy found the lineshape of the ZBCP on the surface to change as a function of the tunnel barrier strength [30] implying that the

³MZMs must appear in pairs since two together form a single fermion. This is a consequence of how these quasiparticles are written mathematically [25].

origin of the ZBCP must be different from MFs⁴. Even more surprisingly, experiments done using the same experimental technique but by different groups had different reports: no ZBCPs were observed in the vortex core by Levy *et al.* [29], while the more recent STM study of $\text{Cu}_x\text{Bi}_2\text{Se}_3$ by Tao *et al.* [32] resolved elliptically-shaped vortices on the surface hosting ZBCPs.

The apparent discrepancy between the point-contact spectroscopy [26] and STS measurement [29] regarding the presence of MF surface state may be remedied by taking into account the quasi-2D Fermi surface of $\text{Cu}_x\text{Bi}_2\text{Se}_3$, as suggested by the angle-resolved photoemission spectroscopy (ARPES) and quantum oscillation experiment [33], which can only support a quasi-2D TSC and not a 3D TSC. For such a TSC MF surface state is expected only at step edges and on the side surface of the (001) plane [34]. In order to unambiguously identify such edge states, it is desirable to use a technique that has both spatial and spectroscopic access such as STM [35]. The sub-nanoscale spatial and (sub-)meV energy resolution of low-temperature STM is ideally suited to measure localized states, such as the MZM, and correlate their presence or absence with the simultaneously acquired topography. Furthermore, with regards to superconductivity, the STS measured on the surface can be analysed to understand the possible symmetry of the SC gap structure. Complementary information maybe obtained from the internal structure of imaged vortices [36, 37]. Via quasiparticle interference (QPI) imaging, STM can provide information regarding the bands in which pairing takes place [38] as well as the symmetry of the electronic states [39, 40], when acquired at energies close to or within the SC gap.

An open question in the family of doped Bi_2Se_3 TSCs is the unit-cell location and charge state of the dopant. In principle, any near surface dopant gives rise to a change in the local density of states (LDOS) at the surface, which can be probed by STM. Indeed, Refs. [41, 42] have identified defects in pristine Bi_2Se_3 as deep as five atomic layers below the surface based on their characteristic appearance in STM images and by comparison with first principles calculations. Similar ideas can be used to identify the dopant-induced defect. Further, *ab initio* simulations of the STM images should identify the bonding configuration of the defect and thereby its charge state. The latter tells us the number and type of carriers contributed by the defect. The density of these defects multiplied by the number of carriers from each defect gives the increase in charge carrier concentration expected.

Among the three members of the doped Bi_2Se_3 family investigated in this thesis, $\text{Cu}_x(\text{PbSe})_5(\text{Bi}_2\text{Se}_3)_6$ is the only member where topological superconductivity with gap nodes is realized in the bulk but no STM experiments to directly probe the superconducting gap has been performed so far. This is largely because this system is more difficult to grow as compared to $\text{Cu}_x\text{Bi}_2\text{Se}_3$ or $\text{Sr}_x\text{Bi}_2\text{Se}_3$ and only a handful of groups in the world have attempted to grow this material. For this system, we want to not only clarify the structure of the superconducting gap on the surface, but also its relation to the superconductor $\text{Cu}_x\text{Bi}_2\text{Se}_3$.

⁴Theoretical work [31] could later show that the particular lineshape in a conductance experiment depends on the type and the energy dispersion of the MF and could mimic a typical Andreev reflection spectrum.

Apart from the intrinsic route to topological superconductivity as for doped Bi_2Se_3 , we attempted to obtain a TSC by a different route, namely via the topological proximity effect [43]. Here an s -wave SC (Pb) was grown on a bulk TI film (Chapter 4). If the 2D surface state of the TI migrates into the SC Pb and is proximitized, one obtains a 2D TSC. Signatures of 2D topological superconductivity include appearance of dispersive in-gap Majorana states at the 1D boundary of the 2D superconductor [19]. MZMs are expected inside vortex cores of a 2D TSC as discussed in the theoretical works [12, 44], localized at the two ends of the vortex line. The MZM at each end arises due to the proximitization of the TSS on the top and bottom surface of the TI, respectively. However, the present case may differ from the scenario considered in Refs. [12, 44], since only the TSS of the top surface of the TI is expected to migrate in the SC and be proximitized. Hence we consider the other possibility that an odd number of MZMs appear inside the vortex cores and their partner MZMs appear at the physical edge of the system [45], since MZMs must always appear in pairs.

(This thesis is written by me in the first person plural form. All contributions to the experimental work is specifically indicated at the beginning of each chapter.)

1 Cu doped Bi₂Se₃: a quasi-2D TSC

Y. Ando proposed the experiments on which this chapter is based. M. Bagchi grew the crystals and performed bulk characterization. STM data was acquired primarily by J. Brede with contributions from M. Bagchi. STM data was analyzed by M. Bagchi under the supervision of J. Brede.

1.1 Introduction

In the year 2010, Hor *et al.* [46] were the first to observe superconductivity in Cu doped Bi₂Se₃ crystals (Cu_xBi₂Se₃, 0.12 ≤ x ≤ 0.15) below a critical temperature T_c of 3.8 K. However, these samples, grown using the melt-growth technique, had a low superconducting shielding fraction (SF) of ~20% and did not show zero resistivity. A year later, Kriener *et al.* [47] found that upon electrochemical intercalation of Cu into Bi₂Se₃, followed by annealing and a quenching process, Cu_xBi₂Se₃ crystals with higher SF ~50% and zero resistivity below T_c can be obtained. Although superconductivity was observed for x values between 0.09–0.6, maximum SF was obtained only between 0.3 – 0.5, with a T_c of 3.4 K. Note that while T_c is robust and reproducible for all x values, the SF is different and can even differ for samples with same x value.

It is common belief that the dopant leads to superconductivity in the material by increasing the carrier density¹. However, superconducting Cu_xBi₂Se₃ typically shows a carrier density of around 10²⁰ cm⁻³ only and it does not change much with the Cu concentration [47]. Kriener *et al.* [47] pointed out that this carrier density was too low in view of the high T_c . They also found that the Cu concentration varied on a sub-mm scale suggesting that superconductivity would occur in small regions with optimum Cu concentration. At present more evidence exists regarding the inhomogeneity of Cu concentration in the crystals based on transmission electron microscopy measurements [49]: different layered structures with nonuniform low-Cu content and high-Cu-content were identified. Kriener *et al.* [47] came to the conclusion that the inhomogeneous nature of superconductivity in the material could be responsible for the high T_c [50]. We add that disorder in the material can also lead to an enhancement in the T_c due to Anderson localization [51, 52].

Later, in the year 2015, Sr [53] and Nb [54] were also found to induce superconductivity in Bi₂Se₃ upon doping, with a T_c of around 3 K. These samples were not air-sensitive, like Cu_xBi₂Se₃, and had large SF close to 100%, even when melt-grown. Around the

¹ARPES [48] results support this notion; they report that even after doping the band structure of Bi₂Se₃ is intact and only the Fermi level moves deeper inside the conduction band, ~0.25 eV above the conduction band minimum.

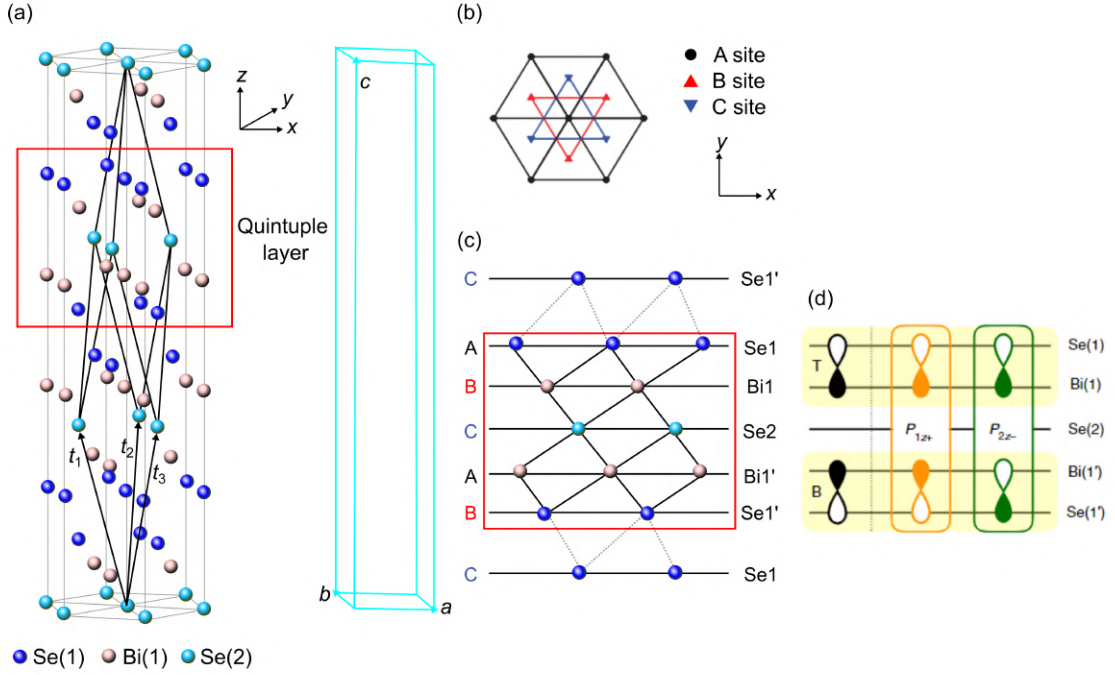


Figure 1.1: Crystal structure of Bi_2Se_3 . (a) Crystal structure of Bi_2Se_3 . $t_{1,2,3}$ are the lattice vectors of the rhombohedral unit cell. The hexagonal unit cell is indicated on the side. (b) Top view along the z -direction. The hexagonal lattice in one layer is rotated with respect to the next and the stacking follows an ABC order. (c) Side view of the QL stacking. A QL is inversion symmetric about the Se2 layer. (d) The conduction (valence) band around the Γ point is formed by the symmetric (antisymmetric) superposition of p_z orbitals from the top (bottom) Se-Bi layers inside a QL. Figure and text assembled using Refs. [56, 57].

same time, Sasaki *et al.* [55] used the same scheme (intercalating Cu) to make a related TI heterostructure $(\text{PbSe})_5(\text{Bi}_2\text{Se}_3)_6$, also superconducting.

For superconductivity in these doped Bi_2Se_3 systems to be considered as 3D topological superconductivity, we can use the simple criterion discussed before, i.e., the Fermi surface must enclose an odd number of time-reversal-invariant momenta points. In case of $\text{Cu}_x\text{Bi}_2\text{Se}_3$, ARPES and quantum oscillation experiments [33] have shown that the shape of the Fermi surface changes as function of carrier density. For carrier density $\sim 10^{20} \text{ cm}^{-3}$, the Fermi surface is open cylindrical in shape that encloses two time-reversal-invariant momenta points (Γ and Z) which disqualifies it as a 3D TSC. However, there is still the possibility of weak quasi-2D topological superconductivity. On the other hand, $\text{Sr}_x\text{Bi}_2\text{Se}_3$ was reported to have a carrier density lower than $\text{Cu}_x\text{Bi}_2\text{Se}_3$, $\sim 2 \times 10^{19} \text{ cm}^{-3}$ [53, 58], meaning that the Fermi surface could be closed, enclosing only the Γ point, and hence be a 3D TSC. However, recent ARPES and quantum oscillation experiments [59] conclude that the Fermi surface in this case too is cylinder-like with a carrier density of $\sim 10^{20} \text{ cm}^{-3}$.

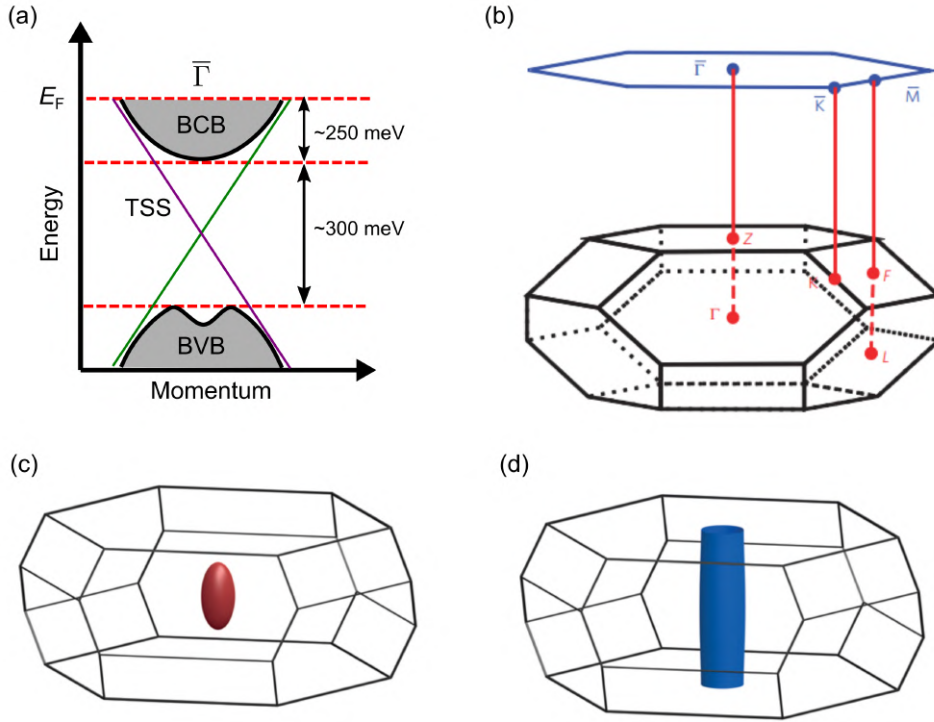


Figure 1.2: Band structure around $\bar{\Gamma}$ and evolution of Fermi surface with carrier density. (a) Schematic representation of the topological surface state (TSS) and bulk bands [bulk conduction band (BCB) and bulk valence band (BVB)] near the $\bar{\Gamma}$ point for doped Bi_2Se_3 based on ARPES data [48], which show that the band structure of undoped Bi_2Se_3 is preserved. (b) Brillouin zone for Bi_2Se_3 from Ref. [56]. The blue hexagon is the 2D Brillouin zone of the projected (001) surface. (c,d) Calculated Fermi surface, scaled with respect to the Brillouin zone, for a carrier density of $\approx 10^{19} \text{ cm}^{-3}$ (c, closed Fermi surface) and $\approx 10^{20} \text{ cm}^{-3}$ (d, open Fermi surface), from Ref. [33].

In the next two subsections we attempt to give further insight into why the family of doped Bi_2Se_3 are considered as TSCs.

1.1.1 Crystal structure

We start with the crystal structure of the mother compound of doped Bi_2Se_3 superconductors, i.e., Bi_2Se_3 , the pristine TI. The structure of Bi_2Se_3 is shown in Fig. 1.1(a). The unit cell is indicated in the rhombohedral (black lines) and hexagonal notation (blue parallelepiped on the side). It consists of three quintuple layers (QLs) where each QL has an alternating stacking of Se and Bi hexagonal atomic layers. The unit cell has threefold rotational symmetry about the z axis, three mirror planes along the yz and equivalent planes, inversion symmetry with Se2 site as the inversion center and other symmetry operations belonging to the D_{3d} point group. The atomic layers are

strongly coupled to each other whereas between two QLs the coupling is weak- of the van der Waals type, meaning that this and any derived material can be simply cleaved to obtain a fresh surface.

1.1.2 Phase diagram of possible superconducting states

The valence electronic structure of Bi₂Se₃ is governed by the outermost p orbitals of Bi($6s^26p^3$) and Se($4s^24p^4$). After considering hybridization between the orbitals and effect of crystal field (energy splitting between p_x , p_y and p_z orbitals), the states that are closest to the Fermi level are P_{1z}^+ from Bi orbitals in the bonding state (+ or even parity) and P_{2z}^- from Se orbitals in the antibonding state (- or odd parity). With the additional ingredient of spin-orbit coupling these orbitals of opposite parity intersect, i.e., band inversion takes place. This inversion occurs at the Γ point and as a consequence a topological surface state appears around this point inside the bulk bandgap [56, 60].

The low-energy Hamiltonian of Bi₂Se₃ in the normal state [56, 60], taking into account spin-orbit coupling and crystal symmetries, in the (P_{1z}^+ , P_{2z}^-) basis near the Γ point is given by

$$H_0(\mathbf{k}) = -\mu + m\sigma_x + v\sigma_z(k_x s_y - k_y s_x) + v_z k_z \sigma_y \quad (1.1)$$

where μ is the chemical potential, $2m$ is the bulk band gap, s_i (σ_i) are the Pauli matrices in the spin (orbital) space. $s_z = \pm 1$ denotes electron spin parallel (antiparallel) to the z direction. v is the Fermi velocity in the x, y plane of the Bi/Se layers and v_z is the Fermi velocity in the z direction. The third term on the right indicates the spin-momentum locking for the bulk Fermi surface giving it a helical in-plane spin texture. For this Hamiltonian the low-energy spectrum of the bulk states is given as

$$E_{\pm} = -\mu \pm \sqrt{m^2 + v^2 k_x^2 + v^2 k_y^2 + v_z^2 k_z^2} \quad (1.2)$$

The surface state together with the bulk bands are sketched in Fig. 1.2(a). In going from undoped to the doped Bi₂Se₃ crystal the surface state and the bulk bands remain well defined. Doping primarily leads to an increased carrier concentration (rise in μ) according to ARPES results [48]. However, this in turn can trigger a transition in the shape of the Fermi surface. Based on the ratio of μ/m the Fermi surface can be closed (ellipsoid) or open (cylindrical) [sketch in Fig. 1.2(c,d)]. In Ref. [60] the ratio is calculated to be ≥ 1.4 .

It is important to note that $H_0(\mathbf{k})$ is rotationally isotropic around the z axis while the crystal has only threefold rotational symmetry. This is an artifact of the theoretical description considered. This is remedied by considering an additional term, $H_w(\mathbf{k})$ - the hexagonal warping term. This term is typically small but finite for Bi₂Se₃ and its derivatives [61]. It has the form:

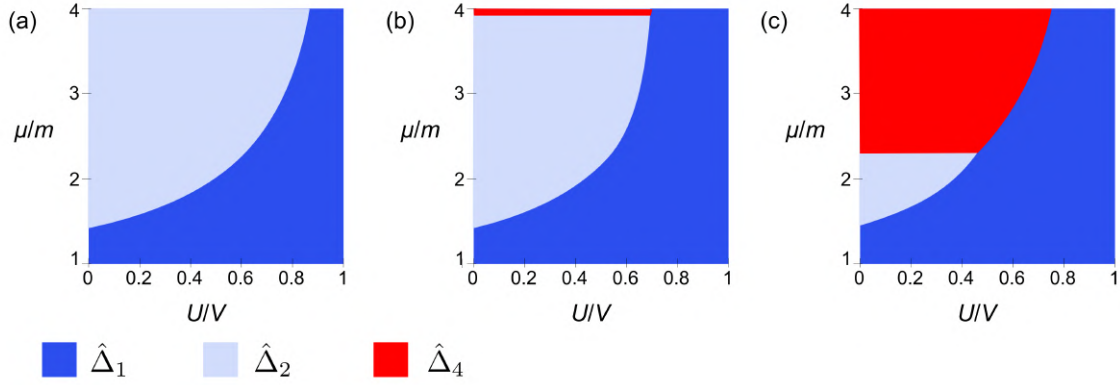


Figure 1.3: Phase diagram of superconducting order parameters for different values of hexagonal warping. (a) - (c) The order parameters $\hat{\Delta}_1$, $\hat{\Delta}_2$ and $\hat{\Delta}_4$ are represented by the blue, light gray and red areas, respectively. The different values of the hexagonal warping term for (a-c) are 0, 0.3, and 1, respectively. Image modified from Ref. [63]. μ = chemical potential, $2m$ = bulk band gap, $U(V)$ = intraorbital (interorbital) electron interaction.

$$H_w(\mathbf{k}) = \lambda \left(k_x^3 - 3k_x k_y^2 \right) \sigma_z s_z$$

where λ is the spin-orbit coupling parameter. The origin of this term is the spin-orbit interaction in presence of crystalline anisotropy. The term will affect surface and bulk bands modifying the band dispersion such that it is hexagonally distorted in the $k_x k_y$ plane. Further, this term gives an out-of-plane spin component to the otherwise completely in-plane spin texture of both the surface state and bulk conduction band. The term vanishes along mirror-symmetric directions (since s_z is odd under mirror operation [62]) and this has implications for the superconducting pairing states of the system, as will be discussed shortly.

Superconductivity in doped Bi_2Se_3 materials is described in the theoretical work of Fu *et al.* [7] using the above bulk Bi_2Se_3 Hamiltonian and the Bogoliubov–de Gennes (BdG) Hamiltonian for a superconductor. Attractive interaction between electrons is discussed using a U - V model where U describes attraction between electrons in the same orbital and V describes attraction between electrons from different orbitals. The relevant orbitals for Cooper pairing of electrons are the ones from the top and bottom of the QL since they form the conduction band. Moreover, due to the TI-spin-orbit-coupling term in the normal state Hamiltonian and inversion symmetry inside the QL, these two orbitals have opposite spin helicity. If pairing of electrons takes place within the same orbital we obtain Cooper pairs with antiparallel spins (spin-singlet s -wave like) whereas inter-orbital pairing results in a spin-triplet state², illustration of Fig. 1. So far only phonon mediated pairing has been

²The description of spin is for visualization only since spin is not a good quantum number here.

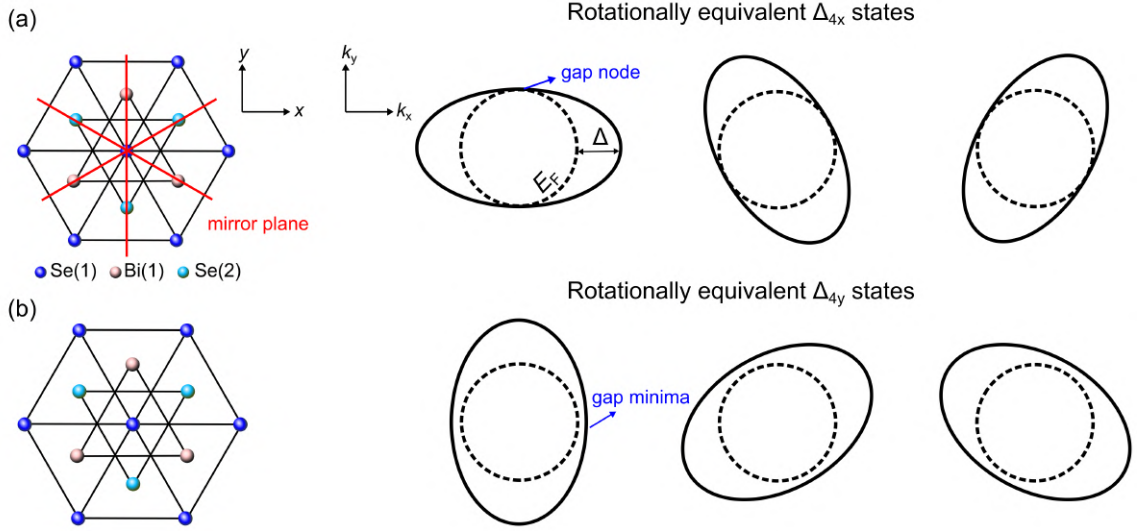


Figure 1.4: Symmetry of the Δ_{4x} and Δ_{4y} states with respect to the crystal lattice. The ab -plane crystal structure of $\text{Cu}_x\text{Bi}_2\text{Se}_3$ (left) and superconducting gap structure (right) - solid lines depict the superconducting gaps and dashed lines are the Fermi surfaces. (a) Three rotationally equivalent Δ_{4x} state with twofold symmetry and gap nodes along a crystallographic mirror plane. (b) Three rotationally equivalent Δ_{4y} state with twofold symmetry and gap minima along a Se-Se direction.

discussed for this system both theoretically [64] and experimentally [65], since electron-electron interaction in the system is weak. The identified phonon modes propagate along the ΓZ direction and have small momenta. The inelastic neutron scattering experiment [65] found that the phonons along the ΓZ close to the zone center have a much broader linewidth as compared to other modes as well as compared to undoped Bi_2Se_3 . A broader linewidth indicates a shorter lifetime, i.e., they are very active and likely play a part in the formation of Cooper pairs. They also suggest that the broadening of the phonons could promote interorbital pairing.

Discussion of details of the pairing symmetry of doped Bi_2Se_3 is done using the crystalline symmetry group D_{3d} since the presence of spin-orbit coupling in the system makes the notion of spin-singlet or triplet state not well defined. Based on the D_{3d} point group symmetry of the crystal there are four possible pairing states [7, 34] (the link between crystal symmetry and superconducting gap structure is discussed in Appendix A.4.1). They are referred to as $\Delta_1(A_{1g})$, $\Delta_2(A_{1u})$, $\Delta_3(A_{2u})$, and $\Delta_4(E)$, with their point group symmetry representation in brackets. Out of the four, only Δ_1 is of conventional kind, i.e., a spin-singlet with a isotropic full gap. The other three can be considered as topological since they are found to be odd-parity states.

Using Ref. [63] we now discuss the phase diagram of the system in the $(U/V, \mu/m)$ plane (see Fig. 1.3). They have calculated the T_c and the condensation energy at zero temperature for the different pairing states. Since the Δ_3 state always has a lower T_c in comparison to

the others it is disregarded. Instead, the ground state of the systems is formed by either Δ_1 , or Δ_2 or Δ_4 . From Fig. 1.3(a) we see that singlet pairing Δ_1 is possible when intraorbital interaction is larger than interorbital one ($U > V$). Moreover, in the absence of any hexagonal distortion either Δ_1 or Δ_2 forms the ground state depending on the chemical potential. In the presence of hexagonal warping, large chemical potential and strong interorbital attraction, Δ_4 forms the ground state [Fig. 1.3(b-c)].

The Δ_4 state again is a linear superposition of two degenerate pairing states, the Δ_{4x} and Δ_{4y} . We can write $\Delta_4(\mathbf{k}) = \eta_1 \Delta_{4x} + \eta_2 \Delta_{4y}$, where the vector $\boldsymbol{\eta} = (\eta_1, \eta_2)$. Both Δ_{4x} and Δ_{4y} break the threefold rotational symmetry of the crystal structure of Bi_2Se_3 , they are twofold symmetric in the xy plane having either two point nodes or gap minima, respectively. They are differentiated based on whether the gap nodes or minima lie along a mirror plane of the crystal lattice (Δ_{4x}) or normal to it (Δ_{4y}) [see sketch in Fig. 1.4(a,b)]. The gap anisotropy in either case depends on the warping term and the details of the pairing interaction [34]. Note that it is the warping term that lifts the nodes in Δ_{4y} but since the gap nodes for Δ_{4x} lie on a mirror plane of the crystal they are unaffected³. Sketch of the superconducting gap structures for all the pairing states can be found in the review article by Yonezawa [66].

Experimentally it was found that the Δ_4 state is realized for samples with doping level ~ 0.3 . However, the gap node/minima was always found to lie either along a mirror plane or in-between. This means that instead of a superposition of the Δ_{4x} and Δ_{4y} states, the system chooses one of them, i.e., $\boldsymbol{\eta} = (1,0)$ or $(0,1)$. Further, each of the two states are themselves superpositions of three rotationally equivalent ones, due to the threefold symmetry of the lattice. Again selection of one out of the three equivalent ones bestows a special *nematic* character to the superconducting state. Since $\boldsymbol{\eta}$ dictates the orientation of the gap in k -space it is also called the nematic director.

In support of the early experiments which found the nematic director to be oriented along the Se-Se direction in one case, i.e., a Δ_{4x} state [28], and rotated by 90° in another, i.e., a Δ_{4y} [67], recent experiments [68] show the director to be different from sample to sample for similar doping levels and that it does not change into an equivalent direction upon thermal cycling. The pinning of the nematic director is likely due to the sample dependent local environment that is created as a result of dopant intercalation following by quenching during growth [68]. The resulting strain provides the necessary in-plane crystalline anisotropy that is needed to pin the direction of $\boldsymbol{\eta}$ as predicted theoretically [69, 63, 70]. Although a high-resolution x-ray diffraction (XRD) experiment did report a tiny ($\sim 0.02\%$) in-plane lattice distortion [71], this has now been contradicted [72] and requires further clarification.

Interestingly, a non-trivial SC state other than the Δ_4 maybe realized in this system, as suggested by theoretical calculations [34, 60]. It is a chiral superconducting state which

³The reflection symmetry associated with the mirror plane necessitates that any quantity that is odd under this symmetry, must go to zero at the position of the mirror plane. This holds for the warping term as well as for the odd-parity pairing state. In other words, the mirror plane protects the gap nodes of the odd-parity pairing state.

is fully gapped and does not break the rotational symmetry of the underlying lattice. This state may have been observed in recent experiments [68] where the samples measured were of doping levels higher than the optimum value of 0.3.

1.1.3 STM experiments

Tao *et al.* [32] provided the first direct visualization of the nematic director on the *surface* of Cu_xBi₂Se₃. They observed elongated vortices for an out-of-plane magnetic field. These vortices were elongated in a direction that coincided with one of the three equivalent mirror planes of the Bi₂Se₃ lattice and were twofold symmetric. Since a vortex elongates along the direction of the gap node or minima and its anisotropy reflects the anisotropy in the superconducting gap structure, a Δ_{4x} SC state was deduced. Although the gap nodes in this case lie along a mirror plane and are expected to be robust, the SC gap spectra in the region revealed otherwise. The latter was only consistent with a twofold anisotropic gap function with lifted nodes. The twofold symmetry of the gap function was also demonstrated by the angular dependence of the SC gap as a function of magnetic field rotated in-plane with respect to the crystal lattice. Interestingly, they also observed a ZBCP inside the vortex cores while an earlier measurement by Levy *et al.* [29] did not show any.

Our STM experiments on Cu_xBi₂Se₃ were done on the heels of the arXiv publication by Tao *et al.* [32]. We have reproduced their observations partly, in particular the STS spectra which suggest an anisotropic gap function and the twofold symmetry of the SC gap as a function of the orientation of an in-plane magnetic field. Going beyond their work, we find an edge mode at the side surface of the (001) plane. Such an edge mode as a possible signature of 2D MF suggests quasi-2D topological superconductivity [34]. Moreover, by measuring samples of different doping level and growth technique we have identified the common defect that occurs as a result of Cu doping.

1.2 Sample growth and bulk characterization

Cu_xBi₂Se₃ ($x = 0.25 - 0.35$) crystals were grown primarily by the method of electrochemical intercalation following the recipe of Kriener *et al.* [47]. Crystals with higher doping levels ($x = 0.6$) were also synthesized. Additionally, a small number of samples were grown using the melt-growth technique of Hor *et al.* [46].

It is important to note that the samples do not superconduct directly after the Cu intercalation process in the electrochemical technique or if the starting materials (Bi, Se, Cu) are made to react at temperatures above their melting point and then cooled down to room temperature in the melt-growth process. To establish superconductivity, the Cu-intercalated or melt-grown sample must be quenched from a high temperature of $\sim 560^\circ$ by quick immersion into cold water. This requirement suggests that Cu takes a metastable position in the Bi₂Se₃ unit cell. The possible Cu (dopant) sites for this material discussed in Chapter 2.

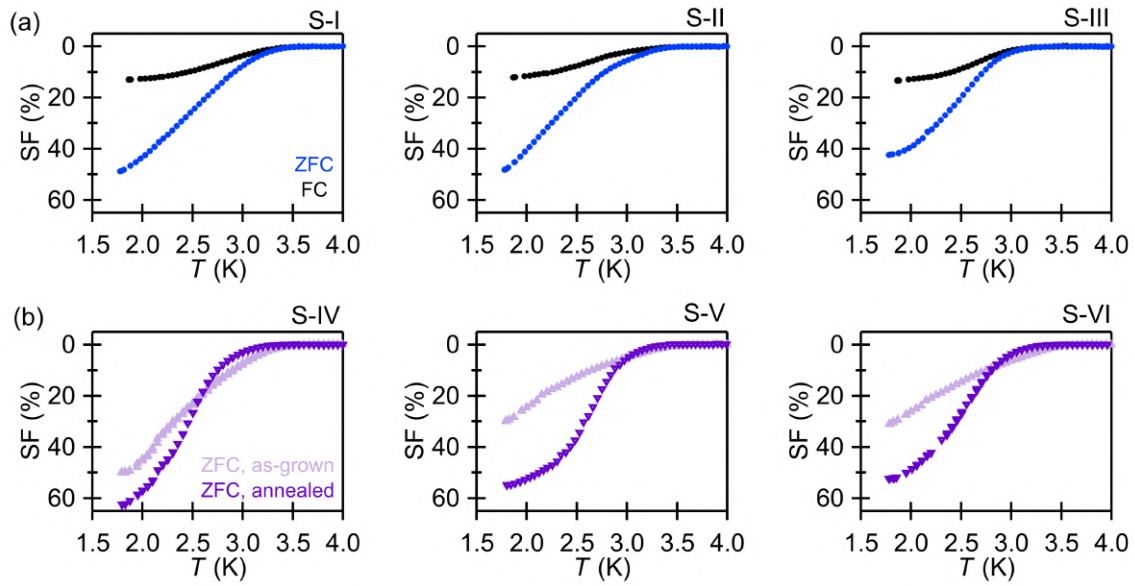


Figure 1.5: SC shielding fraction of different $\text{Cu}_{0.3}\text{Bi}_2\text{Se}_3$ crystals as determined by SQUID magnetometry. (a) Temperature dependence of superconducting shielding fraction for zero-field-cooled (ZFC) and field-cooled (FC) magnetization data in a magnetic field of 0.2 mT, applied parallel to the sample plane, for three as-grown samples, S-I, S-II and S-III. (b) ZFC curves showing SF of three samples measured directly after growth and after annealing at RT under argon atmosphere. A significant increase in the SF of the samples is observed upon annealing.

Bulk characterization of the samples were done by measuring the dc magnetization M (magnetic moment per unit volume, units: emu/cm³) using a commercial SQUID magnetometer. The sample was zero-field-cooled (ZFC) down to 1.8 K, thereafter a magnetic field (H) of 0.2 mT was applied parallel to the sample plane and the magnetization was measured upon increasing the temperature. We calculate the superconducting shielding fraction (SF) (the fraction of the sample volume from which the magnetic field is expelled due to superconductivity) using the expression $SF (\%) = (-4\pi M/H) * 100$. Note that due to a diamagnetic signal expected from a superconductor, the magnetization in this case is negative. Figure 1.5(a) shows the SFs for three samples out of more than 50 that were grown. The superconducting transition temperature T_c , defined as the onset of the diamagnetic or Meissner signal, was found to be between 3.3 and 3.5 K for the different samples. This Meissner T_c corresponds to the midpoint of the transition observed in a resistivity measurement.

The SF of the samples were found to improve significantly after they were kept in an argon atmosphere at room temperature over an extended period of time [Fig. 1.5(b)], although such an increase was accompanied by a lowering of the T_c by ~ 0.2 K. A possible explanation for this effect is that with time under an inert atmosphere more Cu atoms acquire the site that induces superconductivity.

A small kink around 2.2 K [see Fig. 1.5(b)] can be found in the magnetization data sometimes which likely originates from the transition of normal fluid helium to superfluid helium in the cryostat space close to the SQUID coils and is not intrinsic to the measured sample. This temperature is known as the lambda point of helium since around this point the specific heat capacity as a function of temperature resembles the Greek letter (λ).

1.3 Results from STM characterization

We characterized the Cu_xBi₂Se₃ samples using STM and STS. The samples were mechanically cleaved under UHV conditions to expose clean surfaces. However, large portions of the surface were found to be not atomically flat and unsuitable for characterization by surface-sensitive probes. Among the areas that were found to be suitable for scanning, most of them were nonsuperconducting (NSC). In other words, the probability to find superconducting regions on the sample is surprisingly low⁴. We have arrived at this conclusion based on experiments done on several samples (also cleaved multiple times) and are supported by Tao *et al.* [32].

In the next two subsections we report on the superconductivity that was found for a particular area on the sample.

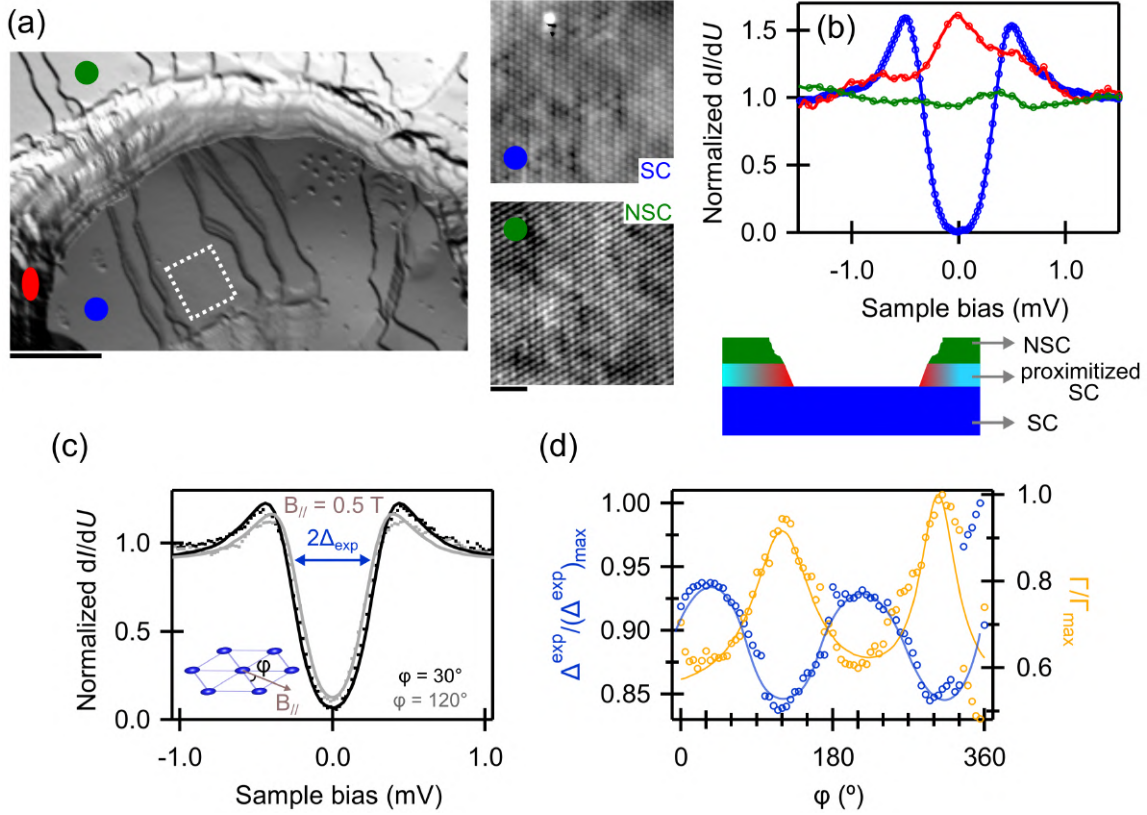


Figure 1.6: Zero-bias conductance peak on a step edge separating SC and NSC region; SC gap as a function of in-plane field orientation. (a) 3D rendered topograph of a crater with a maximum height difference of 48 nm between top and bottom terraces. Both terraces further show smaller crystallographic steps and is atomically resolved (right panel). Scale bar corresponds to 100 nm (left) and 2 nm (right). (b) Normalized dI/dU spectra taken on the bottom (blue trace), sidewall (red trace) and top (green trace) of the crater showing a SC gap, a zero-bias conductance peak and no features in the DOS, respectively. Positions of the spectra are marked in (a). A sketch (cross-sectional view) of the region is given below. The interpreted SC character of the different layers is indicated. (c) Normalized dI/dU spectra measured in the region marked with a dashed white square in (a), with an in-plane magnetic field ($B_{//}$) of 0.5 T for different orientations. Inset shows the definition of the field orientation with respect to the top Se lattice, represented by blue spheres. The definition of Δ_{exp} is indicated and is obtained from the fit. (d) Angular dependence of $\Delta_{\text{exp}}/\Delta_{\text{max}}$ under $B_{//}=0.5$ T (blue open circles). The solid line is a guide to the eye to highlight a twofold symmetry. Corresponding variation in $\Gamma/\Gamma_{\text{max}}$ (yellow open circles), also obtained from the fit, shows a twofold symmetry phase shifted by 90° in comparison to $\Delta_{\text{exp}}/\Delta_{\text{max}}$. Scan/stabilization parameters: (a) $U = 900$ mV, $I = 20$ pA (left); $U = 3$ mV, $I = 200$ pA (right); (b) $U = 3$ mV, $I = 100$ pA (blue, red); $U = 3$ mV, $I = 200$ pA (green); (c) $U = 3$ mV, $I = 200$ pA. $U_{\text{mod}} = 100 \mu\text{V}_p$ for (b) and (c).

1.3.1 Zero-bias conductance peak on a side surface

We examine a topographically unusual region, as shown in Fig. 1.6(a), where a ~ 48 nm high step separates two flat terraces. Atomic resolution images taken on both terraces show a sixfold symmetric lattice indicating Se termination for both. Additionally, several triangular defects can be seen for the image taken on the lower terrace. We have characterized the area using spectroscopy. Normalized dI/dU point spectra measured for three locations [blue, red and green spot in Fig. 1.6(a)] are shown in Fig. 1.6(b). Based on these and other measured spectra we find a full SC gap (blue trace) on the lower terrace while no gap or a flat DOS (green trace) is measured on the upper terrace. We interpret the data as: the SC layers are encapsulated by NSC layers. The NSC layers are locally ripped off, thereby forming a crater that leads down to the SC region, which was created by chance during the cleaving process. A sketch can be found in Fig. 1.6(b) (lower panel). Since the NSC layers are in direct contact with the SC layers, superconductivity must extend into the NSC layers for a limited thickness forming what is indicated as the proximitized SC layers. Upon taking spectroscopy on the edge/sidewall of the proximitized region (highlighted with red color in the sketch) we find a $\sim 50\%$ increase in conductance around zero-bias in comparison to the normal-state conductance (red trace). This ZBCP, which is observed for different points along the sidewall, may have a non-trivial origin such as the 2D dispersive Majorana mode running along the side surfaces⁵ of a quasi-2D TSC [34]. Ideally one would expect a corresponding 1D mode to exist along the atomic step edges⁶ that can be seen at the bottom of the crater in the SC region. However, we do not observe any in-gap states in those step edges, most likely since the small step height and its orientation makes it impossible to probe the side of the step adequately. Additionally, the peak feature inside the gap cannot be directly associated with a 2D linearly dispersing state for which a linearly increasing DOS is expected as a function of energy. In this case one must consider differences between a measured dI/dU spectrum which is taken to be proportional to the sample DOS and the simplistic picture of sample DOS at $T=0$.

We must also point out that the observed ZBCP can have a trivial source in the form of an Andreev reflection peak. A way to distinguish between the sources would be to measure conductance spectra as a function of tunneling barrier strength, which in an STM experiment is easily done by using different STM setpoint current. The conductance lineshape is expected to change as a function of tunneling barrier strength only in case of Andreev reflection [73]. Unfortunately this simple experiment could not be done since stabilizing for higher setpoint currents on the sidewall area turned out to be not possible.

Next, we performed further characterization of the superconducting area marked by the dashed white square in Fig. 1.6(a). We applied an in-plane magnetic field ($B_{//}$) of 0.5 T and measured the superconducting gap as a function of the orientation of $B_{//}$ with respect

⁴There are two possibilities: (i) superconductivity on the surface of these samples is not homogeneous or (ii) some intrinsic mechanism does not allow superconductivity to be observed on the surface using STM.

⁵This is the side surface of the (001) plane. This is a 2D boundary.

⁶This forms a 1D boundary.

to a Se-Se direction [angle is denoted as ϕ , see inset of Fig. 1.6(c)]. A noticeable difference between spectra taken for $\phi= 30^\circ$ and 120° can be found in Fig. 1.6(c) by comparing the experimental gap size (indicted as $2\Delta_{\text{exp}}$). For all spectra taken between $\phi= 0^\circ$ and 360° we have extracted Δ_{exp} using the Dynes fit routine (fit expression and meaning of the fit parameters is explained in Appendix A.4.2). Although the quality of the fit was found to be dependent on the values of T_{eff} and Γ , the gap value was weakly sensitive for a range T_{eff} and Γ (discussion on T_{eff} in Appendix A.3). The angular dependence of normalized Δ_{exp} is summarized in Fig. 1.6(d) and shows a clear twofold symmetry with maxima around $\phi= 30^\circ$ and 210° (in-between Se-Se direction) and minima for $\phi= 120^\circ$ and 300° (along Se-Se direction)⁷. This variation in SC gap or smearing of the gap edge and filling up of the gap bottom under a $B_{//}$ field is consistent with the Volovik effect which is pronounced in the case of nodal superconductors [74]. The effect arises due to the Doppler shift in the quasiparticle energy from the presence of a supercurrent which flows to shield the bulk of the superconductor from the applied field. The Doppler shift in the quasiparticle energy can lead to the generation of maximum number of broken Cooper pairs or quasiparticles, leading to a smaller gap, when the field is perpendicular to the direction of the nodes. We have visualized the presence of quasiparticles by tracing the variation of the fit parameter Γ while keeping T_{eff} and the gap size Δ fixed [Fig. 1.6(d), orange circles]. A twofold symmetry is visible, only phase shifted by 90° with respect to Δ_{exp} . A maximum amount of quasiparticles are generated for $B_{//}= 120^\circ$ and 300° which should be the direction perpendicular to the gap nodes/minima. A more detailed discussion on this topic can be found in the additional data section B.1 on $\text{Cu}_x(\text{PbSe})_5(\text{Bi}_2\text{Se}_3)_6$ where similar observations were made.

We point out that we did not observe any vortex lattice in this region likely due to the area being unsuitable for geometric reasons such as the area being too small for a vortex lattice. In summary, we have deduced a twofold symmetry in the SC gap structure with gap node/minima along a direction in-between the Se-Se directions. Our observations are consistent with those of Tao *et al.* [32] who also observed the gap minima/nodes to coincide with one of the three equivalent mirror planes of the Bi_2Se_3 lattice. To ascertain the presence of a node or a minima in the gap structure we further examine the superconducting gap spectrum in the following section.

1.3.2 Fitting of superconducting gap spectra

We evaluated the SC gap spectrum from two different spots [Fig. 1.7(a,b)], taken in the SC area of Fig. 1.6. Fits to three different gap functions: isotropic, twofold-nodal and twofold-anisotropic are shown (discussion on the Dynes fitting routine can be found in Appendix A.4.2). They are obtained by fixing the temperature to $T_{\text{eff}}=0.7$ K and varying Γ and $\Delta_{\mathbf{k}}$ for fit optimization. Here $\Delta_{\mathbf{k}}= \Delta_0$, $\Delta_1|\cos\theta_{\mathbf{k}}|$ and $\Delta_0 + \Delta_1|\cos\theta_{\mathbf{k}}|$ for isotropic, nodal and anisotropic gap functions, respectively. Δ_0 corresponds to the purely isotropic part of

⁷A jump in the datapoints can be observed for $\phi= 335^\circ$ to 355° . This could be due to an instability in the magnet or a change in the tip apex conditions.

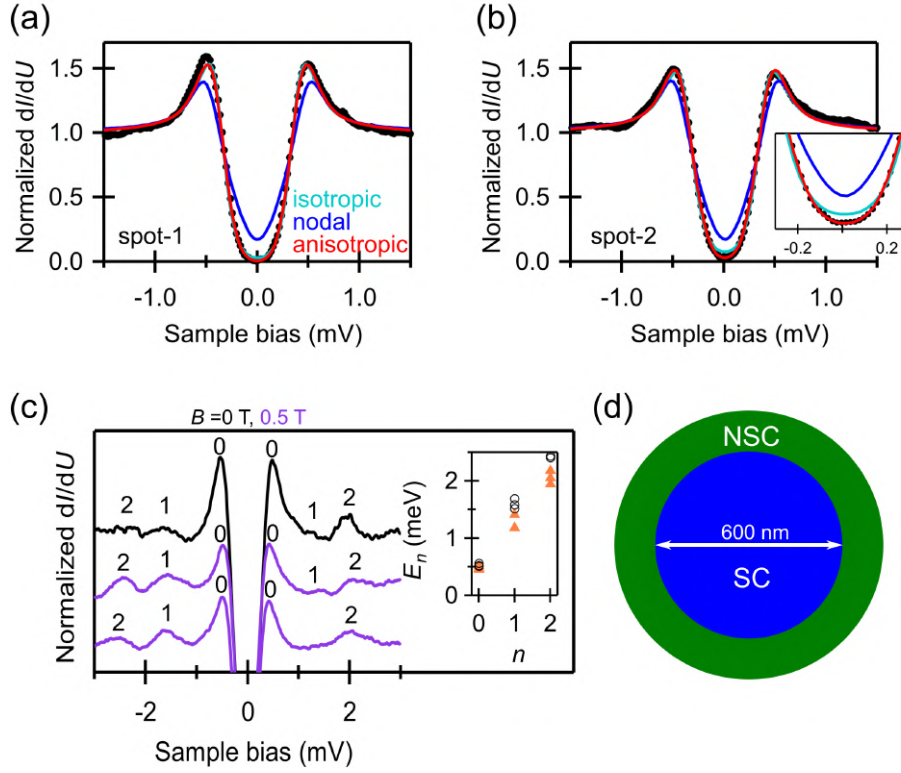


Figure 1.7: Fitting of superconducting gap spectra and peaks outside the superconducting gap. (a,b) High-resolution gap spectra obtained in the SC region described in Fig. 1.6 for different locations, spot-1 (a) and spot-2 (b). Fits to the spectra assuming three different gap functions [isotropic (cyan), nodal (blue), and node-lifted anisotropic (red)] are overlaid on the data. (c) Zoom-in around coherence peaks of gap spectra over a larger bias range for $B=0$ T (black trace) and $B_{//}=0.5$ T (violet traces). The violet traces are averaged over 13 spectra each. Two peaks (indicated with 1 and 2) are identified on positive and negative bias outside the coherence peaks ('0') in each case. Inset shows the energy of the peak positions versus the peak index n . Orange triangles (black open circles) correspond to peaks at positive (negative) bias. Stabilization parameters: $U = 3$ mV, $I = 100$ pA (a), $I = 200$ pA (b,c). (d) Schematics (top view) of the region from Fig. 1.6 where a SC region of ~ 600 nm in diameter (dimension of the crater) is surrounded by NSC region.

the gap function and the $\cos\theta_{\mathbf{k}}$ accounts for the anisotropy in Δ_1 . Upon comparing the quality of the three fit curves in Fig. 1.7(a,b) (see inset) we conclude that the anisotropic gap best describes the data. While the nodal fit fails entirely due to the presence of a hard gap around zero-bias (E_F), the isotropic gap fits the data well near the coherence peaks but fails near the bottom of the gap. In comparison, the anisotropic gap results in a good fit both near the coherence peaks and the gap bottom. The parameter values obtained from the anisotropic gap fit to the SC gap of spot-1 are $\Delta_0=0.27$ meV, $\Delta_1=0.17$ meV, $\Gamma=1$ μ eV; for spot-2 $\Delta_0=0.21$ meV, $\Delta_1=0.23$ meV, $\Gamma=4$ μ eV. This gives an anisotropy ratio of $(\Delta_0+\Delta_1)/\Delta_0=1.63$ and 2.1 for spot-1 and spot-2, respectively. Similar values of 1.8 and 1.2 were reported by Tao *et al.* [32] on the surface of $\text{Cu}_x\text{Bi}_2\text{Se}_3$. Note that in both spot-1 and spot-2 we have measured a total gap, i.e., $\Delta_0+\Delta_1$ of 0.44 meV.

The above analysis precludes the presence of nodes in the gap function of $\text{Cu}_x\text{Bi}_2\text{Se}_3$. Instead it consists of gap minima along with a twofold symmetry in the surface plane. Additionally, adjacent to the coherence peaks of the SC gap we observe oscillatory features in the dI/dU spectra, both for positive and negative bias voltage [Fig. 1.7(c)]. Depending on the spatial position where the spectrum is taken these features appear more or less pronounced-ruling out the possibility that they are part of the background density of states, i.e., a tip artifact. Moreover, application of a magnetic field does not particularly change the bias positions or lead to further broadening of the features [compare black and violet trace in Fig. 1.7(c)].

To understand the possible origin of the above features it is helpful to have an idea of the geometric configuration of the area under consideration. The topograph of Fig. 1.6(a) is approximated schematically in Fig. 1.7(d): a SC region of diameter ~ 600 nm is surrounded by a NSC region. Such a configuration may result in quasiparticles (unpaired electrons) inside the SC which have a energy higher than the gap energy to undergo Andreev reflections at opposing boundaries. Constructive interference between the incident and Andreev reflected particle leads to oscillations in the local density of states which can be observed in the tunneling spectra in the form of multiple peaks and are known as Tomasch oscillations [75, 76]. A intuitive picture of the Tomasch effect can be found in Refs. [77, 78]. The energy of the n th conductance peak for the effect is given by the expression [79]:

$$E_n \simeq \left(\Delta^2 + \left[\frac{nhv'_F}{2d} \right]^2 \right)^{1/2} \quad (1.3)$$

where Δ is the SC gap, v'_F is the renormalized Fermi velocity, n is the peak number, and d is the thickness of the superconductor. For the three spectra given in Fig. 1.7(c) we have indexed the peaks, with $n=0$ being the coherence peaks of the gap. Upon plotting the energy of the peaks versus the peak index [inset of Fig. 1.7(c)] we find that the positive and negative bias/energy peaks for a given index are not perfectly symmetric and do not occur at the exact same energy position across different spectra (the orange triangles and open circles do not overlap). However, considering the average of the data points for each peak index, E_n vs. n and E_n^2 vs. n^2 can be fit to a straight line. From the fit we have extracted

Δ and d , based on Eq. 1.3. Assuming a Fermi velocity of 5.8×10^5 m/s⁸ [80] we obtain $\Delta = 0.74 \pm 0.2$ meV and $d = 1 \mu\text{m} \pm 50$ nm. These values are comparable to the extracted gap size of 0.44 meV and exposed SC region of diameter 600 nm. Moreover the larger value d obtained from this analysis lends support to the picture we presented earlier that the SC region extends beyond the exposed region of the crater going underneath the NSC layers.

Sometimes peak features in the form of a 'dip-hump' are observed in the conductance spectra outside the SC gap. They are attributed to phonon structure where energy of the phonon mode (Ω) is given as, $\Omega = E_{\text{dip}} - \Delta$. Such features were reported for cuprates, iron-based and heavy fermion superconductors [81, 82] and more recently in magic-angle twisted trilayer graphene [83]. In the present case we rule out this possibility since such phonon modes were not reported in the measurements of Tao *et al.* [32]. Moreover, a clear 'dip' preceding the peak, which is unique to inelastic tunneling processes that are involved in phonon mode excitations, is not resolved in our spectra.

1.3.3 Structural defects: Non-QL step height and atomic defects

In this section we provide an overview of the topographic variations on the surface of Cu_xBi₂Se₃, summarized in Fig. 1.8. We will not provide any correlation between particular topographic features and the observation of superconductivity since the data quality is insufficient for any systematic analysis.

The doped samples are expected to cleave along the vdW gap to expose an atomically flat Se layer of Bi₂Se₃. However, large flat terraces corresponding to such a layer were found only for limited scan regions on the sample. As an example two such areas are shown in Fig. 1.8(a,b). While region-I (R-I) shows moderate coverage, the steps in region-II (R-II) are heavily covered with atom clusters with signs of irregular growth along the steps. Further, steps with little or moderate coverage usually show the Bi₂Se₃ quintuple layer step height of ~ 1 nm while higher coverage leads to different values, as observed in the case R-I and R-II, respectively [Fig. 1.8(c)].

The observed atom clusters on the surface reside in the vdW gap of the crystal and are left behind on the surface after cleaving. Assuming that the clusters are made of Cu, we note that the coverage of these atoms clusters is highly inhomogeneous. For example, for an area of 230 nm by 230 nm [Fig. 1.8(a)] and 30 nm by 30 nm [Fig. 1.8(d)], we expect ~ 100000 and ~ 1800 Cu atoms, respectively⁹. While the former case matches our expectation, the latter is far from it.

Apart from the vdW gap, Cu atoms may occupy various positions in the Bi₂Se₃ quintuple layer giving rise to structural defects. This defect will have a unique appearance in the STM image as it perturbs the LDOS on the surface. Proper identification of the defect

⁸Renormalized Fermi velocity would be lower, hence it is an upper bound.

⁹In the unit cell area of 0.148 nm^2 , on the surface we expect 0.3 Cu atoms (doping value). Based on this we calculate the amount of Cu atoms expected for the area of the two images. For the actual amount of Cu atoms in Fig. 1.8(a), we find a lower bound (143000 atoms) from the area covered by the atoms clusters and assuming that the Cu atoms here are arranged similar to the Se lattice.

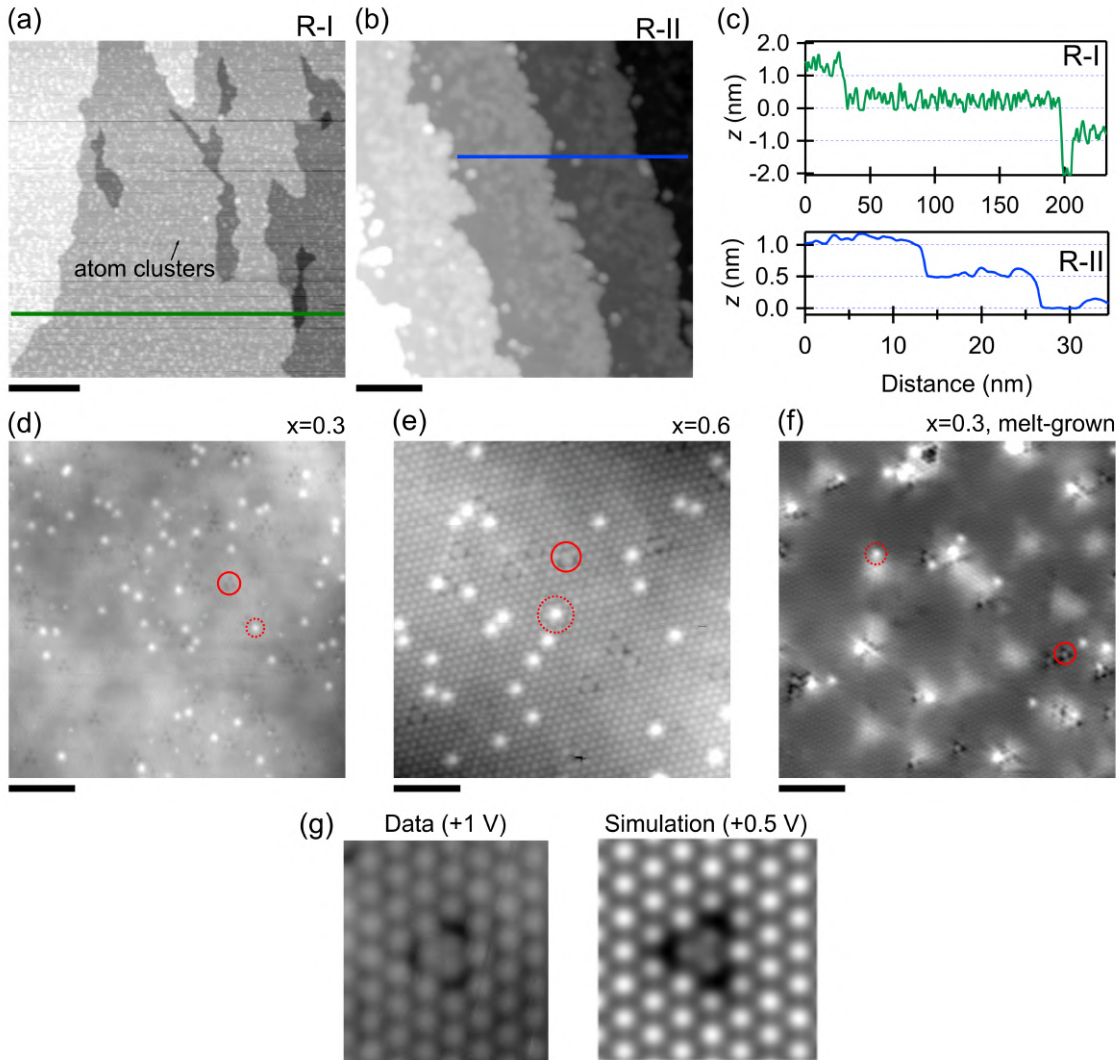


Figure 1.8: Non-QL step height and atomic defects. (a,b,c) Typical topographic images on the surface of $\text{Cu}_x\text{Bi}_2\text{Se}_3$ (a,b) with corresponding terrace heights (c) obtained along the green line in (a) and blue line in (b). (d,e,f) Two kinds of defects are marked by red solid and dashed circles. These defects can be seen in samples grown using the electrochemical intercalation method for $x=0.3$ (d) and $x=0.6$ (e) as well as the sample obtained using melt-growth (f). (g) Zoom image of defect marked with solid red circle is compared with simulated image from Ref. [84], both for positive bias. Scale bars: (a) 50 nm; (b) 10 nm; (d) 6 nm; (e) 3 nm, 1 nm; (f) 5 nm. Scan parameters:(a) $U = 4 \text{ V}$, $I = 20 \text{ pA}$; (b) $U = 900 \text{ mV}$, $I = 100 \text{ pA}$; (d) $U = 1 \text{ V}$, $I = 20 \text{ pA}$; (e) $U = 1 \text{ V}$, $I = 100 \text{ pA}$; (f) $U = 1 \text{ V}$, $I = 2 \text{ nA}$.

is possible after comparison with *ab initio* simulated images [85]. Figure 1.8(d-f) show images, that were obtained on samples which differ in doping level and growth technique, with considerable amount of defects. The two common ones are encircled with red solid and dashed lines. With the help of Ref. [84], the former is identified to be substitutional Cu defect in the second Bi layer. However, the density of this defect ($\sim 8.1 \times 10^{19} \text{ cm}^{-3}$) can account for only 4% of the expected nominal Cu dopant concentration ($2.1 \times 10^{21} \text{ cm}^{-3}$). Experimentally we have ascertained that this defect is indeed associated with Cu doping since we have observed this defect on Bi₂Se₃ after thermally evaporating Cu onto it under UHV conditions and at room temperature (data not presented). At present we have no reason to believe that this defect is associated with superconductivity since the Bi₂Se₃ crystal did not turn superconducting. Moreover, it is known that a Bi substitution defect leads to *p*-type doping [86] and hence the presence of this defect conflicts with the notion that electron doping induces superconductivity in the material.

The second most abundant defect (marked with a dashed circle) with a density of $\sim 4 \times 10^{19} \text{ cm}^{-3}$ is a substitution of the Se atom on the top layer by Bi (Bi antisites). The presence of this defect may be indirectly related to the Cu dopants, i.e., the Cu atoms replace Bi atoms and the Bi atoms in turn replace Se atoms, thereby creating Bi antisites defects. Any other defect found in the images, are not unique to Cu_xBi₂Se₃ and typically found in undoped Bi₂Se₃ as well [58].

1.3.4 Measuring LDOS over a large bias range

dI/dU spectrum, which is proportional to the LDOS of the sample, when taken for a larger bias range can be used to identify the underlying band structure close to the Γ point. A typical dI/dU spectrum on Bi₂Se₃ [as found in Refs. [42, 87] and our data in Fig. 1.9(a)] shows a minimum in the LDOS which is identified as the Dirac point (DP) of the TSS. The onset of the BCB and BVB are identified from the change in slope of the dI/dU signal on either side of the DP and such that the difference in energy corresponds to the bulk bandgap of ~ 0.3 V. The spectrum obtained in a NSC area of Cu_xBi₂Se₃ closely resembles the spectrum on undoped Bi₂Se₃ [Fig. 1.9(a)]. It is possible that the true position of the DP is obscured by some tip-states or that the DP has moved in comparison to undoped Bi₂Se₃. In literature, *ab initio* calculations predict the latter in case of stacking faults in the crystal [88].

Moving to the spectrum acquired on a superconducting region of Cu_xBi₂Se₃ [Fig. 1.9(b)] we find that it is rather atypical, i.e., we cannot assign the different parts of the Bi₂Se₃ band structure in a manner that we have discussed in the last paragraph. Or in other words this method of assignment of the onset of the BCB and BVB gives us uncharacteristically large bandgap values. Interestingly, our spectrum bears similarity to the one obtained by Tao *et al.* [32] on Cu_xBi₂Se₃, in a SC area [Fig. 1.9(b), gray trace]. In both spectra clear signatures of the TSS is missing. In this regard, *ab initio* calculations show that expansion of the vdW gap due to dopant intercalation can cause the TSS to move to lower QLs [89] and in that case it will not show up in our dI/dU spectrum.

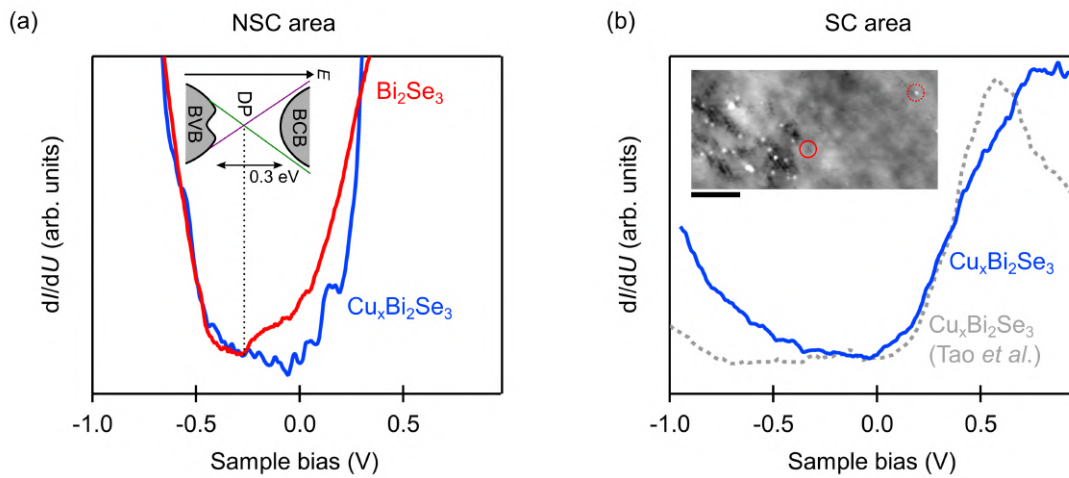


Figure 1.9: Large-scale spectroscopy on Bi_2Se_3 and $\text{Cu}_x\text{Bi}_2\text{Se}_3$. (a) Normalized dI/dU spectra on the surface of undoped Bi_2Se_3 (red trace) and NSC region of $\text{Cu}_x\text{Bi}_2\text{Se}_3$ (blue trace). Inset shows a cartoon of the Bi_2Se_3 band structure. Vertical dashed line indicates that the minimum in the LDOS is identified as the DP. (b) dI/dU spectra on the SC region of $\text{Cu}_x\text{Bi}_2\text{Se}_3$, our data (blue trace) and data from Ref. [32] (gray trace). Inset shows a topographic image of the SC region with previously identified defects, scale bar is 10 nm. Stabilization parameters: (a) $U = -900$ mV, $I = 1$ nA (red trace); $U = 900$ mV, $I = 200$ pA (blue trace); (b) $U = 950$ mV, $I = 200$ pA (blue trace). Scan parameters: (b) $U = 900$ mV, $I = 200$ pA (blue trace); $U = 1$ V, $I = 100$ pA (gray trace).

1.4 Conclusion

We now summarize the main points of our experiment. For carrier concentrations of $\sim 10^{20}$ cm⁻³, the Fermi surface of Cu_xBi₂Se₃ is shown to be open cylindrical in shape. Such a Fermi surface can support a quasi-2D TSC with dispersive Majorana modes only at step edges and at the side surface of the (001) plane. By examining such a side surface of a proximitized SC region we have found in-gap states as possible evidence of Majorana modes. Moreover, we did not find any in-gap states on the top surface.

Regarding the SC state itself, our spectroscopy data show an anisotropic gap structure on the surface of Cu_xBi₂Se₃: it is twofold symmetric with gap minima lying on one of the three equivalent mirror planes of the Bi₂Se₃ unit cell. According to the theory of Fu [34] this observation is compatible with the Δ_{4x} SC state but with lifted nodes. Such mirror symmetry protected nodes can be lifted on the surface due to the breaking of inversion symmetry which allows for different gap functions in the same symmetry channel to mix; an understanding which is presented in detail in the theoretical section of Chapter 3.

Note that for the above nematic state to be realized, based on the phase diagram of the superconducting order parameter, the chemical potential should be at least 2.3 times half the bulk bandgap (150 meV), meaning that the chemical potential is ~ 350 meV away from the center of the bulk bandgap or at least 195 meV inside the conduction band. We are unable to confidently identify the onset of the BCB from our spectroscopy data taken in a SC region and hence cannot comment on where the chemical potential lies with respect to the BCB.

In terms of topographic characterization of these samples, we have found structural defects in the form of non-quintuple-layer step heights and step bunching, which are indicative of strains in the sample. A point defect induced by Cu doping was identified. However, its density can only account for 4% of the expected nominal Cu dopant concentration.

2 Dopant position and absence of surface superconductivity in Sr doped Bi_2Se_3

This chapter discusses results from two publications:

(1) Y. R. Lin*, M. Bagchi*, S. Soubatch, T.-L. Lee, J. Brede, F. C. Bocquet, C. Kumpf, Y. Ando, and F. S. Tautz, "Vertical position of Sr dopants in the $\text{Sr}_x\text{Bi}_2\text{Se}_3$ superconductor", Phys. Rev. B 104, 054506 (2021) (*equal contribution).

(2) M. Bagchi, J. Brede, and Y. Ando, "Observability of superconductivity in Sr-doped Bi_2Se_3 at the surface using scanning tunneling microscope", Phys. Rev. Mater. 6, 034201 (2022).

The second publication is included as a part of this thesis. My contribution to this publication includes sample growth, bulk characterization, STM characterization, data analysis, preparation of all figures and a first draft of the description of the experimental section of the paper.

2.1 Overview

$\text{Sr}_x\text{Bi}_2\text{Se}_3$ is another member of the family of doped Bi_2Se_3 superconductors showing a pronounced twofold symmetry in bulk measurements of upper critical field [90], calorimetry [91] and specific heat [92] under a rotating magnetic field in the ab -plane which is then related to the symmetry of the superconducting gap. By examining the in-plane symmetry of the gap with respect to the crystal lattice a Δ_{4y} gap structure was found in each case. Interestingly, Sun *et al.* [92] also observed this twofold symmetry in the specific heat signal measured in the normal state, which they have explained by considering the Zeeman shift of bulk states with opposite spins for different orientations of the in-plane magnetic field. A finite contribution of the Zeeman shift in the form of increased amount of quasiparticles for certain field direction is possible only if there is an anisotropy in the normal state bulk density of states itself. Note that this observation of an anisotropy in the density of states prior to the superconducting transition was found only in case of $\text{Sr}_x\text{Bi}_2\text{Se}_3$ and in particular in the specific heat measurement. Other exciting experiments on $\text{Sr}_x\text{Bi}_2\text{Se}_3$ include those performed by Kostylev *et al.* [93] where the orientation of the SC state with respect to the lattice could be controlled through the application of an external uniaxial stress .

Such challenging experiments on $\text{Sr}_x\text{Bi}_2\text{Se}_3$, as opposed to $\text{Cu}_x\text{Bi}_2\text{Se}_3$, were possible due to the samples being insensitive to air and showing a significantly better superconducting SF of more than 90%. Moreover, $\text{Sr}_x\text{Bi}_2\text{Se}_3$, which can only be grown via the melt-growth technique [46], tends to be 'harder' than the $\text{Cu}_x\text{Bi}_2\text{Se}_3$ samples obtained using

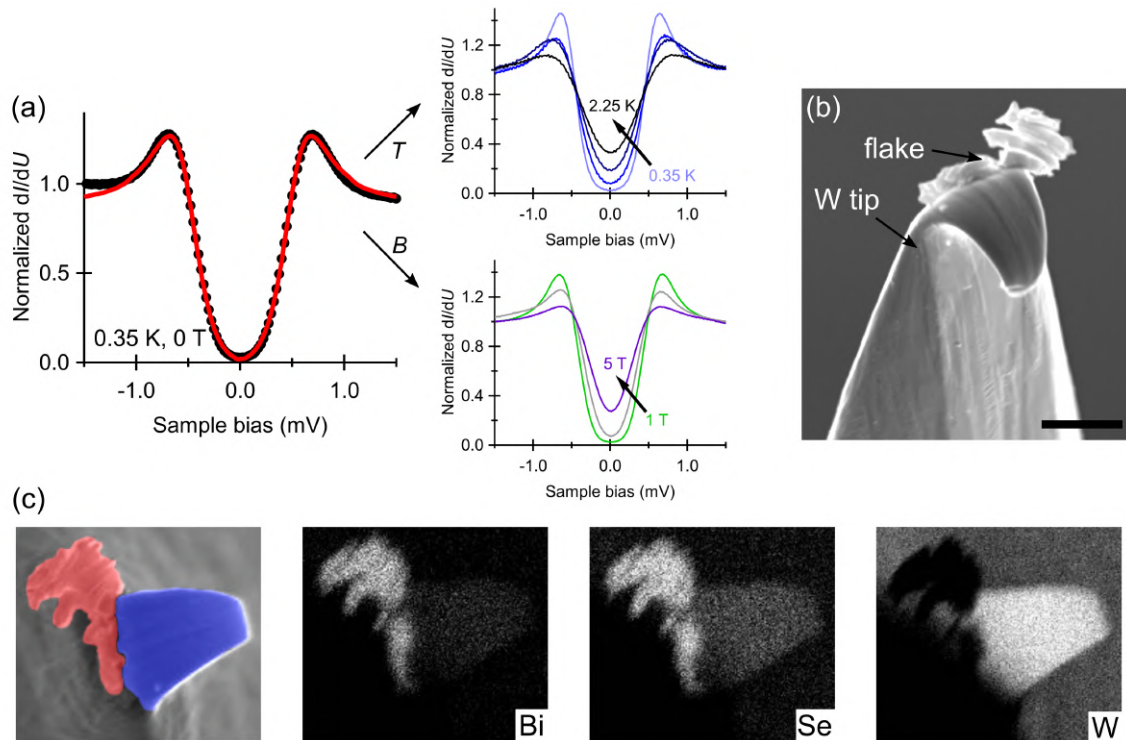


Figure 2.1: Transfer of SC Sr_xBi₂Se₃ flakes onto the STM tip. (a) A SC gap of 0.5 meV is observed on the sample surface at a system temperature of 0.35 K and no magnetic field. Its reaction to increasing temperature (top right) and magnetic field (bottom left) confirms that the gap is SC in nature. (b) SEM image of the W-tip that was used to measure the data in (a), showing a flake that is several microns in size. Scale bar corresponds to 5 μm . (c) The flake from (b) is imaged at a different angle; the flake is shaded in red and the tip part in blue. EDX analysis shows the chemical species of Bi and Se on the flake region and W in the tip region (white color corresponds to high intensity).

electrochemical intercalation and therefore easier to handle. These positive attributes motivated us to select this member, among other doped Bi_2Se_3 materials, to elucidate the position of the dopant in the unit cell using STM and the technique of normal incidence x-ray standing wave (NIXSW) [publication (1)]. The STM measurements could not identify any unique defect that could be assigned to the Sr dopant. Furthermore if we summed over the defect densities for all observed defects we are more than an order of magnitude lower than the defect density expected to be observed in a STM image for a nominal doping level of $x=0.06$ (1 Sr atom in ~ 6 unit cell). On the other hand the NIXSW data provided strong constraints on the position of the dopant. It excluded the possibility that the dopants reside in the vdWs gap and suggested that they are instead located inside the quintuple layer, close to the mirror symmetric Se layers on the top and bottom. Our interpretation is in agreement with those of Li *et al.* [94] (TEM studies on $\text{Sr}_x\text{Bi}_2\text{Se}_3$) and Froehlich *et al.* [95] (neutron-scattering experiments on $\text{Cu}_x\text{Bi}_2\text{Se}_3$).

We performed further spectroscopic experiments on the surface of $\text{Sr}_x\text{Bi}_2\text{Se}_3$ with our results presented in publication (2). While STS characterization on the surface of $\text{Sr}_x\text{Bi}_2\text{Se}_3$ had been performed by Du *et al.* [97] and Kumar *et al.* [98], closer inspection of their data showed inconsistencies between the bulk and surface values of T_c and H_{c2} . Similar inconsistencies were noted by Wilfert *et al.* [99] for Tl-doped Bi_2Te_3 and Nb-doped Bi_2Se_3 who pointed out that nominally normal conducting tips can become unintentionally superconducting during the course of the experiment. In this regard we are able to provide hard evidence by performing scanning electron microscopy (SEM) and energy-dispersive x-ray analysis (EDX). For example, in Fig. 2.1¹ we have measured a superconducting gap of 0.5 meV, much larger than the expected size from the bulk T_c of 2.6 K. Its reaction to temperature and magnetic field is different from the expectation for a bulk crystal; a sizable gap is measured at T of 2.25 K or for a magnetic field of 5 T at base temperature. Upon imaging the W tip apex used for the measurement we find a several micron large flake [Fig. 2.1(b)]. By performing an EDX analysis [Fig. 2.1(c)] we have ascertained that this flake was picked up from the sample and is not part of the tip material, proving that contamination of the STM tip with sample flakes can cause spurious observation of superconductivity.

With the above knowledge we performed careful spectroscopy measurements on the surface of $\text{Sr}_x\text{Bi}_2\text{Se}_3$ using clean metallic tips (at least 10 fresh W-tips were used on 5 different $\text{Sr}_x\text{Bi}_2\text{Se}_3$ samples for multiple cleaves) and came to the conclusion that a SC gap is never observed on the surface even though bulk measurements show a SC SF greater than 75%. To explain this peculiar observation we proposed that intrinsic electric field near the surface of doped Bi_2Se_3 leads to the suppression of the superconducting gap. The electric field arises due to the negative carriers present in the surface state of an n-type Bi_2Se_3 crystal being screened out only after a length scale of ~ 1 nm from the surface (can be estimated based on the Thomas-Fermi screening model). The strength of the electric field can be estimated from the experimentally observed upward band bending of ~ 100 meV, a measure

¹This particular dataset was obtained on the CPSBS sample [Ch. 3] but our observations can be reproduced on any superconducting doped Bi_2Se_3 sample.

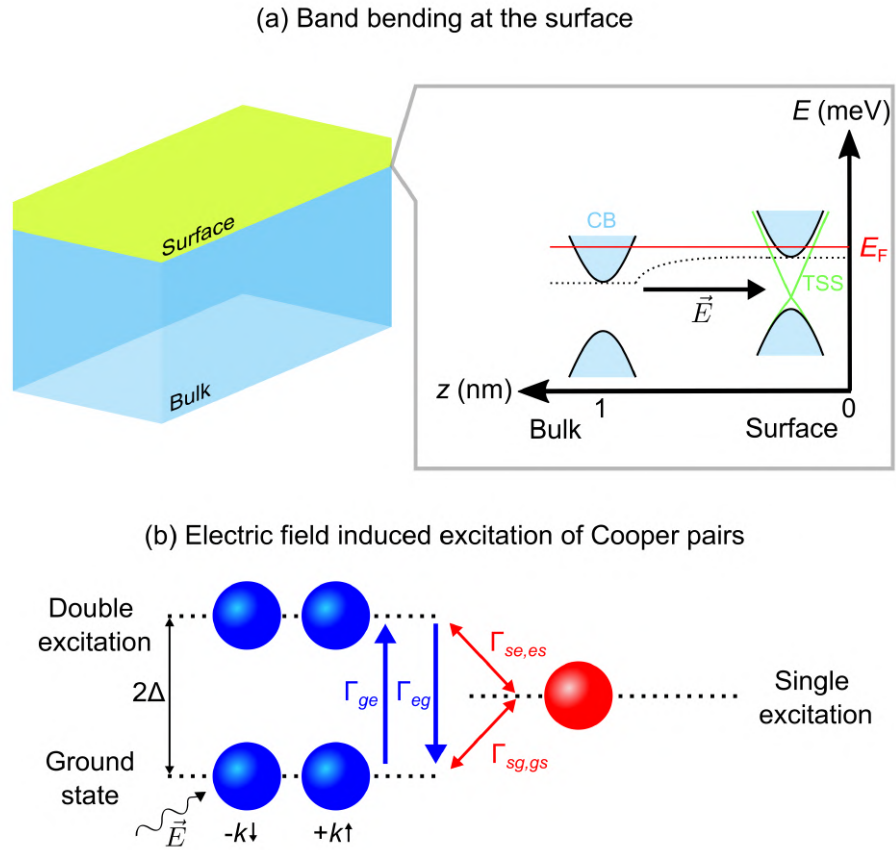


Figure 2.2: Upward band bending at the surface and electric field induced breaking of Cooper pairs. (a) Schematics showing the upward band bending of the conduction band (CB) in going from the bulk to the surface due to the presence of a local electric field over a length scale of ~ 1 nm. (b) Transition scheme for the Sauter-Schwinger effect in BCS superconductors in presence of an intense electric field, as depicted in Ref. [96]. Γ_{ge} and Γ_{eg} are the transition rates between the ground and excited states. This is a double excitation which 'preserves the coherent interaction of the pair'. Cooper pairs are destroyed through single excitations whose transition rates are denoted as Γ_{se} , Γ_{es} , Γ_{sg} , and Γ_{gs} .

of the surface potential which exists over a distance of ~ 1 nm, giving a value of 10^8 V/m [Fig. 2.2(a)]. Electric fields of this order can lead to a double excitation of the ground state Cooper pair (the Sauter-Schwinger Effect) or single excitations which break the Cooper pairs [96]. All possible transitions are depicted in Fig. 2.2(b). Effectively such excitations or quasiparticles fill up the gap and no SC gap is observed in an averaging technique such as STS, even though the ground state and the doubly excited state still possess superconducting properties, i.e., a finite pair potential. However, we have confirmed that a superconducting gap is reproducibly observed when micron size $\text{Sr}_x\text{Bi}_2\text{Se}_3$ flakes are picked up by the tip. The superconducting gap on these flakes persist when redeposited onto the sample surface. To explain this phenomenon we proposed that mechanical strain experienced by the flake during transfer could destroy the topological surface state which in turn should lead to the disappearance of the local electric field and allow for superconductivity to extend to the surface. The discrepancies in the SC properties observed in earlier STM studies [97, 98] can now be easily reconciled by assuming that a flake was present on the tip. Importantly, the measured superconducting properties of the flake on the STM tip is dictated by the specific geometry of SC material (see Ref. [100]) and needs to be taken into account when interpreting the measured values. However, such a constraint should not apply when the flake is measured by redepositing on the sample. The superconducting properties of the flake should then reflect those of the bulk of the sample.

It may be possible to restore superconductivity on the surface of $\text{Sr}_x\text{Bi}_2\text{Se}_3$. For this purpose one must get rid of the electric field. Metals screen out the electric field the fastest, meaning that we must increase the bulk carrier density or heavily n-dope the sample. To this end we grew PdTe_2 and deposited Cu atoms on the surface. Unfortunately, only a weak n-doping was observed in the latter case. Significant n-doping may be achieved by depositing alkali metal atoms on the surface of $\text{Sr}_x\text{Bi}_2\text{Se}_3$.

Observability of superconductivity in Sr-doped Bi_2Se_3 at the surface using scanning tunneling microscope

Mahasweta Bagchi , Jens Brede ,* and Yoichi Ando [†]
Physics Institute II, University of Cologne, D-50937 Köln, Germany

 (Received 22 December 2021; accepted 15 February 2022; published 7 March 2022)

The superconducting materials family of doped Bi_2Se_3 remains intensively studied in the field of condensed matter physics due to strong experimental evidence for topologically nontrivial superconductivity in the bulk. However, at the surface of these materials, even the observation of superconductivity itself is still controversial. We use scanning tunneling microscopy (STM) down to 0.4 K to show that on the surface of bulk superconducting $\text{Sr}_x\text{Bi}_2\text{Se}_3$, no gap in the density of states is observed around the Fermi energy as long as clean metallic probe tips are used. Nevertheless, using scanning electron microscopy and energy-dispersive x-ray analysis, we find that micrometer-sized flakes of $\text{Sr}_x\text{Bi}_2\text{Se}_3$ are easily transferred from the sample onto the STM probe tip and that such flakes consistently show a superconducting gap in the density of states. We argue that the superconductivity in $\text{Sr}_x\text{Bi}_2\text{Se}_3$ crystals does not extend to the surface when the topological surface state (TSS) is intact, but in microflakes, the TSS has been destroyed due to strain and allows the superconductivity to extend to the surface. To understand this phenomenon, we propose that the local electric field, always found in electron-doped Bi_2Se_3 in the presence of the TSS due to an intrinsic upward band bending, works against superconductivity at the surface.

DOI: [10.1103/PhysRevMaterials.6.034201](https://doi.org/10.1103/PhysRevMaterials.6.034201)

I. INTRODUCTION

Shortly after the discovery of superconductivity in Cu-doped Bi_2Se_3 crystals [1], Fu and Berg [2] proposed that any electron-doped Bi_2Se_3 is a viable candidate for hosting topological superconductivity with spin-triplet-like pairing. The spin-triplet-like nature of the pairing was successively confirmed by temperature-dependent nuclear magnetic resonance Knight shift (K_s) experiments [3], which found no change in K_s below T_c for magnetic fields applied parallel to the c axis. Moreover, the same experiments found that the threefold-symmetric Bi_2Se_3 lattice showed a two-fold anisotropy of K_s when the magnetic field was rotated in the ab plane. This indicates a spontaneous rotational symmetry breaking of the superconducting state. The twofold symmetry of the superconducting state was also observed in specific heat [4], which indicates that this symmetry breaking is due to an anisotropy in the superconducting gap amplitude and points to nematic superconductivity [5]. A recent high-resolution x-ray diffraction (XRD) experiment clarified [6] that a tiny ($\sim 0.02\%$) lattice distortion dictates the nematic axis. Theoretically, this nematic superconductivity is expected in doped Bi_2Se_3 superconductors for the superconducting gap function having E_u symmetry [2,7,8], which is topologically nontrivial.

Concurrently with the bulk characterization, surface sensitive techniques, in particular scanning tunneling microscopy (STM) and spectroscopy (STS), were used to study the superconducting properties at the surface of doped Bi_2Se_3 crystals.

Already in 2013, Levy *et al.* [9] reported the observation of both normal-conducting and superconducting (SC) domains at the surface of Cu-doped Bi_2Se_3 . These SC domains showed a fully gapped local density of states (LDOS) at the Fermi level that could be well-described within the Bardeen-Cooper-Schrieffer (BCS) theory. The observed gap width was $\Delta = 0.4$ meV at the surface and bulk resistance versus temperature measurements showed a superconducting transition at around 3.65 K. Moreover, vortices with a diameter of about 30 nm were observed at the surface under an applied out-of-plane magnetic field of more than 0.5 T, and the upper critical field was determined to be $\mu_0 H_{c2} \approx 1.65$ T. Interestingly, no zero bias conductance peaks were observed in the vortex core by Levy *et al.* [9], while a more recent STM study of Cu-doped Bi_2Se_3 by Tao *et al.* [10] resolved an Abrikosov lattice consisting of elliptically-shaped vortices on the surface, which also hosted a zero bias conductance peak. However, Tao *et al.* [10] also documented two different SC domains with largely different gap sizes of 0.46 and 0.77 meV, and 96% of the surface areas they studied did not show any superconductivity.

Such differences in the superconducting properties observed at the surface of Cu-doped Bi_2Se_3 may be related to the comparatively poor superconducting volume fraction of only about 40%–50% [11] and associated inhomogeneity of the superconducting phase throughout the sample. In this regard, $\text{Sr}_x\text{Bi}_2\text{Se}_3$ is better suited to STM studies since the superconducting volume fraction reaches more than 90% [12] and thus one expects to avoid the ambiguity between local probe and bulk measurements that arises due to inhomogeneity.

However, at the surface of a $\text{Sr}_x\text{Bi}_2\text{Se}_3$ crystal with a bulk T_c of 2.4 K, Han *et al.* [13] observed a superconducting gap

*brede@ph2.uni-koeln.de

[†]ando@ph2.uni-koeln.de

which only dropped to 75% of the normal state conductance at the Fermi energy despite a gap size of $\Delta \approx 0.5$ meV. The authors attributed their observation to their relatively high measurement temperature of 1 K. In 2017, Du *et al.* [14] observed on the surface of a $\text{Sr}_x\text{Bi}_2\text{Se}_3$ crystal with a bulk T_c of 3 K, SC domains with the gap size of $\Delta \approx 0.42$ –1.15 meV. Moreover, for a domain with $\Delta \approx 0.8$ meV a $T_c = 5$ K and $\mu_0 H_{c2} \approx 5$ T was reported. Note that in the bulk of $\text{Sr}_x\text{Bi}_2\text{Se}_3$, $\mu_0 H_{c2}$ amounts only to about 1.5 T [15]. A recent work by Kumar *et al.* [16] reported a superconducting gap of $\Delta \approx 0.19$ –0.31 meV on the surface of a $\text{Sr}_x\text{Bi}_2\text{Se}_3$ crystal with the bulk T_c of 2.9 K.

With regards to such inconsistencies, Wilfert *et al.* [17] recently showed that for Tl-doped Bi_2Te_3 and Nb-doped Bi_2Se_3 , the superconducting gaps on the surface were exclusively observed due to the nominally normal conducting probe tips becoming unintentionally superconducting during the experiments. Similar experimental pitfalls were also reported for Cu-doped Bi_2Se_3 by Levy *et al.* [9]. Interestingly, Wilfert *et al.* [17] concluded that for Tl-doped Bi_2Te_3 and Nb-doped Bi_2Se_3 , superconductivity does not extend to the surface where the topological surface state resides.

Here, to clarify this complicated situation, we use transport measurements to characterize the bulk T_c and the carrier concentration of high-quality single crystals of $\text{Sr}_x\text{Bi}_2\text{Se}_3$ and subsequently perform high-resolution studies of STM and STS on the surface of crystals which are cleaved under ultra high vacuum conditions (UHV). Our base temperature is 0.4 K.

II. EXPERIMENTAL METHODS

Crystal growth. Single crystals of $\text{Sr}_x\text{Bi}_2\text{Se}_3$ (nominal $x = 0.06$) are grown from high-purity elemental Sr chunk (99.99%), Bi shots (99.9999%), and Se shots (99.9999%) by a conventional melt-growth method. The raw materials with a total weight of 4.0 g are mixed and sealed in an evacuated quartz tube. The tube is heated to 850 °C for 48 h. It is then slowly cooled from 850 °C to 600 °C within 80 h and finally quenched into water at room temperature.

Transport measurements. Resistivity and Hall measurements on the samples are performed in a Quantum Design Physical Properties Measurement System (PPMS) in the standard four-terminal configuration using a low-frequency ac lock-in technique.

STM measurements. STM experiments are carried out under UHV conditions with a commercial system (Unisoku USM1300) operating at 0.4 K. Data are acquired at 0.4 K unless mentioned otherwise. Topograph and dI/dU maps are recorded in the constant-current mode. Point spectroscopy data is obtained by first stabilizing for a given set-point condition and then disabling the feedback loop. dI/dU curves are then recorded by means of a lock-in amplifier by adding a small modulation voltage U_{mod} to the sample bias voltage U . High resolution dI/dU spectra of superconducting gaps were normalized by fitting a second degree polynomial to the data outside the SC gap and dividing by the fitted polynomial. We have used both PtIr and W probe tips. All PtIr tips used are commercially obtained from Unisoku. The W tips are made in-house. Both types are electrochemically etched. The PtIr

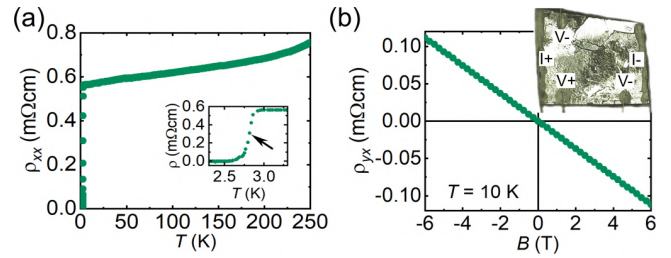


FIG. 1. (a) Temperature dependence of the resistivity (ρ_{xx}) of a $\text{Sr}_x\text{Bi}_2\text{Se}_3$ crystal used for this work. The inset shows the superconducting transition with the mid-point $T_c = 2.8$ K. (b) Magnetic-field dependence of the Hall resistivity (ρ_{yx}) measured at 10 K, which gives the carrier density of $3.4 \times 10^{19} \text{ cm}^{-3}$. The inset shows a picture of the $\text{Sr}_x\text{Bi}_2\text{Se}_3$ sample with contacts for resistivity and Hall measurements.

tips are either fresh new tips or they have been prepared by Ar ion sputtering (at an argon pressure of 3×10^{-6} mbar and a voltage of 1 kV), followed by repeated heating by electron bombardment (~ 15 W) for 20 s. Further tip forming is done by scanning on the Cu(111) surface until a clean signature of the surface state is obtained in spectroscopy. The absence of a superconducting gap on Cu(111) is also verified prior to measurements on $\text{Sr}_x\text{Bi}_2\text{Se}_3$. For STM measurements, $\text{Sr}_x\text{Bi}_2\text{Se}_3$ crystals are cleaved at room temperature and under UHV conditions. The crystal is cleaved by breaking off a 10 mm sized pole glued on the sample. The two-component epoxy glue (EPO-TEK H21D) is hardened by heating to 373 K under high vacuum conditions. STM data are processed using the WSXM software [18] and IGOR PRO 9.0.

SEM and EDX analysis. Scanning electron microscope (SEM) image of the tip is obtained using the Raith Pioneer II system and the Jeol JSM-6510 SEM. Elemental chemical analysis of the material on the tip apex is done by energy-dispersive x-ray (EDX) analysis, performed using an Oxford Instruments AztecOne system with an x-act silicon drift detector that is combined with the Jeol SEM.

III. RESULTS AND DISCUSSION

A. Bulk properties

We have characterized the bulk properties of our $\text{Sr}_x\text{Bi}_2\text{Se}_3$ single crystals using resistivity (ρ_{xx}) and Hall resistivity (ρ_{yx}) measurements. An optical image of a typical sample ($5\text{mm} \times 4\text{mm} \times 0.7\text{mm}$) including the electrical contacts is shown in the inset of Fig. 1(b). The temperature dependence of the resistivity is metallic [Fig. 1(a)] with the onset of superconductivity and zero resistivity occurring at 2.90 and 2.65 K, respectively [inset of Fig. 1(a)]. The superconducting transition temperature T_c , defined by the mid-point of the resistive transition, is 2.8 K. The residual resistivity of 0.56 mΩ cm, which points to a high scattering rate that is always present in doped Bi_2Se_3 superconductors, is unusually large for an unconventional non-*s*-wave superconductor; nevertheless, it has been elucidated that in doped Bi_2Se_3 superconductors where the orbital degrees of freedom play an important role, the generalized Anderson's theorem protects the unconventional pairing from disorder [22,23].

TABLE I. Summary of bulk carrier density n reported for $\text{Sr}_x\text{Bi}_2\text{Se}_3$.

Reference	nominal Sr doping	carrier density n (10^{19} cm^{-3})
Liu 2015 [12]	0.062	2.65
Shruti 2015 [15]	0.1	1.85
Huang 2017 [19]	0.066	2.75
Kuntsevich 2019 [20]	0.064, 0.068	2.2, 2.1
Li 2018 [21]	0.05	5.7–10
Li 2018 [21]	0.08	6.8–9.2
this work	0.06	3.4–6.2

The carrier density in our samples is determined from ρ_{yx} measured at 10 K as a function of perpendicular magnetic field B [Fig. 1(b)]. The $\rho_{yx}(B)$ behavior is strictly linear in B and can be described by a single band, yielding a carrier density of $n = 3.4 \times 10^{19} \text{ cm}^{-3}$, which is extremely low for a superconductor with T_c of the order a few Kelvin. Table I gives an overview of the carrier density of $\text{Sr}_x\text{Bi}_2\text{Se}_3$ samples (varying nominal doping) as reported in literature along with the values observed for our samples. From Shubnikov-de Haas investigations by Köhler *et al.* [24] it is known that a carrier density of $n \approx 4 \times 10^{19} \text{ cm}^{-3}$ in Bi_2Se_3 corresponds to a Fermi energy of $E_F \approx 160 \text{ meV}$, which we use as a lower bound for the Fermi energy in the bulk of our $\text{Sr}_x\text{Bi}_2\text{Se}_3$ crystals. As an upper bound one can assume a simple parabolic dispersion for the bulk conduction band (BCB). Here, a carrier density of $n \approx 4 \times 10^{19} \text{ cm}^{-3}$ corresponds to $E_F \approx 270 \text{ meV}$ for an effective mass of $m_{\text{eff}} = 0.15m_e$ [24,25], with m_e the free electron mass.

The shielding fraction of our samples estimated from the zero-field-cooled magnetization measurement lies between 75% to 100% [26]. The actual data of one of the samples measured here, which showed the shielding fraction of 76%, were previously shown in Ref. [26].

B. Surface properties

A typical topograph of the cleaved $\text{Sr}_x\text{Bi}_2\text{Se}_3$ surface is shown in Fig. 2(a). The surface is atomically flat with some characteristic native defects, which we have previously discussed in detail [26]. A representative $(dI/dU)/(I/U)$ spectrum, which is proportional to the local density of states (LDOS), is shown in Fig. 2(b). The minimum of the LDOS is at -310 mV and corresponds to the Dirac point (DP). Based on the band structure of Bi_2Se_3 , which is well-known from ARPES experiments [13,25,27,28] and schematically depicted in Fig. 2(c), we assign the increase in slope at around -400 mV and below to the onset of the bulk valence band (BVB), and the increase at -100 mV and above to the BCB, respectively. Therefore, at the *surface* of this sample, the Fermi energy lies about 100 meV above the bottom of the BCB, which is much lower than the estimate of $E_F \approx 160\text{--}270 \text{ meV}$ based on transport measurements. However, this apparent disagreement is straightforwardly reconciled if we consider band bending to be present at the surface of electron-doped Bi_2Se_3 .

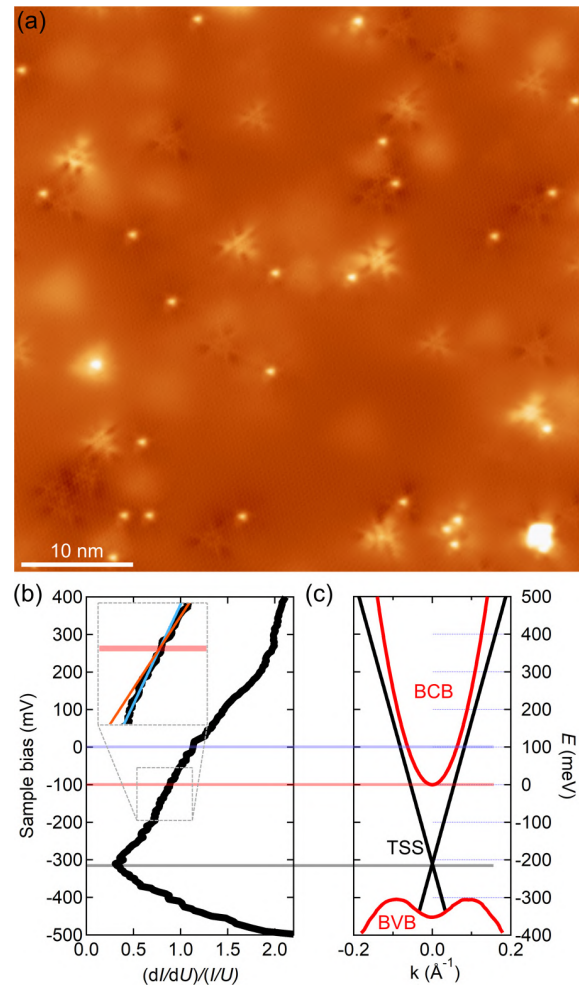


FIG. 2. (a) Typical STM image of the (001) surface of $\text{Sr}_x\text{Bi}_2\text{Se}_3$ crystal directly after cleaving. Only a small number of native defects (discussed in Ref. [26]) are visible. Scan parameter: $U = +100 \text{ mV}$ and $I = 20 \text{ nA}$. (b) Representative $(dI/dU)/(I/U)$ spectrum taken far away from any defect; inset shows a magnification of the range indicated by the gray dashed box to highlight a slight change in slope across -100 mV (red and blue lines with different slopes are a guide to the eye). Stabilization parameter: $U = -900 \text{ mV}$, $I = 2 \text{ nA}$, and $U_{\text{mod}} = 10 \text{ mV}_p$. (c) Schematic diagram of the band structure of $\text{Sr}_x\text{Bi}_2\text{Se}_3$: zero energy is set at the bottom of the bulk conduction band (BCB). Grey, red, and blue lines from (b) to (c) mark the Dirac point (DP) of the topological surface state (TSS), bottom of the conduction band, and the Fermi level, respectively. The Fermi level at the surface lies at $\sim 100 \text{ meV}$ in the BCB.

Band bending occurs due to charge transfer caused by the equilibration of the Fermi level at an interface. The charge transfer creates an electric field and the associated potential shifts the bands in the vicinity. In the case of a topological insulator, the existence of the TSS causes the charge distribution to be different near the surface compared to the bulk. When the TSS is electron-doped, the electrons in the TSS can be viewed as a negative surface charge σ_s . This surface charge is related to the surface potential $V_0 = V(z=0) \propto -\sigma_s$ through Poisson's equation and the condition of overall charge neutrality. Hence, the surface charge in the TSS causes a positive

potential leading to upward band bending of the BCB when going from the bulk to the surface. In other words, at the surface, charge equilibration causes fewer electrons in the BCB than in the bulk. For highly doped semiconductors, the decay of the potential into the bulk may be estimated within the Thomas-Fermi screening model as $V(z) = V_0 \exp(-z/r_{\text{TF}})$, where $r_{\text{TF}} \approx \sqrt{(\epsilon_0 \pi^2 \hbar^2)/(k_{\text{F}} m_{\text{eff}} e^2)} \approx 0.6 \text{ nm}$ is the Thomas-Fermi screening length and $k_{\text{F}} \approx 0.7 \text{ \AA}^{-1}$. Interestingly, calculations within the density functional theory (DFT) in Refs. [29,30] show that even for pristine Bi_2Se_3 an intrinsic upward band bending of the BCB of the order of $\sim 100 \text{ meV}$ takes place due to charge equilibration between bulklike states and the TSS when the Fermi energy lies above the DP. In these calculations, the BCB has recovered its bulk value at 2 or 3 nm below the surface.

To further validate our assignment of the spectral features in our $(dI/dU)/(I/U)$ data, we have performed additional spectroscopic characterization of the surface electronic structure by mapping the spatial variations of the LDOS. Typical dI/dU maps taken at the indicated bias voltages are shown in Figs. 3(a) and 3(b). The spatial modulation of the LDOS due to quasiparticle interference (QPI), as opposed to structural effects, is evident due to the decrease of the wavelength of the QPI patterns as the bias voltage is increased. Based on the band structure depicted in Fig. 2(c), the QPI at the indicated bias voltages can be due to scattering of carriers in the BCB or TSS. While contributions of scattering bulk carriers can not be ruled out, we will show in the following that the dominant contribution is due to the TSS.

For the TSS, the largest possible scattering vector \mathbf{q} is related to the wavevector \mathbf{k} through $\mathbf{q} = 2\mathbf{k}$. However, the condition $\mathbf{q} = 2\mathbf{k}$ corresponds to 180° backscattering, which is strongly suppressed for a TSS with spin-momentum locking. Therefore the dominant scattering vectors of the TSS will be smaller [31–33]. Even for Bi_2Se_3 , it has been predicted that the hexagonal warping of the TSS [34] will open new scattering channels at energies sufficiently above the DP [32]. Since the strength of the warping term in $\text{Sr}_x\text{Bi}_2\text{Se}_3$ is unknown, we simply use $\mathbf{q} \approx 1.5\mathbf{k}$ (which is known for the more strongly warped TSS of Bi_2Te_3 [33]) as a lower bound for the expected scattering vector length and $\mathbf{q} = 2\mathbf{k}$ as the upper bound. These two \mathbf{q} -vectors are indicated by semicircles in the Fourier transform (FT) of the dI/dU maps [insets of Figs. 3(a) and 3(b)] by taking $|\mathbf{k}|$ at the relevant energy from the TSS dispersion depicted in Fig. 2(c).

We only observe clear QPI at bias voltages $\geq 100 \text{ mV}$, i.e., more than 400 meV above the DP. At this energy the iso-energy surface of the TSS of Bi_2Se_3 has a hexagonal shape [32] and the TSS acquires a significant out-of-plane spin-polarization, enabling scattering vectors connecting opposite sides of the iso-energy surface mainly through the vertical spin component [31,34]. For the hexagonal iso-energy surface the expected \mathbf{q} vector is still close to $2\mathbf{k}$, which is in agreement with the substantial intensity in the FT of Fig. 3(a) near $\mathbf{q} = 2\mathbf{k}$. Extrapolating the iso-energy surface to 700 meV above the DP by considering the simple warping term [34] extracted from the data for Bi_2Se_3 [32], one expects a snowflakelike shape which is better known for Bi_2Te_3 [31,33,34]. The scattering vector $\mathbf{q} \approx 1.5\mathbf{k}$ would dominate in such an isoenergy surface, which is in agreement with the FT of Fig. 3(b).

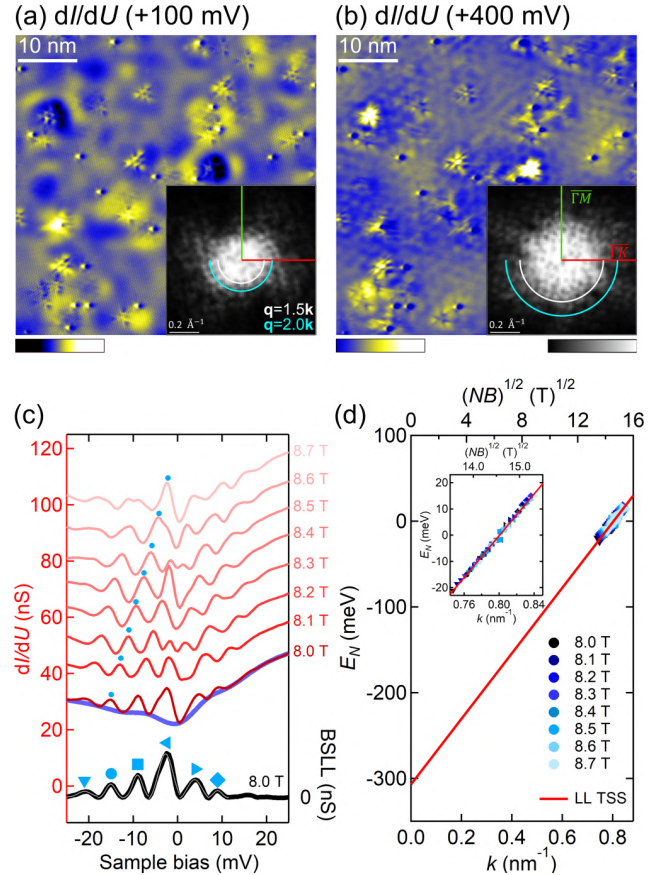


FIG. 3. [(a) and (b)] Differential conductance images at the sample bias of +100 (a) and +400 mV (b); the insets provide the corresponding Fourier-transform images. Blue and white semi-circles mark the expected positions of the scattering vector \mathbf{q} with $\mathbf{q} = 2\mathbf{k}$ and $1.5\mathbf{k}$, respectively, with \mathbf{k} the wave vector of the TSS. Set-point current: 20 nA. (c) dI/dU spectra recorded in the perpendicular magnetic field from 8 to 8.7 T with 0.1 T interval. Spectra are shifted vertically for clarity. All spectra are taken with stabilization parameters of $U = 50 \text{ mV}$, $I = 2 \text{ nA}$, $U_{\text{mod}} = 1 \text{ mV}_p$, and averaged over 20 repeated measurements. The bottom-most curve (black) is the background-subtracted Landau-level (LL) spectrum at 8 T. The background for the 8.0-T curve is shown in violet. In the background-subtracted LL spectrum, six peaks can be clearly identified and give the energy positions of the LLs. The LL peak marked with a blue circle can be tracked for different fields in the raw data shown in red. The peak position, which gives the eigenenergy E_N of each LL, is determined by fitting a single Gaussian to each peak and the error in E_N from the fit is always less than 0.2 meV. The combined fitting result is shown in thin grey line. (d) The eigenenergy E_N of the six LLs identified in the STS data for all B -field values are plotted as a function of \sqrt{NB} , where N is the LL index (top axis); the corresponding momentum k on the TSS is shown on the bottom axis. A linear fit (red line) with Eq. (1) gives $E_D = -306 \text{ mV}$ and $v_F = 5.8 \times 10^5 \text{ m/s}$.

However, we note that at these high energies above the DP hybridization of the TSS with bulk bands certainly needs to be considered explicitly and will lead to modification of the dispersion relation of the TSS that go beyond what is captured by a simple warping term. Moreover, since at these energies

the isoenergy surfaces not only have contributions from the TSS but also from the BCB [32], scattering of bulk electrons and interband scattering between TSS and BCB may also contribute to the observed QPI.

Given these difficulties in interpreting the observed QPI, we have also examined the response of the LDOS to an external magnetic field of more than 8 T applied along the surface normal. Under these conditions, electrons are quantized into Landau levels. In the case of Dirac electrons of the TSS, the energy E_N of the N th LL is to first approximation given as

$$E_N = E_D + \text{sgn}(N)v_F\sqrt{2eB\hbar|N|}, \quad (1)$$

where N is the Landau level index, v_F is the Fermi velocity, B is the magnetic field and E_D is the Dirac point energy.

In Fig. 3(c), a set of Landau levels is visible in the LDOS in a range of -25 meV to $+25$ meV around the Fermi energy. In order to extract the energy positions of the peaks, we subtracted the background from the STS curves using a cubic spline fit for the background (in violet), and each peak was fitted using a single Gaussian function. The background-subtracted data (black) are shown for 8.0 T along with the raw data with fits (grey). We identified the positions of six LLs and plotted their energy positions as a function of \sqrt{NB} (in the range of 8.0 to 8.7 T) in Fig. 3(d). By assigning the LL index of 28 to the highest peak, we can fit all the peak positions to Eq. (1) with reasonable values of E_D (-306 mV) and v_F (5.8×10^5 m/s). The close-up of the fit near the data points is shown in the inset of Fig. 3(d); although the data points are very linear in this plot of E vs \sqrt{NB} , one cannot definitely tell from the data alone if the dependence on N is linear (which is expected for BCB) or \sqrt{N} (expected for TSS). Nevertheless, the constraint of the DP energy and v_F allows us to elucidate that the \sqrt{N} dependence gives a more consistent analysis (see Appendix B). Therefore we conclude that the observed LLs confirm that the spectral features at these energies are dominated by the TSS.

C. Superconductivity of the surface

With our understanding of the electronic structure at the surface of $\text{Sr}_x\text{Bi}_2\text{Se}_3$ established in the previous subsection, we now turn to the superconducting properties. All spectroscopy experiments to this end were done at a nominal system temperature of about 0.4 K and spectra were acquired on defect-free parts of the surface such as the one depicted in Fig. 4(a).

Surprisingly, high resolution spectroscopy taken around the Fermi energy shows substantial variations. Representative spectra are gathered in Fig. 4(b) where each trace corresponds to a spectrum taken with a different tip. Some spectra exhibit a flat LDOS [red trace in Fig. 4(b)], while others show a superconducting gap but with various gap sizes [black, blue, violet and green traces in Fig. 4(b)]. We have quantified the superconducting gap by fitting the spectra using the Dynes formula [35]. The differential conductance is given by

$$G_N \frac{\partial}{\partial V} \int_{-\infty}^{\infty} N_S(E) [f(E, T_{\text{eff}}) - f(E - eV, T_{\text{eff}})] dE, \quad (2)$$

with G_N the normal-state conductance, $f(E, T_{\text{eff}})$ the Fermi function, and $N_S(E)$ the density of states in the BCS theory

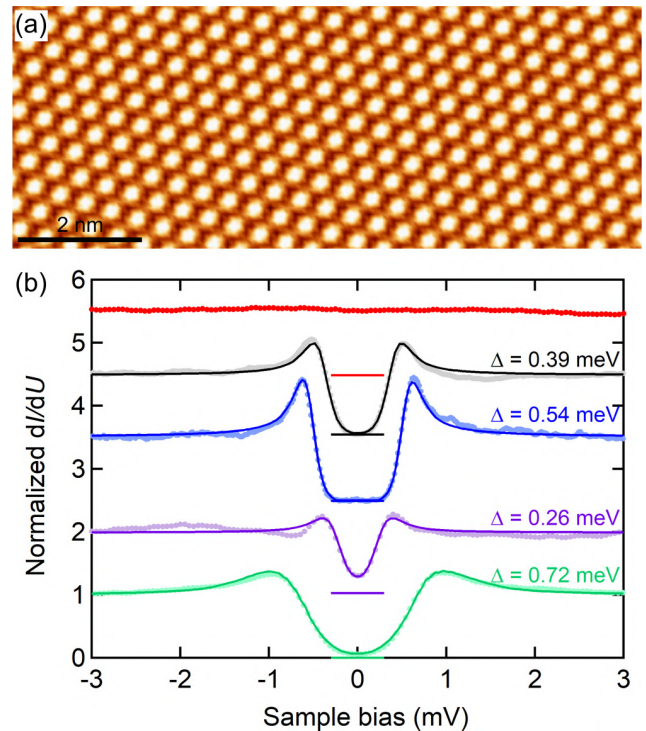


FIG. 4. (a) Atomic-resolution image on the topmost Se layer. (b) Representative high resolution spectra (solid circles) taken with different tips at different positions on the surface: Substantial variations ranging from a flat LDOS at the Fermi level (red curve) to a full gap (blue curve) were observed. Spectra are offset vertically for clarity. Fitting of the data to the Dynes formula [35] yields the superconducting gap Δ of 0.39 (black), 0.54 (blue), 0.26 (violet), and 0.72 meV (green). Scan/stabilization parameters: (a) $U = -900$ mV, $I = 200$ pA; (b) $U = 5$ mV (red, black, green, and violet), $U = 3$ mV (blue), $I = 200$ pA (red), $I = 200$ pA (black), $I = 500$ pA (blue), $I = 100$ pA (violet), $I = 25$ nA (green), and $U_{\text{mod}} = 50 \mu\text{V}_p$. Except for the green curve taken at 1.7 K, all the spectra were taken at 0.4 K. The effective temperature T_{eff} in the fit for the black, blue, and violet fit is 0.7 K, while that for the green curve is 2 K. The Γ value for the fits are 0.02, 0.0001, 0.05, and 0.0003 meV for black, blue, violet, and green curves, respectively.

given as

$$N_S(E) = \text{Re} \left(\frac{(E - i\Gamma)}{\sqrt{(E - i\Gamma)^2 - \Delta^2}} \right), \quad (3)$$

where Γ is an effective broadening parameter and Δ is the superconducting gap. The effective temperature T_{eff} is determined independently (see Appendix A). We have used a total of 10 different new or freshly prepared PtIr tips and one W tip. Across all tips, the minimum and maximum Δ values observed were 0.19 and 0.73 meV, respectively. Our best fits yield Γ values that are always below our energy resolution of about $100 \mu\text{eV}$.

The large scatter in the superconducting gap size at the surface is unexpected for a sample with a sharp bulk superconducting transition. Indeed, the sharp transition observed in the bulk suggest homogeneity in the sample and therefore a more or less uniform gap size of $\Delta \approx 1.76k_B T_c \approx 0.4$ meV is expected. As already mentioned in the introduction, a similar

TABLE II. Overview of surface studies on superconducting doped Bi_2Se_3 materials.

$\text{X}_x\text{Bi}_2\text{Se}_3$	Tip	Bulk T_c (K)	Δ (meV)	Surface SC confirmed ^a	SC material on tip	TSS confirmed
$\text{Cu}_{0.2}$ [9]*	Ir	3.65	0.4 / 0.6 ^b	Yes / -	No / Yes	No
$\text{Cu}_{0.31}$ [10]*	PtIr	3	0.46 / 0.77	Yes / No	No / -	No
$\text{Nb}_{0.25}$ [46]*	-	3.5	0.24–0.76 ^c	No	-	No
Nb_x [17]*	W	-	0.79	No	Yes	Yes
$\text{Nb}_{0.25}$ [47]**	-	3.4	-	-	-	Yes
$\text{Tl}_{0.06}\text{Bi}_2\text{Te}_3$ [17]*	W	2.3	1	No	Yes	Yes
$\text{Sr}_{0.08}$ [13]**	-	2.4	0.52	No	-	Yes
$\text{Sr}_{0.2}$ [14]*	-	3	0.42–1.15 ^c	No	-	Yes
$\text{Sr}_{0.1}$ [16]*	-	2.9	0.19–0.31 ^c	No	-	No
$\text{Sr}_{0.06}$ ^{*d}	PtIr	2.8	0.19–0.73	No	Yes	Yes
$\text{Sr}_{0.06}$ ^{*d}	W	2.8	0.26–0.37	No	Yes	Yes

Experimental technique: *STM, **STM and ARPES.

^aObservation of a vortex lattice along with identification of NSC/SC boundary with the same tip apex.

^bThe gap of 0.6 meV was attributed to a superconducting tip.

^cAll SC gaps presented are taken into consideration.

^dThis work.

discrepancy between the superconducting gaps measured by STM and that expected from the superconducting transition temperature of the bulk has been reported in several publications on doped Bi_2Se_3 compounds, a summary is shown in Table II.

To make sure that superconducting gaps measured at the surface with STM are related to the superconducting state of the bulk, we applied an external magnetic field. Since $\text{Sr}_x\text{Bi}_2\text{Se}_3$ is known to be a type-II superconductor [15], vortices are expected to be generated in applied fields greater than the lower critical field $\mu_0 H_{c1}$. In the inset of Fig. 5, we show a 200 nm by 200 nm topography

overlaid with a mapping of normalized differential conductance at zero bias taken in an applied field of 0.3 T. One can infer that the LDOS is completely uniform in this area, i.e., no vortex is observed in the entire field of view.

The absence of any vortex formation strongly suggests that the superconducting state probed by STM differs from the one in the bulk of $\text{Sr}_x\text{Bi}_2\text{Se}_3$. Before addressing the origin of this difference, we first need to establish whether the superconducting gaps observed by STM are an intrinsic property of the surface or an artifact due to the probe tip. For this purpose, we have first taken a high resolution spectrum on $\text{Sr}_x\text{Bi}_2\text{Se}_3$ (red trace in Fig. 5), and thereafter exchanged the sample against a nonsuperconducting copper sample and repeated the measurement with the same tip on the Cu(111) surface (black trace in Fig. 5). It is evident that the superconducting gap observed with this tip is essentially identical for both $\text{Sr}_x\text{Bi}_2\text{Se}_3$ and Cu(111) surfaces, thereby establishing unambiguously that the superconducting gap originates not from the sample surface but from the probe tip.

Having clarified that the superconducting gaps reproducibly observed on $\text{Sr}_x\text{Bi}_2\text{Se}_3$ are due to superconducting probe tips and *not* due to superconductivity of the $\text{Sr}_x\text{Bi}_2\text{Se}_3$ surface itself, we now address the mechanism by which the tips made out of nonsuperconducting PtIr (or W) turn superconducting.

To this end, we have characterized a probe tip which showed a superconducting gap during STM experiments in more detail. Figure 6(a) shows an SEM image of the PtIr tip apex that is found to be covered with micrometer-sized flakes. The EDX spectrum [Fig. 6(b)] taken on a micro-flake marked by a dashed green circle shows prominent Bi and Se peaks, thus establishing that materials from the $\text{Sr}_x\text{Bi}_2\text{Se}_3$ crystal have been transferred onto the tip. Combined with the observation that a superconducting energy gap was measured with this probe tip prior to SEM characterization, one may conclude that the micrometer-sized $\text{Sr}_x\text{Bi}_2\text{Se}_3$ flakes found on the PtIr tip are superconducting.

To further support this conclusion, we have performed additional STM experiments in which we attempted to redeposit

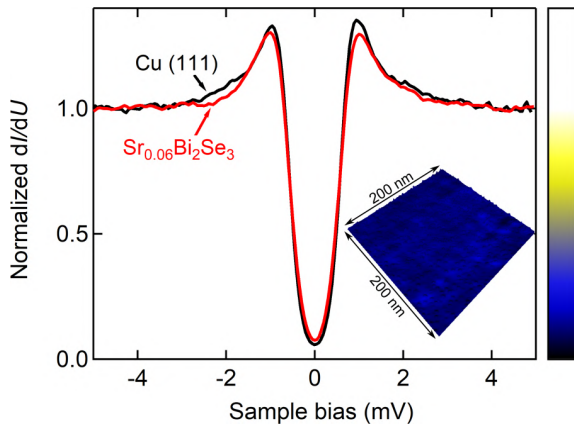


FIG. 5. Normalized dI/dU spectrum taken with a PtIr tip on $\text{Sr}_x\text{Bi}_2\text{Se}_3$ showed a superconducting gap (red curve) after prolonged scanning. The same gap was observed on Cu(111) surface (black curve) demonstrating that the tip must be superconducting. Stabilization parameters are $U = 5$ mV, $I = 200$ pA (red), $I = 25$ nA (black), $U_{\text{mod}} = 50 \mu\text{V}_p$. The inset shows a topograph superimposed with a spectroscopy grid of 20 by 20 points, taken at a sample bias of 0 mV, at an applied magnetic field of 0.3 T. A homogeneous dI/dU signal close to zero is observed even in the presence of a magnetic field, which points to the absence of vortices and suggests that the superconducting gap originates not from the sample surface but from the probe tip.

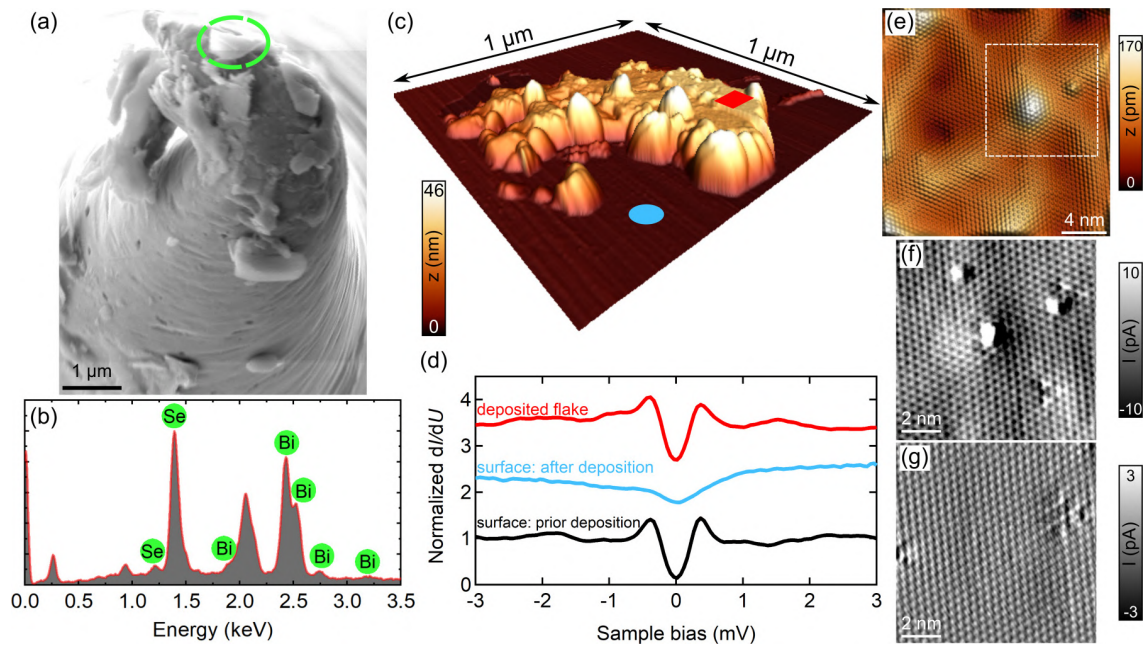


FIG. 6. (a) SEM image of the apex of a PtIr tip after scanning on the sample. The apex is found to be covered with several micrometer-sized flakes. The dashed green circle marks the flake on which the EDX measurement shown in (b) was performed. (b) Result of the EDX analysis of the flake showing the Se peak at 1.379 keV and the Bi double peaks at 2.423 and 2.526 keV. (c) 3D-rendered STM image of a flake deposited on the flat Se layer by a very mild collision between the tip and sample. The deposited material has an apparent height of 23 nm and covers an area of roughly $0.2 \mu\text{m}^2$. The red box marks the area where the atomic-resolution image (e) of the flake was obtained. Scan parameter: $U = -3 \text{ V}$, $I = 10 \text{ pA}$ for (c); $U = -900 \text{ mV}$, $I = 100 \text{ pA}$ for (e). The dashed white square in (e) encloses the area where the current image (f) was taken. (d) Black curve shows the superconducting gap measured prior to the deposition of the flake; the area where the spectrum was taken [shown in the image (g)] presents unstrained Se lattice. After the deposition of the flake, the point STS (blue curve) taken on the area of the Se layer marked by blue circle in (c) shows only a weak proximity-induced gap, indicating that the tip LDOS is not gapped under the apex configuration after the flake has left. Nevertheless, the same tip apex measures a superconducting gap (red curve) on the deposited flake in the area marked by the red box in (c). Stabilization parameter for (d): $U = 5 \text{ mV}$, $I = 100 \text{ pA}$, $U_{\text{mod}} = 50 \mu\text{V}_p$. Scan parameters for the current images: $U = -900 \text{ mV}$, $I = 100 \text{ pA}$ for (f); $U = 5 \text{ mV}$, $I = 100 \text{ pA}$ for (g).

a flake onto the sample surface. Although no reproducible procedure could be established to this end, we found that mild tip-sample interactions sometimes lead to an accidental redeposition of a flake as shown in Fig. 6(c). This flake has an apparent height of $\sim 25 \text{ nm}$ and it extends by about one micrometer. High-resolution imaging on a flat area of the flake [red square in Fig. 6(c)] clearly shows atomic resolution. The resolved hexagonal lattice locally has a lattice constant of about 0.4 \AA in agreement with the Se layer of $\text{Sr}_x\text{Bi}_2\text{Se}_3$. However, one may also recognize nano-scale modifications of the surface height. We have thus compared the average in-plane atom densities of the flat part of the flake [Fig. 6(f)] with the $\text{Sr}_x\text{Bi}_2\text{Se}_3$ surface prior to redeposition of the flake [Fig. 6(g)]. Specifically, we have counted 613 atoms/100 nm^2 in Fig. 6(f) and 627 atoms/100 nm^2 in Fig. 6(g). This yields a reduction of about 2%. Note that the observed difference in average in-plane packing density only demonstrates that there must be some strain in the flake and it does not mean a homogenous tensile strain of 2%. Indeed, a detailed analysis of grain boundaries in Bi_2Se_3 given in Ref. [36] showed variations in the magnitude of in-plane strain ranging from 20% to -20% occurring on nanometer length scales. Extracting similar quantitative values of the strain-tensor of the flake requires additional

data and theoretical modeling, which is beyond the scope of this work.

The dI/dU spectra taken prior to the redeposition of the flake, an example of which is shown in black in Fig. 6(d), clearly presents a superconducting gap; we observed similar spectra everywhere on the $\text{Sr}_x\text{Bi}_2\text{Se}_3$ surface. However, after the redeposition of the flake, the situation changed: While the spectrum shown in red in Fig. 6(d), which was taken on the redeposited flake [in the area marked by the red square in Fig. 6(c)], presents a superconducting gap similar to that observed prior to redeposition, the spectrum shown in blue, which was taken outside of the flake (in the region marked by the blue circle), does not present a fully-developed gap. These spectroscopic observations are consistent with the interpretation that a flake formed the tip-apex prior to redeposition and it is superconducting both before and after the redeposition.

IV. DISCUSSION

As already mentioned, the Hall resistivity data of our $\text{Sr}_x\text{Bi}_2\text{Se}_3$ crystal points to the electron density of $\sim 4 \times 10^{19} \text{ cm}^{-3}$ corresponding to the Fermi energy of 160 to 270 meV measured from the conduction band bottom, whereas the STS data on the same crystal shows that at the

surface, the Fermi energy is only ~ 100 meV from the conduction band bottom. This difference indicates unambiguously that there is an upward band bending of the BCB present at the surface. This upward band bending is partly due to the an intrinsic effect always present in Bi_2Se_3 due to charge equilibration between bulklike states and the TSS [29,30], which can also be viewed as a result of many-body Coulomb interactions between the bulk and surface electrons [37]. Note that band bending at the surface can also reflect additional factors [38], such as the contact potential due to the interface with the STM tip [39] or by adsorbates. In Cu-doped Bi_2Se_3 , the Coulomb interactions between bulk and surface electrons was claimed to cause an upward band bending of the BCB by about 200 meV at the surface within the length scale of about 1 nm [37].

The contact potential can be roughly estimated from the difference in work function of the metallic tip ϕ_m and that of Bi_2Se_3 . Importantly, the latter is large $\phi_{\text{Bi}_2\text{Se}_3} \approx 5.6$ eV [40] so that $\phi_{\text{Bi}_2\text{Se}_3} > \phi_m$ is generally fulfilled. Hence, the contact potential would only lead to the bulk bands bending down at the surface and it cannot be the cause of the observed upward band bending.

Intuitively, band bending due to adsorbates will lead to upward or downward band bending for adsorption of acceptor or donor molecules, respectively. In this context, in particular photoemission experiments suffer from photoexcited adsorbate layers [41], that act as electron donors and, similar to the adsorption of alkali metals [42], inevitably cause downward band bending. However, the experimental conditions of our STM measurements ensure an adsorbate-free surface and more generally, downward band bending is incompatible with the experimental observations.

Importantly, while the details regarding the origin of the observed band bending can be complex, there is agreement that the experimentally measured surface potential of ~ 100 meV will be screened over a typical length scale of ~ 1 nm [29,30,37]; in other words, near the surface, the bulk electrons experience an electric field of the order of 10^8 V/m.

The puzzling fact is that the bulk of our $\text{Sr}_x\text{Bi}_2\text{Se}_3$ crystals show robust superconductivity with $T_c = 2.8$ K and a high shielding fraction [26], while the STS measurements found no superconducting gap anywhere on the surface down to a temperature of 0.4 K, when clean and nonsuperconducting probe tips are used. This absence of superconductivity on the surface has been a problem in many STM experiments performed on doped Bi_2Se_3 superconductors, but the present study found that during the prolonged scanning of the tip on the $\text{Sr}_x\text{Bi}_2\text{Se}_3$ surface, the tip will always accumulate microflakes of $\text{Sr}_x\text{Bi}_2\text{Se}_3$ which show superconductivity. This finding helps to clarify some discrepancies in the observed SC gaps in earlier STM studies [13,14,16], which were inconsistent with the bulk T_c . Note that our experimental observation is essentially consistent with those on superconducting Tl-doped Bi_2Te_3 and Nb-doped Bi_2Se_3 reported by Wilfert *et al.* [17], who concluded that superconductivity does not extend to the surface in these superconductors.

Since recent experimental [43] and theoretical [44] works found a suppression of superconductivity under a strong electric field of the order of 10^8 V/m in conventional

superconductors, we speculate that the local electric field associated with the experimentally observed band bending has a similar effect on superconductivity in $\text{Sr}_x\text{Bi}_2\text{Se}_3$. Indeed, since the upward band bending is a consequence of the existence of the TSS, one would expect the electric field to disappear (and the superconductivity to extend to the surface) when the TSS is destroyed. In this regard, there have been interesting reports that the strain on the surface can destroy the TSS in Bi_2Se_3 [36,45]. Motivated by these observations, we speculate that during the transfer of the $\text{Sr}_x\text{Bi}_2\text{Se}_3$ flakes onto the tip, the flakes experience mechanical strain and the TSS is destroyed, allowing the superconductivity to extend to the surface of the flake. Although a detailed analysis of the strain in the flakes on our STM tips is beyond the scope of this work, we note that the atomic-resolution imaging on the flat parts of a flake [Fig. 6(c)] shows dislocation features and a reduced atomic packing density, indicative of a strain in the flake.

Since the surface potential is an intrinsic effect linked inherently to the presence of the TSS in doped Bi_2Se_3 and hence should be a general phenomena in the family of doped Bi_2Se_3 superconductors, our speculation, that the appearance of superconductivity on the surface is related to the loss of TSS due to strain, gives a clue to understand earlier STM studies that are listed in Table II.

It is prudent to mention that the pioneering STM work by Levy *et al.* [9] gave persuasive evidence for superconductivity extending to the surface of Cu-doped Bi_2Se_3 crystals (i.e., appearance of vortices in an applied magnetic field and the observation of a domain boundary between superconducting and nonsuperconducting regions); nevertheless, the topographic images of the superconducting domains in Ref. [9] showed many structural defects such as step bunching and grain boundaries that are consistent with strains in their samples. Moreover, no evidence was shown for the TSS to remain intact on these surfaces. Another STM study [10] of Cu-doped Bi_2Se_3 likewise showed experimental proof (vortex lattice in an applied magnetic field) that superconductivity can extend to the sample surface; however, less than 4% of the studied surface area exhibited superconductivity and the remaining 96% of the surface showed no superconducting gap. Interestingly, the topographic images in Ref. [10] showed lots of structural defects, such as non-quintuple-layer step heights, in particular for the superconducting regions.

Han *et al.* [13] used ARPES to demonstrate that the TSS of their $\text{Sr}_x\text{Bi}_2\text{Se}_3$ samples was intact and the STS data showed a superconducting gap, but their data are also fully compatible with a superconducting flake having been transferred to the tip. The superconductivity observed on the surface of $\text{Sr}_x\text{Bi}_2\text{Se}_3$ by STM in the works by Kumar *et al.* [16] and Du *et al.* [14] showed values of Δ , T_c , and $\mu_0 H_{c2}$ that are incompatible with the bulk values; this problem can be straightforwardly reconciled if a superconducting flake was present on the tip. Interestingly, Kumar *et al.* [16] also performed hard point-contact spectroscopy and found an increase in T_c with increasing pressure. It would be instructive to clarify if the strain due to the pressure from the tip leads to a destruction of the TSS.

V. CONCLUSION

While our $\text{Sr}_x\text{Bi}_2\text{Se}_3$ crystals present robust bulk superconductivity with $T_c = 2.8$ K, our STM measurements at 0.4 K with a fresh tip found no superconducting gap on the surface. This result is similar to many previous STM experiments on doped Bi_2Se_3 superconductors. To understand this discrepancy, we propose that the upward band bending of 60 to 170 meV, which we elucidated at the surface, is playing a key role. Because recent DFT calculations found [29,30] that this upward band bending is an inevitable consequence of the existence of the TSS and hence is intrinsic to the electron-doped Bi_2Se_3 family of materials, we argue that the electric field suppresses the superconductivity at the surface in doped Bi_2Se_3 superconductors. In this regard, it was found both experimentally [43] and theoretically [44] that a strong electric field can kill superconductivity in conventional superconductors.

Intriguingly, after prolonged scanning on the $\text{Sr}_x\text{Bi}_2\text{Se}_3$ surface, the STS data taken with all probe tips eventually showed a superconducting gap whose origin can be assigned to the probe tip itself, and the *ex situ* SEM/EDX analysis of the tip establishes that micrometer-sized flakes of $\text{Sr}_x\text{Bi}_2\text{Se}_3$ are transferred onto the tip apex during the scanning of the surface. Furthermore, we were able to redeposit a $\text{Sr}_x\text{Bi}_2\text{Se}_3$ flake back onto the $\text{Sr}_x\text{Bi}_2\text{Se}_3$ surface inside the STM and confirmed that the flakes which were transferred onto the tip are indeed superconducting. Since recent works reported that the TSS can be destroyed by strain [36,45] and we actually observed lattice distortions on the redeposited flakes, we speculate that the strain in the flakes picked up by the tips destroys the TSS and allows the superconductivity to extend to the surface of the flake. This speculation that strain allows the superconductivity to extend to the surface can explain many of the puzzles in the past STM experiments [9,10,13,14,16,17].

ACKNOWLEDGMENTS

This project has received funding from the European Research Council (ERC) under the European Union's Horizon 2020 research and innovation programme (Grant agreement No. 741121) and was also funded by the DFG under CRC 1238 - 277146847 (Subprojects A04 and B06) as well as under Germany's Excellence Strategy - Cluster of Excellence Matter and Light for Quantum Computing (ML4Q) EXC 2004/1-390534769.

APPENDIX A: EFFECTIVE TEMPERATURE

At milli-Kelvin temperatures the nominal sample temperature differs from the effective electron temperature of the tunneling junction due to experimental broadening. This (generally unknown) experimental broadening has a similar effect in high resolution spectroscopy of SC gaps as the thermal broadening, hence one defines an effective temperature T_{eff} which is calibrated by fitting the dI/dU spectrum of a well-known superconductor. For this purpose we fit the superconducting gap of a Nb tip made of a high purity Nb wire measured on a nonsuperconducting Au(111) surface at a nominal temperature of 400 mK. We use the Dynes equation from the main text, but fix Γ close to zero leaving only

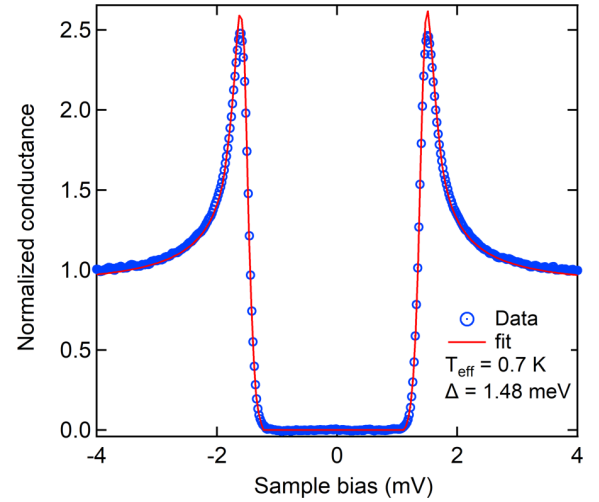


FIG. 7. STS taken with a Nb-tip on the Au(111) surface at $T = 400$ mK. The superconducting gap of the Nb tip (blue trace) and can be fitted using the BCS theory (red trace) with $\Delta = 1.48$ meV which yields an effective electron temperature $T_{\text{eff}} = 700$ mK. Stabilization parameter: $U = 4$ mV, $I = 500$ pA, and $U_{\text{mod}} = 50 \mu\text{V}_p$.

the effective temperature T_{eff} and the superconducting gap Δ as fit parameters. The best fit to the experimental data is shown in Fig. 7. The fit yields $T_{\text{eff}} = 0.7$ K.

APPENDIX B: ANALYSES OF THE LANDAU LEVEL SPECTRUM

In the main text, we argued that the peaks observed in the dI/dU data shown in Fig. 3 are due to Landau quantization of the TSS and not the BCB. Here, we compare the two scenarios in more detail. First, we recall that the reciprocal-space area $A(k)$ enclosed by a cyclotron orbit under the Landau quantization should satisfy the generalized Onsager relation

$$A_N(k) = 2\pi \frac{eB}{\hbar} (N + \lambda), \quad (\text{B1})$$

where N is an integer, e is the elementary charge, B is the magnetic field, and $\lambda = 1/2 - \gamma/(2\pi)$ with γ the Berry phase.

For a circular orbit, Eq. (B1) becomes

$$\pi k_N^2 = 2\pi \frac{eB}{\hbar} (N + \lambda). \quad (\text{B2})$$

By using this k_N^2 in the parabolic dispersion relation $E = (\hbar k^2)/(2m_{\text{eff}})$ for the BCB, the quantized energy levels for Schrödinger electrons are given by

$$E_N = E_{\text{BCB}} + \hbar \frac{eB}{m_{\text{eff}}} \left(N + 1/2 - \frac{\gamma}{2\pi} \right), \quad (\text{B3})$$

where E_{BCB} is the energy of the bottom of the BCB. Since $\gamma = 0$ for Schrödinger electrons, one obtains

$$E_N = E_{\text{BCB}} + \hbar \omega_c (N + 1/2). \quad (\text{B4})$$

On the other hand, for the linear dispersion relation $E = E_D + v_F \hbar k$ of the Dirac electrons in the TSS, an analogous

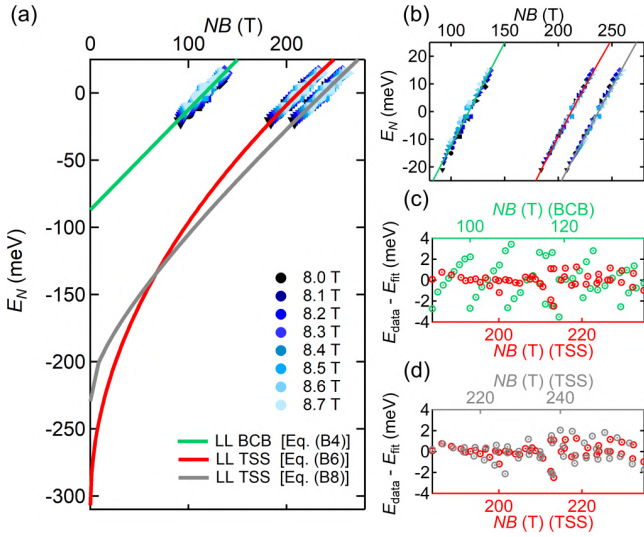


FIG. 8. (a) The E_N values of the six LLs identified in the STS spectra for all B fields shown in Fig. 3(c) are plotted as a function of NB , where N is the LL index for the three cases under consideration (BCB, TSS with a linear dispersion, and TSS with a curved dispersion). A LL index of 16 is assigned to the highest peak for the case of the BCB, 28 for the case of a linear TSS dispersion, and 31 for the case of a curved TSS dispersion. The fit using Eq. (1) for the linear TSS dispersion is shown with the red curve and yields $E_D = -306 \pm 3$ meV and $v_F = 5.81 \pm 0.06 \times 10^5$ m/s. If the LL spectrum is assumed to originate from the BCB, the data should be fit using Eq. (B4), and the best fit shown with the green linear line results in values of -87 ± 2 meV for the bottom of the BCB and $0.155 \pm 0.004m_e$ for the effective mass m_{eff} . Consideration of a realistic TSS dispersion including a quadratic term leads to the fit using Eq. (B8), and the best fit shown with the grey curve results in $E_D = -230 \pm 5$ meV and $v_F = 2.13 \pm 0.09 \times 10^5$ m/s (assuming $m_{\text{eff}} = 0.25m_e$ and $g = 55$). A close-up of the three fits near $E_N = 0$ meV is shown in (b). The deviations of the data from the fits are shown in (c) and (d), in which green symbols are for the BCB case, red symbols are for the linear TSS dispersion, and grey symbols are for the curved TSS dispersion.

consideration yields

$$E_N = E_D + v_F \sqrt{2eB\hbar \left(|N| + 1/2 - \frac{\gamma}{2\pi} \right)}. \quad (\text{B5})$$

Since $\gamma = \pi$ for Dirac electrons, one obtains

$$E_N = E_D + \text{sgn}(N)v_F \sqrt{2eB\hbar|N|}, \quad (\text{B6})$$

which is already shown in the main text as Eq. (1).

Therefore by extracting E_N of the Landau levels, one can in principle distinguish between electrons stemming from the BCB (proportional to N) and those from the TSS (proportional to $\sqrt{|N|}$). However, in the present experiment, the experimentally observed peaks in the LDOS due to Landau quantization are far above the band bottom of both BCB and TSS. Consequently, the relevant LLs located near the Fermi energy have relatively large indices. In such a case, the distinction between $\sqrt{|N|}$ [red curve in Fig. 8(a)] and N [green straight

line in Fig. 8(a)] becomes subtle due to the ambiguity in the assignment of N .

Nonetheless, we have made a trial to analyze the data shown in Fig. 3 assuming that they originate from the Landau quantization of the BCB whose bottom should be located about 100 meV below E_F . The fit of the experimental data (assuming N of the highest LL to be 16) to Eq. (B4) shown with the green straight line in Fig. 8(b) is considerably worse than for the analysis presented in the main text, which assumed the highest LL index of 28 and used Eq. (1), shown in Fig. 8(b) with the red curve. We highlight the unsatisfactory agreement between the experimental data and the fit for the BCB scenario by plotting their deviations in Fig. 8(c).

It is prudent to note that the dispersion of the actual TSS in Bi_2Se_3 deviates from a simple linear function [48]. This deviation can be approximated by considering a quadratic term in the dispersion relation. Therefore, for completeness, we have also performed an analysis based on the dispersion relation

$$E = E_D + v_F \hbar k + \frac{\hbar^2}{2m_{\text{eff}}} k^2. \quad (\text{B7})$$

Using this dispersion and including the Zeeman energy, the following expression for the eigenenergies of the LLs is obtained for the electron branch of the curved Dirac cone [48]:

$$E_N = E_D + \hbar\omega_c N + \sqrt{2\hbar v_F^2 eBN + \left(\frac{\hbar\omega_c}{2} - \frac{g_s \mu_B B}{2} \right)^2}. \quad (\text{B8})$$

In the case of Bi_2Se_3 , the g factor of $g_s = 55$, the effective mass of $m_{\text{eff}} = 0.25m_e$ and the Fermi velocity of $v_F = 3 \times 10^5$ m/s are established to accurately describe Shubnikov-de Haas oscillations [48]. We found that the LL spectrum observed in $\text{Sr}_x\text{Bi}_2\text{Se}_3$ can be well explained [grey curve in Fig. 8(a)] by assuming a reduced Fermi velocity of $v_F = 2.13 \times 10^5$ m/s and the highest LL index of 31. The reduction in the Fermi velocity is in line with the case of superconducting $\text{Cu}_x\text{Bi}_2\text{Se}_3$, where a reduction of up to 30% was observed [37].

It should be remarked that in this analysis based on Eq. (B7), we have to assume a Dirac-point energy of $E_D = -230$ meV. While this is in apparent disagreement with the DP energy of about -310 meV deduced from the minimum in the LDOS shown in Fig. 2, it can be straightforwardly reconciled by considering a tip-induced band bending that causes a shift in the DP energy; namely, as the bias voltage is increased, the electric field between the tip and the surface becomes stronger, causing the DP to shift in energy. Such a shift of about -80 meV was deduced previously for Bi_2Se_3 by comparing STS and ARPES measurements [49]. Hence, our experimental LL spectrum is well described by both models of the TSS, i.e., Eqs. (1) and (B8). Due to the ambiguity in the assignment of the LL index, a more rigorous distinction is difficult. Nevertheless, regardless of the model for the TSS, the observed LL spectrum supports the existence of upward band bending near the surface.

- [1] Y. S. Hor, A. J. Williams, J. G. Checkelsky, P. Roushan, J. Seo, Q. Xu, H. W. Zandbergen, A. Yazdani, N. P. Ong, and R. J. Cava, Superconductivity in $\text{Cu}_x\text{Bi}_2\text{Se}_3$ and Its Implications for Pairing in the Undoped Topological Insulator, *Phys. Rev. Lett.* **104**, 057001 (2010).
- [2] L. Fu and E. Berg, Odd-Parity Topological Superconductors: Theory and Application to $\text{Cu}_x\text{Bi}_2\text{Se}_3$, *Phys. Rev. Lett.* **105**, 097001 (2010).
- [3] K. Matano, M. Kriener, K. Segawa, Y. Ando, and G. Zeng, Spin-rotation symmetry breaking in the superconducting state of $\text{Cu}_x\text{Bi}_2\text{Se}_3$, *Nat. Phys.* **12**, 852 (2016).
- [4] S. Yonezawa, K. Tajiri, S. Nakata, Y. Nagai, Z. Wang, K. Segawa, Y. Ando, and Y. Maeno, Thermodynamic evidence for nematic superconductivity in $\text{Cu}_x\text{Bi}_2\text{Se}_3$, *Nat. Phys.* **13**, 123 (2017).
- [5] S. Yonezawa, Nematic superconductivity in doped Bi_2Se_3 topological superconductors, *Condens. Matter* **4**, 2 (2019).
- [6] A. Y. Kuntsevich, M. A. Bryzgalov, V. A. Prudkoglyad, V. P. Martovitskii, Y. G. Selivanov, and E. G. Chizhevskii, Structural distortion behind the nematic superconductivity in $\text{Sr}_x\text{Bi}_2\text{Se}_3$, *New J. Phys.* **20**, 103022 (2018).
- [7] Y. Ando and L. Fu, Topological crystalline insulators and topological superconductors: From concepts to materials, *Annu. Rev. Condens. Matter Phys.* **6**, 361 (2015).
- [8] M. Sato and Y. Ando, Topological superconductors: A review, *Rep. Prog. Phys.* **80**, 076501 (2017).
- [9] N. Levy, T. Zhang, J. Ha, F. Sharifi, A. A. Talin, Y. Kuk, and J. A. Stroscio, Experimental Evidence for s -Wave Pairing Symmetry in Superconducting $\text{Cu}_x\text{Bi}_2\text{Se}_3$ Single Crystals Using a Scanning Tunneling Microscope, *Phys. Rev. Lett.* **110**, 117001 (2013).
- [10] R. Tao, Y.-J. Yan, X. Liu, Z.-W. Wang, Y. Ando, Q.-H. Wang, T. Zhang, and D.-L. Feng, Direct Visualization of the Nematic Superconductivity in $\text{Cu}_x\text{Bi}_2\text{Se}_3$, *Phys. Rev. X* **8**, 041024 (2018).
- [11] M. Kriener, K. Segawa, Z. Ren, S. Sasaki, S. Wada, S. Kuwabata, and Y. Ando, Electrochemical synthesis and superconducting phase diagram of $\text{Cu}_x\text{Bi}_2\text{Se}_3$, *Phys. Rev. B* **84**, 054513 (2011).
- [12] Z. Liu, X. Yao, J. Shao, M. Zuo, L. Pi, S. Tan, C. Zhang, and Y. Zhang, Superconductivity with topological surface state in $\text{Sr}_x\text{Bi}_2\text{Se}_3$, *J. Am. Chem. Soc.* **137**, 10512 (2015).
- [13] C. Q. Han, H. Li, W. J. Chen, F. Zhu, M.-Y. Yao, Z. J. Li, M. Wang, B. F. Gao, D. D. Guan, C. Liu, C. L. Gao, D. Qian, and J.-F. Jia, Electronic structure of a superconducting topological insulator Sr-doped Bi_2Se_3 , *Appl. Phys. Lett.* **107**, 171602 (2015).
- [14] G. Du, J. Shao, X. Yang, Z. Du, D. Fang, J. Wang, K. Ran, J. Wen, C. Zhang, H. Yang, Y. Zhang, and H.-H. Wen, Drive the Dirac electrons into Cooper pairs in $\text{Sr}_x\text{Bi}_2\text{Se}_3$, *Nat. Commun.* **8**, 14466 (2017).
- [15] Shruti, V. K. Maurya, P. Neha, P. Srivastava, and S. Patnaik, Superconductivity by Sr intercalation in the layered topological insulator Bi_2Se_3 , *Phys. Rev. B* **92**, 020506(R) (2015).
- [16] R. Kumar, A. Vasdev, S. Das, S. Howlader, K. S. Jat, P. Neha, S. Patnaik, and G. Sheet, The pressure-enhanced superconducting phase of $\text{Sr}_x\text{-Bi}_2\text{Se}_3$ probed by hard point contact spectroscopy, *Sci. Rep.* **11**, 4090 (2021).
- [17] S. Wilfert, P. Sessi, Z. Wang, H. Schmidt, M. C. Martínez-Velarte, S. H. Lee, Y. S. Hor, A. F. Otte, Y. Ando, W. Wu, and M. Bode, Scanning tunneling spectroscopy investigations of superconducting-doped topological insulators: Experimental pitfalls and results, *Phys. Rev. B* **98**, 085133 (2018).
- [18] I. Horcas, R. Fernandez, J. Gomez-Rodriguez, J. Colchero, J. Gomez-Herrero, and A. M. Baro, WSxM: A software for scanning probe microscopy and a tool for nanotechnology, *Rev. Sci. Instrum.* **78**, 013705 (2007).
- [19] H. Huang, J. Gu, M. Tan, Q. Wang, P. Ji, and X. Hu, Degradation of topological surface state by nonmagnetic S doping in $\text{Sr}_x\text{Bi}_2\text{Se}_3$ superconductor, *Sci. Rep.* **7**, 45565 (2017).
- [20] A. Y. Kuntsevich, V. P. Martovitskii, G. V. Rybalchenko, Y. G. Selivanov, M. I. Bannikov, O. A. Sobolevskiy, and E. G. Chigevskii, Superconductivity in Cu co-doped $\text{Sr}_x\text{Bi}_2\text{Se}_3$ single crystals, *Materials* **12**, 3899 (2019).
- [21] Z. Li, M. Wang, D. Zhang, N. Feng, W. Jiang, C. Han, W. Chen, M. Ye, C. Gao, J. Jia, J. Li, S. Qiao, D. Qian, B. Xu, H. Tian, and B. Gao, Possible structural origin of superconductivity in $\text{Sr}_x\text{-Bi}_2\text{Se}_3$, *Phys. Rev. Materials* **2**, 014201 (2018).
- [22] L. Andersen, Z. Wang, T. Lorenz, and Y. Ando, Nematic superconductivity in $\text{Cu}_{1.5}(\text{PbSe})_5(\text{Bi}_2\text{Se}_3)_6$, *Phys. Rev. B* **98**, 220512(R) (2018).
- [23] L. Andersen, A. Ramires, Z. Wang, T. Lorenz, and Y. Ando, Generalized Anderson's theorem for superconductors derived from topological insulators, *Sci. Adv.* **6**, eaay6502 (2020).
- [24] H. Köhler, Conduction band parameters of Bi_2Se_3 from Shubnikov-de Haas investigations, *Phys. Status. Solidi B* **58**, 91 (1973).
- [25] J. G. Analytis, J.-H. Chu, Y. Chen, F. Corredor, R. D. McDonald, Z. X. Shen, and I. R. Fisher, Bulk Fermi surface coexistence with Dirac surface state in Bi_2Se_3 : A comparison of photoemission and Shubnikov-de Haas measurements, *Phys. Rev. B* **81**, 205407 (2010).
- [26] Y.-R. Lin, M. Bagchi, S. Soubatch, T.-L. Lee, J. Brede, F. C. Bocquet, C. Kumpf, Y. Ando, and F. S. Tautz, Vertical position of Sr dopants in the $\text{Sr}_x\text{Bi}_2\text{Se}_3$ superconductor, *Phys. Rev. B* **104**, 054506 (2021).
- [27] Y. Xia, D. Qian, D. Hsieh, L. Wray, A. Pal, H. Lin, A. Bansil, D. Grauer, Y. S. Hor, R. J. Cava, and M. Z. Hasan, Observation of a large-gap topological-insulator class with a single Dirac cone on the surface, *Nat. Phys.* **5**, 398 (2009).
- [28] M. Neupane, Y. Ishida, R. Sankar, J.-X. Zhu, D. S. Sanchez, I. Belopolski, S.-Y. Xu, N. Alidoust, M. M. Hosen, S. Shin, F. Chou, M. Z. Hasan, and T. Durakiewicz, Electronic structure and relaxation dynamics in a superconducting topological material, *Sci. Rep.* **6**, 22557 (2016).
- [29] B. M. Fregoso, and S. Coh, Intrinsic surface dipole in topological insulators, *J. Phys.: Condens. Matter* **27**, 422001 (2015).
- [30] P. Rakyta, B. Ujfalussy, and L. Szunyogh, Band bending at the surface of Bi_2Se_3 studied from first principles, *New J. Phys.* **17**, 123011 (2015).
- [31] T. Zhang, P. Cheng, X. Chen, J.-F. Jia, X. Ma, K. He, L. Wang, H. Zhang, X. Dai, Z. Fang, X. Xie, and Q.-K. Xue, Experimental Demonstration of Topological Surface States Protected by Time-Reversal Symmetry, *Phys. Rev. Lett.* **103**, 266803 (2009).
- [32] K. Kuroda, M. Arita, K. Miyamoto, M. Ye, J. Jiang, A. Kimura, E. E. Krasovskii, E. V. Chulkov, H. Iwasawa, T. Okuda, K. Shimada, Y. Ueda, H. Namatame, and M. Taniguchi, Hexagonally Deformed Fermi Surface of the 3D Topological Insulator Bi_2Se_3 , *Phys. Rev. Lett.* **105**, 076802 (2010).
- [33] J. Wang, W. Li, P. Cheng, C. Song, T. Zhang, P. Deng, X. Chen, X. Ma, K. He, J.-F. Jia, Q.-K. Xue, and B.-F. Zhu, Power-law

- decay of standing waves on the surface of topological insulators, *Phys. Rev. B* **84**, 235447 (2011).
- [34] L. Fu, Hexagonal Warping Effects in the Surface States of the Topological Insulator Bi_2Te_3 , *Phys. Rev. Lett.* **103**, 266801 (2009).
- [35] R. C. Dynes, V. Narayanamurti, and J. P. Garno, Direct Measurement of Quasiparticle-Lifetime Broadening in a Strong-coupled Superconductor, *Phys. Rev. Lett.* **41**, 1509 (1978).
- [36] Y. Liu, Y. Y. Li, S. Rajput, D. Gilks, L. Lari, P. L. Galindo, M. Weinert, V. K. Lazarov, and L. Li, Tuning Dirac states by strain in the topological insulator Bi_2Se_3 , *Nat. Phys.* **10**, 294 (2014).
- [37] L. A. Wray, S. Xu, Y. Xia, D. Qian, A. V. Fedorov, H. Lin, A. Bansil, Arun, F. Liang, Y. S. Hor, R. J. Cava, and M. Z. Hasan, Spin-orbital ground states of superconducting doped topological insulators: A Majorana platform, *Phys. Rev. B* **83**, 224516 (2011).
- [38] Z. Zhang and J. T. Yates, Band bending in semiconductors: Chemical and physical consequences at surfaces and interfaces, *Chem. Rev.* **112**, 5520 (2012).
- [39] R. M. Feenstra, Y. Dong, M. P. Semtsiv, and W. T. Masselink, Influence of tip-induced band bending on tunnelling spectra of semiconductor surfaces, *Nanotechnology* **18**, 044015 (2006).
- [40] D. Takane, S. Souma, T. Sato, T. Takahashi, K. Segawa, and Y. Ando, Work function of bulk-insulating topological insulator $\text{Bi}_{2-x}\text{Sb}_x\text{Te}_{3-y}\text{Se}_y$, *Appl. Phys. Lett.* **109**, 091601 (2016).
- [41] E. Frantzeskakis, S. V. Ramankutty, N. de Jong, Y. K. Huang, Y. Pan, A. Tytarenko, M. Radovic, N. C. Plumb, M. Shi, A. Varykhalov, A. de Visser, E. van Heumen, and M. S. Golden, Trigger of the Ubiquitous Surface Band bending in 3D Topological Insulators, *Phys. Rev. X* **7**, 041041 (2017).
- [42] Z.-H. Zhu, G. Levy, B. Ludbrook, C. N. Veenstra, J. A. Rosen, R. Comin, D. Wong, P. Dosanjh, A. Ubaldini, P. Syers, N. P. Butch, J. Paglione, I. S. Elfimov, and A. Damascelli, Rashba Spin-Splitting Control at the Surface of the Topological Insulator Bi_2Se_3 , *Phys. Rev. Lett.* **107**, 186405 (2011).
- [43] G. D. Simoni, F. Paolucci, P. Solinas, E. Strambini, and F. Giazotto, Metallic supercurrent field-effect transistor, *Nat. Nanotechnol.* **13**, 802 (2018).
- [44] P. Solinas, A. Amoretti, and F. Giazotto, Sauter-Schwinger Effect in a Bardeen-Cooper-Schrieffer Superconductor, *Phys. Rev. Lett.* **126**, 117001 (2021).
- [45] S. K. Das and P. Padhan, The effect of mechanical strain on the Dirac surface states in the (0001) surface and the cohesive energy of the topological insulator Bi_2Se_3 , *Nanoscale Adv.* **3**, 4816 (2021).
- [46] A. Sirohi, S. Das, P. Neha, K. S. Jat, S. Patnaik, and G. Sheet, Low-energy excitations and non-BCS superconductivity in $\text{Nb}_x\text{-Bi}_2\text{Se}_3$, *Phys. Rev. B* **98**, 094523 (2018).
- [47] Y. Qiu, K. N. Sanders, J. Dai, J. E. Medvedeva, W. Wu, P. Ghaemi, T. Vojta, and Y. S. Hor, Time reversal symmetry breaking superconductivity in topological materials, [arXiv:1512.03519](https://arxiv.org/abs/1512.03519).
- [48] A. A. Taskin, and Y. Ando, Berry phase of nonideal Dirac fermions in topological insulators, *Phys. Rev. B* **84**, 035301 (2011).
- [49] P. Cheng, C. Song, T. Zhang, Y. Zhang, Y. Wang, J.-F. Jia, J. Wang, Y. Wang, B.-F. Zhu, X. Chen, X. Ma, K. He, L. Wang, X. Dai, Z. Fang, X. Xie, X.-L. Qi, C.-X. Liu, S.-C. Zhang, and Q.-K. Xue, Landau Quantization of Topological Surface States in Bi_2Se_3 , *Phys. Rev. Lett.* **105**, 076801 (2010).

3 Rotation of gap nodes in Cu doped $(\text{PbSe})_5(\text{Bi}_2\text{Se}_3)_6$

This chapter is presented in the form of a manuscript. My contribution includes sample growth, bulk characterization, STM data acquisition and analysis and a first draft of the manuscript. Attached version of the main text and supplementary material has been edited by Y. Ando and A. Ramires. Theory for the manuscript is done by A. Ramires. Attached version of the additional data section (see Appendix B.1) is presented as written by myself.

3.1 Overview

Still in search of materials with a surface quality more suited to being probed by STM, we turned our attention to a lesser known member of the doped Bi_2Se_3 family: $\text{Cu}_x(\text{PbSe})_5(\text{Bi}_2\text{Se}_3)_6$ (CPSBS), where topological superconductivity along with gap nodes is realized in the *bulk*. However, no STM experiments to directly probe the superconducting gap on the *surface* had been performed so far. In this chapter we report on the first STM experiment on CPSBS as well as the parent compound $(\text{PbSe})_5(\text{Bi}_2\text{Se}_3)_6$ (PSBS).

Our main finding is that on the surface of CPSBS, the orientation of the superconducting gap node is rotated away from the unique crystallographic mirror plane, in contradiction to the observations of bulk measurements such as specific-heat and thermal-conductivity [101, 57]. Further the gap node is likely lifted. To understand this result we employed a symmetry-based theoretical analysis (work by A. Ramires). We found that the unavoidable inversion symmetry breaking at the surface allows for the mixing of different superconducting order parameters in the same symmetry channel leading to the lifting of the otherwise mirror symmetry protected gap nodes. Further, the rotation of the minima is possible only when order parameters of different symmetry channels mix. This can happen if the effective symmetry on the surface is different from the bulk. There is indication that disorder weakens the effect of the PbSe layers in superconducting regions such that the twofold rotational symmetry of the bulk PSBS crystal does not hold true on the surface. Instead the threefold rotational symmetry of Bi_2Se_3 layers is likely restored on the surface.

Hence our work highlights the role of crystal symmetry in understanding topological superconductivity in doped Bi_2Se_3 , in particular how and why the superconducting gap structure on the surface may differ from the bulk. The symmetry-based theoretical analysis also helps to gain insight with regard to the observations made on the sister compound $\text{Cu}_x\text{Bi}_2\text{Se}_3$.

Note on crystal symmetry: In PSBS (and CPSBS), a bilayer of PbSe alternates with two quintuple layers of Bi_2Se_3 . Hence, in going from Bi_2Se_3 to PSBS there is symmetry reduction from the D_{3d} point group (rhombohedral symmetry) to the C_{2h} (monoclinic

symmetry). The relation between the crystal structure of Bi_2Se_3 and PSBS is discussed in detail in the supplementary section 6 of Ref. [101]. The monoclinic a and b axis of PSBS is defined such that the b axis has the same length and direction as the b axis of the hexagonal unit cell of Bi_2Se_3 . Also note that the point group D_{1d} used in the main text is equivalent to C_{2h} .

Note on band structure of PSBS and CPSBS: PSBS is expected to cleave in the vdWs gap of the 2 QLs of Bi_2Se_3 . Hence, after cleaving, the surface termination layer is a single QL of Bi_2Se_3 atop the PbSe layer, hereafter referred to as the $m=1$ layer. By the same logic, a $m=2$ surface can be obtained when cleaving a sample having at least 3 QLs of Bi_2Se_3 between the PbSe layers. ARPES data [102] on the $m=1$ surface shows a single, parabolic electronlike 2D band. This band is also observed on the cleaved surface of CPSBS [103]. The Fermi surface of the material is found to be cylindrical in shape which is expected due to its multilayered quasi-2D hetero-structure.

Note that no topological bands are expected for the $m=1$ or 2 surfaces. The topological SS is expected if there is at least 6 QLs of Bi_2Se_3 [104] (~ 3 QLs for Bi_2Te_3 [105, 106]). There is a marked difference between the bands for $m=1$ and 2 which suggests that the band inversion that is necessary for the topological SS to appear takes place in going from 1 to 2 QL. However, between 2 and 5 QLs of Bi_2Se_3 the top and bottom surface state hybridize to open up a gap. This band is spin degenerate and has a hybridization gap and therefore not topological.

Rotation of gap nodes in the topological superconductor



Mahasweta Bagchi,¹ Jens Brede,^{1,*} Aline Ramires,^{2,†} and Yoichi Ando^{1,‡}

¹*Physics Institute II, University of Cologne, D-50937 Köln, Germany*

²*Paul Scherrer Institute, CH-5232 Villigen PSI, Switzerland*

(Dated: September 18, 2023)

Abstract

Among the family of odd-parity topological superconductors derived from Bi_2Se_3 , $\text{Cu}_x(\text{PbSe})_5(\text{Bi}_2\text{Se}_3)_6$ (CPSBS) has been elucidated to have gap nodes. Although the nodal gap structure has been established by specific-heat and thermal-conductivity measurements, there has been no direct observation of the superconducting gap of CPSBS using scanning tunnelling spectroscopy (STS). Here we report the first STS experiments on CPSBS down to 0.35 K, which found that the vortices generated by out-of-plane magnetic fields have an elliptical shape, reflecting the anisotropic gap structure. The orientation of the gap minima is found to be aligned with the bulk direction when the surface lattice image shows twofold symmetry, but, surprisingly, it is rotated by 30° when twofold symmetry is absent. In addition, the superconducting gap spectra in zero magnetic field suggest that the gap nodes are most likely lifted. We argue that only an emergent symmetry at the surface, allowing for a linear superposition of gap functions with different symmetries in the bulk, can lead to the rotation of the gap nodes. The absence of inversion symmetry at the surface additionally lifts the nodes. This result establishes the subtle but crucial role of crystalline symmetry in topological superconductivity.

* brede@ph2.uni-koeln.de

† aline.ramires@psi.ch

‡ ando@ph2.uni-koeln.de

I. INTRODUCTION

Topological superconductivity is a current hot topic in condensed matter physics due to its close relevance to Majorana fermions [1]. However, not many materials have been conclusively identified as topological superconductors. The family of bulk superconductors derived from Bi_2Se_3 presents a rare case, in which odd-parity topological superconductivity has been well established [1, 2]. In this class of materials, despite the three-fold rotational symmetry of the lattice, bulk superconducting (SC) properties consistently show peculiar twofold symmetry [3–9] that points to the realization of an odd-parity gap function with E_u symmetry. Although this gap function is unconventional and strongly anisotropic, the superconductivity is nonetheless protected from disorder due to the generalized Anderson’s theorem, thanks to the additional orbital degrees of freedom and layered structure [10–12].

Interestingly, the E_u -symmetric gap function under D_{3d} symmetry is generally a linear superposition of two basis functions, conventionally called Δ_{4x} and Δ_{4y} , which have nodes along a mirror plane of the crystal lattice or normal to it, respectively. The coefficients of the superposition form the nematic director \mathbf{n} [13]. In the presence of a principal rotation axis with threefold symmetry, there are three degenerate superpositions of these basis functions, corresponding to three distinct nematic directors. The selection of one of these superpositions endows a nematic character to the SC state. Note that only the mirror-symmetry-protected nodes are expected to be robust under the D_{3d} symmetry, while others can be lifted by perturbations such as a warping term in the normal state electronic structure [13]. Elucidating the factors that dictate the nematic axis is important not only for understanding the topological superconductivity in the Bi_2Se_3 -based compounds but also for finding ways to manipulate the SC gap [14].

Experimentally, the orientation of the gap minima differs among experiments even for the same compound [2]. For example, in $\text{Cu}_x\text{Bi}_2\text{Se}_3$, the direction of the gap minima has been reported to be 90° rotated between bulk [4] and surface [15] measurements. In this regard, there is a complexity arising from the threefold rotational symmetry of the Bi_2Se_3 lattice, which allows for three equivalent rotational domains [2, 4]; when contributions from two or more domains are superposed, the apparent symmetry may look like, e.g., Δ_{4x} even when the true symmetry is Δ_{4y} [4, 16].

Fortunately, this complexity is absent in the superconductor $\text{Cu}_x(\text{PbSe})_5(\text{Bi}_2\text{Se}_3)_6$ (here-

after called CPSBS) [9, 11, 17] which has a monoclinic crystal structure and a topologically nontrivial twofold symmetric gap function [1, 18, 19]. Specifically, Andersen *et al.* [9] showed that the gap function in CPSBS has nodes located on the unique crystallographic mirror plane, giving rise to nodal superconductivity in the bulk, which was evinced by specific-heat [9] and thermal-conductivity [11] measurements in the mK-regime. In this work, we use scanning tunneling microscopy (STM) and spectroscopy (STS) to directly access the SC gap on the surface of CPSBS. On a relatively clean surface, we found that vortices generated under out-of-plane magnetic fields are elongated in a twofold-symmetric manner, and the elongation occurs in the direction perpendicular to the bulk gap nodes. This is contrary to the naive expectation that the coherence length should be longer along the direction of the gap nodes [15], but it is actually consistent with recent theoretical calculations which showed that the vortex anisotropy in a p -wave superconductor should rotate by 90° as a result of impurity scattering [20]. On a more disordered surface where the twofold lattice symmetry is smeared, we found that the vortex anisotropy axis is rotated by 30° , pointing to the rotation of the gap nodes/minima on the surface. Our symmetry analysis shows that rotation of the gap nodes is indeed possible in the presence of an emergent symmetry at the surface and, furthermore, the inversion symmetry breaking at the surface would lead to lifting of the nodes. The latter conclusion is consistent with the observed gap spectra. Our work hence offers a framework to understand the intricate relation between crystal symmetry and the gap function in a topological superconductor.

II. RESULTS

A. Elongated vortices

We examine the SC gap structure on the surface of CPSBS by applying an out-of-plane magnetic field and imaging the vortex lattice of CPSBS in the mixed state. Even though a major portion of the cleaved surface of CPSBS does not show superconductivity, we were able to observe superconductivity on the sample surface at roughly 17% of the total scan area (see [21] for details), which is slightly better than the case of $\text{Cu}_x\text{Bi}_2\text{Se}_3$ [15]. Figure 1(a,b) and (c,d) shows the spatially resolved normalized zero-bias conductance (ZBC) on the superconducting surface of CPSBS for two different samples, S-I and S-II, and for

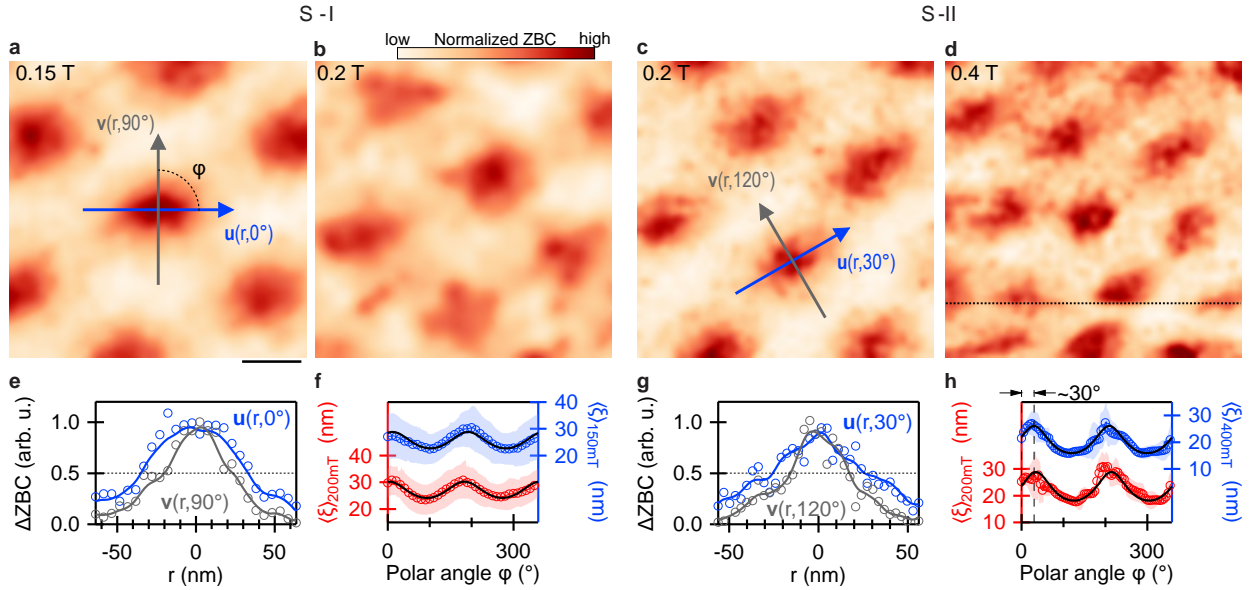


FIG. 1. **Elongated vortices in CPSBS.** (a,b) Normalized zero-bias conductance (ZBC) maps taken on sample S-I (a,b) in the out-of-plane magnetic field of 0.15 and 0.2 T. Stabilization parameters: $U = 5$ mV, $I = 200$ pA and $U_{\text{mod}} = 100 \mu\text{V}_p$. (c,d) Similar maps for sample S-II in 0.2 T and 0.4 T. Stabilization parameters: $U = 1$ mV, $I = 50$ pA and $U_{\text{mod}} = 100 \mu\text{V}_p$. Gaussian smoothing was applied to all maps to filter spatial variations of the ZBC smaller than the vortex size (unsmoothed data is shown in [21]). The discontinuity [dotted line in (d)] is due to the vortex lattice motion during the measurement. (e,g) Line profiles of the change in normalized ZBC (ΔZBC) taken across a vortex centre along the vectors shown in (a) and (c); solid lines and open circles are smoothed and raw data, respectively. (f,h) Angular dependence of the average vortex radius $\langle \xi \rangle$. Open circles denote the average of 53 (56) vortices measured for sample S-I at 0.15 T (0.2 T); for sample S-II, the average was from 6 (7) vortices at 0.2 T (0.4 T). The shaded area indicates the standard deviation and the solid black line is a fit to the ellipse equation. The polar angle was measured from the horizontal axis, which is parallel to the monoclinic b -axis.

out-of-plane magnetic fields between 0.15 and 0.4 T (additional data for other fields are shown in [21]). A vortex lattice is clearly resolved, and the vortex density increases with increasing field. Importantly, all the observed vortices are deformed — the vortices in sample S-I are roughly elongated along the horizontal axis, while those in sample S-II are rotated by about 30° in comparison.

Naively, one would expect that elongated vortices reflect an anisotropy in the Ginzburg-Landau (GL) in-plane coherence length, which results from the SC gap anisotropy in k -space, with the longest (shortest) coherence length associated with directions for which the gap value is the smallest (largest) [15]. However, it was recently pointed by theory that the local density of states (LDOS) around vortices imaged by STM experiments can acquire

different geometries depending on the strength of impurity scattering [20]. In particular, it was shown that for a p -wave superconductor, the LDOS is elongated along the the direction perpendicular to the gap nodes, in contrast to the naive GL prediction for clean systems. We will discuss the relation between the vortex elongation and the gap nodes/minima in Sec. II-C.

It is prudent to mention that a vortex-shape anisotropy can also be caused by a Fermi-velocity anisotropy [22, 23]. However, the ARPES measurements on superconducting CPSBS [24] found no such anisotropy within the experimental error of $\sim 2\%$. Even if there were some unexpected Fermi-velocity anisotropy in the region of the vortex lattice, we do not expect it can lead to an anisotropy of the vortex shape in the present case, because CPSBS is in the dirty limit [21] and a vortex-shape anisotropy cannot result purely from a Fermi-velocity anisotropy in the dirty limit [22]. Also, a vortex can appear elongated if the magnetic field is not perpendicular to the sample surface [25]; to dismiss this possibility, we intentionally tilted the applied magnetic field by about 10° both along the short and long vortex axes (see Fig. S9 in [21]) and observed no significant change in the anisotropy. Hence, it can be concluded that the elongation of the vortex stems from the anisotropic gap.

To quantify the vortex elongation, we first determine the vortex lattice (see [21] for details) and then take line-cuts of the ZBC at each lattice site corresponding to a vortex centre. Examples of such line-cuts are shown in Fig. 1 (e) and (g) for directions crossing the vortex shown in (a) and (c), respectively. We follow Sera *et al.* [20] to define the vortex-core radius ξ as the half width at half maximum, and determined it as a function of the polar angle φ . We obtained this $\xi(\varphi)$ for 53 (56) vortices in sample S-I at 0.15 T (0.2 T) and for 6 (7) vortices in sample S-II at 0.2 T (0.4 T). Note that ξ is not necessarily equal to the GL coherence length due to the scattering-induced LDOS [20]. The $\xi(\varphi)$ data are averaged over all vortices in each data set to yield $\langle \xi(\varphi) \rangle$, which is plotted for sample S-I in Fig. 1 (f) and for sample S-II in (h). The observed φ -dependence is reasonably well fit by the ellipse equation, and the fitting gives the ratio between the major and minor axes, $\gamma \equiv \langle \xi_{\text{major}} \rangle / \langle \xi_{\text{minor}} \rangle$, of ~ 1.25 (~ 1.55) for sample S-I (S-II). The fitting also gives the rotation angle of $\sim 30^\circ$ for the vortices in sample S-II.

B. Superconducting gap spectra

As discussed above, our observation of elongated vortices points to an anisotropic SC gap. To investigate the anisotropy in the SC gap function, we analyzed the representative dI/dU -spectra (Fig. 2) measured in zero field at the lowest fridge temperature of 0.35 K for samples S-I and S-II. We fit the spectra by using a generalization of Dynes formula [26] for the momentum-resolved superconducting DOS,

$$N_{\mathbf{k}}(E) = \left| \text{Re} \left[(E - i\Gamma) / \sqrt{(E - i\Gamma)^2 - \Delta_{\mathbf{k}}^2} \right] \right|, \quad (1)$$

where we assume a circular Fermi surface. Γ is an effective broadening parameter due to pair-breaking scattering and $\Delta_{\mathbf{k}}$ is the SC gap that can have a \mathbf{k} -dependence. We fit a twofold symmetric gap with $\Delta_{\mathbf{k}} = \Delta_0 + \Delta_1 |\cos \theta_{\mathbf{k}}|$: when the gap is nodal, $\Delta_0 = 0$. The

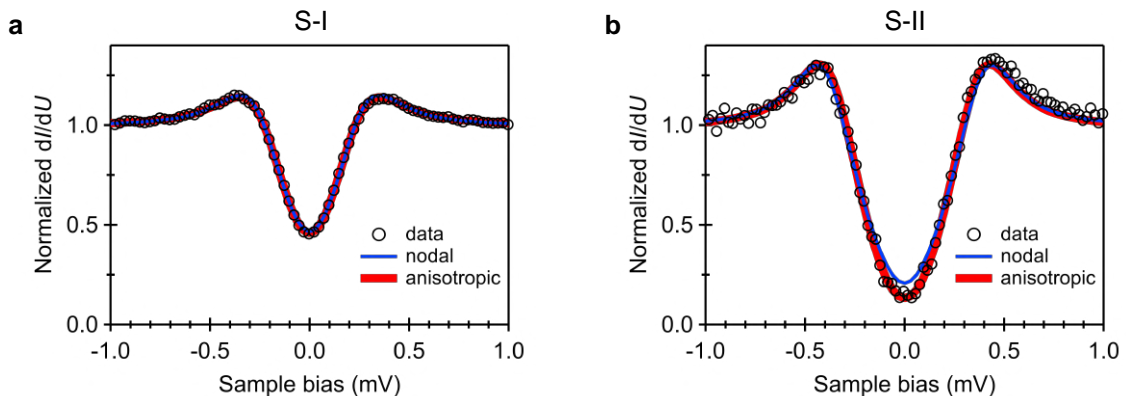


FIG. 2. **Superconducting gap spectra.** Representative high-resolution gap spectra taken in zero field, at the base temperature of 0.35 K and in the same area as the vortex maps. The spectrum in (a) is a result of averaging 10000 individual spectra covering an area of $(500 \text{ nm})^2$, while the data in (b) is after averaging 5000 individual spectra taken at the same spot to enhance the resolution. The fits of the data to Eq. (1) assuming two different gap functions [nodal (blue) and node-lifted anisotropic (red) types] are overlaid on the data. In these fits, the effective temperature was fixed at 0.7 K. The set of parameters $(\Delta_0, \Delta_1, \Gamma)$ obtained from the fits in (a) for sample S-I are $(0, 0.26, 0.03)$ and $(0.07, 0.18, 0.05)$ for the nodal and node-lifted scenarios, respectively, and those for sample S-II in (b) are $(0, 0.39, 0)$ and $(0.11, 0.26, 0.01)$ for the two scenarios (all in mV unit). Any error of the fitting routine is well below the experimental uncertainty due to the spatial inhomogeneity of the total gap magnitude, which was about 0.05 meV in each area [21]. Stabilization parameters: $U = 5 \text{ mV}$, $I = 500 \text{ pA}$ for sample S-I (a) and $U = 3 \text{ mV}$, $I = 50 \text{ pA}$ for sample S-II (b).

tunnelling conductance dI/dU is given by

$$\frac{dI}{dU} \propto \int N_{\mathbf{k}}(E) f'(E + eU) d\mathbf{k} dE, \quad (2)$$

where $f(E)$ is the Fermi-Dirac distribution function at the effective temperature T_{eff} . The effective temperature of our STM experiments at the fridge temperature of 0.35 K was independently determined by a measurement of pure Nb [27] to be 0.7 K, so we fixed $T_{\text{eff}} = 0.7$ K and used Γ , Δ_0 and Δ_1 as fitting parameters.

In Fig. 2, we show fits to two different types of gap function: (i) nodal gap ($\Delta_0 = 0$) and (ii) twofold symmetric gap with lifted nodes ($\Delta_0 \neq 0$). As is described in detail in [21], the size of the SC gap on the CPSBS surface varies with location. Thanks to a relatively large local gap, the data in Fig. 2(b) from sample S-II have a low ZBC which helps to infer if the nodes are lifted: The nodal fit of the spectrum yields a ZBC that is higher than the data even for $\Gamma = 0$, which is clearly unreasonable given the dirty-limit nature of CPSBS [21]. On the other hand, a reasonable fit is obtained for the anisotropic gap with lifted nodes, yielding $\Delta_0 = 0.11$ meV and $\Delta_1 = 0.26$ meV with $\Gamma = 10$ μ eV. Hence, the data in Fig. 2(b) strongly suggest that the nodes are lifted at the surface. Here we should note that the conclusion of lifted nodes is based on the fits to the commonly-assumed sinusoidal gap function, and it may not be valid if the anisotropic gap has a non-sinusoidal function with unusually steep node. The large anisotropy ratio $(\Delta_0 + \Delta_1)/\Delta_0 \simeq 3.4$ implies a pronounced minima in the gap function, which is consistent with the finite quasiparticle scattering even in the absence of vortices. Due to a smaller local gap resulting in a large ZBC, the data in Fig. 2(a) from sample S-I do not allow us to distinguish between nodal and the node-lifted scenarios; nevertheless, the fit with the anisotropic gap function yields a reasonable result with an anisotropy ratio of ~ 3.6 . In fact, the spectra obtained at all the SC regions are consistent with the anisotropic gap function (see Fig. S11 in [21]), even though the value of Δ_0 and Δ_1 varies significantly. This large variation appears to reflect the fact the the superconductivity in CPSBS (and in all other Bi_2Se_3 -based superconductors) is weakened or disappear at a larger part of the surface, whose origin is a topic of on-going research: For example, in a recent paper [27] it was proposed that a strong electric field due to intrinsic surface band bending may break Cooper pairs near the surface. In the case of CPSBS, the strength of surface band bending would vary depending on the density of Cu dopants found

on the surface.

To strengthen the conclusion of the anisotropic gap, we performed additional experiments on sample S-III to measure the dependence of the SC gap spectra on the direction of the in-plane magnetic field, φ (see [21] for details). The φ -dependence of the spectra, in particular the conductance at zero bias, is clearly twofold symmetric (see Fig. S12 in [21]). A similar phenomenon was reported for $\text{Cu}_x\text{Bi}_2\text{Se}_3$ [15] and was taken as additional evidence for an anisotropic gap. These observations are also in good agreement with the theoretical prediction by Nagai [28], who showed that the angular dependence of the zero-energy density of states has deep minima when the in-plane magnetic field is aligned with the direction of the nodes in the Δ_4 gap realized in $\text{Cu}_x\text{Bi}_2\text{Se}_3$.

C. Orientation of the gap minima

We now turn to the topographic images of CPSBS and those of pristine $(\text{PbSe})_5(\text{Bi}_2\text{Se}_3)_6$ (called PSBS) to identify the orientation of the gap minima. Figure 3(a) shows the schematics of the crystal structure of PSBS/CPSBS. Upon cleaving the PSBS crystal, one usually obtains a surface that is terminated by a single quintuple layer (QL) of the Bi_2Se_3 unit on top of the PbSe layer [29]. Figure 3(d) shows a typical topograph on such a surface, where a clear one-dimensional (1D) stripe pattern with atomically resolved top Se layer is observed. Although the lattice in CPSBS is more disordered due to Cu intercalation, a similar stripe pattern is observed in atomic-resolution images on a SC area of CPSBS of sample S-I [Fig. 3(f)] as well as on a non-superconducting (NSC) area of sample S-II [Fig. 3(e)]. The stripe corrugation is less pronounced in the SC area of sample S-I [Fig. 1(g)].

The 1D stripe can be understood as a commensuration effect (similar to a moiré pattern) arising from the stacking of the square PbSe lattice and the hexagonal Bi_2Se_3 lattice. One can see in Fig. 3(a) that the crystal structure repeats every six Se atoms in the layer 5 and every five Pb atoms in layer 6 along the a -axis, and this repetition defines the unit length along the a -axis. As shown in Fig. 3(c), the stripe periodicity agrees with the length of the monoclinic a -axis, which clearly indicates that the stripes come from this commensuration of Se and Pb sublattices. This in turn allows for a unique determination of the in-plane monoclinic lattice vectors on the hexagonal top Se layer, i.e., the stripes are running along the b -axis. While we were not able to resolve the crystal lattice in the SC area of sample S-II

where the vortex lattice shown in Fig. 1(c,d) was recorded (a similar case was reported by Tao *et al.* [15] for $\text{Cu}_x\text{Bi}_2\text{Se}_3$), we know from X-ray diffraction analysis that in our CPSBS sample the orientation of the monoclinic axes is macroscopically identical. This is further verified in STM since we only observed one fixed orientation of the 1D-stripe with respect to our scan coordinates, globally.

In Fig. 3(b), we replot the anisotropic ξ with respect to the hexagonal lattice and the monoclinic axes for both samples S-I and S-II. Focusing first on the data for S-I, it is to

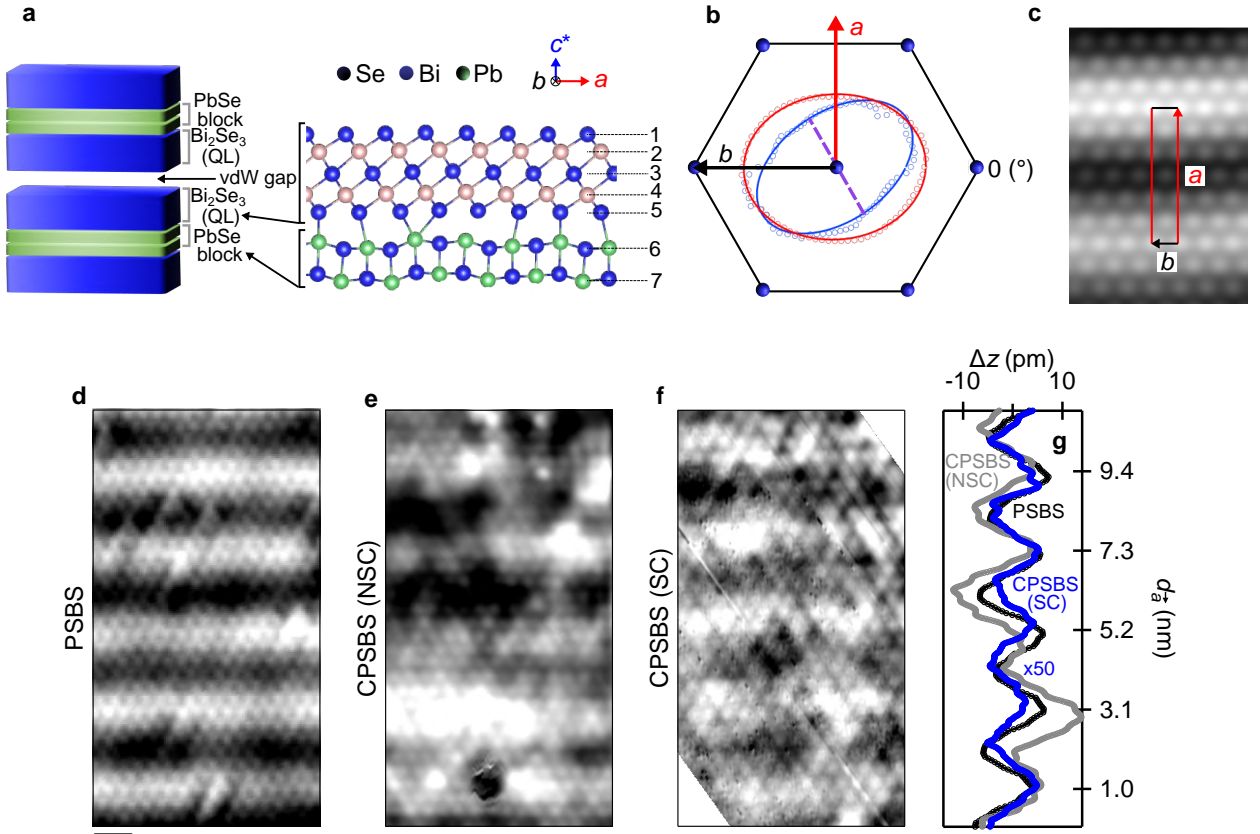


FIG. 3. Crystal structure and the gap anisotropy. (a) Schematics of the crystal structure of PSBS. (b) Average profile (open circles) and the fit to the ellipse equation (solid line) of vortices at 0.2 T for sample S-I (red) and S-II (blue) [the same data as in Figs. 1(f) and (h)] with respect to the top Se lattice and the monoclinic *a* and *b* axes; the mirror plane is parallel to *a*. (c) Fourier-filtered image of (d) overlaid with the monoclinic unit vectors; the stripe periodicity of ~ 2.1 nm agrees with the *a* unit length. (d) Atomically resolved topmost Se layer on the cleaved surface of PSBS showing 1D stripes running across the whole surface. The stripe pattern is also observed on the non-superconducting areas of the CPSBS surface in sample S-II (e) and the superconducting area of sample S-I (f). Scale bar corresponds to 1 nm. (g) Averaged STM height profile along the vertical direction in (d) to (f). Scan parameters: $U = 900$ mV, $I = 20$ nA for (d); $U = 30$ mV, $I = 500$ pA for (e); $U = 900$ mV, $I = 200$ pA for (f).

be remarked that the vortex core is elongated roughly along the monoclinic b -axis, whereas the gap nodes in the bulk lie along the a -axis [9]. This fact indicates that the vortex-shape anisotropy is not dictated by the GL coherence length anisotropy but by the maxima of the LDOS in the presence of impurity scattering. A recent theoretical work has reported that the maxima in the LDOS can be rotated by 90° in the presence of impurity scattering [20]. This result can be understood in terms of the quasiparticle trajectory picture, which has been useful for understanding the rotation of vortices as a function of applied bias [30–32]. The effect of impurities in superconductors can be understood in terms of a self-energy renormalization of the frequency and gap matrices [33] introduced by a scattering potential. For an anisotropic s -wave superconductor, impurities self-average the gap to become isotropic, so any anisotropy in the LDOS promoted by the anisotropy of the gap is lost in the dirty limit. In contrast, in sign-changing nodal superconductors, impurities lead to a renormalization of the frequency, but not of the superconducting gap, as it averages to zero [33]. This renormalization can be understood as an effective bias, as it increases the frequency, and the conclusions for the rotation of the vortex anisotropy as a function of bias can then be generalized to the rotation of the vortex anisotropy as a function of impurity scattering. Figure 4 gives a schematic representation of this mechanism.

It is worthwhile to note that p -wave superconductivity is commonly known to be fragile against impurity scattering; however, in CPSBS the generalized Anderson theorem [11] protects the unconventional pairing even in the dirty limit. Note also that this impurity effect on the vortex shape was not considered in the previous work on $\text{Cu}_x\text{Bi}_2\text{Se}_3$ [15], which concluded that the gap minima at the surface are 90° rotated compared to the bulk.

Interestingly, the elongation axis of the vortices in sample S-II shown in Fig. 1(c,d) is 30° rotated from that in sample S-I. Following the conclusion that the vortex elongation occurs in the direction of gap maxima in CPSBS, the data in Fig. 1(c,d) suggest that on the SC surface of sample S-II, the gap minima are rotated from the monoclinic a axis by 30° , which is perpendicular to one of the mirror planes of D_{3d} symmetry and corresponds to the Δ_{4y} gap. In correspondence with this result, the in-plane magnetic-field-direction dependence of the gap spectra observed in sample S-III, which was discussed in Sec. II-B, also shows that the gap minima is rotated from the a axis by $\sim 20^\circ$ (see [21] for details). As shown in Fig. S13 in [21], the SC areas of both samples S-II and S-III are so disordered that the stripe pattern indicating the twofold symmetry of the lattice is no longer observed. This implies

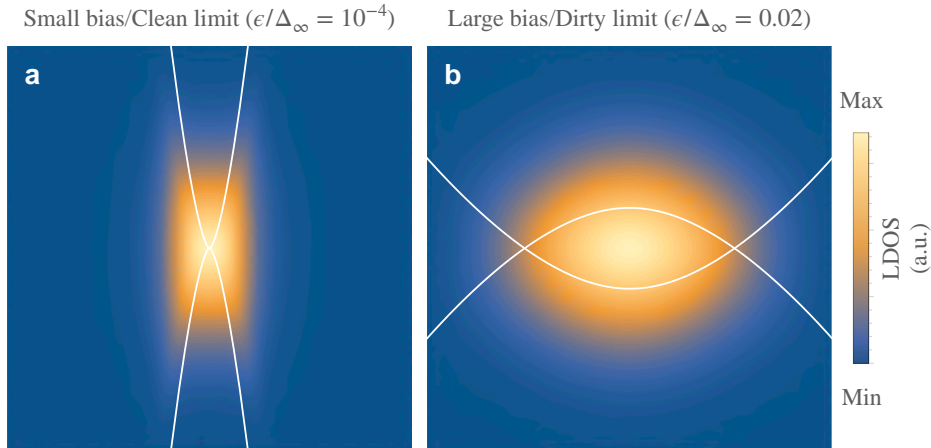


FIG. 4. **Quasiclassical trajectory picture.** (a) Small bias or clean limit, with small ϵ/Δ_∞ ratio. (b) Large bias or dirty limit with larger ϵ/Δ_∞ ratio. The enveloping curves of the quasiparticle paths at which the LDOS diverges are shown in white lines. The plots follow the analytical form given by Nagai *et al.* [31] [Eq. (3.45) of their paper] for a nodal superconductor with two-fold symmetry, $\lambda(\theta) = \cos(\theta)$. The density plots correspond to the LDOS given by the integral over the poles determined by the enveloping curves smeared by $\delta/\Delta_\infty = 0.05$ and with an isotropic exponential decay characterized by $l/\xi_0 = 400$. Here Δ_∞ is the gap magnitude in the bulk, ϵ is the energy scale of either the bias or the scattering rate, and ξ_0 the coherence length. The field of view corresponds to $0.2\xi_0$ along the x and y directions.

that the threefold symmetry of the Bi_2Se_3 QLs is effectively restored due to disorder in both samples. In the next section, we argue that the rotation of the gap minima observed on the SC surface of samples S-II and S-III can be understood as a consequence of this emergent symmetry.

III. THEORETICAL ANALYSIS

We now present a symmetry analysis which provides a consistent picture for the above observations, under the assumption that the superconductivity observed on the surface inherits the unconventional pairing from the bulk. We emphasize that, although the nature of the superconductivity on the surface is apparently different from that of the bulk, it must be unconventional itself, because vortices cannot be anisotropic in the dirty limit of a conventional superconductor.

We start the discussion from the perspective of the Bi_2Se_3 QLs with D_{3d} point group symmetry. The minimal model for the normal state electronic structure that properly captures the topological properties of the bands is given in terms of two effective orbitals with

opposite parity formed by a symmetric, labelled as 1, or antisymmetric, 2, combination of p_z orbitals within the QLs [34, 35]. In the orbital-spin basis $\Phi_{\mathbf{k}}^\dagger = (c_{1\uparrow}^\dagger, c_{1\downarrow}^\dagger, c_{2\uparrow}^\dagger, c_{2\downarrow}^\dagger)_{\mathbf{k}}$, the normal-state Hamiltonian can be parametrized as:

$$\hat{H}_0(\mathbf{k}) = \sum_{a,b} h_{ab}(\mathbf{k}) \hat{\tau}_a \otimes \hat{\sigma}_b, \quad (3)$$

where $\hat{\tau}_{a=1,2,3}$ are Pauli matrices encoding the orbital degrees of freedom (DOF), $\hat{\sigma}_{b=1,2,3}$ are Pauli matrices encoding the spin DOF, and $\hat{\tau}_0$ and $\hat{\sigma}_0$ are two-dimensional identity matrices in orbital and spin space, respectively. In the presence of time-reversal [acting as $\hat{\Theta} = K \hat{\tau}_0 \otimes (i\hat{\sigma}_2)$, where K stands for complex conjugation] and inversion (implemented as $\hat{P} = \hat{\tau}_3 \otimes \hat{\sigma}_0$) symmetries, the only allowed terms in the Hamiltonian have indexes $(a, b) = \{(0, 0), (2, 0), (3, 0), (1, 1), (1, 2), (1, 3)\}$. The properties of the $\hat{\tau}_a \otimes \hat{\sigma}_b$ matrices under the point group operations allow us to associate each of these terms to a given irreducible representation (irrep) of D_{3d} , therefore constraining the momentum dependence of the form factors $h_{ab}(\mathbf{k})$ by symmetry. More details on the description of the normal state are given in [21]. The important features to keep in mind are the following: (0, 0) and (3, 0) correspond to intra-orbital hopping, (2, 0) corresponds to inter-orbital hopping, (1, a), with $a = \{1, 2, 3\}$ correspond to spin-orbit coupling terms. In particular, (1, 3) is associated with trigonal warping and is very small within the parameter range of validity of this effective model [35].

Following the parametrization of the normal state, the order parameters can be generally written as:

$$\hat{\Delta}(\mathbf{k}) = \sum_{a,b} d_{ab}(\mathbf{k}) \hat{\tau}_a \otimes \hat{\sigma}_b (i\hat{\sigma}_2). \quad (4)$$

Focusing on local pairing mechanisms, the allowed momentum-independent gap matrices are associated with antisymmetric matrices $\hat{\tau}_a \otimes \hat{\sigma}_b (i\hat{\sigma}_2)$. These can be classified according to the irreps of the of D_{3d} point group, as displayed in the second column of Table I [18].

The QLs of Bi_2Se_3 have D_{3d} symmetry. In CPSBS, the presence of the PbSe layers reduces the point group symmetry from D_{3d} to D_{1d} , and the irreps are mapped according to the third column of Table I. The SC order parameter in the bulk of CPSBS is believed to be of the form [2, 2], given its twofold symmetry and the presence of nodes along the mirror plane [9, 11]. This is an odd-parity order parameter which is inter-orbital and spin-triplet in

$[a,b]$	D_{3d}	D_{1d}	C_{1v}	C_{3v}
$[0,0]$	A_{1g}	A_{1g}	A_1	A_1
$[3,0]$				
$[2,3]$	A_{1u}	A_{1u}	A_2	A_2
$[1,0]$	A_{2u}	A_{2u}	A_1	A_1
$[2,1]$	E_u	A_{2u}	A_1	E
$[2,2]$		A_{1u}	A_2	

TABLE I. **Classification of superconducting order parameters.** Here we focus on momentum-independent SC order parameters in the microscopic basis for materials in the family of Bi_2Se_3 . The $[a, b]$ indexes in the first column correspond to the parametrization of the SC gap function according to Eq. 4. The second to fifth columns give the irreducible representation associated with each order parameter for the cases of D_{3d} , D_{1d} , C_{1v} , and C_{3v} point group symmetry, respectively.

nature. Note that, in the case of D_{1d} symmetry, this order parameter belongs to A_{1u} irrep. This is a one-dimensional irrep and the notion of nematicity does not apply as the threefold symmetry is explicitly broken by the lattice. Note, though, that the order parameter with indices $[2, 3]$ belongs to the same A_{1u} symmetry channel in D_{1d} . This means that an order parameter in A_{1u} is generally a linear superposition of $[2, 2]$ and $[2, 3]$. Even if pairing is primarily driven by interactions promoting the order parameter $[2, 2]$, the combination of spin-orbit coupling terms $(1, 2)$ and $(1, 3)$ in the normal state Hamiltonian could lead to the development of SC correlations with $[2, 3]$ character. Nevertheless, as the trigonal warping term $(1, 3)$ is small in the Bi_2Se_3 -family of compounds [35], the corresponding mixing should also be small in the bulk of CPSBS, leading to a lifting of nodes that might be too small to be observed experimentally. This information is schematically conveyed in the second row of Figure 5.

At the surface of CPSBS inversion symmetry is broken and the point group is reduced to C_{1v} . The irreps associated to the order parameters with momentum-independent gap matrices are mapped according to the fourth column of Table I. Now the order parameter $[2, 2]$ belongs to irrep A_2 , and any order parameter in this symmetry channel should again be a linear superposition of $[2, 2]$ and $[2, 3]$. Note that due to inversion symmetry breaking at the surface, the normal-state Hamiltonian includes all (a, b) coefficients, allowing for multiple pairs of terms in the normal state to promote the mixing of the $[2, 2]$ and $[2, 3]$ order parameters (see detailed discussion in [21]). These surface terms in the normal-state Hamiltonian contribute further to the lifting of gap nodes, as illustrated in the third row of

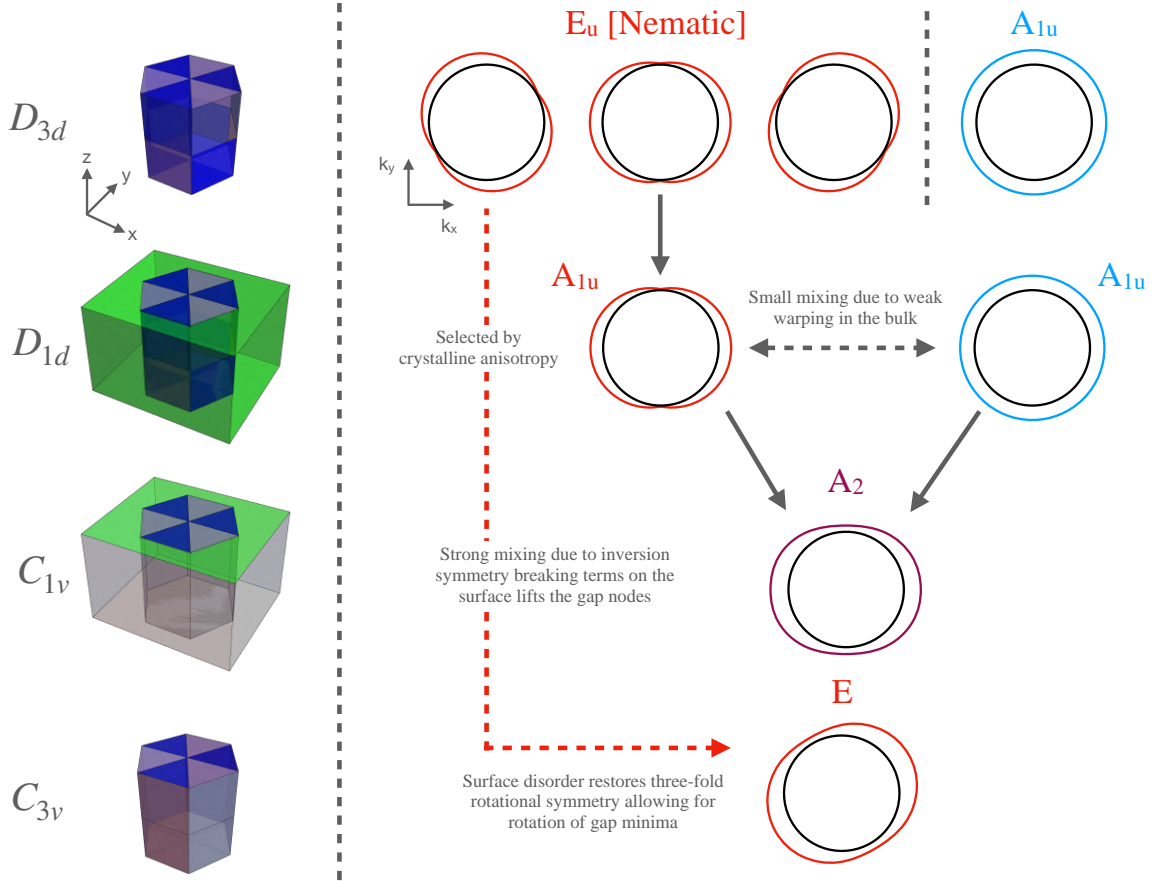


FIG. 5. **Symmetry analysis of the superconducting order parameter.** Left: Representative objects following the same point group symmetries as Bi_2Se_3 (D_{3d}), CPSBS (D_{1d}), and the surface of CPSBS (C_{1v} or C_{3v} , without or with disorder, respectively). The colour of the objects matches the corresponding Bi_2Se_3 and PbSe blocks in Figure 3(a). Right: SC gaps (coloured lines) at the Fermi surfaces (black circles) for the symmetry channels relevant for the discussion in the text. More details on the parameters used to generate the figures for each symmetry scenario are given in the Supplementary Information [21].

Figure 5, so that the node lifting at the surface would be stronger than that in the bulk. Here it should be emphasized that, as any gap in C_{1v} should still be symmetric or antisymmetric under reflections along the $k_y k_z$ -plane, the gap cannot be rotated under these symmetry considerations. For a rotation of gap nodes or gap minima to take place, a mixing of order parameters in different symmetry channels of C_{1v} would be required.

A possible origin of such a mixing is the strong disorder at the surface. The rotation of the gap minima was detected only in locations at which no stripe pattern could be observed by STM (see Fig. S13 in [21]), suggesting that in these disordered areas the effect of the PbSe layers is weakened and the threefold rotational symmetry present in the Bi_2Se_3 layers is

effectively restored. Under these considerations, the point group symmetry at the disordered surface can be identified as C_{3v} . Interestingly, this point group has a two-dimensional irrep labelled as E , which would allow for mixing of gaps $[2, 2]$ and $[2, 1]$ that are associated with different irreps in C_{1v} . Under the C_{3v} symmetry, by changing the mixing of these two order parameters in the absence of warping, we find that the gap minima can be tuned to any position along the circular Fermi surface. In particular, a ratio $d_{21}/d_{22} = 1$ generates minima at 30° from the bulk nodes. While the stability of this particular ratio requires an analysis of the energetics of the system, which is beyond the scope of this paper, the rotation by 30° corresponds to having the nodes along the a -axis of the hexagonal notation [9] for D_{3d} symmetry. It is plausible that this ratio is in fact stable, as this is the direction of the nodes realized in $\text{Cu}_x\text{Bi}_2\text{Se}_3$.

The last row of Figure 5 schematically shows a gap that could be generated at the surface under these considerations. Here, it should be remarked that the two-component nature of the order parameter in the quintuple layers of Bi_2Se_3 -based materials with D_{3d} symmetry is a necessary condition to explain the rotation of the gap at the surface of CPSBS. Therefore, the tunnelling spectra and the vortex anisotropy observed in our experiment provides one more piece of evidence for the intrinsically nematic nature of the SC gap in Bi_2Se_3 -based materials.

IV. DISCUSSIONS

We start our discussions by revisiting some of the experimental findings on $\text{Cu}_x\text{Bi}_2\text{Se}_3$ samples. Some of the discrepancies between the bulk [4] and the surface [15] regarding the direction of the gap minima may be resolved by considering the effect of impurity scattering discussed in Sec. II-C. However, in the literature, even in the bulk measurements on $\text{Cu}_x\text{Bi}_2\text{Se}_3$, there are reports which differ in the position of the gap minima with respect to the underlying lattice by 90° [3, 4]. Recent Knight-shift measurements [16] ruled out a multidomain effect in the bulk of the sample which was previously proposed [4] as the possible reason for the different orientations of the gap. It was proposed in [16] that the specific local environment in the sample caused by lattice distortion or strain from dopant intercalation and/or quenching (which is necessary for obtaining superconductivity) may be responsible for determining the nematic axis. A high-resolution x-ray diffraction (XRD)

experiment on $\text{Sr}_x\text{Bi}_2\text{Se}_3$ reported a tiny ($\sim 0.02\%$) in-plane lattice distortion [36], while a multimodal synchrotron XRD experiment with a slightly lower resolution did not find any distortion [37]. Therefore, the situation in doped- Bi_2Se_3 superconductors is complicated and it is still unclear what dictates the orientation of the gap minima in them.

In contrast, the orientation of the gap minima in the bulk of CPSBS is robust due to the reduced symmetry of the crystal lattice which has only one mirror plane, and the rotation of the gap minima observed here is a pronounced manifestation of the decisive role of crystalline symmetry in determining the anisotropic axis of the SC gap. The rotation of the gap minima also signifies the intrinsically nematic nature of the SC order parameter in Bi_2Se_3 -based materials, which suggests that the pairing mechanism must be the same for all superconductors in this family of materials.

It is useful to mention that according to the theoretical calculations reported in [20], the effect of impurity scattering is different for p -wave and anisotropic s -wave order parameters even when the angular dependence of the gap magnitude $|\Delta_{\mathbf{k}}|$ is the same; in the latter case, there is no sign change in the anisotropic SC gap and the vortex shape becomes isotropic in the presence of strong scattering. Therefore, the observation of elongated vortices in the dirty limit gives additional evidence for the topological odd-parity gap function.

The present result on CPSBS, taken together with the complications in the orientation of the gap minima in $\text{Cu}_x\text{Bi}_2\text{Se}_3$, clearly shows that the odd-parity gap function is highly sensitive to crystal symmetry in the topological superconductors derived from Bi_2Se_3 . The symmetry-based analysis of the possible superpositions of different gap functions presented here gives a useful framework to understand odd-parity topological superconductors.

Methods

Material: We grew $(\text{PbSe})_5(\text{Bi}_2\text{Se}_3)_6$ single crystals using a modified Bridgeman method as described previously [9, 17]. Cu was electrochemically intercalated using the recipe of Kriener *et al.* [38] with a nominal x value of 1.36. The SC shielding fraction of the resulting CPSBS sample was measured using a Quantum Design superconducting quantum interference device (SQUID) magnetometer (see Fig. S1 in [21]) and was 59% for sample S-I and 61% for sample S-II.

STM experiments: STM experiments were carried out under UHV conditions with a commercial system (Unisoku USM1300) operating at 0.35 K. STM images were recorded in

the constant-current mode at the set current I and sample bias voltage U . dI/dU curves and dI/dU maps were obtained either using a lock-in amplifier by modulating U_{bias} and demodulating I , or by recording a series of I - U curves followed by numerical differentiation. The dI/dU maps displayed in Fig. 1 were smoothed by using a standard Gaussian filter with the smallest (3×3 points) kernel, corresponding to $15 \times 15 \text{ nm}^2$ (a), $20 \times 20 \text{ nm}^2$ (b) and $9.35 \times 9.35 \text{ nm}^2$ (c,d), with up to three iterations. The dI/dU spectra displayed in Fig. 2 were obtained by taking the numerical derivative of raw I - U data and subsequently applying a simple low-pass filter (binominal 21 passes). All STM data were analyzed using Igor Pro 9. We used in-house electrochemically etched W tips, first prepared on the Cu(111) crystal. Tip forming is done until a clean signature of the surface state is observed in spectroscopy. Prior to STM measurements, the crystals were cleaved under UHV conditions as described in [27].

Acknowledgment: This project has received funding from the European Research Council (ERC) under the European Union’s Horizon 2020 research and innovation programme (grant agreement No 741121) and was also funded by the DFG under CRC 1238 - 277146847 (Subprojects A04 and B06) as well as under Germany’s Excellence Strategy - Cluster of Excellence Matter and Light for Quantum Computing (ML4Q) EXC 2004/1 - 390534769. AR is supported by the Swiss National Science Foundation through the Ambizione Grant No. 186043.

-
- [1] Sato, M. & Ando, Y. Topological superconductors: a review. Rep. Prog. Phys. **80**, 076501 (2017).
 - [2] Yonezawa, S. Nematic superconductivity in doped Bi_2Se_3 topological superconductors. Condens. Matter **4**, 2 (2019).
 - [3] Matano, K., Kriener, M., Segawa, K., Ando, Y. & Zheng, G.-q. Spin-rotation symmetry breaking in the superconducting state of $\text{Cu}_x\text{Bi}_2\text{Se}_3$. Nat. Phys. **12**, 852–854 (2016).
 - [4] Yonezawa, S. et al. Thermodynamic evidence for nematic superconductivity in $\text{Cu}_x\text{Bi}_2\text{Se}_3$. Nat. Phys. **13**, 123–126 (2017).
 - [5] Liu, Z. et al. Superconductivity with topological surface state in $\text{Sr}_x\text{Bi}_2\text{Se}_3$. J. Am. Chem. Soc. **137**, 10512–10515 (2015).

- [6] Pan, Y. *et al.* Rotational symmetry breaking in the topological superconductor $\text{Sr}_x\text{Bi}_2\text{Se}_3$ probed by upper-critical field experiments. *Sci. Rep.* **6**, 28632 (2016).
- [7] Shen, J. *et al.* Nematic topological superconducting phase in Nb-doped Bi_2Se_3 . *npj Quant. Mater.* **2**, 59 (2017).
- [8] Asaba, T. *et al.* Rotational symmetry breaking in a trigonal superconductor Nb-doped Bi_2Se_3 . *Phys. Rev. X* **7**, 011009 (2017).
- [9] Andersen, L., Wang, Z., Lorenz, T. & Ando, Y. Nematic superconductivity in $\text{Cu}_{1.5}(\text{PbSe})_5(\text{Bi}_2\text{Se}_3)_6$. *Phys. Rev. B* **98**, 220512 (2018).
- [10] Scheurer, M. S., Hoyer, M. & Schmalian, J. Pair breaking in multiorbital superconductors: An application to oxide interfaces. *Phys. Rev. B* **92**, 014518 (2015).
- [11] Andersen, L., Ramires, A., Wang, Z., Lorenz, T. & Ando, Y. Generalized Anderson’s theorem for superconductors derived from topological insulators. *Sci. Adv.* **6**, eaay6502 (2020).
- [12] Zinkl, B. & Ramires, A. Sensitivity of superconducting states to the impurity location in layered materials. *Phys. Rev. B* **106**, 014515 (2022).
- [13] Fu, L. Odd-parity topological superconductor with nematic order: Application to $\text{Cu}_x\text{Bi}_2\text{Se}_3$. *Phys. Rev. B* **90**, 100509 (2014).
- [14] Kostylev, I., Yonezawa, S., Wang, Z., Ando, Y. & Maeno, Y. Uniaxial-strain control of nematic superconductivity in $\text{Sr}_x\text{Bi}_2\text{Se}_3$. *Nat. Commun.* **11**, 4152 (2020).
- [15] Tao, R. *et al.* Direct visualization of the nematic superconductivity in $\text{Cu}_x\text{Bi}_2\text{Se}_3$. *Phys. Rev. X* **8**, 041024 (2018).
- [16] Kawai, T. *et al.* Direction and symmetry transition of the vector order parameter in topological superconductors $\text{Cu}_x\text{Bi}_2\text{Se}_3$. *Nat. Commun.* **11**, 235 (2020).
- [17] Sasaki, S., Segawa, K. & Ando, Y. Superconductor derived from a topological insulator heterostructure. *Phys. Rev. B* **90**, 220504 (2014).
- [18] Fu, L. & Berg, E. Odd-parity topological superconductors: Theory and application to $\text{Cu}_x\text{Bi}_2\text{Se}_3$. *Phys. Rev. Lett.* **105**, 097001 (2010).
- [19] Ando, Y. & Fu, L. Topological crystalline insulators and topological superconductors: From concepts to materials. *Annu. Rev. Condens. Matter Phys.* **6**, 361–381 (2015).
- [20] Sera, Y., Ueda, T., Adachi, H. & Ichioka, M. Relation of superconducting pairing symmetry and non-magnetic impurity effects in vortex states. *Symmetry* **12**, 175 (2020).
- [21] See Supplemental Information for additional data and discussions.

- [22] Odobesko, A. et al. Anisotropic vortices on superconducting Nb(110). Phys. Rev. B **102**, 174502 (2020).
- [23] Kim, H., Nagai, Y., Rózsa, L., Schreyer, D. & Wiesendanger, R. Anisotropic non-split zero-energy vortex bound states in a conventional superconductor. Appl. Phys. Rev. **8**, 031417 (2021).
- [24] Nakayama, K. et al. Observation of two-dimensional bulk electronic states in the superconducting topological insulator heterostructure $\text{Cu}_x(\text{PbSe})_5(\text{Bi}_2\text{Se}_3)_6$: Implications for unconventional superconductivity. Phys. Rev. B **92**, 100508 (2015).
- [25] Galvis, J. A. et al. Tilted vortex cores and superconducting gap anisotropy in 2H-NbSe₂. Commun. Phys. **1**, 30 (2018).
- [26] Dynes, R. C., Narayanamurti, V. & Garno, J. P. Direct measurement of quasiparticle-lifetime broadening in a strong-coupled superconductor. Phys. Rev. Lett. **41**, 1509–1512 (1978).
- [27] Bagchi, M., Brede, J. & Ando, Y. Observability of superconductivity in Sr-doped Bi₂Se₃ at the surface using scanning tunneling microscope. Phys. Rev. Mater. **6**, 034201 (2022).
- [28] Nagai, Y. Field-angle-dependent low-energy excitations around a vortex in the superconducting topological insulator $\text{Cu}_x\text{Bi}_2\text{Se}_3$. J. Phys. Soc. Jpn. **83**, 063705 (2014).
- [29] Nakayama, K. et al. Nanomosaic of topological Dirac states on the surface of $\text{Pb}_5\text{Bi}_{24}\text{Se}_{41}$ observed by nano-ARPES. Nano Lett. **19**, 3737–3742 (2019).
- [30] Ichioka, M., Hayashi, N., Enomoto, N. & Machida, K. Vortex structure in d-wave superconductors. Phys. Rev. B **53**, 15316–15326 (1996).
- [31] Nagai, Y., Ueno, Y., Kato, Y. & Hayashi, N. Analytical formulation of the local density of states around a vortex core in unconventional superconductors. J. Phys. Soc. Jpn. **75**, 104701–104701 (2006).
- [32] Kaneko, S.-i. et al. Quantum limiting behaviors of a vortex core in an anisotropic gap superconductor. J. Phys. Soc. Jpn. **81**, 063701 (2012).
- [33] Maki, K. Gapless superconductivity. In Parks, R. D. (ed.) Superconductivity, vol. 2, chap. 18, 1035–1105 (Marcel Dekker, 1969).
- [34] Zhang, H. et al. Topological insulators in Bi₂Se₃, Bi₂Te₃ and Sb₂Te₃ with a single Dirac cone on the surface. Nature Physics **5**, 438–442 (2009).
- [35] Liu, C.-X. et al. Model Hamiltonian for topological insulators. Phys. Rev. B **82**, 45122 (2010).
- [36] Kuntsevich, A. Y. et al. Structural distortion behind the nematic superconductivity in

$\text{Sr}_x\text{Bi}_2\text{Se}_3$. New J. Phys. **20**, 103022 (2018).

[37] Smylie, M. P. et al. Multimodal synchrotron X-ray diffraction across the superconducting transition of $\text{Sr}_{0.1}\text{Bi}_2\text{Se}_3$. arXiv: 2207.13221 (2022).

[38] Kriener, M. et al. Electrochemical synthesis and superconducting phase diagram of $\text{Cu}_x\text{Bi}_2\text{Se}_3$. Phys. Rev. B **84**, 054513 (2011).

Author contributions: Y.A. conceived the experiment and A.R. constructed the theory. M.B., supported by J.B. and Y.A., grew the crystals and performed the measurements and data analysis. M.B., A.R. and Y.A. wrote the manuscript with inputs from J.B.

Competing Interests: The authors declare that they have no competing financial interests.

Correspondence: Correspondence and requests for materials should be addressed to Y.A. (ando@ph2.uni-koeln.de).

Data availability: The data that support the findings of this study are available at the online depository figshare with the identifier **** and Supplementary Information. Source data are provided with this paper.

Supplementary Information for “Rotation of gap nodes in the topological superconductor $\text{Cu}_x(\text{PbSe})_5(\text{Bi}_2\text{Se}_3)_6$ ”

I. SAMPLE CHARACTERIZATION

Figure S1 shows the shielding fractions (SF) of three CPSBS samples that were synthesized from the same batch of PSBS crystals. The STM data obtained on sample S-I and on sample S-II is shown in the main text and the data on sample S-III is presented in this supplement. Samples S-I to S-III show a bulk T_c between 2.5 and 2.6 K.

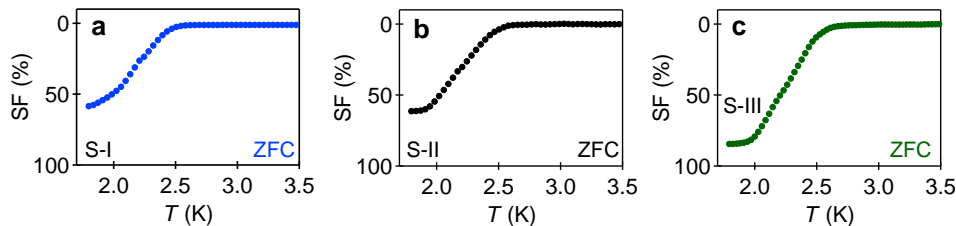


FIG. S1. (a,b,c) Zero-field-cooled (ZFC) magnetization data showing shielding fractions of 59% for Sample S-I (a), 61% for Sample S-II (b) and 84% for Sample S-III (c).

II. SUPPLEMENTAL DATA FOR SAMPLE S-I

The superconducting regions of sample S-I clearly show the structural 1D stripe [Fig. S2(a)], allowing the determination of the monoclinic a and b axis. The monoclinic a axis in this sample is about 145° with respect to the horizontal axis [Fig. S2(b)]. The spatially averaged superconducting gap measured in this region is shown in Fig. S2(c) (same data as Fig. 2(a) of the main text). Moreover, we have experimentally ascertained that the T_c in this region is lower than 1.7 K.

When the external magnetic field is applied normal to the surface, a nearly hexagonal vortex lattice is clearly resolved [Fig. S2(e-g)]. We extrapolate the upper critical field at the surface to about 0.4 T from the magnetic-field dependence of the zero-bias conductance (ZBC) as shown in Fig. S3(d).

We note considerable variations among the shape of different vortices in Fig. S2(e-g), but as discussed in the main text, on average, vortices are elongated roughly at 55° from the horizontal (i.e. at 90° with respect to the a -axis).

III. SUPPLEMENTAL DATA FOR SAMPLE S-II

We characterized the vortex area of sample S-II by taking low-resolution STS-grids in various magnetic fields, as shown in Fig. S3(a-g). The vortex lattice clearly evolves with the magnetic field until the superconductivity is fully suppressed at around ~ 1 T. At low fields, a nearly triangular lattice is observed, in which the distance d_{vortex} between nearest-neighbors is given as $d_{\text{vortex}} \approx 1.075 (\Phi_0/B)^{1/2}$. We plot the average distance between the vortices for varying magnetic fields together with the profile expected for a triangular lattice in Fig. S3(h). We extract the superconducting (SC) gap at each field by averaging the spectra in-between the vortices for a small bias range around E_F . These spectra change systematically as a function of the magnetic field [Fig. S3(i)]. The magnetic-field dependence of the zero-bias conductance (ZBC) normalized to that at 0 T is shown in Fig. S3(j).

The temperature dependence of the SC gap spectra was measured up to the fridge temperature T_{fridge} of 1.7 K [Fig. S3(k)]. Since the effective base temperature of 0.7 K calibrated for $T_{\text{fridge}} = 0.35$ K suggests that the noise in our STM system heats the electrons by $T_{\text{noise}} \simeq 0.35$ K, we fix $T_{\text{eff}} = T_{\text{fridge}} + 0.35$ K when we fit the spectra with the anisotropic gap function discussed in the main text. We can calculate the average gap $\langle \Delta \rangle = \Delta_0 + (2/\pi)\Delta_1$ from the Δ_0 and the Δ_1 values obtained from the fits of the spectra, and the result is plotted in Fig. S3(l) as a function of temperature.

S-I, region I

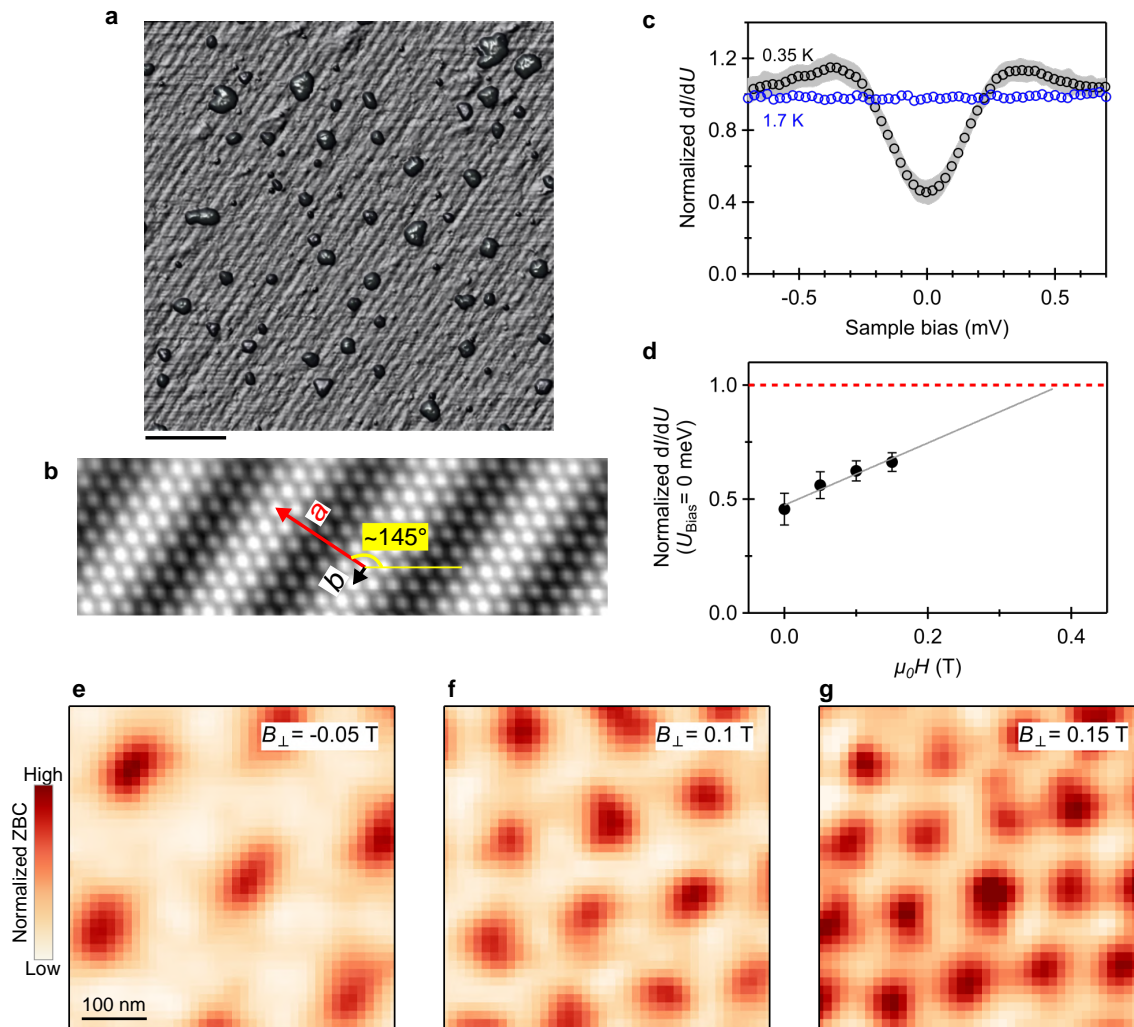


FIG. S2. (a) Pseudo 3D representation of an STM topograph on the SC area of sample S-I. Scale bar corresponds to 20 nm. The structural 1D stripe is clearly observed in the region together with islands/clusters of Cu atoms. (b) Fourier-filtered atomic resolution image taken in the area as in (a) with the monoclinic a and b axes indicated. The a axis is at an angle of about 145° with respect to the horizontal axis for *as-acquired data*. (c) Normalized dI/dU spectra acquired in the region in (a) for a fridge temperatures of 0.35 K (gray open circles) and 1.7 K (blue open circles). The data points correspond to a spatial average of 100 STS over $500 \text{ by } 500 \text{ nm}^2$. The light gray area is the standard deviation of the data, as described in the text. (d, e, f, g) Magnetic-field dependence of the normalized ZBC values (d) as obtained from the the zero field grid and grids taken in the presence of a magnetic field [presented in (e - f)]. Red dashed line corresponds to the normal-state conductance. Error bars in (d) correspond to the one sigma standard deviation of the ZBC value of the respective grid. Scan/stabilization parameters: (a) $U = 900 \text{ V}$, $I = 100 \text{ pA}$; (b) $U = 900 \text{ V}$, $I = 200 \text{ pA}$; (e, f, g) $U = 5 \text{ mV}$, $I = 500 \text{ pA}$ (e, f) $I = 100 \text{ pA}$ (g).

IV. FITTING VORTEX PROFILES WITH THE GINZBURG-LANDAU DERIVED EXPRESSION

Zero bias conductance (ZBC) profiles across vortex cores in STM experiments are commonly analyzed [1, 2] with the Ginzburg-Landau (GL) derived expression for the superconducting order parameter,

$$\sigma(r, 0) = \sigma_0 + (1 - \sigma_0) \left(1 - \tanh \left[r / (\sqrt{2} \xi_{\text{GL}}) \right] \right), \quad (\text{S1})$$

where σ_0 is the normalized ZBC away from a vortex centre and r is the distance to the vortex core centre. In Fig. S4 we plot line cuts of the vortex cores discussed in Fig. 1 of the main text together with the fit of the raw data to Eq. (S1). The r -dependences of the ZBC in sample S-I does not really follow Eq. (S1), but from this analysis we obtain ξ_{GL} of about 28 (47) nm for the short (long) axis of the vortex in sample S-I [Fig. S4 (a)] and about 20 (35) nm in S-II [Fig. S4 (b)]. The values are in reasonable agreement with the estimate of ξ_{GL}

S-II, region I

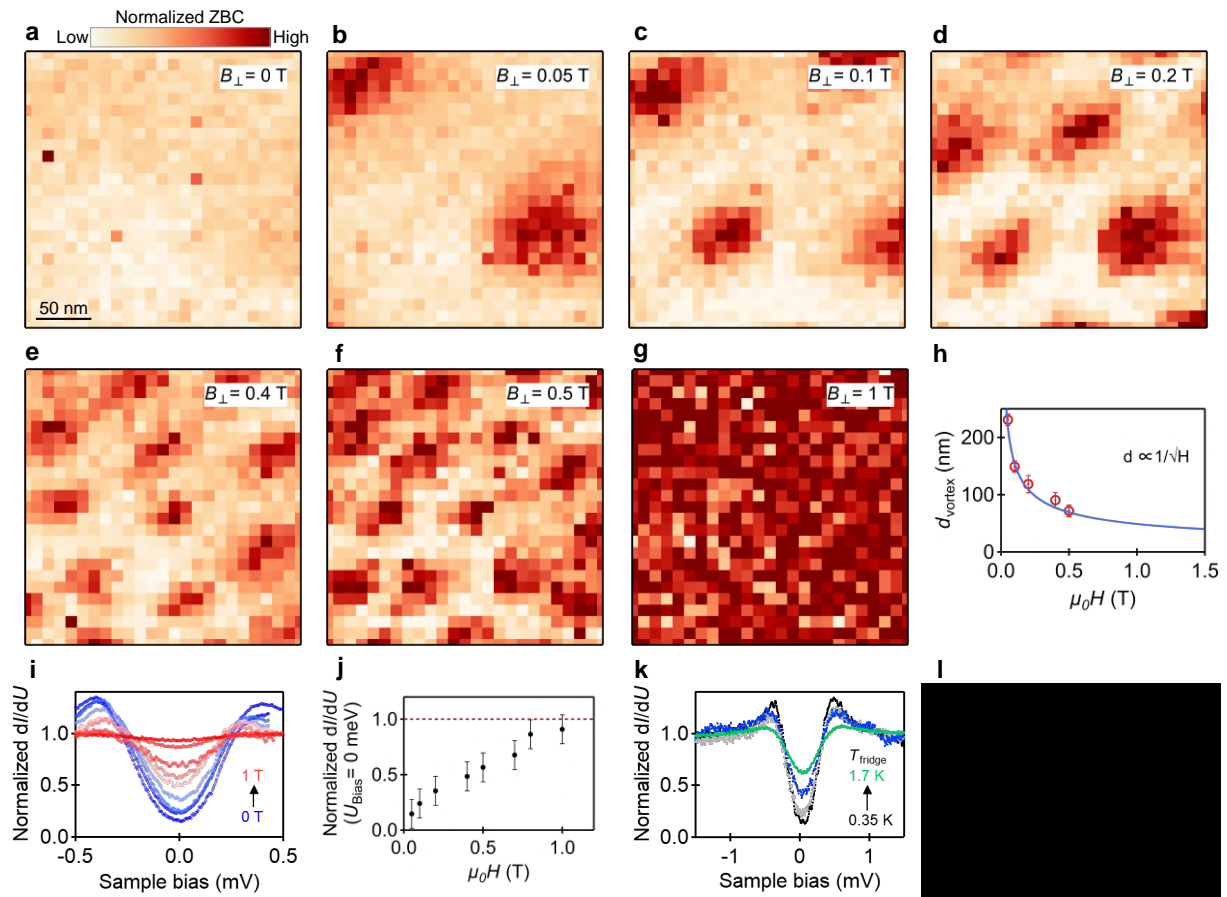


FIG. S3. (a)-(g) Normalized ZBC maps showing the evolution of the vortex lattice in a field of view of 250 nm by 250 nm under various out-of-plane magnetic fields as indicated. The spectrum at each grid point was obtained in the I - V mode. Stabilization parameters: $U = 3$ mV, $I = 50$ pA (100 sweeps). A majority of the vortices are oriented along one direction in all cases. (h) The distance between vortices plotted as a function of the applied magnetic field. The blue curve shows the simulated profile assuming a perfect triangular lattice; deviation of the data points from the simulation curve indicates imperfect ordering. Error bars are given by the larger of the resolution of our STS grid (~ 10 nm) or the standard deviation of the nearest-neighbour distance of all lattice points in the field of view. (i) Normalized dI/dU spectra for various magnetic fields; the curves are obtained by averaging over the grids that lie outside the vortices; the plotted spectra correspond to 0, 0.05, 0.1, 0.2, 0.4, 0.5, 0.7, 0.8, and 1.0 T. (j) Magnetic-field dependence of the normalized ZBC values obtained from the data in (i); the red dashed line signifies the normal-state conductance. Errors bars correspond to a fixed value which is the standard deviation of the ZBC obtained from the zero field grid. (k) SC gap spectra measured in zero field at the fridge temperatures of 0.35, 0.7, 1.1 and 1.7 K; the black curve is also shown in Fig. 2 of the main text. (l) The average gap $\langle \Delta \rangle$ calculated from the Δ_0 and Δ_1 values obtained from the fits to the data in (k) plotted against the effective temperature.

for sample S-I (S-II) based on the measured upper critical field $H_{c2} \approx 0.4$ T (1 T),

$$\xi_{GL} = \sqrt{\frac{\Phi_0}{2\pi\mu_0 H_{c2}}} \approx 40 \text{ nm (18 nm)},$$

with Φ_0 the (superconducting) magnetic flux quantum and μ_0 the vacuum permeability.

V. EXTENDED DATA FOR FIG. 1 OF THE MAIN TEXT

Here, we give extended data for Fig. 1 of the main text consisting of the unsmoothed ZBC maps, the lattice vectors of the vortex lattice, and the comparison of the average vortex profile based on the analysis of smoothed data as discussed in the main text with the results obtained by fitting the raw data to Eq. (S1).

We determine the vortex lattice for each ZBC map by calculating the centre of every area of the map that exceeds an appropriate threshold value of the ZBC (typically about 0.5). From all lattice points we then determine the three average lattice vectors (\mathbf{a}_1 , \mathbf{a}_2 and \mathbf{a}_3). The results of this procedure are superimposed onto the raw data in Fig. S5 (b) and (e). Interestingly, we find that the hexagonal vortex lattice observed in sample S-I is compressed along the vortex lattice vector \mathbf{a}_3 by about 15 to 20%. Moreover, the vortex lattice

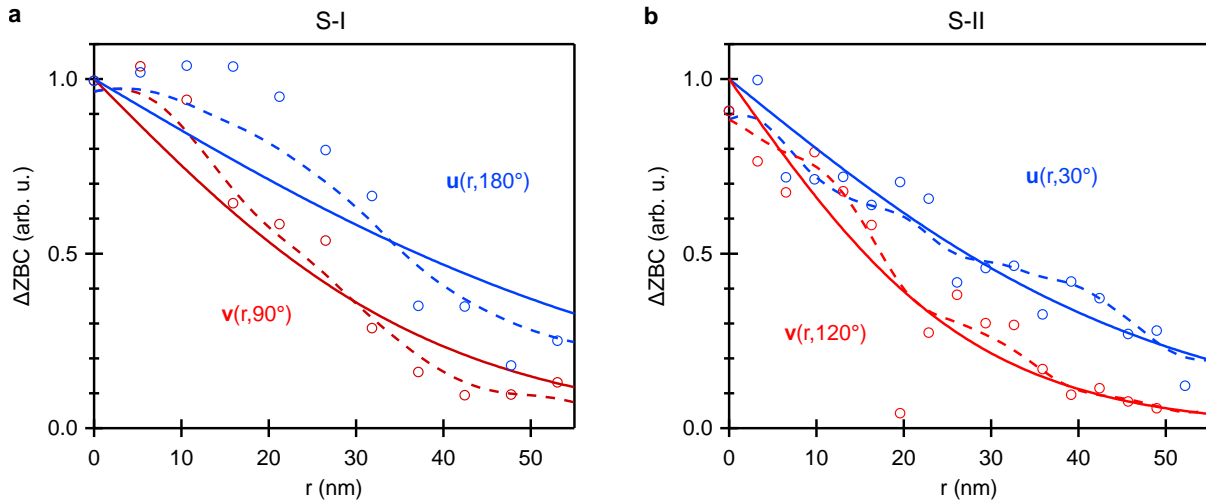


FIG. S4. (a) Line profiles of the vortices taken from Fig. 1(e) of the main text. Open circles, dashed lines, and solid lines refer to raw data, smoothed curve, and GL fits to Eq. (S1), respectively. The smoothing was performed for the analysis of the half width at half maximum mentioned in the text by using a standard Gaussian filter with the smallest (3×3 pixels) kernel with up to three iterations. Blue (red) data are taken along the major (minor) vortex axis; note that the images in Fig. 1(a,b) of the main text are rotated clockwise by 55° to align the monoclinic a -axis with the vertical axis. (b) The same as (a) but for line profiles shown in Fig. 1(g) of the main text. The GL fit gives $\xi_{GL} = 28 \pm 2$ nm (47 ± 6 nm) for the short (long) axis for the vortex of sample S-I and 20 ± 2 nm (35 ± 2 nm) for the vortex of sample S-II.

(\mathbf{a}_2) is rotated by about 10 to 15° with respect to the crystallographic a -axis. We conservatively estimate the experimental uncertainty due to thermal drift and piezoelectric creep as 10% for the compression and 10° for the rotation. We leave the exploration of the origin of this interesting vortex lattice deformation for future studies.

Instead, we analyze the vortex shape at each lattice site by taking line profiles as a function of polar angle and determine ξ (defined as the half width at half maximum) from smoothed data and ξ_{GL} by fitting the raw data to Eq. (S1) as shown in Fig. S4. We numerically average $\xi_{GL}(\varphi)$ (and $\xi(\varphi)$) of all lattice sites and plot the results in Fig. S5 (c) and (f) for the vortex lattice at 0.15 and 0.2 T, respectively. On the one hand, we observe considerable variations in the vortex shape between different lattice sites, which likely reflects differences in the local scattering potential; on the other hand, a clear two-fold symmetry with a minimal average vortex extension parallel to the a -axis is apparent. Comparing $\langle \xi_{GL} \rangle$ and $\langle \xi \rangle$ we find the same qualitative behavior.

As mentioned above, we observed significant variations in the vortex shape anisotropy between different lattice sites in sample S-I. Therefore, to achieve a high level of confidence in the determination of the vortex elongation axis, we have analyzed a relatively large number of ZBC maps at 0.15 and 0.2 T which are shown in Fig. S6 and Fig. S7, respectively. The data shown in Fig. 1 (f) of the main manuscript is the average of all the lattice sites indicated in Fig. S6 and Fig. S7.

The same analysis as discussed for sample S-I above was also performed for the vortex lattice observed in sample S-II which is shown in Fig. 1 (c) and (e) of the main text. The results are shown in Fig. S8. On the one hand, we observe a rotation of lattice vector \mathbf{a}_2 of -15 to -23° with respect to the crystallographic a -axis, which is clearly different from the orientation observed for sample S-I; on the other hand, the entire vortex lattice in S-II is noticeably distorted (likely due to disorder related pinning of vortices) and does not allow for a meaningful analysis of the vortex lattice anisotropy.

The vortex shape analysis performed at each lattice site yields the average $\langle \xi_{GL} \rangle$ and $\langle \xi \rangle$ respectively plotted for 0.2 and 0.4 T in Fig. S8 (c) and (f). The noticeably smaller standard deviations compared to the data obtained for sample S-I is likely attributed to reduced vortex lattice motion due to the pinning centers and less thermal smearing due to the larger superconducting gap. Regardless of the origin, most vortices in sample S-II have similar elliptical shape with the same orientation of the major axis which is about 60° rotated with respect to the crystallographic a -axis and clearly different from the orientation observed in sample S-I.

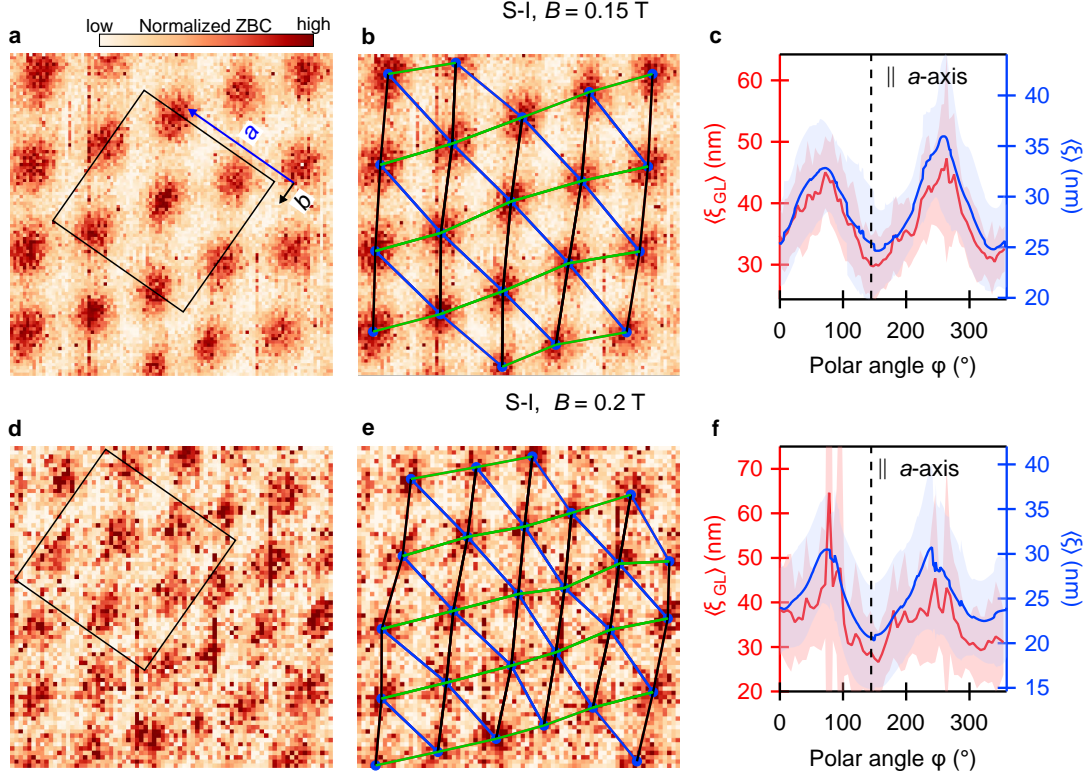


FIG. S5. (a) Larger region of the vortex lattice in sample S-I in the out-of-plane magnetic field of $B = 0.15$ T. The black square indicates the data show in Fig. 1(a) of the main text. The monoclinic a -axis and b -axis are given. The vortex lattice in the field of view of $500 \text{ nm} \times 500 \text{ nm}$ is determined and the results are superimposed onto the raw data in (b). Blue dots mark the lattice points corresponding to vortex centres. The lattice vectors \mathbf{a}_1 (black), \mathbf{a}_2 (blue), \mathbf{a}_3 (green) are indicated and their average lengths are $|\mathbf{a}_1| = (133 \pm 8) \text{ nm}$, $|\mathbf{a}_2| = (138 \pm 9) \text{ nm}$ and $|\mathbf{a}_3| = (111 \pm 7) \text{ nm}$. The average angle between \mathbf{a}_2 and the monoclinic a -axis is $\angle_{\mathbf{a}_2, a} = (12 \pm 4)^\circ$. Line profiles of the normalized ZBC are taken as a function of the polar angle φ at each lattice point and the GL in-plane coherence length is determined by fitting the raw data to Eq. (S1). (c) The average $\langle \xi_{GL} \rangle$ of all lattice points is plotted in red, where the light shaded region indicates the standard deviation. For comparison, the average vortex core radius $\langle \xi \rangle$, which is determined from the half width at half maximum of the smoothed data as discussed in the main text, is shown in blue. (d,e,f) The same analysis as in (a,b,c) for the vortex lattice in 0.2 T shown in Fig. 1(b) of the main text. The vortex lattice parameters for (e) are: $|\mathbf{a}_1| = (113 \pm 7) \text{ nm}$, $|\mathbf{a}_2| = (116 \pm 9) \text{ nm}$, $|\mathbf{a}_3| = (94 \pm 13) \text{ nm}$ and $\angle_{\mathbf{a}_2, a} = (15 \pm 6)^\circ$.

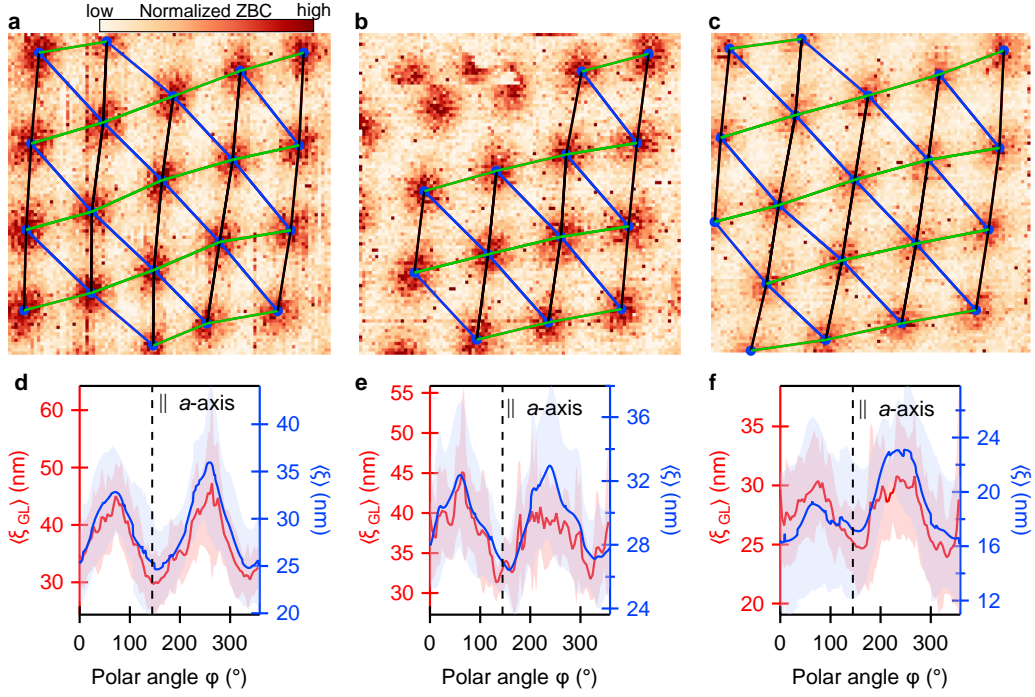


FIG. S6. All the data of the vortices in sample S-I in the out-of-plane magnetic field of $B = 0.15$ T used for the averaging to generate Fig. 1(f) of the main text. Panels (a,d) are the same as those shown in Fig. S5(b,c). The field of view of panels (b) and (c) is $500 \text{ nm} \times 500 \text{ nm}$, and the data are analysed and presented in the same way as in Fig. S5(b,c). Vortex lattice parameters: $|\mathbf{a}_1| = (133 \pm 5) \text{ nm}$, $|\mathbf{a}_2| = (145 \pm 4) \text{ nm}$, $|\mathbf{a}_3| = (114 \pm 5) \text{ nm}$ and $\angle_{\mathbf{a}_2, \mathbf{a}_1} = (13 \pm 3)^\circ$ for (b); $|\mathbf{a}_1| = (132 \pm 10) \text{ nm}$, $|\mathbf{a}_2| = (140 \pm 7) \text{ nm}$, $|\mathbf{a}_3| = (119 \pm 7) \text{ nm}$ and $\angle_{\mathbf{a}_2, \mathbf{a}_1} = (12 \pm 3)^\circ$ for (c).

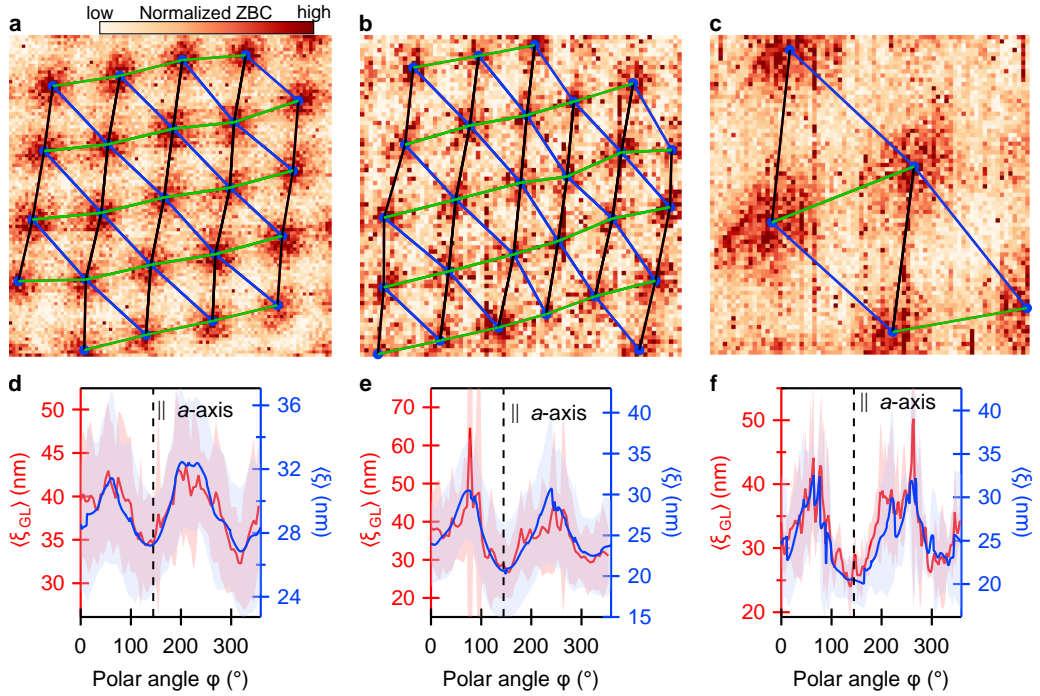


FIG. S7. All the data of the vortices in sample S-I in the out-of-plane magnetic field of $B = 0.2$ T used for the averaging to generate Fig. 1(f) of the main text. Panels (b,e) are the same as those shown in Fig. S5(e,f). The field of view of panels (a) and (c) is $500 \text{ nm} \times 500 \text{ nm}$ and $200 \text{ nm} \times 200 \text{ nm}$, respectively. The data are analysed and presented in the same way as in Fig. S5(e,f). Vortex lattice parameters: $|\mathbf{a}_1| = (108 \pm 3) \text{ nm}$, $|\mathbf{a}_2| = (124 \pm 7) \text{ nm}$, $|\mathbf{a}_3| = (105 \pm 4) \text{ nm}$ and $\angle_{\mathbf{a}_2, \mathbf{a}_1} = (10 \pm 4)^\circ$ for (a); $|\mathbf{a}_1| = (107 \pm 3) \text{ nm}$, $|\mathbf{a}_2| = (109 \pm 6) \text{ nm}$, $|\mathbf{a}_3| = (94 \pm 6) \text{ nm}$ and $\angle_{\mathbf{a}_2, \mathbf{a}_1} = (11 \pm 5)^\circ$ for (c).

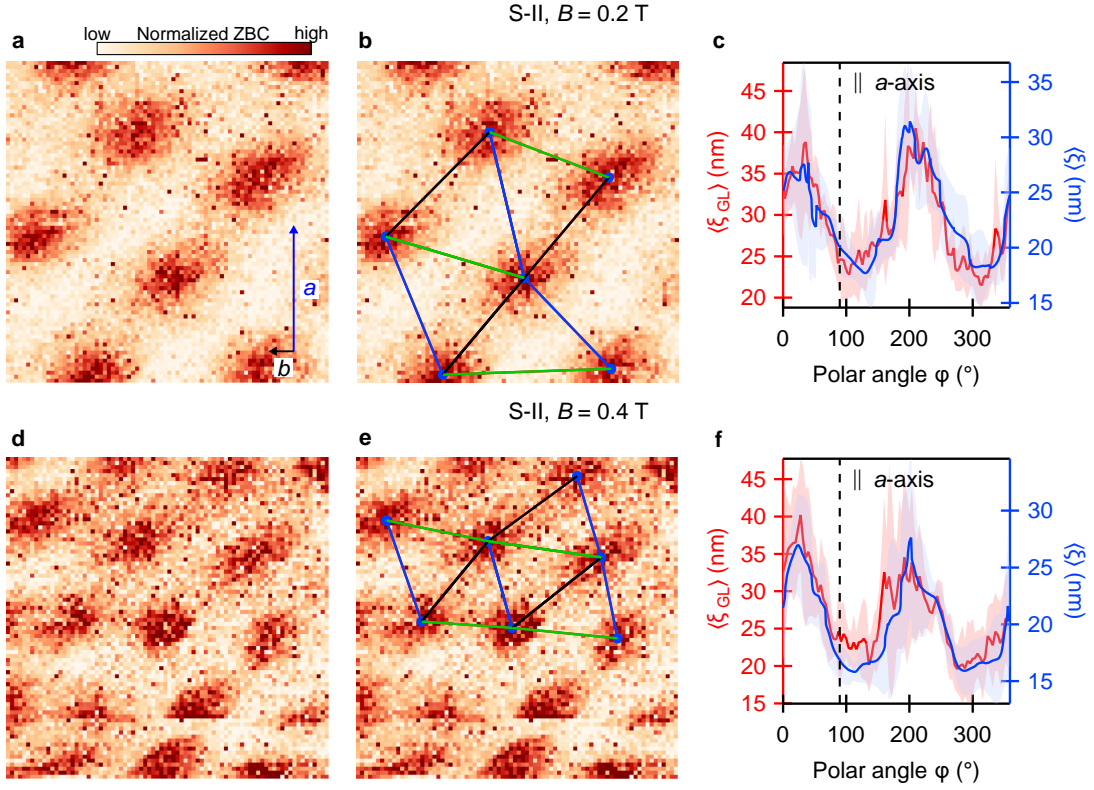


FIG. S8. (a,b) The vortex lattice in sample S-II in the out-of-plane magnetic field of $B = 0.2$ T show in Fig. 1(c) of the main text. The vortex lattice in the field of view of $250 \text{ nm} \times 250 \text{ nm}$ is determined and the results are superimposed onto the raw data in (b). Blue dots mark the lattice points corresponding to vortex centres. The lattice vectors \mathbf{a}_1 (black), \mathbf{a}_2 (blue), \mathbf{a}_3 (green) are indicated and their average lengths are $|\mathbf{a}_1| = (105 \pm 8) \text{ nm}$, $|\mathbf{a}_2| = (113 \pm 10) \text{ nm}$ and $|\mathbf{a}_3| = (115 \pm 13) \text{ nm}$. The average angle between \mathbf{a}_2 and the monoclinic a -axis is $\angle_{\mathbf{a}_2, a} = (-23 \pm 15)^\circ$. Line profiles of the normalized ZBC are taken as a function of the polar angle φ at each lattice point and the GL in-plane coherence length is determined by fitting the raw data to Eq. (S1). (c) The average $\langle \xi_{\text{GL}} \rangle$ is plotted in red, where the light shaded region indicates the standard deviation. For comparison, the average vortex core radius $\langle \xi \rangle$, which is determined from the smoothed data as discussed in the main text, is shown in blue. (d-f) The same analysis as in (a-c) for the vortex lattice in 0.4 T shown in Fig. 1(d) of the main text. The vortices shown here are used for the averaging to generate Fig. 1(h) of the main text. The vortex lattice parameters for (e) are $|\mathbf{a}_1| = (86 \pm 4) \text{ nm}$, $|\mathbf{a}_2| = (72 \pm 8) \text{ nm}$, $|\mathbf{a}_3| = (83 \pm 8) \text{ nm}$ and $\angle_{\mathbf{a}_2, a} = (-15 \pm 3)^\circ$.

VI. INFLUENCE OF THE IN-PLANE MAGNETIC FIELD ON THE VORTEX ELONGATION

To dismiss the possibility that the observed vortex elongation is a mere consequence of a magnetic field that is not exactly out-of-plane but is tilted away from the z axis, we performed the following experiment: We applied an intentional in-plane magnetic field of the magnitude of 35 mT with the azimuthal angle of 40° and 130° . The resultant magnetic field is $\sim 10^\circ$ off from the z axis. As shown in Fig. S9, we did not observe any noticeable change in the vortex anisotropy in spite of the intentional misalignment of the field. Also, the averaged orientation of the vortices did not change upon rotating the in-plane component within the experimental uncertainty of about 10° .

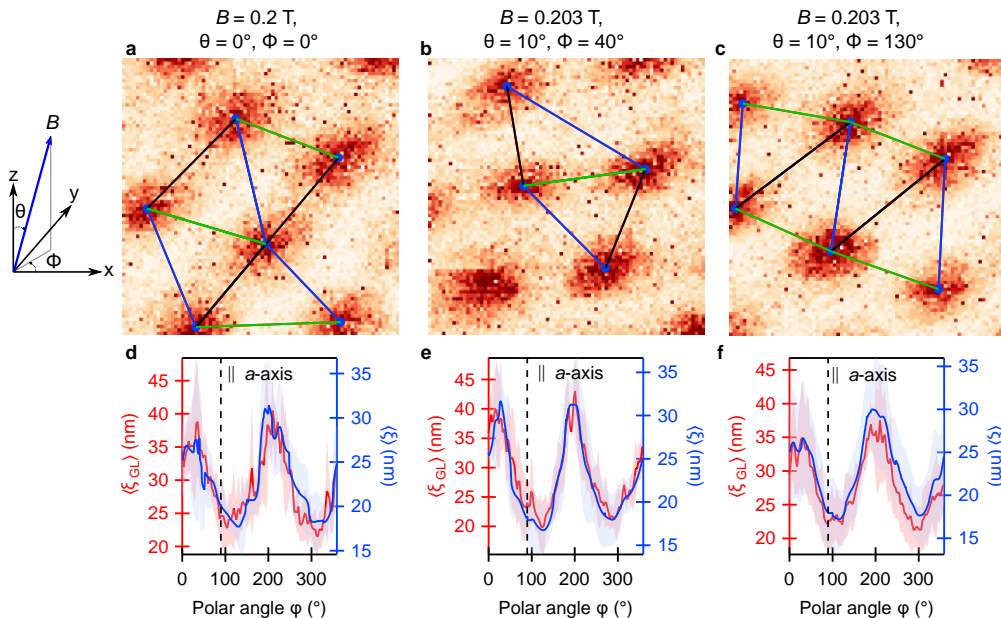


FIG. S9. (a) Normalized ZBC maps in the perpendicular magnetic field of 0.2 T ($\theta = 0^\circ$). (b,c). An additional in-plane magnetic field of 35 mT applied in the direction of $\phi = 40^\circ$ (b) and $\phi = 130^\circ$ (c); these in-plane magnetic fields cause θ to become 10° with the total magnetic field of 0.203 T. The definition of θ and ϕ is shown on the left. Stabilization parameters: $U = 1$ mV, $I = 50$ pA and $U_{\text{mod}} = 100 \mu\text{V}_p$. (d,e,f) The average $\langle \xi_{GL} \rangle$ and $\langle \xi \rangle$ calculated from the lattice sites indicated by blue dots in (a,b,c). Note that the panels (a,d) are the same as Fig. S8(b,c).

VII. ABSENCE OF VORTEX BOUND STATES

No Caroli-de Gennes-Matricorn states were observed in the core of a single isolated vortex in CPSBS (Fig. S10). The absence of bound states in the vortex core is expected for a dirty superconductor [3]. Based on the values for residual resistivity (ρ_0) and carrier density (n) in Ref. [4], we estimate the mean free path (l) in our sample [$l = \hbar k_F / (\rho_0 n e^2)$] to be on the order of only a few nanometer, while the average in-plane coherence length (ξ_{GL}) is measured to be about 25 nm, i.e., CPSBS is a dirty superconductor. Importantly, despite being in the dirty limit, a clear anisotropy in the vortex shape is observed.

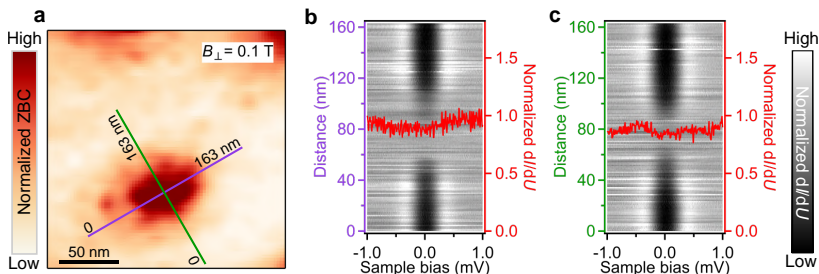


FIG. S10. (a) Normalized ZBC map at $B_{\perp} = 0.1$ T showing a single isolated vortex. (b) Normalized dI/dU spectra along the purple line (long axis) in (a). Each horizontal row is a dI/dU spectrum vs sample bias. The color scale represents the dI/dU intensity and the vertical axis corresponds to the distance along the purple line in (a). The red dI/dU spectrum superimposed on the map is taken at the center of the vortex and highlights the absence of any vortex bound states. (c) A similar map as done in (b) for the green line (short axis) in (a), clearly illustrating the vortex anisotropy. Stabilization parameters: $U = 1$ mV, $I = 50$ pA (100 sweeps) for (a); $U = 3$ mV, $I = 50$ pA (200 sweeps) for (b) and $U = 3$ mV, $I = 50$ pA (200 sweeps) for (c).

VIII. STATISTICAL OVERVIEW OF THE SC REGIONS OBSERVED BY STM ON THE SURFACE

Tao *et al.* [5] reported that the probability to find SC regions on the surface of $\text{Cu}_x\text{Bi}_2\text{Se}_3$ was less than 5% in their STM study. Our experience was similar during the scanning on the surface of CPSBS. It is more common to find non-superconducting areas. In our experiments a single scan area corresponds to $1.5 \mu\text{m}$ by $1.5 \mu\text{m}$, which is the maximum range for the scan piezo. A new scan area on the sample is accessed by moving the sample stage with respect to the tip holder. In Table I, we show the total number of scan areas along with the number of areas in which SC was observed. By multiplying the number of scan areas with the area of a single scan frame, we estimate a SC area of $6.75 \mu\text{m}^2$ out of $13.5 \mu\text{m}^2$ in sample S-I, $6.8 \mu\text{m}^2$ out of $65 \mu\text{m}^2$ in sample S-II and $11.3 \mu\text{m}^2$ out of $63 \mu\text{m}^2$ in sample S-III.

We previously reported for $\text{Sr}_x\text{Bi}_2\text{Se}_3$ [6] that spurious superconducting gap was often observed due to picking up of a superconducting material on the tip from the sample, and it was also the case in CPSBS. Identification of a boundary between a superconducting and non-superconducting region with the same tip apex conditions was used as the criteria for ascertaining a superconducting gap to reside on the sample side, rather than on the tip side.

Sample	Number of scan areas	Number of SC regions
S-I	6	3
S-II	29	3
S-III	28	5

TABLE I. Summary of total number of regions scanned and number of SC regions found on three CPSBS samples.

IX. SPATIAL VARIATION OF THE SUPERCONDUCTING GAP SPECTRUM

In Fig. S11 we give an overview of the superconducting gaps measured for the various superconducting regions observed in the three different samples S-I, S-II and S-III (see also Table I). For each region, a large-area spectroscopy grid was evaluated. The open black circles and the light gray shaded area give the arithmetic mean ($\bar{x} = \sum_{i=1}^n X_i/n$) and the corresponding standard deviation ($\text{SD} = \sqrt{\frac{\sum_{i=1}^n (x_i - \bar{x})^2}{(n-1)}}$), respectively. One can see that when there is a large ZBC, the data can be reasonably fit with both the nodal (blue trace) and the anisotropic (red trace) gap functions discussed in the main text. We observe significant variations of the gap magnitude, which is presumably due to differences in local Cu-concentration and/or electric field induced weakening of superconductivity [6].

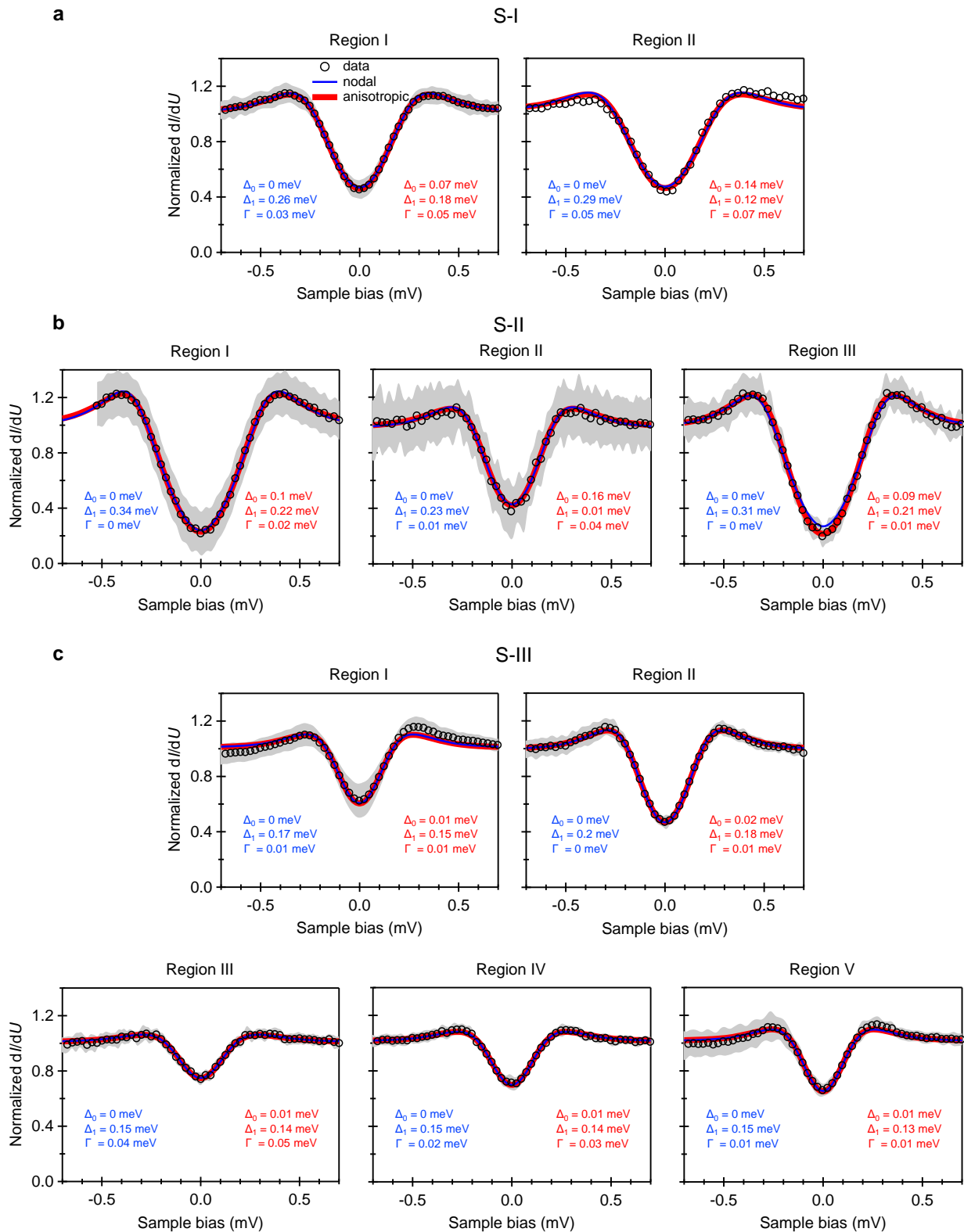


FIG. S11. Variations in the superconducting gap observed in samples S-I, S-II, and S-III. For each region we show the spatial average (black open circles) and the corresponding standard deviation (light gray area). The spatial average is obtained by numerically averaging 100 STS over 500 by 500 nm², 900 STS over 300 by 300 nm², 60 STS over 25 by 500 nm², 28 STS over 50 by 500 nm², 1600 STS over 500 by 500 nm², 80 STS over 20 by 1500 nm², 200 STS over 40 by 500 nm², 50 STS over 25 by 1400 nm², 300 STS over 500 by 500 nm², for region I (sample S-I), region I – III (sample S-II), and region I – V (sample S-III), respectively. For region II of sample S-I, a point STS is shown. The blue and red traces correspond to the nodal and anisotropic fit to the data, respectively, as described in the text. Stabilization parameters: $U = 1.5$ to 5 mV, $I = 50$ or 500 pA.

X. ORIENTATION OF SUPERCONDUCTING GAP MINIMA ON SAMPLE S-III SURFACE

Similar to sample S-II, no structural stripe pattern was observed in sample S-III (see Sec. XI). Moreover, the smaller SC magnitude paired with significant spatial inhomogeneity prohibited a reliable evaluation of the anisotropy of superconducting vortices. Due to this difficulty, we probed the anisotropy in the superconducting gap of region II of sample S-III by measuring the response to an in-plane magnetic field (B_{\parallel}) of 0.25 T, a technique used for $\text{Cu}_x\text{Bi}_2\text{Se}_3$ by Tao *et al.* [5]. When the magnetic field is rotated by an angle φ in the ab -plane of the crystal, the gap spectra show a clear variation [Fig. S12(a,b)].

The influence of B_{\parallel} on the zero-energy DOS was calculated within the Kramer–Pesch approximation by Nagai [7] and the result is in good agreement with our experimental data [Fig. S12(b)]. From this comparison, one can identify the orientation of the gap minima with respect to the crystallographic axes in Fig. S12(c) and compare it to the orientation of the gap minima observed in sample S-I and S-II. The orientation of the gap minima in sample S-III is close to that in sample S-II and is off by only $\sim 10^\circ$. In this regard, it is useful to note that Tao *et al.* [5] reported a rotation of the gap minima by up to 20° away from the zero-field position when the in-plane magnetic field was applied. It is likely that the same effect is observed here.

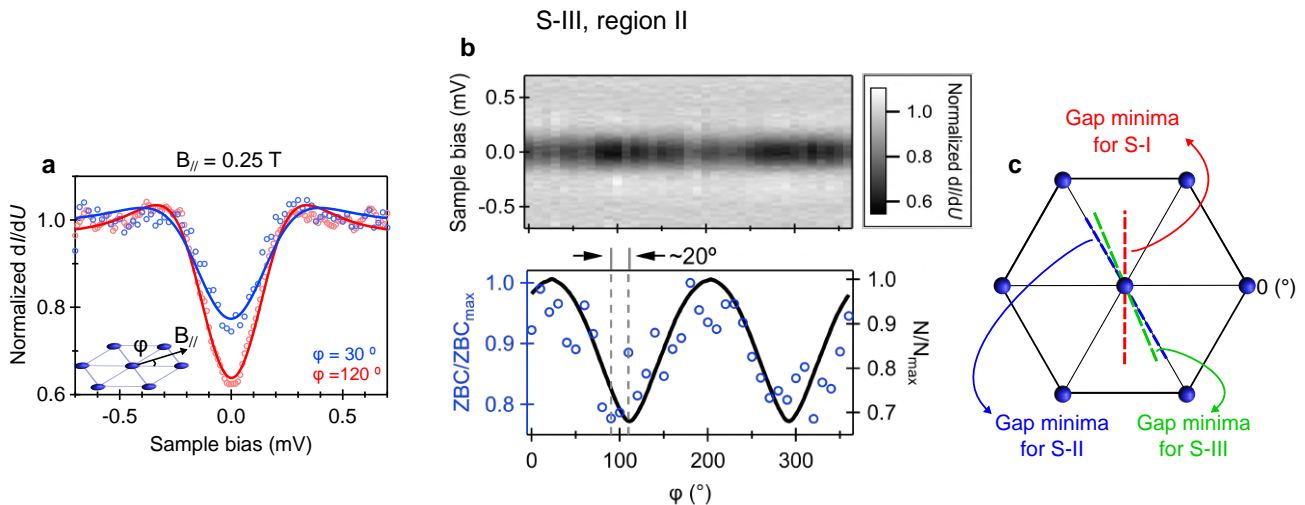


FIG. S12. (a) Point STS taken in region II of sample S-III, but in the presence of an in-plane magnetic field (B_{\parallel}) of 0.25 T for different field orientations (φ). The definition of φ is indicated in the inset. Solid lines are fits to the data. Here, the measured superconducting gaps are fit using Γ as the only fitting parameter; $T_{\text{eff}} = 0.7$ K, $\Delta_0 = 0.02$ meV and $\Delta_1 = 0.18$ meV are fixed. (b) A twofold oscillation is clearly visible in the raw data of dI/dU at zero bias (top) and this angular dependence of the zero-bias DOS can be fit with the changes in zero energy DOS (N) calculated by Nagai [7] (bottom) to quantify the minima at approximately 110° and 290° . (c) The positions of the minima in the superconducting gap structure obtained for samples S-I (red dashed line), S-II (blue dashed line) and S-III (green dashed line). Stabilization parameters: (a,b) $U = 1.5$ mV, $I = 100$ pA.

XI. TOPOGRAPHY AND SPECTROSCOPY ON PSBS AND CPSBS

In Fig. S13, we show large scale topography images taken on the surface of PSBS, non-superconducting (NSC) areas of CPSBS, and superconducting areas of CPSBS found on samples S-I, S-II and S-III. The clear 1D stripe on the surface of PSBS becomes more disordered on the NSC surface of CPSBS. The stripe was not observed in the SC regions of S-II and S-III but found on the SC regions of S-I.

The image shown in Fig. S13(h) corresponds to the area where the vortices were observed for S-II. The area was disordered, which made it impossible to obtain clear atomic-resolution images. In comparison, the SC areas on S-I and S-III [Fig. S13(g,i)] are less disordered and atomic-resolution images could be obtained.

We note a correlation between the superconducting gap as discussed in Sec. IX and the amount of (presumably) Cu remaining on the surface. The superconducting region in sample S-III shows few and small clusters [white spots in Fig. S13(i)] and the smallest superconducting gap, S-I exhibits extended and larger clusters [white areas in Fig. S13(g)] and an intermediate superconducting gap and S-II is entirely covered with Cu showing the largest superconducting gap.

We show in Figs. S13(c, f, j) large scale dI/dU spectra taken on the different surfaces. As discussed in the main text, the cleaved surface of PSBS is a single QL of Bi_2Se_3 above the PbSe layer. The ARPES data [8] on this surface show a single, parabolic electron-like band with an onset around ~ -600 meV. The onset of this band is clearly seen in our dI/dU spectrum [Fig. S13(c)], since the LDOS shows a minima exactly around ~ -600 meV.

On the cleaved surface of CPSBS, the ARPES data [9] show two electron-like bands, both 2D in nature, at the onset energies of -600 meV and -280 meV. It is difficult to identify these bands in the spectroscopy curves [Fig. S13(f,j)] due to the significant additional DOS around these energies. Neither is it possible to conclude any shift of the surface bands in comparison to the spectrum on PSBS.

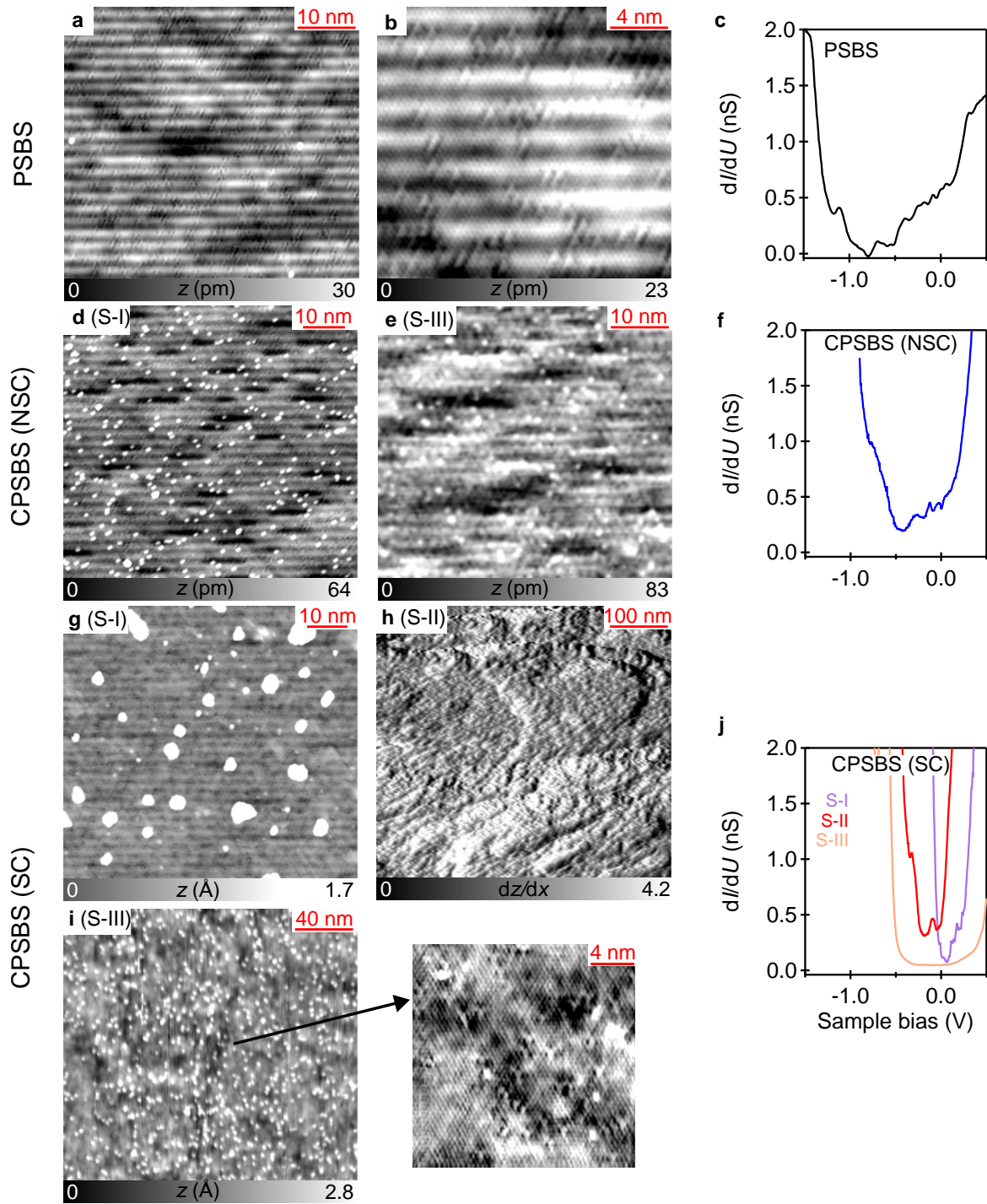


FIG. S13. (a, b, d, e, g, h and i) STM topographs on the cleaved surface of PSBS (a,b), on a non-superconducting surface of CPSBS (d,e), and on a SC area of CPSBS in sample S-I (g), sample S-II (h) and sample S-III (i). The image (h) is a differential image; no atomic-resolution image could be obtained in the SC area of sample S-II due to higher corrugation. However, it was possible to resolve the lattice in the SC area found in S-I and S-III in spite of the significant coverage of Cu clusters. The atomic resolution image for S-III is shown on the right side of (i). (c, f, j) dI/dU spectrum on the surface of PSBS (c), CPSBS (NSC) (f) and CPSBS (SC) (S-I, S-II and S-III) (j). Scan/stabilization parameters: $U = 900$ mV, $I = 20$ nA for (a); $U = 900$ mV, $I = 20$ nA for (b); $U = 500$ mV, $I = 500$ pA for (c); $U = 950$ mV, $I = 50$ pA for (d); $U = -10$ mV, $I = 1$ nA for (e); $U = -900$ mV, $I = 500$ pA for (f); $U = 900$ mV, $I = 100$ pA for (g); $U = 1$ V, $I = 10$ pA for (h); $U = -900$ mV, $I = 500$ pA (right: $U = -5$ mV, $I = 5$ nA) for (i); $U = 500$ mV, $I = 500$ pA (S-I), $U = -600$ mV, $I = 1$ nA (S-II) and $U = -900$ mV, $I = 2$ nA (S-III) for (j).

XII. SYMMETRY ANALYSIS

A. Symmetry of the Bi₂Se₃ quintuple layers

The Bi₂Se₃ quintuple-layer structure is associated with point group D_{3d} [10, 11]. This group consists of twelve symmetry operations organized in six conjugacy classes: \hat{E} , the identity; \hat{P} , inversion; $2\hat{C}_3$: two rotations along the z-axis by $\pm 120^\circ$; $3\hat{C}'_2$: three rotations by 180° along the x-axis and equivalent in-plane axes; $2\hat{S}_6$: rotations by $\pm 60^\circ$ along the z-axis followed by in-plane mirror reflection; $3\hat{\sigma}_d$: three vertical mirrors passing through the yz-plane and equivalent planes. The irreducible representations can be identified from the character table for D_{3d} , as displayed in Table II.

irrep	\hat{E}	$2\hat{C}_3$	$3\hat{C}'_2$	\hat{P}	$2\hat{S}_6$	$3\hat{\sigma}_d$
A_{1g}	+1	+1	+1	+1	+1	+1
A_{2g}	+1	+1	-1	+1	+1	-1
E_g	+2	-1	0	+2	-1	0
A_{1u}	+1	+1	+1	-1	-1	-1
A_{2u}	+1	+1	-1	-1	-1	+1
E_u	+2	-1	0	-2	+1	0

TABLE II. Character table for the point group D_{3d} .

1. Description of the normal state

The normal state Hamiltonian can be described by two effective orbitals of opposite parity, referred as P_{1z+} and P_{2z-} [11, 12]. In the basis $\Phi_{\mathbf{k}}^\dagger = (c_{1\uparrow}^\dagger, c_{1\downarrow}^\dagger, c_{2\uparrow}^\dagger, c_{2\downarrow}^\dagger)_{\mathbf{k}}$, the Hamiltonian can be parametrized as:

$$\hat{H}_0(\mathbf{k}) = \sum_{a,b} h_{ab}(\mathbf{k}) \hat{\tau}_a \otimes \hat{\sigma}_b, \quad (\text{S2})$$

where $\hat{\tau}_{a=1,2,3}$ are Pauli matrices encoding the orbital degrees of freedom (DOF), $\hat{\sigma}_{b=1,2,3}$ are Pauli matrices encoding the spin DOF, and $\hat{\tau}_0$ and $\hat{\sigma}_0$ are two-dimensional identity matrices in orbital and spin space, respectively. In the presence of time-reversal and inversion symmetries, the only allowed terms in the Hamiltonian have the subscripts $(a, b) = \{(0, 0), (2, 0), (3, 0), (1, 1), (1, 2), (1, 3)\}$. Time-reversal symmetry is defined as $\hat{\Theta} = K\hat{\tau}_0 \otimes (i\hat{\sigma}_2)$, where K stands for complex conjugation, and the parity operator as $\hat{P} = \hat{\tau}_3 \otimes \hat{\sigma}_0$. The properties of the $\hat{\tau}_a \otimes \hat{\sigma}_b$ matrices under the point group operations allow us to associate each of these terms to a given irreducible representation of D_{3d} , therefore constraining the momentum dependence of the form factors $h_{ab}(\mathbf{k})$ by symmetry. Table III provides the details on the properties of each term in the normal-state Hamiltonian and an expansion of $h_{ab}(\mathbf{k})$ for small momenta.

(a, b)	\hat{P}	\hat{C}_3	\hat{C}'_2	$\hat{\sigma}_d$	Irrep	$h_{ab}(\mathbf{k})$	Process
(0, 0)	+1	+1	+1	+1	A_{1g}	$C_0 + C_1 k_z^2 + C_2(k_x^2 + k_y^2)$	Intra-orbital hopping
(2, 0)	-1	+1	-1	+1	A_{2u}	$B_0 k_z$	Inter-orbital hopping
(3, 0)	+1	+1	+1	+1	A_{1g}	$M_0 + M_1 k_z^2 + M_2(k_x^2 + k_y^2)$	Intra-orbital hopping
(1, 1)	-1	y	-1	+1	E_u	$-A_0 k_y$	SOC
(1, 2)	-1	x	+1	-1	E_u	$A_0 k_x$	SOC
(1, 3)	-1	+1	+1	-1	A_{1u}	$R_1 k_x(k_x^2 - 3k_y^2)$	SOC

TABLE III. Parametrization of the normal-state Hamiltonian given in Eq. (S2) for materials in the family of Bi₂Se₃. The columns labeled by \hat{P} , \hat{C}_3 , \hat{C}'_2 and $\hat{\sigma}_d$ indicate how the basis matrices $\hat{\tau}_a \otimes \hat{\sigma}_b$, indicated by (a, b) , transform under the respective point group operations, such that one can associate these with different irreducible representations of D_{3d} (Irrep). The seventh column gives the expansion of the accompanying form factors $h_{ab}(\mathbf{k})$ for small momentum, and the last column the associated physical process. The value of the coefficients for Bi₂Se₃ and other materials in this family can be found by first principles calculations (see for example Table IV in Ref. [17]).

Note that the three first terms in Table III are spin-independent: (0, 0) and (3, 0) are even and associated with intra-orbital hopping, while (2, 0) is odd and encodes inter-orbital hopping. The last three terms are spin-dependent and inter-orbital in character, therefore all odd. The terms (1, 1) and (1, 2) are associated with a Rashba-like spin-orbit coupling. The term (1, 3) is associated with trigonal warping of the Fermi surface and is usually dropped from the effective Hamiltonians since these carry at least terms of third order in momenta. Note that the coefficients C_1 , B_0 , and M_1 for CPSBS are smaller than the ones used for doped Bi₂Se₃ materials

given the presence of the PbSe layers. The Fermi surface of CPSBS was experimentally shown to be cylindrical (2D Fermi surface) [9], while the Fermi surface in doped Bi₂Se₃ materials can be either ellipsoidal (3D) or cylindrical (2D).

2. Classification of order parameters with momentum-independent gap matrices in the microscopic basis

Given these symmetries, we can classify all order parameters with \mathbf{k} -independent gap matrices in the microscopic basis according to the irreps of D_{3d} . Following [4], the order parameters can be generally written as:

$$\hat{\Delta} = \sum_{a,b} d_{ab} \hat{\tau}_a \otimes \hat{\sigma}_b (i\hat{\sigma}_2). \quad (\text{S3})$$

The allowed momentum-independent gap matrices can be determined by first searching for matrices satisfying $\hat{\Delta} = -\hat{\Delta}^T$, following fermionic antisymmetry. These can be classified according to the irreducible representations of D_{3d} , as displayed in Table IV. These order parameters are constructed in the orbital basis, so one needs to transform them to the band basis in order to discuss the presence of nodes and their locations. Following the discussion in the SM of [4], we find the nodes highlighted in the last two columns of Table IV.

[a,b]	Irrep	Spin	Orbital	Parity	Matrix Form	Zero at 3D FS	Zero at 2D FS
[0,0]	A_{1g}	Singlet	Intra	Even	$\hat{\tau}_0 \otimes \hat{\sigma}_0 (i\hat{\sigma}_2)$	-	-
[3,0]					$\hat{\tau}_3 \otimes \hat{\sigma}_0 (i\hat{\sigma}_2)$	-	-
[2,3]	A_{1u}	Triplet	Inter	Odd	$\hat{\tau}_2 \otimes \hat{\sigma}_3 (i\hat{\sigma}_2)$	-	-
[1,0]	A_{2u}	Singlet	Inter	Odd	$\hat{\tau}_1 \otimes \hat{\sigma}_0 (i\hat{\sigma}_2)$	along the k_z axis $k_x = k_y = 0$	-
[2,1]	E_u	Triplet	Inter	Odd	$\hat{\tau}_2 \otimes \hat{\sigma}_1 (i\hat{\sigma}_2)$	along the k_x axis $k_z = k_y = 0$	along the $k_x k_z$ plane* $k_y = 0$
[2,2]					$\hat{\tau}_2 \otimes \hat{\sigma}_2 (i\hat{\sigma}_2)$	along the k_y axis $k_z = k_x = 0$	along the $k_y k_z$ plane** $k_x = 0$

TABLE IV. Superconducting order parameters for materials in the family of Bi₂Se₃. Here we focus on the order parameters with momentum-independent gap matrices in the microscopic basis and highlight the associated irreducible representation (Irrep) and the spin, orbital character, and parity of the respective gap matrix. We write the order parameter in the matrix form $\hat{\tau}_a \otimes \hat{\sigma}_b (i\hat{\sigma}_2)$. Here we factor out $(i\hat{\sigma}_2)$ so that one can directly relate $b = 0$ to a singlet state and $b = \{1, 2, 3\}$ with the $\{x, y, z\}$ components of the d -vector parametrization for triplet states. * Nodes are lifted if trigonal warping is introduced in the (1, 3) term in the normal state. ** Nodes are not lifted if trigonal warping is introduced in the (1, 3) term in the normal state.

B. Symmetry reduction for the bulk of CPSBS

For CPSBS, the presence of the (PbSe)₅ layers reduces the point group symmetry to D_{1d} (isomorphic to C_{2h}). In CPSBS \hat{C}_3 is not a symmetry transformation anymore, but \hat{C}'_2 and $\hat{\sigma}_d$ are still valid symmetry operations which allow us to generate the character table for the reduced group from the table for D_{3d} . The point group D_{1d} is formed by four operations organized in four conjugacy classes, therefore there are four irreducible representations, as displayed in Table V. The irreducible representations from D_{3d} to D_{1d} are mapped as follows: $A_{1g/u} \rightarrow A_{1g/u}$, $A_{2g/u} \rightarrow A_{2g/u}$, $E_{g/u} \rightarrow \{A_{1g/u}, A_{2g/u}\}$. The last correspondence means that the two dimensional irreducible representations of D_{3d} are split in D_{1d} .

irrep	\hat{E}	\hat{C}'_2	\hat{P}	$\hat{\sigma}_d$
A_{1g}	+1	+1	+1	+1
A_{2g}	+1	-1	+1	-1
A_{1u}	+1	+1	-1	-1
A_{2u}	+1	-1	-1	+1

TABLE V. Character table for the point group D_{1d} obtained from a reduction of the character table for D_{3d} by eliminating the columns corresponding to the conjugacy classes labelled as $2\hat{C}_3$ and $2\hat{S}_6$.

1. Description of the normal state

Given the presence of parity and time-reversal symmetries, the only terms allowed in $\hat{H}_0(\mathbf{k})$ are the same as the ones enumerated for the case of D_{3d} symmetry, but now these are mapped to different irreducible representations. The main consequence for our model is that the parameter A_0 does not need to be the same for the (1, 1) and (1, 2) terms (see Table VI).

(a, b)	\hat{P}	\hat{C}'_2	$\hat{\sigma}_d$	Irrep	$h_{ab}(\mathbf{k})$
(0, 0)	+1	+1	+1	A_{1g}	$C_0 + C_1 k_z^2 + C_2(k_x^2 + k_y^2)$
(2, 0)	-1	-1	+1	A_{2u}	$B_0 k_z$
(3, 0)	+1	+1	+1	A_{1g}	$M_0 + M_1 k_z^2 + M_2(k_x^2 + k_y^2)$
(1, 1)	-1	-1	+1	A_{2u}	$-A_1 k_y$
(1, 2)	-1	+1	-1	A_{1u}	$A_2 k_x$
(1, 3)	-1	+1	-1	A_{1u}	$R_1 k_x(k_x^2 - 3k_y^2)$

TABLE VI. Parametrization of the normal-state Hamiltonian given in Eq. (S2) for materials in the family of Bi_2Se_3 with reduced D_{1d} symmetry, applicable to the bulk of CPSBS. Note the different coefficients for (1, 1) and (1, 2) terms.

2. Order parameter discussion

Concerning the order parameters, the reduction of the point group symmetry in principle allows for new kinds of superpositions, as suggested by Table I in the main text. Note that [0, 0] and [3, 0] belong to A_{1g} , [2, 3] and [2, 2] belong to A_{1u} , and that [1, 0] and [2, 1] belong to A_{2u} . According to experiments, the order parameter that is in agreement with the symmetry protected nodes in the bulk of CPSBS is [2, 2]. By symmetry, the most general form of the order parameter in D_{1d} is a linear superposition of [2, 2] and [2, 3]. A superposition of these two types of order parameters generally lifts the nodes present in the case of a pure [2, 2] order parameter. The mixing of [2, 2] and [2, 3] order parameters is only possible in the presence of both SOC terms (1, 2) and (1, 3) in the normal state Hamiltonian. As the trigonal warping term (1, 3) is negligibly small, this mixing should also be small in the bulk. The smallness of trigonal warping explains the robustness of the nodes (or their transformation to near nodes with experimentally inaccessible minima) in the bulk of CPSBS.

C. Symmetry reduction at the surface of CPSBS

At the surface of CPSBS, inversion symmetry is broken and the group is reduced to C_{1v} with only two elements, therefore only two conjugacy classes and irreducible representations. The irreps are mapped according to $\{A_{1g}, A_{2u}\} \rightarrow A_1$ and $\{A_{2g}, A_{1u}\} \rightarrow A_2$, as indicated by the C_{1v} character table displayed as Table VII.

irrep	\hat{E}	$\hat{\sigma}_d$
A_1	+1	+1
A_2	+1	-1

TABLE VII. Character table for the point group C_{1v} obtained by reducing the character table for D_{1d} by eliminating the columns corresponding to \hat{P} and \hat{C}'_2 .

1. Description of the normal state

Note that in the absence of inversion symmetry all (a, b) terms in the normal state Hamiltonian are symmetry allowed. The new terms in the normal state Hamiltonian are summarized in Table VIII.

2. Order parameter discussion

The order parameters are now mapped such that [0, 0], [3, 0], [1, 0], and [2, 1] belong to the A_1 irrep, while [2, 3] and [2, 2] belong to the A_2 irrep. Note that the latter is the same type of mixing found for D_{1d} symmetry. Again, according to experiments, the order parameter that is in agreement with the symmetry protected nodes in CPSBS is [2, 2]. By symmetry, the most general form of the order parameter in C_{1v} is a linear superposition

(a, b)	$\hat{\sigma}_d$	TRS	Irrep	$h_{ab}(\mathbf{k})$	Process
(0, 0)	+1	+	A_1	$C_0 + C_1 k_z^2 + C_2 (k_x^2 + k_y^2)$	Intra-orbital hopping
(0, 1)	+1	-	A_1	$c_1 k_y + c_1' k_z$	SOC
(0, 2)	-1	-	A_2	$c_2 k_x + c_2' k_x (k_x^2 - 3k_y^2)$	SOC
(0, 3)	-1	-	A_2	$c_3 k_x + c_3' k_x (k_x^2 - 3k_y^2)$	SOC
(1, 0)	+1	+	A_1	$c_4 + c_4' k_z^2 + c_4'' (k_x^2 + k_y^2)$	Inter-orbital hopping
(1, 1)	+1	-	A_1	$-A_1 k_y + a_1 k_z$	SOC
(1, 2)	-1	-	A_2	$A_2 k_x$	SOC
(1, 3)	-1	-	A_2	$R_1 k_x (k_x^2 - 3k_y^2) + r_1 k_x$	SOC
(2, 0)	+1	-	A_1	$B_0 k_z + b_0 k_y$	Inter-orbital hopping
(2, 1)	+1	+	A_1	$c_5 + c_5' k_z^2 + c_5'' (k_x^2 + k_y^2)$	SOC
(2, 2)	-1	+	A_2	$c_6 k_x k_z + c_6' k_y k_z$	SOC
(2, 3)	-1	+	A_2	$c_7 k_x k_z + c_7' k_y k_z$	SOC
(3, 0)	+1	+	A_1	$M_0 + M_1 k_z^2 + M_2 (k_x^2 + k_y^2)$	Intra-orbital hopping
(3, 1)	+1	-	A_1	$c_8 k_y + c_8' k_z$	SOC
(3, 2)	-1	-	A_2	$c_9 k_x + c_9' k_x (k_x^2 - 3k_y^2)$	SOC
(3, 3)	-1	-	A_2	$c_{10} k_x + c_{10}' k_x (k_x^2 - 3k_y^2)$	SOC

TABLE VIII. Parametrization of the normal-state Hamiltonian given in Eq. (S2) for materials in the family of Bi_2Se_3 with reduced C_{1v} symmetry, applicable to the surface of CPSBS. Here we entered new symmetry allowed coefficients b_0 , a_1 , r_1 , and c_i , c_i' , and c_i'' , for $i = \{1, \dots, 10\}$.

of [2, 2] and [2, 3]. As discussed above, the mixing of these two types of order parameters would generally lift the nodes. Note that, in presence of only C_{1v} symmetry, these two order parameter components can be coupled by multiple pairs of terms in the normal state Hamiltonian.

D. Symmetry reduction at the surface of CPSBS with disorder

At the surface of CPSBS, superconductivity was only observed in areas with no stripe pattern. This suggests that the influence of the PbSe layers in the superconducting areas is weakened and the three-fold rotational symmetry of the Bi_2Se_3 layers in the bulk is restored in these regions. We consider then the point group symmetry of the surface of Bi_2Se_3 , identified as C_{3v} . The irreps are mapped according to $\{A_{1g}, A_{2u}\} \rightarrow A_1$, $\{A_{2g}, A_{1u}\} \rightarrow A_2$, and $\{E_u, E_g\} \rightarrow E$, as indicated by the C_{3v} character table displayed as Table IX.

irrep	\hat{E}	$2\hat{C}_3$	$3\hat{\sigma}_d$
A_1	+1	+1	+1
A_2	+1	+1	-1
E	2	-1	0

TABLE IX. Character table for the point group C_{3v} obtained by reducing the character table for D_{3d} by eliminating the columns corresponding to \hat{P} , $3\hat{C}_2'$, and $2\hat{S}_6$.

1. Description of the normal state

Note that in the absence of inversion symmetry all (a, b) terms in the normal state Hamiltonian are symmetry allowed. The new terms in the normal state Hamiltonian are summarized in Table X.

(a, b)	$\hat{\sigma}_d$	TRS	Irrep	$h_{ab}(\mathbf{k})$	Process
(0, 0)	+1	+	A_1	$C_0 + C_1 k_z^2 + C_2(k_x^2 + k_y^2)$	Intra-orbital hopping
(0, 1)	+1	-	E	$m_1 k_y$	SOC
(0, 2)	-1	-	E	$-m_1 k_x$	SOC
(0, 3)	-1	-	A_2	$m_2 k_x(k_x^2 - 3k_y^2)$	SOC
(1, 0)	+1	+	A_1	$m_3 + m'_3 k_z^2 + m''_3(k_x^2 + k_y^2)$	Inter-orbital hopping
(1, 1)	+1	-	E	$-A_0 k_y$	SOC
(1, 2)	-1	-	E	$A_0 k_x$	SOC
(1, 3)	-1	-	A_2	$R_1 k_x(k_x^2 - 3k_y^2)$	SOC
(2, 0)	+1	-	A_1	$B_0 k_z$	Inter-orbital hopping
(2, 1)	+1	+	E	$m_4(k_x^2 - k_y^2)$	SOC
(2, 2)	-1	+	E	$-m_4 k_x k_y$	SOC
(2, 3)	-1	+	A_2	$m_5 k_x k_z(3k_x^2 - k_y^2)$	SOC
(3, 0)	+1	+	A_1	$M_0 + M_1 k_z^2 + M_2(k_x^2 + k_y^2)$	Intra-orbital hopping
(3, 1)	+1	-	E	$m_6 k_y$	SOC
(3, 2)	-1	-	E	$-m_6 k_x$	SOC
(3, 3)	-1	-	A_2	$m_7 k_x(k_x^2 - 3k_y^2)$	SOC

TABLE X. Parametrization of the normal-state Hamiltonian given in Eq. (S2) for materials in the family of Bi_2Se_3 with reduced C_{3v} symmetry, applicable to the surface of doped Bi_2Se_3 and the disordered surfaces of CPSBS. Here we entered new symmetry allowed coefficients m_i , m'_i , and m''_i , for $i = \{1, \dots, 7\}$.

E. Parametrization of normal state Hamiltonian and gaps for Figure 5 in the main text

For the generation of Figure 5, we used the following first principle parameters extracted from Ref. [12] for the starting Hamiltonian with D_{3d} symmetry:

$$\begin{aligned}
A_0 &= 3.33 \text{ eV}\text{\AA}^{-1}, \\
C_0 &= -0.0083 \text{ eV}, \\
C_2 &= 30.4 \text{ eV}\text{\AA}^{-2}, \\
M_0 &= -0.28 \text{ eV}, \\
M_2 &= 44.5 \text{ eV}\text{\AA}^{-2}, \\
R_1 &= 50.6 \text{ eV}\text{\AA}^{-3}.
\end{aligned} \tag{S4}$$

We set $B_0 = C_1 = M_1 = 0$ (in the respective units) to eliminate the k_z dependence.

In the presence of D_{1d} symmetry, $A_1 \neq A_2$. As we do not have access to first principles calculations, we choose $A_{1,2} = A_0 \pm A_0/10$. The gap anisotropy does not seem to strongly depend on the ratio A_1/A_2 .

For the new terms at the surface, we also do not have access to a first principles calculation, so we set these to be a fixed percentage (p) of the value of terms with similar momentum dependence in the original normal state Hamiltonian with inversion symmetry.

For the case with D_{1d} symmetry we set

$$\begin{aligned}
c_1 &= b_0 = c_8 = -pA_1 \\
c_2 &= c_3 = c_9 = c_{10} = pA_2 \\
c'_2 &= c'_3 = c'_9 = c'_{10} pR_1 \\
c_4 &= c_5 = pC_0 \\
c'_4 &= c'_5 = pC_1, \\
c''_4 &= c''_5 = pC_2 \\
r_1 &= pA_2
\end{aligned} \tag{S5}$$

and take $a_1 = c_6 = c'_6 = c_7 = c'_7 = c'_8 = 0$ to eliminate the k_z dependence.

For the case with C_{3v} symmetry we set

$$\begin{aligned}
m_1 &= m_6 = pA_0 \\
m_2 &= m_7 = pR_1 \\
m_3 &= pC_0 \\
m'_3 &= pC_1 \\
m''_3 &= pC_2
\end{aligned} \tag{S6}$$

and take $m_4 = 0$ as there is no such terms in our parametrization of the normal state Hamiltonian with D_{3d} symmetry, and we take $m_5 = 0$ to eliminate the k_z dependence.

For Figure 5 in the main text, we used a chemical potential shift of $\mu = 0.4\text{eV}$, the order parameter magnitude of $d = 0.01\text{eV}$, and the surface factor $p = 0.01$. For the gap with C_{1v} symmetry we choose $d_{22}/d_{23} = \sqrt{2}$ and for the gap with C_{3v} symmetry we choose $d_{22}/d_{21} = 1$. The choice of p and ratio of order parameters were such that we could find order parameter superpositions that have gap anisotropy and gap minima rotation comparable to the experimental observations. A more microscopic derivation of such parameters would be desirable, but goes beyond the scope of this work.

-
- [1] Eskildsen, M. R. et al. Vortex imaging in the π band of Magnesium Diboride. *Phys. Rev. Lett.* **89**, 187003 (2002).
 - [2] Bergeal, N. et al. Scanning tunneling spectroscopy on the novel superconductor CaC_6 . *Phys. Rev. Lett.* **97**, 077003 (2006).
 - [3] Renner, C., Kent, A. D., Niedermann, P., Fischer, O. & Lévy, F. Scanning tunneling spectroscopy of a vortex core from the clean to the dirty limit. *Phys. Rev. Lett.* **67**, 1650–1652 (1991).
 - [4] Andersen, L., Ramires, A., Wang, Z., Lorenz, T. & Ando, Y. Generalized Anderson’s theorem for superconductors derived from topological insulators. *Sci. Adv.* **6**, eaay6502 (2020).
 - [5] Tao, R. et al. Direct visualization of the nematic superconductivity in $\text{Cu}_x\text{Bi}_2\text{Se}_3$. *Phys. Rev. X* **8**, 041024 (2018).
 - [6] Bagchi, M., Brede, J. & Ando, Y. Observability of superconductivity in Sr-doped Bi_2Se_3 at the surface using scanning tunneling microscope. *Phys. Rev. Mater.* **6**, 034201 (2022).
 - [7] Nagai, Y. Field-angle-dependent low-energy excitations around a vortex in the superconducting topological insulator $\text{Cu}_x\text{Bi}_2\text{Se}_3$. *J. Phys. Soc. Jpn.* **83**, 063705 (2014).
 - [8] Nakayama, K. et al. Manipulation of topological states and the bulk band gap using natural heterostructures of a topological insulator. *Phys. Rev. Lett.* **109**, 236804 (2012).
 - [9] Nakayama, K. et al. Observation of two-dimensional bulk electronic states in the superconducting topological insulator heterostructure $\text{Cu}_x(\text{PbSe})_5(\text{Bi}_2\text{Se}_3)_6$: Implications for unconventional superconductivity. *Phys. Rev. B* **92**, 100508 (2015).
 - [10] Andersen, L., Wang, Z., Lorenz, T. & Ando, Y. Nematic superconductivity in $\text{Cu}_{1.5}(\text{PbSe})_5(\text{Bi}_2\text{Se}_3)_6$. *Phys. Rev. B* **98**, 220512 (2018).
 - [11] Zhang, H. et al. Topological insulators in Bi_2Se_3 , Bi_2Te_3 and Sb_2Te_3 with a single Dirac cone on the surface. *Nature Physics* **5**, 438–442 (2009).
 - [12] Liu, C.-X. et al. Model Hamiltonian for topological insulators. *Phys. Rev. B* **82**, 45122 (2010).

4 Pb(111) thin film on TlBiSe₂: a 2D TSC?

Y. Ando proposed the experiments on which this chapter is based. Y. Wang grew the TlBiSe₂ crystals. M. Bagchi acquired transport data. Pb deposition on TlBiSe₂ was carried out by M. Bagchi and J. Brede. STM data was acquired primarily by J. Brede with contributions from M. Bagchi. STM data was analyzed by M. Bagchi under the supervision of J. Brede.

4.1 Motivation: topological proximity effect

More than a decade ago Fu and Kane made a proposal [12] for constructing Majorana fermions (MF) in a condensed matter system built out of a normal *s*-wave superconductor (SC) and a topological insulator (TI). Soon after, the crux of the proposal was realized by growing epitaxial thin films of Bi₂Se₃ [13] and Bi₂Te₃ [107] on the superconductor NbSe₂. For a thickness of 6 QL Bi₂Se₃ film grown epitaxially on NbSe₂¹, a superconducting gap was measured on the surface using STS, while ARPES data confirmed the formation of the topological surface state for the same film thickness and above. Similar observations were made on Bi₂Te₃/NbSe₂, with the additional observation of Abrikosov vortices in the proximitized TI. Although zero-energy vortex core states were found, it could not be identified as a signature of MZM since the insufficient energy resolution of the experiment prevented any distinction between the non-trivial zero mode and trivial vortex states. To circumvent this problem, Xu *et al.* [108] demonstrated a different experimental signature for a MZM. They showed that unlike a vortex in a conventional superconductor where the ZBCP of the vortex bound state splits immediately as one moves away from the vortex core, the ZBCP in the vortex cores of their proximitized Bi₂Te₃ film only splits after a finite distance off the vortex center, giving a Y-shaped spatial profile. This unexpected behaviour of the vortex bound states was attributed to a MZM. Later experiments on Bi₂Te₃/Pt/Nb(110)/Al₂O₃ [109] have resulted in similar conclusions.²

All the above experiments managed to epitaxially interface a bulk superconductor and a TI. However, experiments such as those involving a superconducting qubit implemented using a TI Josephson junction require the growth of a superconductor on a TI surface. Growing common SCs such as Nb, Al or NbN epitaxially on a TI has proved to be quite challenging. Hence, a different experimental route to realizing the Fu and Kane proposal

¹Growth of Bi₂Se₃ or Bi₂Te₃ on NbSe₂ proceeds via an interface layer which essentially consists of a bilayer of Bi(110).

²Recently, Kim *et al.* [110] have observed "anisotropic non-split zero-energy vortex bound states in a conventional superconductor" indicating that the latter may not be a unambiguous signature of MZMs.

is desirable. In this regard, experiments by Shoman *et al.* [111] and then Trang *et al.* [43] suggest an alternate approach.

Shoman *et al.* [111] interfaced the TI TlBiSe₂ with one-bilayer Bi, a metal³. ARPES measurements on the heterostructure showed that the Dirac point of the surface state (SS) of TlBiSe₂ is considerably higher in energy as compared that measured on the surface of TlBiSe₂ itself; interpreted as migration of the SS into the Bi bilayer. The migration of the SS was attributed to the "spin-dependent hybridization of the wave functions at the metal-TI interface" [111] and the phenomena was termed as topological proximity effect (TPE).

The covalent nature of bonding in TlBiSe₂ plays a key role in the TPE. The dangling bonds on the cleaved surface of TlBiSe₂ will lead to a strong hybridization with any metal deposited on its surface. This is not the case for Bi₂Se₃ or Bi₂Te₃. Their cleaved surfaces have no open bonds, allowing for only weak hybridization [113] with the deposited metal and no change in band structure [114] as a result.

The other requirement for TPE is that the deposited metal should grow well on the TI surface as a thin film, resulting in quantized 2D bands. The hybridization between TI SS and 2D metal band at the interface is at the heart of TPE. Further, as pointed out in Ref. [111], for this kind of hybridization between two bands their spin states must agree. Hence for hybridization with the TI surface state it is preferable that metal bands are spin split, as in the case of 2D-Bi. The spin dependent hybridization between the bands is expected to make the effect stronger.

In short, TPE makes the TI SS accessible on the surface of SC/TI. The final step in the road to realizing a Fu-Kane heterostructure via the TPE is to use a metal that can induce Cooper pairing in the electrons of the TI SS. Trang *et al.* [43] grew such a heterostructure. In their experiment, a *s*-wave superconductor [Pb(111)] is grown on TlBiSe₂. The TPE is verified in ARPES experiment where TI SS is shown to migrate to the top of the superconducting thin film. Further, they observe a gap opening at points along the $\bar{\Gamma}\text{M}$ and $\bar{\Gamma}\text{K}$ where the Dirac-cone crosses the Fermi level (E_F). This enables them to conclude an isotropic superconducting gap on the Dirac-cone Fermi surface and they speculate that pairing in this case should be of the kind predicted by Fu and Kane [12], i.e., a 2D TSC is realized.

Using Fig. 4.1 we summarize the ARPES results. The Dirac cone SS is seen around $\bar{\Gamma}$ point for pristine TlBiSe₂. For Pb on TlBiSe₂, along with the SS, several M-shaped bands appear. They are ascribed to the quantum well states (QWSs) due to the quantum confinement of electrons in the Pb thin film; also seen for Pb(111) thin film on Si(111). The energy positions of these QWSs vary as a function of thickness of the Pb film. By comparing with the energy location of the QWS between calculations for free-standing *n*-ML Pb film and ARPES data, they have identified the thickness of Pb film grown on TlBiSe₂ to be 17 ML (5 nm). The QWSs can also be identified in our spectroscopy measurements and will be discussed later.

³Bilayer of Bi(111) thin film is recognized to be a 2D TI with 1D helical edge states [112, 35].

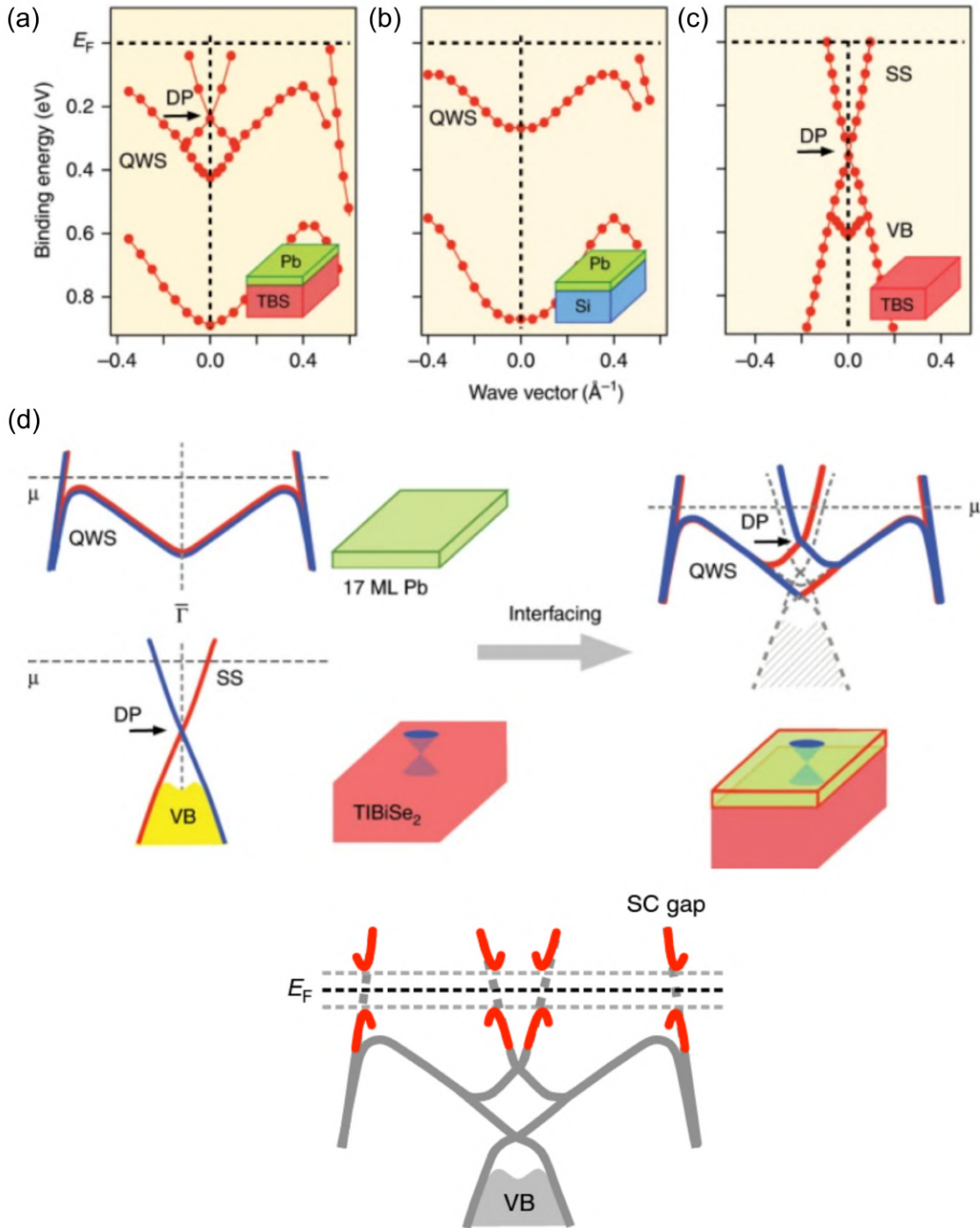


Figure 4.1: Migration of topological surface states to the surface of Pb film. (a)-(c) Experimental band dispersions extracted from the peak positions of MDCs/EDCs. (d) Schematics of the hybridization between topological Dirac-cone state and QWSs followed by illustration of the superconducting-gap opening on the QWS- and TSS-derived bands. Figure taken from [43].

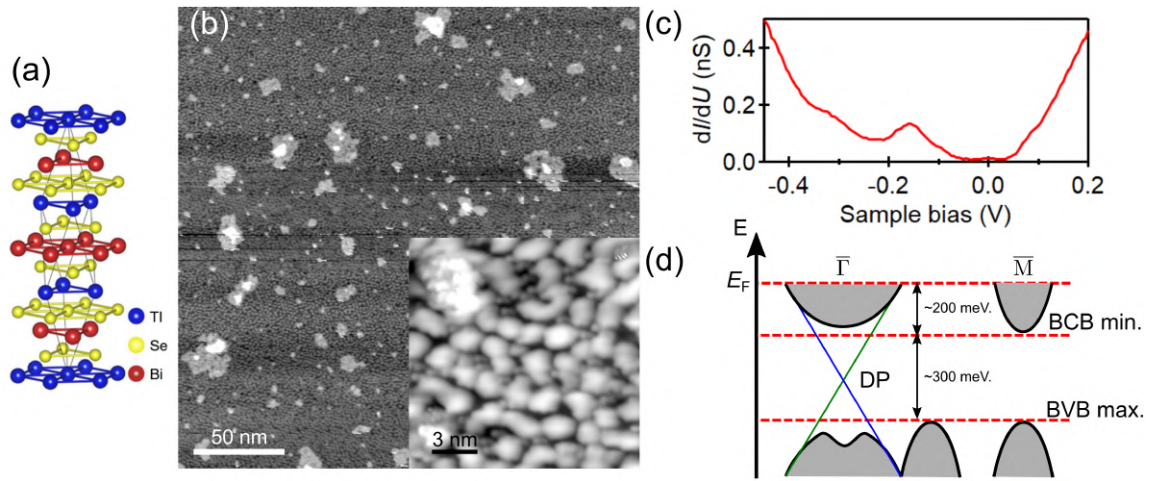


Figure 4.2: Morphology and spectroscopy on the surface of TlBiSe₂. (a) Crystal structure of TlBiSe₂ (modified from Ref. [43]). (b) A 250 nm by 250 nm STM image of the cleaved surface of TlBiSe₂ (inset: a zoomed image showing a disordered surface with a corrugation of ~400 pm). (c, d) dI/dU spectrum (top) and a cartoon (below) showing the expected bandgap of ~0.3 V based on ARPES data.

Apart from bands of Pb, a Dirac cone like band appears above the highest QWS. This band cannot originate from Pb since it is not observed for Pb on Si(111). However the photoelectron escape depth in ARPES experiment is only ~0.5-1 nm, which would preclude ARPES intensity from the TI, almost 5 nm from the surface. This led the authors to conclude that the Dirac cone of TlBiSe₂ has migrated to the surface of Pb film. Since the QWSs and TI SS are momentum resolved in the ARPES data, the authors are also able to show a SC gap opening in the specific TI band, giving strong credibility to their main claim. Although ARPES has given compelling evidence for a 2D TSC, it cannot operate in the presence of an external magnetic field and other local spectroscopic techniques such as STM must be used to probe the spatially localized MFs that are expected to emerge in vortex cores of a 2D TSC.

In this chapter we investigate the SC/TI heterostructure of Pb (111) thin film on TlBiSe₂ using the surface sensitive technique of STM. Our primary goal is to look in the vortex cores for signatures of Majorana modes. In the next sections, we first look at the morphology of the TlBiSe₂ surface layer and then calibrate the deposition of Pb film before proceeding to grow the film on our TI surface.

4.2 TlBiSe₂: morphology

We compare and contrast the bulk TI TlBiSe₂ with Bi₂Se₃. As opposed to the Bi₂Se₃ stacking sequence of Se-Bi-Se-Bi-Se, we have -Tl-Se-Bi-Se-Tl- and the absence of a vdWs gap [see Fig. 4.2(a)]. The 'cleaving' plane in this case is between the Tl and Se layer due

to the larger interlayer distance of 209 pm, or weaker bonding, as compared to 167 pm between Bi and Se layers. Fig. 4.2(b) shows the as-cleaved surface of TlBiSe₂. Inset of Fig. 4.2(b) is a zoomed image showing a disordered worm-like surface. A very similar surface was reported by Pielmeier *et al.* [115]. Using a combined STM/AFM⁴ system they were able to obtain atomic resolution within the worms showing a hexagonal lattice, with neighbouring islands having the same structure and orientation. By counting individual atoms they found that half the atoms of the topmost layer were lost in the cleaving process. Although this layer is damaged, the lower layers were shown to be intact and crystalline from the superstructure spots that were rotated by 30° with respect to the Bragg spots. The predominant step height observed by them was 0.75 nm which corresponds to the Tl-Tl distance. This led them to conclude that the topmost layer was made of Tl atoms. Their observation was corroborated by the XPS study from Kuroda *et al.* [116] which showed a splitting of both doublet peaks of the Tl 5d core level, indicating two types of environments for the Tl atoms. A possible explanation is that the Tl atoms are present in the bulk and also on the surface.

We performed electronic characterization of this surface in terms of spectroscopy. dI/dU spectrum, which is proportional to the LDOS, taken on the cleaved surface of TlBiSe₂ is shown Fig. 4.2(c). It is difficult to identify the Dirac point (DP) and the bottom of the bulk conduction band (BCB) from the spectrum alone due to additional density of states around -150 meV, most likely coming from the layer of Tl atoms on the surface. Based on the ARPES data for this surface in Refs. [117, 118, 43], one expects a bandgap between 200–300 meV. Further the ARPES data shows the Fermi level to lie 200 meV inside the BCB, in agreement with the estimate based on the carrier density obtained in transport measurements on this sample (see Fig. 4.3).

We also point out that concrete evidence for the presence of the topological surface state (TSS) in terms of observation of Landau levels could not be measured as spectroscopy on this surface is challenging.

4.3 UHV growth of Pb thin film on TI

It is very difficult to grow thin films of common superconductors such as Nb, V among others, on semiconducting substrates. However, high quality ultrathin superconducting films of Pb have been grown on semiconducting Si and Ge substrates with great success in the past [119–122]. Thin films of Pb were also found to be superconducting, even down to an atomic layer [123].

For an fcc metal like Pb the lowest surface energy corresponds to the (111) surface ($E_{111}^s < E_{100}^s < E_{110}^s$). Hence growth along the [111] direction is preferred for room temperature as well as low temperature growth of Pb films. The thickness for a monolayer of Pb film in the [111] direction is 0.285 nm⁵.

⁴AFM: Atomic force microscope

⁵The distance between (111) planes of a fcc lattice is given as $\frac{a}{\sqrt{3}}$, where a is the lattice constant of the

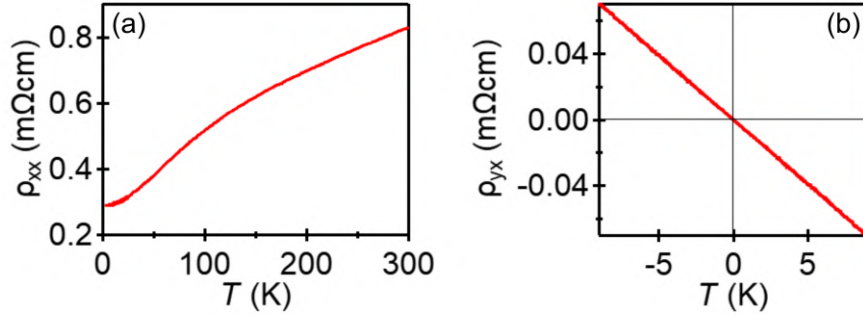


Figure 4.3: Bulk characterization of TlBiSe₂ crystals. (a) Temperature dependence of resistivity (ρ_{xx}) of a TlBiSe₂ crystal belonging to the same batch as the ones used for the STM experiments in this chapter. (b) Magnetic-field dependence of the Hall resistivity (ρ_{yx}) measured at 2 K, which gives a carrier density of $8 \times 10^{19} \text{ cm}^{-3}$.

As a first step, we calibrated the growth by comparison with the well-known systems such as Pb films on Cu(111) and Si(111) 7x7 surface for a nominal thickness of 10 ML of Pb. Below we discuss the growth and calibration for the Pb film on our TI surface.

We aim to grow 17 ML or 4.85 nm of Pb on our TI surface. For this purpose the TI crystal is first cleaved in UHV to reveal a shiny mirror-like surface. Pb atoms are then deposited on this crystal using a Knudsen cell evaporator while keeping the crystal/substrate at liquid N₂ temperatures. Low growth temperatures prevent clustering of the Pb atoms upon reaching the surface. The deposition time for Pb was based on the rate obtained using the quartz microbalance available in the preparation chamber. Rate was found to be 0.02 ML/s at Knudsen cell temperature of 540 °C.

Since the deposition rate on the sample may not be exactly the same as the deposition rate on the microbalance, due to the different physical positions of the two in our preparation chamber in relation to the evaporator, we made a separate calibration using the STM. We evaluated the coverage of nominally 5 ML of Pb on TlBiSe₂. The sample was prepared by depositing Pb on the TI at low temperatures followed by annealing to room temperature for 30 minutes before inserting in the STM. As a result the Pb film transitioned to form worm-like high islands [see Fig. 4.4(a)]. By evaluating the coverage on this area the tooling factor was determined. The corrected deposition rate found was 0.018 ML/s.

4.4 Characterization of the Pb film on TlBiSe₂

Figure 4.5(a) shows the surface morphology of a 15 ML Pb film deposited on TlBiSe₂ surface while keeping the sample temperature at ~ 80 K. Instead of a uniform 15 ML thickness, we observe several atomic layers on the surface. Each layer has a hexagonal lattice structure [Fig. 4.5(b)] which reconfirms growth along the [111] direction. Upon

conventional cell.

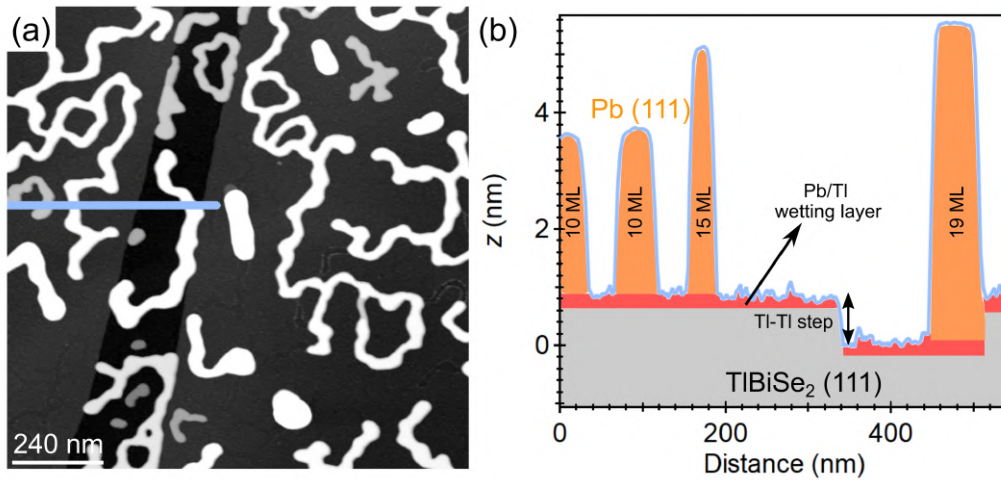


Figure 4.4: Pb coverage on TlBiSe₂ surface. (a) A 1.2 μm by 1.2 μm STM image showing high islands of Pb on the TlBiSe₂ surface. (b) Line profile taken along the blue line in (a).

zooming in on a smaller area in Fig. 4.5(c) and taking a line profile [Fig. 4.5(d)] along the blue line, we identify 5 different steps, each of height that matches the distance between fcc(111) planes of Pb [note that in the bigger image of Fig. 4.5(a) some of the holes are ~ 3 ML deeper].

The electronic structure of the different terraces over a large energy window is documented using STS. In Fig. 4.5(e) we show dI/dU spectra taken on two different Pb layers [positions indicated in panel (c)]. The spectra show several peaks, with the peak positions changing from one step to the next. Peaks in the dI/dU spectra correspond to peaks in the LDOS and are attributed to the QWSs of Pb thin films. In 2D films of Pb the conduction electrons get confined by the substrate on one side and vacuum on the other producing quantum levels (or subbands) known as QWSs. These quantized energy levels show up as peaks⁶ in the LDOS spectroscopy. Energy positions of peaks corresponding to the QWSs depend on the thickness of the island (this determines the depth of the quantum well) and their widths indicate the lifetime of the state. The fact that the QWS peaks in the red curve look broad as compared to the blue curve can be interpreted as an indication of additional scattering for this layer, likely from the 2D boundaries.

Nevertheless, QWS peaks can be used to identify the thickness of the Pb film grown. The positions of QWSs in the blue curve in Fig. 4.5(e) agrees best with those for the 17 ML film in slab calculations for free-standing n -ML Pb film given in Ref. [43] (see Table 4.1). The orange curve in Fig. 4.5(e) taken on the island which is 1 ML higher should then correspond to 18 ML. Hence along the line profile in Fig. 4.5(d) we identify the nearly completely closed layer as the 15th ML. The islands in excess of 15 ML can be added up to roughly give an additional coverage of 1 ML.

⁶It is a peak and not a step-like increase in the LDOS due to a 1D-like Van Hove singularity at the band bottom.

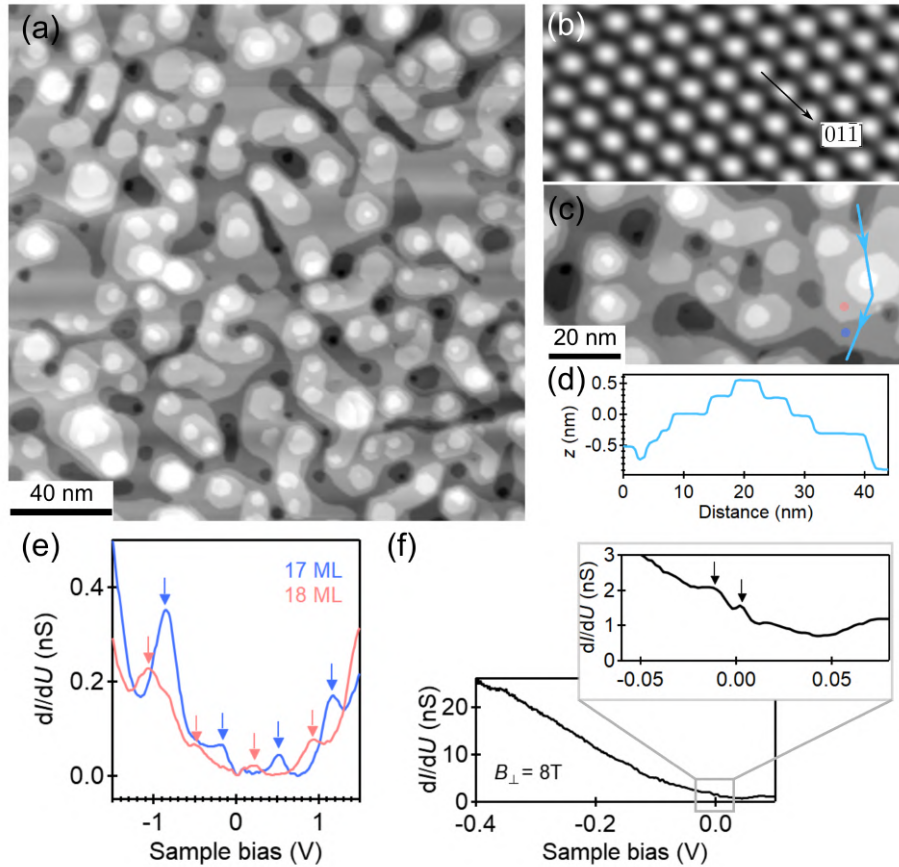


Figure 4.5: Characterization of Pb film on TlBiSe₂. (a) Large scale STM topograph image of the Pb film grown on TlBiSe₂ showing various heights. (b) Atomically resolved image of the Pb surface showing a hexagonal lattice which indicates growth along the [111] direction. (c) A zoomed view in the same area as (a) where 6 different layers can be identified. (d) Line profile taken along the blue line indicated in (c). (e) dI/dU spectra taken on the two points corresponding to two different layers as indicated by the filled circles in (c). The spectra show multiple peaks which are attributed to quantum well states (QWS). (f) dI/dU spectrum recorded in the perpendicular magnetic field of 8 T. Inset shows two peaks about ≈ 14 meV apart around the Fermi level.

ARPES[43]	16 ML	-1.06 eV	-0.33 eV		
	17 ML	-1.51 eV	-0.86 eV	-0.16 eV	
	18 ML	-1.15 eV	-0.52 eV		
STM (this work)	17 ML	-0.85 eV	-0.15 eV	0.53 eV	1.16 eV
	18 ML	-1.07 eV	-0.51 eV	0.22 eV	0.93 eV

Table 4.1: Overview of the locations of the QWS for 16, 17 and 18 ML as given in Ref. [43] and those identified in this work.

We also attempted Landau level spectroscopy in search for the TSS of the TI on the surface. No clear peaks are seen in the LDOS in the presence of an out-of-plane magnetic field of 8 T [see Fig. 4.5(f)]. However, upon zooming in near the Fermi level we see two peaks separated by ~ 14 meV, which fit to Landau levels of the TI surface state with large indices [58] but no further investigation of these peaks was done.

Having characterized the surface electronic properties of our Pb film we now proceed to spectroscopic characterization of its superconductivity. In the remainder of this section we discuss the SC gap (Δ) value, critical temperature (T_c), critical field (H_{c2}) and Ginzburg-Landau coherence length (ξ_{GL}) of our film. We compare such parameters associated with superconductivity of the film to literature values of Pb films on Si(111) surface. They are not expected to match exactly due to the difference in substrates. However, such a comparison can give us an insight into the quality of the film in terms of its superconductivity.

High resolution spectroscopy on the Pb film [Fig. 4.6(a)] at our lowest system temperature of 0.35 K reveals a clear superconducting gap [Fig. 4.6(b)]. A Dynes fit to the spectrum yields a SC gap of 1.2 meV. The gap value is weakly sensitive to the actual values of T_{eff} and Γ used for a certain range. Two such fit results are shown: $T_{\text{eff}}=0.7$ K, $\Gamma=0.05$ meV (black dashed trace) and $T_{\text{eff}}=0.97$ K, $\Gamma=0.1$ meV (red trace). While the red curve reproduces the data near the coherence peaks, both curves fail near the gap bottom, i.e., a Dynes model is not able to describe the superconducting gap fully⁷.

The measured gap value is similar to the gap of 1.3 meV reported for a 20 ML thick Pb film grown on a Si(111) 7×7 substrate, measured at $T=0.4$ K [124].⁸ Next, we trace the SC gap as a function of temperature to experimentally obtain a T_c value of 6.2 K for our film. The extracted gap values for all measured spectra are shown as a function of the system temperature in Fig. 4.6(c). Fitting the data points with the BCS gap equation (red curve) returns a $2\Delta_0/k_B T_c$ of 4.56 as opposed to the BCS ratio of 3.52. The deviation from

⁷I should check if a model which takes into account electron pairing between two bands can fit the data.

⁸Bulk Pb shows a superconducting energy gap of 1.35 meV, T_c of 7.2 K, H_{c2} of 80 mT, ξ_{GL} between 51-83 nm and London penetration depth (λ_L) of 32-39 nm [125]. The values of these bulk parameters are expected to change in 2D-films due to the reduced dimension.

Thickness (MLs)	2	4	5	10	11	13	15	17	18
T_c (K) [122]	3.6/4.8	6.7	6.3	6	6	6.1	6	-	-
T_c (K) [120]	-	-	5	6	6.2	6.3	-	6.5	6.6

Table 4.2: T_c values for different Pb film thickness on Si(111) substrate.

the BCS ratio is well documented in literature for Pb [126] and attributed to the strong electron-phonon interaction present in the system.

Özer *et al.* [120] obtained a linear relation between T_c of Pb film and inverse of its thickness (d): $T_c(d) = T_{c0}(1 - d_c/d)$, where T_{c0} is the bulk value of 7.2 K and $d_c = 1.5$ ML or the thickness of first superconducting layer. Based on this relation we expect a T_c of 6.47 K for a 15 ML Pb film. However, on comparison with another source in literature [122] showing T_c values for Pb films of similar thickness (see Table 4.2), we conclude that our Pb films are good.

We will now use the upper critical field (H_{c2}) value to further evaluate our film. We have taken zero-bias conductance (ZBC) maps in a 150 nm by 150 nm area in the presence of B_{\perp} -fields between 60 and 500 mT at 0.35 K [three such maps are shown in Fig. 4.6(d-f)]. Quantized flux tubes or vortices are observed for all field values, whose density increases with increasing field. The vortices arrange themselves in a periodic lattice which is triangular based on energy considerations, with a lattice spacing given as $d_{\text{vortex}} = 1.075 (\Phi_0/B)^{1/2}$ [127], where Φ_0 is one flux quantum, B is the applied field. Figure 4.6(g) shows the simulated curve together with the observed value of vortex lattice spacing. Except for the data point for the lowest field all others lie below the simulated curve which indicates that the vortex lattice is less than perfect which could be due to vortex pinning at the step edge on the in the TlBiSe₂ substrate.

Next, we take care to measure the SC gap outside the vortices for each field value. This is shown as a waterfall plot in Fig. 4.6(h) (this is not raw data but interpolated for equal spacing in field values). The superconducting gap fully closes at 500 mT which we take as the H_{c2} value for our film. The extracted Δ values of the SC gap as a function of field is shown in panel (i). A less time consuming way to extract the SC gap dependence on field is by extracting the normalized ZBC value outside the vortices, taken from a poor resolution vortex grid. Figure 4.6(i) shows the qualitatively similar outcomes obtained by plotting the SC gap values from STS spectra and $(1 - \text{ZBC})$ values of normalized curves from the vortex grid as a function of field.

Our value of H_{c2} (500 mT) for a 15 ML Pb film is 6.25 times larger than the bulk H_{c2} of 80 mT. This is explained purely in terms of reduced dimension of the film. A reduced film thickness means a smaller mean free path of the electrons, due to the scattering at the new boundaries and interface, which consequently reduces the BCS in-plane coherence length ξ_{GL} (ξ_{GL} is related to the mean free path (l) as $\xi_{\text{GL}} = \sqrt{\xi_0 l}$, where ξ_0 is the coherence length in the clean limit). ξ_{GL} also gives the size of a vortex and relates to H_{c2}

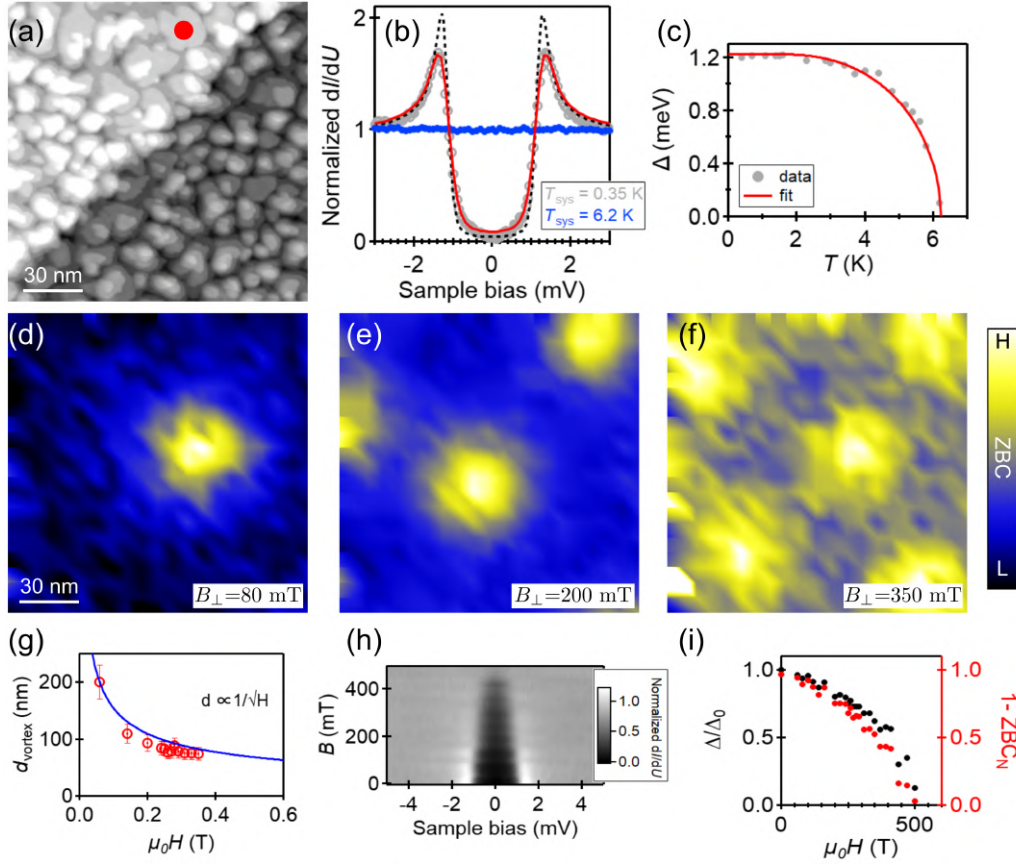


Figure 4.6: Superconducting properties of 15 ML Pb film on TlBiSe₂. (a) STM topograph of the Pb islands on TlBiSe₂. (b) High resolution spectra taken at the spot marked by the red dot in (a) at $T_{\text{sys}}=0.35$ K (gray open circles) and $T_{\text{sys}}=6.2$ K (blue solid circles). Two fit results for the gray data points are shown (red line, black dashed line) using different T_{eff} and Γ values, both resulting in a gap value of 1.2 meV. The gap completely disappears at $T_{\text{sys}}=6.2$ K. (c) The superconducting gap is measured as a function of temperature. The gap value for each spectrum was obtained from the Dynes fit. The data points follow the red curve which is a fit result of the BCS gap equation. (d)-(f) Zero bias conductance (ZBC) maps taken in the same field of view as (a) at magnetic field $B=80$ mT (d), $B=200$ mT (e) and $B=350$ mT (f). (g) Distance between vortices is plotted as a function of the applied B_{\perp} -field. The blue curve is the simulated profile for nearest neighbor distances verses applied B_{\perp} -field for hexagonal closed-packed arrangement of vortices. (h) The superconducting gap is traced as a function of B_{\perp} -field. The SC gap was measured outside vortices in presence of a magnetic field. (i) The superconducting gap sizes (black dots) obtained by fitting the spectra in (h) is plotted as a function of the applied magnetic field. At the same time $(1 - \text{ZBCN})$ of normalized spectra is also traced (red dots).

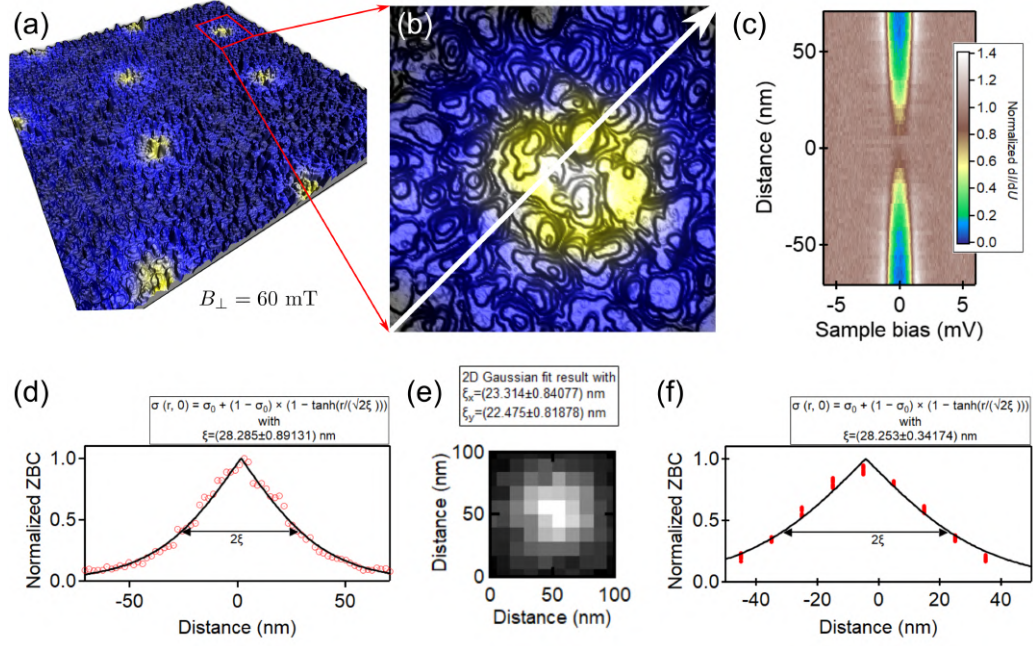


Figure 4.7: Vortex lattice on 15 ML Pb film on TlBiSe₂ at low magnetic field. (a) A 500 nm by 500 nm STM topograph is superimposed with the ZBC map taken in the area for a $B_{\perp} = 60$ mT. The ZBC map shows a well ordered vortex lattice. (b) Zoom in on a single vortex marked in (a) by the red dashed box. (c) STS line profile taken across the single vortex in (b), direction is marked by the white arrow. (d)-(f) The coherence length (ξ_{GL}) of the SC Pb film is evaluated in three different ways. (d) The ZBC value from the STS line profile shown in (c) is fit to Eq. 4.4 to obtain ξ_{GL} . (e) A 2D Gaussian fit to the coarse STS grid in the 100 nm by 100 nm area of (b) gives ξ_{GL} in the horizontal and vertical directions. (f) Lines profiles extracted out of the coarse STS grid of (e) is simultaneously fit to Eq. 4.4.

as $H_{c2}(T) = \Phi_0/2\pi\xi_{GL}^2(T)$. Therefore an H_{c2} of 500 mT corresponds to a vortex size of 25.7 nm and that for 80 mT is 64 nm. This means it is possible to pack more vortices inside the same surface area for a thinner film as compared to a thicker or bulk material. Being able to accommodate more vortices implies that the superconductor can sustain higher magnetic fields or it has a higher H_{c2} value.

The expected vortex size or ξ_{GL} of 25.7 nm is also experimentally ascertained using the procedure explained in Refs. [128, 129]. For this purpose we look at our ZBC map at low field (~ 60 mT) [see Fig. 4.7(a)] where the intervortex distance is ~ 200 nm, so the vortices are isolated and do not interact, and pick out a single vortex in the region [Fig. 4.7(b)]. Figure 4.7(c) shows evolution of the normalized dI/dU spectra as one goes across the centre of the vortex along the white arrow marked in Fig. 4.7(b). The normalized ZBC profile taken out of the line STS is shown in Fig. 4.7(d). This profile is fitted using the formula [128, 129]:

$$\sigma(r, 0) = \sigma_0 + (1 - \sigma_0) \times (1 - \tanh[r/(\sqrt{2}\xi_{GL})]), \quad (4.4)$$

where σ_0 is the normalized ZBC away from a vortex centre, r is the distance to the vortex core center, and ξ_{GL} is the Ginzburg-Landau in-plane coherence length. The fit yields a value of 28.2 nm for ξ_{GL} , in agreement expected value of ~ 26 nm from our H_{c2} characterization of the film.

We explored other routes in terms of data acquisition which would give us the same information on ξ_{GL} in less time without compromising greatly on the accuracy. Thus the parameter ξ_{GL} was also evaluated by taking a poor resolution STS-Grid at zero-bias [Fig. 4.7(e)] in the same area as in Fig. 4.7(b) and fitted with a 2D-Gaussian, which gives an average ξ_{GL} of 23 nm. Also, linecuts [Fig. 4.7(f), red data points] out of the STS-Grid are taken and all data points are simultaneously fit to Eq. 4.4. The ξ_{GL} obtained as a result is identical to the value that was extracted out of the high resolution STS line profile across the vortex center. Henceforth in the chapter this quick evaluation of ξ_{GL} is used.

To summarize the results of this section, we have succeeded in growing 15 ± 1 ML of Pb film on the TlBiSe₂ surface. Our Pb film shows the expected signatures of QWS and it is superconducting with a gap of 1.2 meV, T_c of 6.2 K and H_{c2} of 500 mT. Using the two BCS relations of $2\Delta(0)/k_B T_c = 4.38$ and $\xi_0 = \hbar v_F/\pi\Delta(0)$ we can calculate the BCS coherence length ξ_0^{film} for thin films as $\xi_0^{\text{film}} T_c^{\text{film}} = \xi_0^{\text{bulk}} T_c^{\text{bulk}}$. ξ_0^{film} of our film is 96.4 nm and the observed coherence length ξ_{GL}^{film} is 28.2 nm. From this we deduce an electronic mean free path l in the film of 8.5 nm, indicating that our film is in the dirty limit ($l \ll \xi_0^{\text{film}}$). On comparison of the Δ and T_c of our film with Pb films of similar thickness on Si(111) in literature [124, 120], we conclude that there is room for improvement in terms of film quality. However, the present film was judged to be adequate for the next part of the experiment.

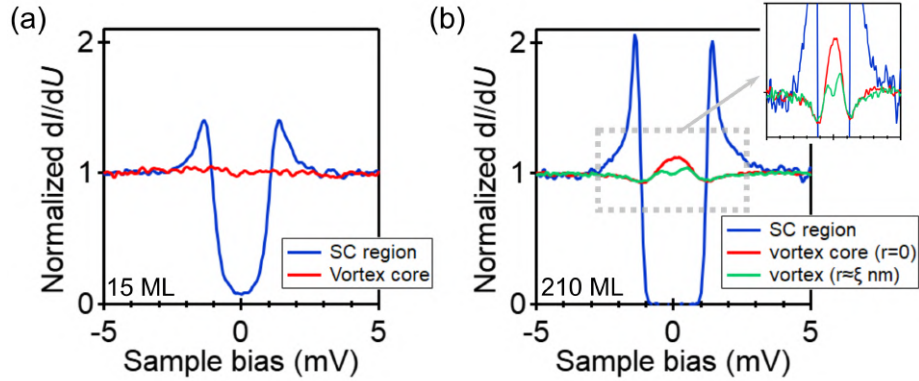


Figure 4.8: Spectroscopy inside vortex core for 15 and 210 ML Pb film on TlBiSe₂. (a) STS taken inside a vortex core (red curve) and outside a vortex (blue curve) for a 15 ML Pb film on TlBiSe₂. The red curve shows a flat density of states inside the vortex core. (b) The superconducting gap (blue curve) measured outside the vortex for the 210 ML film shows a gap size of 1.28 meV, very close to the expected value for bulk Pb. The red and green spectra are taken inside the vortex. The broad peak corresponds to multiple CdGM low-energy excitations. Our energy resolution does not permit us to resolve these states individually which have a typical energy level spacing of Δ^2/E_F .

4.5 Absence of Majorana modes in vortex cores

Our main goal for this experiment was to look inside the vortex core for bound states around E_F . A vortex core bound state shows up as a conductance peak inside the energy range given by the superconducting gap size. The energy of the bound state depends on whether the vortex is trivial or topological which is directly related to the nature of the band in which the superconducting gap opens. The spacing of the energy levels in the vortex is given as $\sim \mu \Delta^2 / E_F$ [130], where μ is the angular momentum quantum number of the particle in a box problem solved for the vortex which has cylindrical symmetry. For a trivial vortex, the bound states are known as Caroli–de Gennes–Matricon (CdGM) states [131] and μ takes half integer values whereas it becomes an integer number for a topological vortex⁹. For the latter, the bound state at zero energy corresponds to a MZM [132, 133].

For our system we calculate the spacing between the bound states originating from the Pb bulk bands and TSS as $10 \mu\text{eV}$ and $6 \mu\text{eV}$, respectively (assuming $\Delta=1.2$ meV, E_F (Pb) = 150 meV and E_F (TSS) = 250 meV). These states can be resolved individually only at the quantum limit (ql), i.e., the temperature at which the thermal smearing is narrower than the width of the energy level, calculated to be around 30 mK in this case ($T_{ql} = T_c \Delta / E_F$). Unfortunately, our energy resolution is only $200 \mu\text{eV}$ (see Appendix A.3) and hence we do not hope to resolve the individual bound states but instead a broad continuum of states

⁹A simple picture is that the level spacing is the same order for both vortex types and in the topological regime the zero-point motion is eaten up by the Berry curvature, just like for the zeroth Landau level of the TSS, discussed in section A.6.

which will give rise to a single broad ZBCP spanning over the SC energy gap width.

In Fig. 4.8(a) we show normalized spectroscopy curves taken inside (red trace) and outside (blue trace) a vortex core of the 15 ML Pb film at 60 mT. No peak features are observed inside the vortex cores for all vortices measured on this sample. A likely reason is that since our film is in the dirty limit, i.e., $l \ll \xi_{GL}$, quasiparticles living inside the vortex are scattered on a length scale smaller than the vortex size or ξ_{GL} . This will result in the mixing of the different quasiparticle energy levels causing the conductance peak to be smeared out or completely destroyed [134], a reasoning that holds true for all the trivial states inside the vortex.

On the other hand, MZMs, expected at the two ends of the vortex line, are non-local as quantum states and are topologically protected from scattering. Hence the origin for the absence of the Majorana mode on the top surface inside the vortex must be different. One possibility is a vortex phase transition from a topological to a trivial state, that occurs for a chemical potential higher than a critical value above the Dirac point of the TSS, as discussed in Ref. [44]. The idea is that the MZM at the two ends of the vortex do not interact with each other as long as there is an energy gap that separates the states from the two ends of the vortex line. Called as 'minigap', it is on the order of $\Delta/(k_F\xi)$ (where Δ is the SC gap, k_F is the Fermi wave vector and ξ is the SC coherence length). When this energy scale becomes much smaller than Δ the vortex line becomes gapless and allows the MZMs to travel along the line and annihilate each other. The transition from gapped to gapless happens as a function of the increasing chemical potential with the transition occurring at a critical value. Beyond this point the vortex line goes into a trivial phase with no MZMs in spite of the presence of the TSS. For the system at hand we find the minigap to be only 42 μeV , hence a phase transition is possible.

Another likely scenario is that the present heterostructure does not map to the requirements of the Fu-Kane model [12], particularly due to the absence of the bottom TI surface state. Instead, our system may be more similar to the one in Ref. [45], based on which we expect an odd number of MZMs inside the vortex cores and the partner modes are taken care of by an extended state running along the physical boundary of the system. In this case it is not possible for the MZMs to annihilate each other. However, due to presence of quasiparticles from the Pb bands, the MZM may no longer be localized at the surface but can move deeper into the bulk of the vortex and will avoid detection in our spectroscopy experiment [132].

To rule out the possibility that a ZBCP was not observed due to an instrumentation fault, we measured the trivial CdGM states in a thick Pb film. From Ref. [129] it is known that a Pb film of thickness below 60 ML falls in the dirty limit whereas a Pb film is in the clean limit 165 ML and above. Hence, we grew a 210 ML Pb film on the TlBiSe₂ surface [Fig. 4.8(b)]. A ZBCP (red trace) was observed for all vortices and the peak was found to split at length scales on the order of the coherence length, i.e., at the vortex edge.

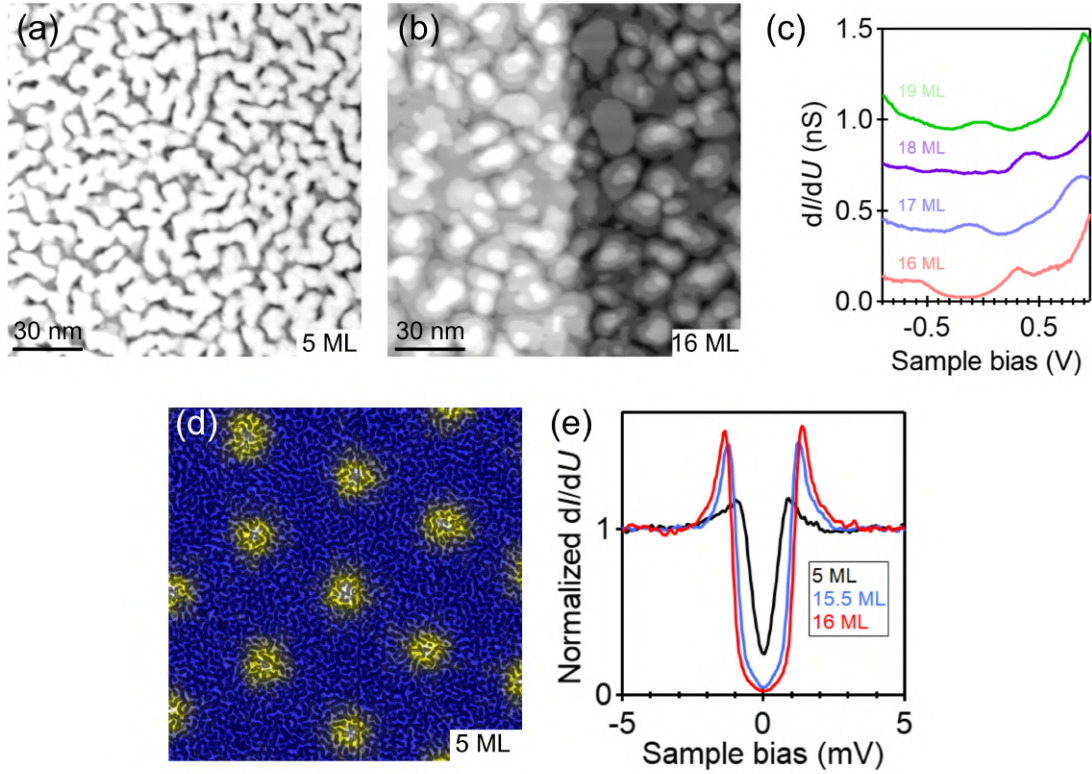


Figure 4.9: Electronic and SC properties of series of Pb film thickness. (a,b) Topograph showing a nominally grown 5 ML (a) and 16 ML (b) Pb film. (c) Large scale STS showing signatures of QWSs for nominally grown 16 to 19 ML. (d) Topograph for a 5 ML film is superimposed with a ZBC map taken with a $B_{\perp}=80$ mT in the same field of view showing a vortex lattice. (e) Evolution of the SC gap from 5 ML to 16 ML.

4.6 Additional experiments

ARPES experiments [43] observed the TPE in Pb-TI heterostructure over a range of Pb film thickness, from 11 to 22 ML. Our Pb film thickness of 15 ML falls within this range. However, it is possible that a critical Pb film thickness exists for observing the Majorana modes. In the following subsections we perform some additional experiments to address such concerns, such as, we grow a series of Pb films of different thickness and measure one sample with a superconducting tip.

4.6.1 Series of Pb thickness

We grew Pb films on TlBiSe₂ starting from a nominal value of 5 ML upto 19 ML (coverage 4.6 to 20.7 ML), with STM images for 5 and 16 ML shown in Fig. 4.9(a-b). While the growth on the former is worm-like, the latter shows a complete closed layer and irregular island-like growth for the next layers. In all cases the films grown are uniformly thick as

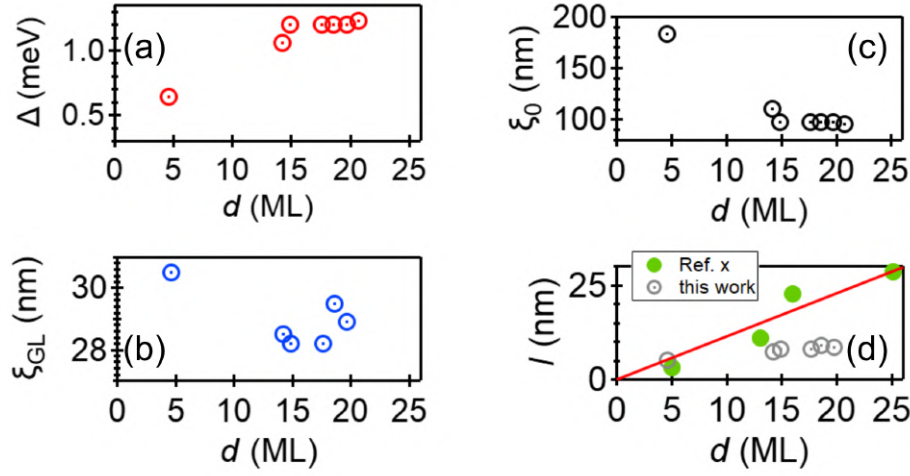


Figure 4.10: Pb film thickness dependence of Δ , ξ_0 , ξ_{GL} and l . (a-d) Variation of Δ (a), ξ_{GL} (b), ξ_0 (c), and l (d) with thickness of the Pb film. Values for l as obtained in Ref. [135], as function of film thickness, are shown as green dots in (d).

large steps directly reflect the step height of TlBiSe₂.

Electronically, all films show signature of QWSs Fig. 4.9(c), with the peak positions varying as a function of thickness of the film. Superconductivity was observed for the smallest film thickness of 5 ML. Figure 4.9(d) shows an ordered vortex lattice in the presence of an out-of-plane field. The superconducting gap further develops with increasing film thickness, as seen in Fig. 4.9(e).

We further evaluate the different films in terms of their superconductivity. In Fig. 4.10 we plot the measured SC gap values in panel (a) and ξ_{GL} in panel (b) as function of the film thickness. ξ_0 for the films can be calculated using the relation $\xi_0^{\text{film}} T_c^{\text{film}} = \xi_0^{\text{bulk}} T_c^{\text{bulk}}$ and $2\Delta(0)/k_B T_c = 4.38$. The measured ξ_{GL} is significantly lower than the calculated ξ_0 as a result of the reduced electronic mean free path (l). Calculated values of l for the films are shown in Fig. 4.10(d) (gray open circles). Upon comparing our values with those obtained by Nam *et al.* [135] for Pb films on Si (green dots in Fig. 4.10(d)) we obtained good agreement only for our 5 ML. For all film thickness above 5 ML our data points lie below their data points. While the red line indicates a linear dependence of l on the film thickness for data points from Ref. [135], our data points remain independent of the film thickness above 15 ML.

In summary, while our films have a SC gap size in accordance with their thickness, the mean free path in the films is significantly reduced and worse in comparison to Pb films on Si(111). This maybe correlated with the absence of Majorana modes in the vortex cores for all film thickness.

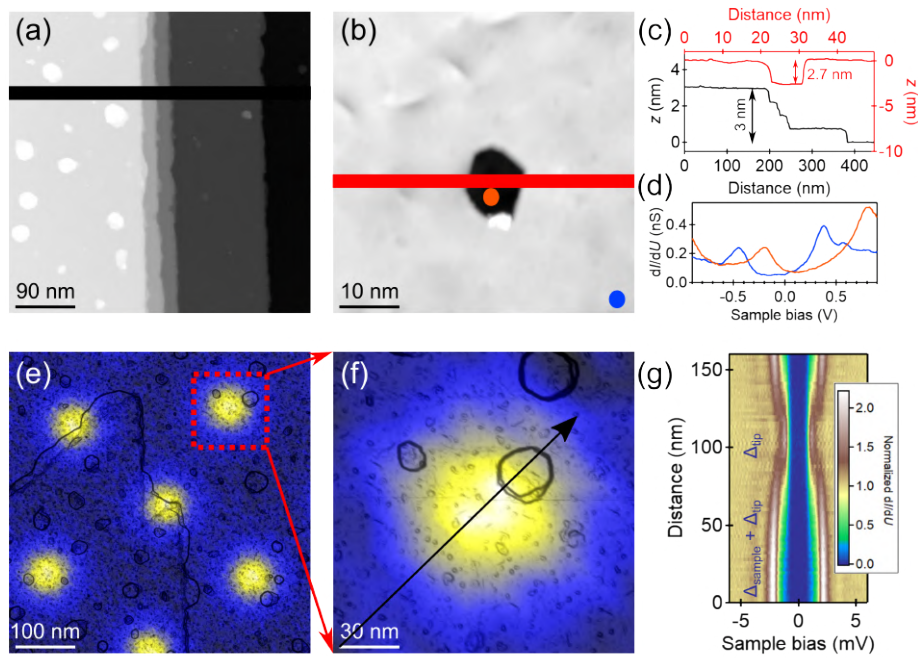


Figure 4.11: Room temperature annealing of 15 ML Pb film and characterization with a SC-tip. (a) STM image showing steps with heights that correspond to distances between TI layers. The TI steps are covered with the annealed Pb film. (b) A hole in the Pb film that likely goes down to 1-2 ML. This thickness of the Pb film measured from the layer exposed by the hole is 2.7 nm. (c) Line profile taken along the black line in (a) and red line in (b). A total step height of 3 nm corresponds to 4 TI-TI steps. A step height of 2.7 nm for the Pb film corresponds to ~9 ML. (d) Large scale STS spectra taken on the blue and orange spots marked in (b). The peaks in the STS correspond to the QWSs. (e) A 500 nm by 500 nm STM topograph is superimposed with a vortex map taken in the area for a $B_{\perp}=50$ mT. Estimated Pb film thickness is 10–11 ML. (f) Zoom in on a single vortex marked in (e) by the red dashed box. (g) STS line profile taken with a superconducting tip, across the single vortex in (f), direction is marked by the black arrow. $\Delta_{\text{sample+tip}}$ is estimated to be ≈ 1.97 meV ($\Delta_{\text{sample}}=0.94$ meV, $\Delta_{\text{tip}}=1.03$ meV).

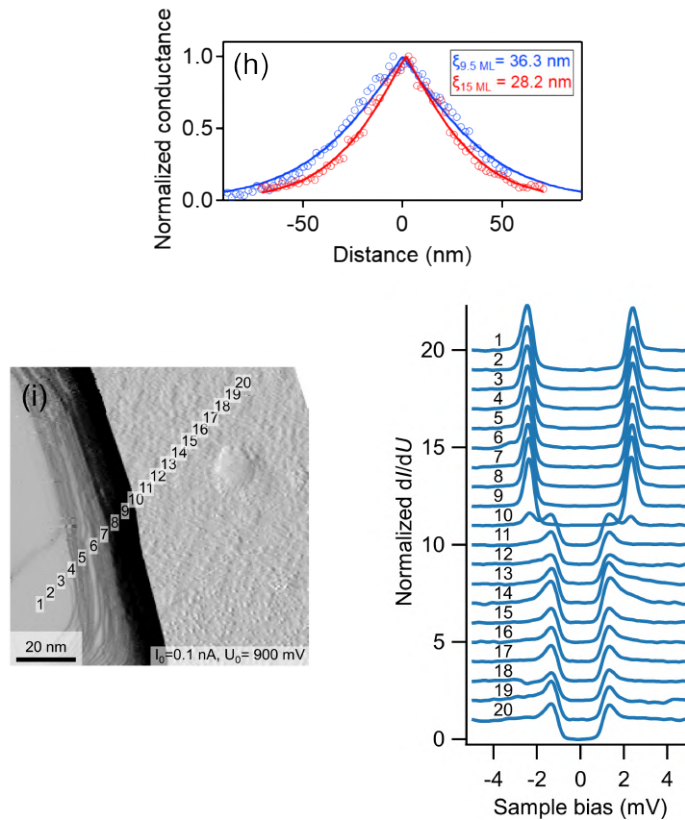


Figure 4.11: Room temperature annealing of 15 ML Pb film and characterization with a SC-tip. (h) Comparison of ξ_{GL} for annealed film of 9.5 ML and as-grown 15 ML from zero-bias conductance profiles across a vortex center. (i) Topograph showing the positions of 20 STS, starting from a 48 ML height Pb island and ending on the wetting layer on the TlBiSe₂ surface. We find an abrupt transition from the gap size of $\sim 2 \text{ meV}$ (a convolution of the Pb island SC gap and the tip SC gap) to a gap of $\sim 1 \text{ meV}$, which corresponds to the SC gap of the tip only.

4.6.2 Room temperature annealing and using a superconducting tip

We expect to reduce scattering at the surface or increase the mean free path of electrons in the Pb film by reducing the surface roughness. This is achieved by annealing the Pb film to RT. Figure 4.11(a,b) shows a uniform Pb film, obtained as a result of annealing, covering the steps of TlBiSe₂, with only a small number of scattered small Pb islands. Sometimes holes of diameter ~ 10 nm [Fig. 4.11(b)] are found in the film which go down to 1–2 ML of Pb film. They can be conveniently used to determine the thickness of the film. In the area shown in Fig. 4.11(a) we have determined the Pb film thickness to be 10–11 MLs [see line profiles in Fig. 4.11(c)]. Signatures of QWSs are also observed for the film [Fig. 4.11(d)].

The SC properties of this film were characterized using a SC STM tip¹⁰. The advantage of using a SC tip in our tunneling experiments is that it significantly improves the energy resolution, otherwise limited by the width of the Fermi function which defines the Fermi edge of a normal metal at finite temperatures. When measuring a superconducting sample with a normal metallic tip, i.e., probing a SC DOS with a Fermi broadened metallic DOS¹¹, the result is a smeared out SC energy gap from the convolution of the two. On the other hand when the tip is in the SC state, we probe the sample by using the sharp BCS-like DOS of the coherence peaks thereby enhancing the energy resolution. In case of tunneling across a SC-insulator-SC junction one observes coherence peaks which are now separated by $2(\Delta_{\text{sample}} + \Delta_{\text{tip}})$. Any feature inside the tip or sample gap at energy $(\pm \epsilon_{\text{sample/tip}})$ will now appear at a shifted position corresponding to $\pm(\epsilon_{\text{sample/tip}} + \Delta_{\text{tip/sample}})$ [136–138].

For an area of 500 nm by 500 nm we have done vortex-mapping using the SC-tip. Note that the vortex lattice is observed not at zero-bias but at the bias corresponding to the coherence peak of the tip-gap, i.e., 1.2 meV. The resulting vortex map is superimposed on the topograph [Fig. 4.11(e)]. STS line profile across a single vortex [black arrow in Fig. 4.11(f)] is shown in Fig. 4.11(g). Far away from the vortex we observe a large gap corresponding to $2(\Delta_{\text{sample}} + \Delta_{\text{tip}})$. This gap evolves with distance to the center of the vortex due to the change in the SC gap of the sample. At the center, the superconducting gap of the sample fully closes and only that of the tip remains, denoted as Δ_{tip} . We do not observe any additional DOS from the vortex core that are expected beyond the coherence peaks of the tip-gap.

Using the STS line profile across the vortex we evaluate ξ_{GL} of the annealed film. To do this, we extract the conductance profile at energy values of ± 1.2 meV, corresponding to the coherence peaks of the tip. This profile (normalized) is shown in Fig. 4.11(h). Fitting to Eq. 4.4 we obtain ξ_{GL} of 36.3 nm. This is an improvement over the 15 ML film (data shown as red open circles in Fig. 4.11(h) for comparison) which had a coherence length of 28.2 nm. A higher value of ξ_{GL} is a direct indication of larger electron mean free path in the film. Hence minor annealing of the Pb film to RT immediately after the deposition leads to reduced surface roughness, hence less scattering and thereby a larger superconducting coherence length.

¹⁰The tip was made superconducting by picking up Pb from the sample.

¹¹At our system temperature of 0.35 K the thermal broadening is given as $3.5k_{\text{B}}T \sim 100 \mu\text{eV}$.

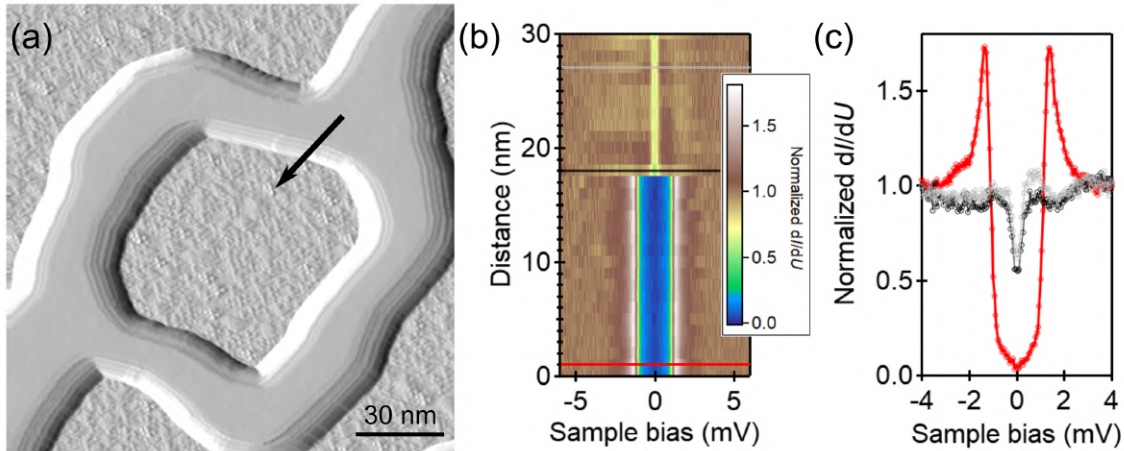


Figure 4.12: Superconducting gap on the wetting layer. (a) Differentiated topograph image showing a 5.7 nm high (20 ML) Pb island on top of the wetting layer on TlBiSe₂ surface. (b) STS line profile taken along the black arrow in (a). A homogeneous superconducting gap on the Pb island abruptly changes to a very shallow gap on the TlBiSe₂ surface. The change takes place over a length scale of ≈ 1 nm. (c) Linecuts out of the waterfall plot in (b) at positions marked by the red, black and grey lines.

Majorana modes are also expected to appear as edge states along the side surface of a 2D TSC [34]. With this in mind we took line spectroscopy starting from a 48 ML high Pb and going over to the surface wetting layer [Fig. 4.11(i)]. For STS number 10 in Fig. 4.11(i), corresponding to the edge of the island, an additional peak in the dI/dU appears outside the coherence peaks of the SC gap of the tip. The energy position of the additional peaks coincides with the coherence peak position of the SC gap of sample plus tip, hence these are likely due to the SC gap of the Pb island. Any contribution from an edge state should appear as additional peaks that are very close to the coherence peak positions of the SC gap of the tip, as upon deconvolution only such peaks can give a zero bias state.

4.6.3 Quality and role of the wetting layer

In this subsection we evaluate the quality of our wetting layer since the TPE is an interface driven effect. The smallest Pb film thickness (closest to the wetting layer) grown by us is 5 ML. This film showed a superconducting gap of 0.64 meV. The other route for indirectly accessing (not as-grown at low temperature) our wetting layer is by warming up the Pb film to room temperatures for an extended time period. The Pb accumulates to form high islands on top of the wetting layer. In Fig. 4.12 a 20 ML high island is imaged on top of the wetting layer on the TlBiSe₂ surface. The SC gap is measured along a line originating on the Pb island and going into the wetting layer [black arrow in Fig. 4.12(b)]. On the island a gap of 1.2 meV is observed [red trace in Fig. 4.12(c)], whereas on the wetting layer no SC

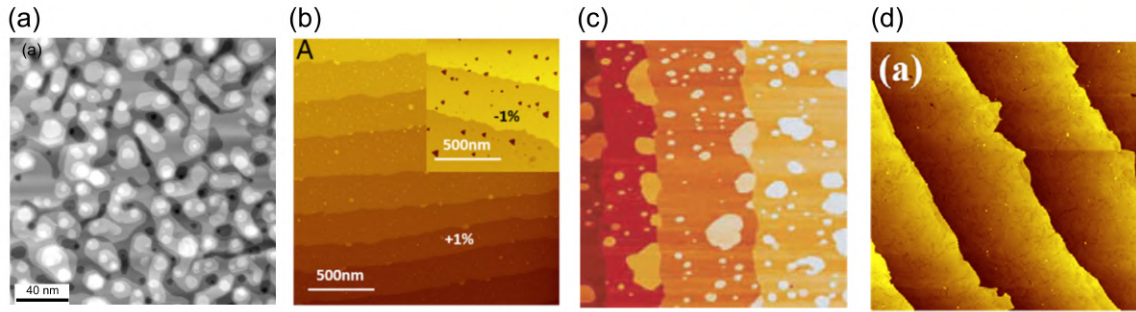


Figure 4.13: Comparison of morphology of Pb film with literature. (a) 15 ML Pb film grown by us on TlBiSe₂. (b) 5 ML Pb film grown on Si(111) from Ref. [135]. (c) 9 ML Pb film on Si(111) with two-atom layer mesas, from Ref. [120]. (d) 25 ML Pb film on Si(111), from Ref. [129].

gap or only a V-shaped gap is observed [gray trace in Fig. 4.12(c)]. A similar feature was observed on the disordered Pb wetting layer grown on Si in Ref. [139]. The poor proximity effect on the wetting layer is an indication of its disordered, diffusive nature and is likely detrimental for the TPE.

4.7 Discussion

ARPES results from Trang *et al.* [43] have claimed that the heterostructure of Pb(111) thin film grown on TlBiSe₂ to be a 2D TSC. However, in our STM experiments we do not observe any signatures of MZMs inside vortex cores and hence cannot support their claim. This means that it is either not a topological superconductor or that the MZMs could not be detected for reasons discussed previously, such as a vortex phase transitions or the states being not localized on the surface. Here, we consider some other possibilities which may have lead to the absence of the MZM, for example the sample quality.

Although we have deposited Pb on TlBiSe₂ following the recipe of Trang *et al.* [43], it is well known from Pb/Si growth that small changes in the growth parameters can have drastic influence on the resulting SC properties of the Pb film; prominent example being a SC crystalline wetting layer versus disordered non-crystalline non-SC Pb wetting layer [139–141]. While STM as an imaging technique provides the opportunity to judge the morphology of the film locally, the intensity of photoelectrons measured in an ARPES experiment is averaged over roughly $\approx 200 \mu\text{m}$ by $200 \mu\text{m}$ (given by the beam spotsize). If we consider a Pb film as shown in Fig. 4.13(a), STM as a local probe identifies 5 different layers in the image and the QWSs associated with each layer, while ARPES would obtain intensity for the QWSs averaged over 0.04 mm^2 . The QWSs coming from the Pb film thickness that has the largest surface area is expected to dominate the ARPES signal, with intensity from the other layers forming a diffuse background. Hence the ARPES QWSs data cannot be used to disprove that on the local scale multiple Pb layers exist.

Compared to Refs. [135, 120, 129] (see Fig. 4.13), our Pb film has the highest surface roughness. As discussed in Sec. 4.6.2, this is easily reduced by annealing the film to RT directly after growth. Since STM is most sensitive to the surface electrons, we propose that the extensive surface scattering resulting from the surface roughness may be responsible for washing out the features expected in spectroscopy measurements on these films. Additional preparation of a wetting layer (not done for both ARPES and STM experiments) can further help improve the film quality by reducing interface scattering, and is discussed in the outlook of the chapter.

While ARPES and STM are both surface sensitive techniques there are some subtle differences that can be illustrated using the topmost atomic layer of TlBiSe₂ as the object of investigation. We remind ourselves that this is a TI layer and it is damaged during cleaving [115]. The TI atoms left behind on the surface from the cleave form crystalline islands upon cooling down the sample. These islands are small and are likely to have topologically trivial bands. The topologically non-trivial surface state of TlBiSe₂ is forced down towards bulk and may even move to the next quintuple layer [142]. ARPES [115] measurement on the sample is able to observe the buried TSS and does not see any contribution from the trivial surface states that originate from the TI termination layer. On the other hand, the STM tunneling current will be almost exclusively dominated by contributions from the TI surface layer. For the buried TSS to show up in the LDOS measurement in STM there must be a finite overlap between the TSS and tip wavefunction which is very small in the present scenario.

While the above reasoning naturally explains the absence of any LLs originating from the TSS in the dI/dU spectrum taken on bare TlBiSe₂ surface, we offer a different explanation for the missing signatures of the TSS on the Pb film grown on TlBiSe₂. Here, we compare the radius of the cyclotron orbits of electrons in a perpendicular magnetic field (r_n) with the electron mean free path. The LLs are smeared out when r_n becomes larger than the electron mean free path. Since $r_n = \sqrt{n}\sqrt{\hbar}/eB$ (conventional system) and $\sqrt{2n+1}\sqrt{\hbar}/eB$ (Dirac system), where n is the LL index and B is the applied field, LLs are easier observed at high magnetic fields where the cyclotron orbit becomes smaller or more localized. For a magnetic field of 9 T (maximum value that can be applied in our system) $r_n = 8.6$ nm for the zeroth LL which is comparable to the electron mean free path of 8 nm in our 15 ML Pb film. We can only expect to observe this LL as higher ones will have a orbit larger than the electron mean free path. However, it may become possible to still observe LLs near the Fermi level (reasons discussed in Appendix A.6).

Improving the quality of our Pb films (taking the electron mean free path as an indicator) may lead to a positive outcome for our experiment. However, there are also some fundamental questions whose answer determine the probability of success of the experiment, such as: If a Majorana mode did exist in the vortex core, to what extent is the wavefunction protected against scattering and disorder? Is it possible to observe a Majorana zero mode in a vortex core of a *dirty* superconductor coupled to a TI? Experimentally, Ménard *et al.* [19, 45] have provided some answers. They show ZBCP in vortex core and at the domain boundary of a system that consists of a monolayer of Pb covering islands of Co-Si grown

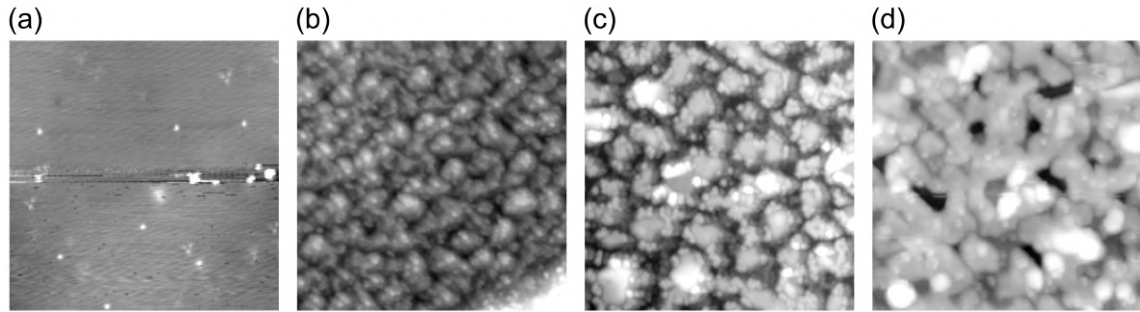


Figure 4.14: Deposition of Pb on Bi₂Se₃. (a) As-cleaved surface of Bi₂Se₃. (b) 1 ML of Pb deposited on the Bi₂Se₃ surface at low temperatures. (c) Sample from (b) is annealed at 130°C for 15 mins. (d) Further annealing at 200°C for 2 mins. All four images have a size of 50 nm by 50 nm.

on a Si(111) surface. Since a monolayer of Pb grown directly on the Si(111) surface is always in the dirty limit and does not show ZBCPs in vortex cores, they interpret their ZBCPs as Majorana modes. Their experiment also serves as a proof that the MZM is robust against disorder that exists in the dirty superconducting Pb monolayer.

4.8 Outlook

We believe that the experiment may have a positive outcome if there is a significant improvement in the quality of the Pb film (particularly the SC coherence length) grown on TlBiSe₂. To achieve this the purity of the Pb source must be ensured. Further, and more importantly, a high quality, crystalline, superconducting Pb wetting layer must be grown on the TlBiSe₂ surface. Recipes for preparing a Pb wetting layer on Si(111) surface exists in literature. It involves deposition of a ML of Pb on Si surface followed by annealing at elevated temperatures of 327 °C. Preliminary test done on the Bi₂Se₃ surface (Fig. 4.14) show that a similar recipe can be adapted for the case of TlBiSe₂. Finally, the surface roughness of the several monolayers thick Pb film should be reduced. As discussed before, short annealing of the Pb film directly after growth may help to achieve the desired results.

Discussion

In this thesis we have investigated members of the doped Bi_2Se_3 family and $\text{Pb}(111)$ thin film grown on TlBiSe_2 for signatures of topological superconductivity using low temperature STM and STS. We now present an overview of our results.

We start our discussion with the doped Bi_2Se_3 family where the phase diagram for the superconducting order parameters shows that in the presence of hexagonal warping of the Fermi surface and large chemical potential (μ) the $\hat{\Delta}_4$ order parameter forms the ground state of the system, among others that are determined by crystal symmetry. For this order parameter the interorbital electron interaction (V) dominates over the intraorbital (U) one, it is of odd-parity and therefore considered as topological. Further, it is a two-component order parameter given by the linear superposition of two (degenerate) basis functions, conventionally called Δ_{4x} and Δ_{4y} . Both of them have a twofold symmetry in the gap structure for a circular Fermi surface in the $k_x k_y$ plane, with a pair of point nodes along the $\pm k_y$ direction (corresponds to a crystallographic mirror plane in real space) for Δ_{4x} and a pair of gap minima along the $\pm k_x$ direction (corresponds to Se-Se direction in real space) for Δ_{4y} . If the system selects one of these superconducting (SC) states it will violate the threefold rotational symmetry of the Bi_2Se_3 crystal and will be referred to as a gap nematic state.

Experimentally there is overwhelming evidence from bulk probes that the above order parameter does get stabilized in optimally doped samples. This is based on the observation of a twofold symmetry in the SC gap amplitude when measuring a superconducting property as a function of the in-plane magnetic field direction. In each case the gap node/minima was found to align with a Bi_2Se_3 -mirror plane or a Se-Se direction which points to the realization of either the Δ_{4x} or Δ_{4y} pairing state, respectively. Initially it was believed that since the threefold symmetry of the Bi_2Se_3 lattice allows for three equivalent rotational domains, superposition of the contribution from different domains could lead to an apparent pairing symmetry that differed from the true symmetry but recent Knight-shift measurements [68] have ruled out the possibility of multi-domains. This means that selection of the particular nematic order, i.e., the Δ_{4x} or Δ_{4y} , must be dictated by a parameter that is specific to the local environment in the sample and that breaks the threefold lattice symmetry, such as an in-plane lattice distortion or strain from dopant intercalation, which can indeed vary from sample to sample.

The above situation is simplified when considering the member CPSBS. Here, due to the reduced crystal symmetry (due to the presence of the additional PbSe layers) the order parameter is non-degenerate and bulk measurements (specific-heat and thermal-conductivity) have found that the Δ_{4x} state is realized with the gap nodes lying along the unique crystallographic mirror plane.

To provide additional evidence for non-trivial superconductivity in this class of materials we have attempted to directly visualize the order parameter on the surface using STM and STS. It is important to note that irrespective of the superconducting shielding fraction of the sample, close to 90% of the surface area accessible in the STM experiment is nonsuperconducting and at times no superconductivity is observed on the surface. We will address this point later, but first we discuss our observations from the limited superconducting surface areas.

Point spectra taken on the surface of $\text{Cu}_x\text{Bi}_2\text{Se}_3$ suggest a twofold anisotropy in the gap structure, anisotropy ratio being $\sim 46\%$. The spectra reflect the integrated local density of states around the Fermi surface and by measuring a hard gap at Fermi energy we conclude that the gap structure cannot have point nodes but it is rather a minima. The position of the gap minima with respect to the lattice is obtained by measuring the average superconducting gap as a function of the orientation of the in-plane magnetic field. Due to the Volovik effect the in-plane field leads to the generation of maximum amount of quasiparticles (thereby broadening the gap edges and filling the gap bottom) when it is orientated perpendicular to the direction of a gap node/minima. Following this logic, we find the gap minima to lie on a mirror plane of the crystal and a 10% anisotropy between the directions of gap minima and maxima. Since no vortices were observed on the area we conclude that the out-plane component of the magnetic field is sufficiently small and cannot cause the anisotropy. Note that the anisotropy deduced from the in-plane field measurement is weaker than that reflected from the fit of the point spectra, but, a theory that quantitatively links the two could not be found in literature.

Additional signatures of an anisotropic gap is found on the surface of CPSBS. Here, we observe elongated vortices for an out-of-plane magnetic field where we find an anisotropy of $\sim 42\%$ between the coherence length along the long and short axis of the vortex. The vortex anisotropy for an out-of-plane field does not change significantly by applying an intentional in-plane component and hence cannot be a mere consequence of field-misalignment. The shape of the vortex is a direct consequence of the shape of the superconducting gap around the Fermi surface, with the vortex elongating in the direction of a gap node/minima. This enables us to determine the position of the gap minima with respect to the lattice. We find that the gap node/minima is rotated by 60° from the unique mirror plane and hence differs from the bulk measurements. Further, upon inspecting the point spectra in the area we find a much larger gap anisotropy of $\sim 70\%$.

Anisotropy in the measured superconducting gap or vortex shape can be simply a consequence of an anisotropy in the Fermi surface itself. Here, we exclude this possibility based on ARPES data which show no signs of a twofold distortion of the Fermi surface. We are able to corroborate this notion on the basis of our QPI data acquired on the surface of Bi_2Se_3 , $\text{Sr}_x\text{Bi}_2\text{Se}_3$, PSBS, NSC and SC region of CPSBS. Moreover, any anisotropy of the Fermi surface is insufficient to explain the rotation of the gap minima as observed in the case of CPSBS. Therefore, the observed anisotropy must be a reflection of the anisotropy in the superconducting gap structure itself.

Our data on $\text{Cu}_x\text{Bi}_2\text{Se}_3$ suggest a Δ_{4x} SC state since the gap minima lies on a mirror

plane. Contrary to expectations, the mirror plane does not protect the expected gap nodes in this case and they are found to be lifted. Interestingly, the same observation has been made by Tao *et al.* [32] as well. They also note a small rotation of the gap minima away from the mirror plane at high magnetic fields. Surprisingly, we have made the observation of rotation of the gap minima on the surface of CPSBS. In CPSBS, since the gap minima is rotated away from the monoclinic mirror plane and we can expect the nodes to be lifted. However, note that the gap minima is rotated away from the monoclinic mirror plane of PSBS to a mirror plane of the Bi_2Se_3 lattice.

We understood most of the above observations with help from our theory collaborator. Symmetry-based theoretical analysis was employed which showed that on the surface the effective symmetry (crystal symmetry plus additional broken or restored symmetry) must be considered to explain aspects of the order parameter. In particular, at the surface the broken inversion symmetry allows for new terms in the normal state Hamiltonian which leads to mixing or superposition of different order parameters with the same symmetry classification. This leads to the lifting of the otherwise symmetry protected gap nodes at the surface (a SC system will always try to lift nodes in gap in order to gain condensation energy unless there is symmetry protection). Rotation of the lifted gap nodes on the surface, as found in the case of CPSBS, is only possible when order parameters of different symmetry are allowed to mix. Hence our work highlights that the superconducting order parameter on the surface of these materials is different from the bulk and it demonstrates the crucial role of symmetry for realizing a given SC state. Future theoretical work must still clarify how the bulk and the surface order parameter can connect if they are different.

From the phase diagram for the superconducting order parameters of the doped Bi_2Se_3 materials we find that the nematic $\hat{\Delta}_4$ order parameter is realized for large carrier concentrations in the material. In $\text{Cu}_x\text{Bi}_2\text{Se}_3$, ARPES and quantum oscillation experiments have shown that for carrier concentrations of $\sim 10^{20} \text{ cm}^{-3}$ the normal state Fermi surface becomes a quasi-2D cylinder from a 3D ellipsoid which suggests the possibility of a quasi-2D TSC. However, clear experimental evidence for quasi-2D topological superconductivity are lacking. One way of proving quasi-2D topological superconductivity is by showing that MF surface states do not appear on the (001) plane of the crystal but only along the corresponding side surface. Only out of sheer luck we accessed such a side surface in our STM experiment on $\text{Cu}_x\text{Bi}_2\text{Se}_3$. And indeed we only observed an in-gap state on the side surface of $\text{Cu}_x\text{Bi}_2\text{Se}_3$ which serves as a possible signature of dispersive MFs. Such in-gap states were not found on the top surface.

Our observations supporting quasi-2D topological superconductivity in the material helps to reconcile the previous STM experiment [29] that measured an *s*-wave like gap on the top surface [(001) plane] without any in-gap states and the point-contact spectroscopy experiment (it averages over different surface terminations) which showed a pronounced zero-bias peak inside the gap [26]. However, this scenario is incompatible with the more recent STM experiment by Tao *et al.* [32] who observe ZBCPs inside vortex cores on the top surface of $\text{Cu}_x\text{Bi}_2\text{Se}_3$ and attribute them to MZMs. These ZBCPs could be due to trivial vortex bound states or a more complicated reason may apply along the lines of the

proposal by Hosur *et al.* [44].

On the other hand for CPSBS a 3D topological superconductivity is not possible- the 2D nature of the bulk electronic states gives rise to a cylindrical Fermi surface which can only support a quasi-2D TSC. Although it obvious that one must measure the side surfaces of these materials in order to establish quasi-2D TSC but due to the vdW gap in the (001) plane, cleaving any plane other than the (001) is non-trivial and hence not easily accessible in an STM experiment.

We now transition to a discussion on the entity that induces superconductivity in Bi_2Se_3 : the dopant. In the theoretical framework for superconductivity in doped Bi_2Se_3 by Fu *et al.* [7] the dopant is expected to increase the carrier concentration in Bi_2Se_3 and thereby lead to a rise in the chemical potential. However, the fact that doping Bi_2Se_3 thin films under UHV conditions [143–145] does not result in superconducting films suggests that donating electrons to the parent Bi_2Se_3 cannot be the only contribution of the dopant. Another evidence is that the increase in charge-carrier concentration in $\text{Cu}_x\text{Bi}_2\text{Se}_3$, as determined from Hall measurements [47], is only $\sim 10\%$ of the expected amount of carriers from the nominal doping value of $x=0.3$ ($2.1 \times 10^{21} \text{ cm}^{-3}$, assuming single electron donation from each Cu atom). Since the key ingredient for getting bulk superconducting samples is the act of heating followed by rapid quenching of the doped sample, position and amount of the dopant in the unit cell are important too. The dopant may influence the phonon mode responsible for electron pairing either due to its position or because of its population. The latter can be thought of as a disorder effect.

To understand the influence of the dopant on the superconducting state, it is intuitive to perform a controlled experiment. Our strategy was to turn to members of the doped Bi_2Se_3 family which had smaller dopant concentration per unit cell, in particular $\text{Sr}_x\text{Bi}_2\text{Se}_3$ ($x=0.06$). Doping Bi_2Se_3 with Sr requires 5 times less amount of dopants as compared to doping with Cu. Moreover, these samples can have a superconducting shielding fraction close to a 100%. Although in terms of the crystal quality they may not be the best. They are known to have a block structure [71], i.e., the sample consists of blocks (crystallites) with the same in-plane (001) alignment but a small misalignment in the axis perpendicular to the plane, due to the melt-growth technique. In Ref. [71] the size of the blocks was estimated to lie between 0.05 - 0.5 mm. To characterize our crystals, we performed normal incidence x-ray standing wave (NIXSW) and photoelectron spectroscopy (PES) in an collaboration project [146]. Since a meaningful NIXSW experiment relies on a sharp x-ray reflection profile, which can be obtained for only good crystalline order in the vertical direction, it means that the block size in our crystals is atleast on the order of 0.1 mm^2 , based on the x-ray spot size. The x-ray reflection profile obtained on $\text{Sr}_x\text{Bi}_2\text{Se}_3$ crystal and undoped Bi_2Se_3 were very similar which further indicted that the doped crystal was of good quality. The NIXSW experiment on $\text{Sr}_x\text{Bi}_2\text{Se}_3$ found that dopant atoms were located close to the outermost Se layers of a QL - they occupy Se lattice sites in these layers, relaxed towards the center of the QL. This study ruled out significant amount of dopant amounts in the vdW gap. Any disordered arrangement of dopant atoms in the vdW gap is also not possible

since this would affect the reflection profile. The position of the dopant identified from this study is not the energetically most favorable site but rather a metastable one. This agrees well with the need for quenching the crystals in last step of growth which cause the dopants to get trapped in such a metastable adsorption site.

The same sample that was characterized with NIXSW together with other $\text{Sr}_x\text{Bi}_2\text{Se}_3$ samples when measured in STM lead to very inconclusive results regarding the dopant. We could not identify any unique defect on the surface of $\text{Sr}_x\text{Bi}_2\text{Se}_3$ in comparison to pristine Bi_2Se_3 that would point to the dopant. Note that the STM measurements did resolve all native defects in doped and undoped samples by comparing their appearance in high-resolution images with literature. Some defects in our crystals could not be assigned by this comparison but since they were seen in both doped as well as undoped samples they cannot not be associated with the Sr dopant. Moreover, in a well-ordered crystalline area on $\text{Sr}_x\text{Bi}_2\text{Se}_3$ even the total density of all defects ($2.6 \times 10^{19} \text{ cm}^{-3}$) did not add up to the amount expected from the nominal doping value ($4.2 \times 10^{20} \text{ cm}^{-3}$). Hence our STM data is in disagreement with our NIXSW data on the point of the dopant homogeneity in these samples. One can argue that the limited area ($0.037 \mu\text{m}^2$) probed in the STM experiment is not representative of the entire sample. However, this is unlikely since our conclusion holds for different samples scanned under different tips conditions. Also there is literature ([147]) on how dopants that exist in different sites in the QL of archetypal TIs like Bi_2Se_3 , Sb_2Te_3 show up in an STM image based on how the defect disturbs the LDOS around the surface atom. Hence it is surprising that we did not find any fingerprint of the dopant. Its absence maybe explained by assuming that the dopant does not in anyway influence the electronic structure on the surface. This argument is supported by the fact that the amount of charge (change in chemical potential) donated by the dopants is too small for the amount of dopants, which immediately implies that the majority of dopants does not interact strongly electronically.

With regards to observing superconductivity on the surface of $\text{Sr}_x\text{Bi}_2\text{Se}_3$ using STM we obtained unexpected results. While our $\text{Sr}_x\text{Bi}_2\text{Se}_3$ crystals showed robust bulk superconductivity, we could not observe a SC gap anywhere on the surface of these crystals. However a SC gap was observed when a flake from the sample was transferred to the tip. These flakes also showed a SC gap when transferred back to the sample. To understand these observations we proposed that SC does not extend to the surface as long as the TSS was intact (evidence for the presence of the TSS is provided in our Landau level spectroscopy data). Electrons in the TSS are screened out by bulk carriers over a length scale of $\sim 1 \text{ nm}$ which means that at the surface there exists a strong electric field (estimated to be of the order of 10^8 V/m) that can work against superconductivity. However, in the flakes the TSS is likely destroyed due to strain that the flake experiences during the mechanical transfer, which allows superconductivity to then extend to the surface¹².

¹²It is still possible that a different reason can explain our observations on $\text{Sr}_x\text{Bi}_2\text{Se}_3$. The fact that superconductivity is always observed when a flake is on the tip can mean that one needs a semiconducting tip to measure these samples and not a metallic one. The reason may be that very strong electric fields exist between the metallic tip and semiconducting sample due to the difference in their work function.

A natural and important question is whether the above hypothesis is applicable on the surface of $\text{Cu}_x\text{Bi}_2\text{Se}_3$ and CPSBS. For a superconducting region on surface of $\text{Cu}_x\text{Bi}_2\text{Se}_3$, no evidence for the TSS is found in our STM studies as well as those by Tao *et al.* [32]. In these areas there is evidence for strain in the samples in the form of structural defects which can locally destroy the surface state and thereby no local electric field should exist in these areas. On the other hand, for CPSBS, it is not immediately clear if there should be any charge density distribution between the surface and bulk (hence band bending and a local electric field) since the bulk carrier density is two orders of magnitude larger than in $\text{Sr}_x\text{Bi}_2\text{Se}_3$, $\sim 10^{21} \text{ cm}^{-3}$ [57]. Note that this is still an order of magnitude lower than standard metals. However, there must be a reason why majority of the surface is always nonsuperconducting. In search of an answer, if we compare superconducting and nonsuperconducting regions on CPSBS, the statement that can be made is that no areas that showed the structural 1D stripe pattern, turned out to be superconducting. The 1D stripe is a fingerprint of the presence of the PbSe layers in the PSBS unit cell. Hence the absence of the stripe in a SC area suggests that there must be dopant atoms present between the PbSe layer and the Bi_2Se_3 QL which decouple the two. Additionally, they can be present inside the Bi_2Se_3 QL as well as on the surface. Taking this as a clue, we speculate that the presence of the dopant atoms in the SC regions (in the right position and amount) favorably suppresses the surface electric field in the area and allows for superconductivity to be observed on the surface¹³.

Moreover, from *ab initio* simulations for the PSBS unit cell¹⁴ we have learnt that an electric field of magnitude $8 \times 10^7 \text{ V/m}$ does exist on the surface layer of PSBS and decays with some oscillations into the inner layers. Hence for future work the above idea can be quantitatively explored together with routes to reverse its effect.

For all the doped Bi_2Se_3 samples, we have been unable to trace any variation in chemical potential as a function of the dopant atom concentration. In principle one can answer such a question by analyzing large scale spectroscopy data. However, we have not been able address these aspects since interpretation of spectroscopy data became difficult due to the insufficient data quality and quantity. In all these crystals one has to search for areas which are superconducting. This is a tedious process in STM since a single scan frame has an access of only $\sim 2.25 \mu\text{m}^2$ and one must move the sample with respect to the tip with the help of the coarse piezo from one area to the next (even by doing so one has access to only $\sim 0.28 \text{ mm}^2$ of the sample). During this process the tip often becomes contaminated due to

One gets rid of this potential difference by having material of the same work function on either side of the tunnel junction. More trivial reasons could involve the act of cleaving the crystal. Our cleaving procedure may be too harsh such that it leads to the loss of the dopants near the surface or surface relaxation in the top QL [148], factors that can be detrimental for SC on the surface.

¹³Additionally we point out that the hypothesis of the surface electric field being detrimental for surface superconductivity does not contradict the experimental observations of proximity effect-SC that exists on the surface of TI thin films grown on top of *s*-wave SCs[13]. The TI films are very thin, on the order of a few QL layers, and hence the electric field due the top SS can cancel with the electric field from the bottom SS [149], and hence allow for SC to extend to the surface despite the presence of the TSS.

¹⁴private communication with G. Bihlmayer

interaction with the sample and is unsuitable for acquiring meaningful data.

The above problem, i.e., not being able to acquire reliable data due to STM-tip contamination, maybe solved by using a dual-mode STM-AFM system at low temperatures to measure these samples. Ref. [150] presents one such technologically advanced system. The AFM can be used to acquire topographic images over large areas of the sample surface and the STM tip can be used sparingly- only when the area is reasonable for scanning with an STM tip or there are indications that it is superconducting.

In parallel to our experiments on doped Bi_2Se_3 , we also briefly explored other routes towards topological superconductivity. In particular via the topological proximity effect where the TI TlBiSe_2 was interfaced with a superconducting $\text{Pb}(111)$ thin film. A 2D TSC is expected to be realized upon migration of the TSS from the TI into the Pb film followed by proximitization of the TSS. As a consequence MZMs should appear inside vortex cores. However, we did not find any states inside the vortex cores of the heterostructure. The possible reason for the absence of MZM on the top surface could be strong interface scattering or the hybridization with the MZM on the other end of the vortex tube due to a vortex phase transition. It is also possible that the MZMs were not detected in STS since they are no longer localized on the surface but live deeper inside the vortex line due to the presence other quasiparticles that originate from the Pb bands.

Appendices

A.1 Scanning tunneling microscopy

¹⁵The principle of the scanning tunneling microscope (STM) is the quantum mechanical tunnel effect where an electron has a non-vanishing probability to cross a potential barrier that, according to classical mechanics, the electron has insufficient energy to enter/pass. Consequently, a *tunneling current* can flow between two metal electrodes that are separated by an insulating material, e.g., vacuum. In a STM setup a metallic tip is brought within a distance of $\leq 10 \text{ \AA}$ (d) from a metallic¹⁶ sample and a bias-voltage (eU) is applied between the tip and sample. This is schematically displayed in Fig. A.1.1(a). The work function (ϕ), i.e., the energy needed to extract an electron from the surface, of both sample and tip is assumed to be the same in this case. In general, the average of the work function of the tip and sample determines the height of the energy barrier faced by the electrons on either side. In equilibrium the Fermi energies of the sample and tip are aligned such that no elastic tunneling can take place. However, applying a negative bias-voltage ($-eU$) shifts the Fermi energy of the sample with respect to the tip, aligning (some) occupied states of the sample with unoccupied states of the tip and thereby allowing for a net tunneling current to flow from the sample to the tip. In a working STM circuit [Fig. A.1.1(b)], the tip can be further moved to different lateral positions on the sample (x, y) with the help of piezo-elements. At each position the distance (d) between the tip and sample is adjusted, again with the piezo, so that a preset constant tunneling current flows. If the sample density of states does not change as a function of x, y , then any change in d , for example due to a step edge, is a reflection of the topography of the sample, i.e., $d(x,y)$ results in a topograph image in the first approximation¹⁷. A small change in d results in an exponential change in the tunneling current which endows low temperature stable STMs with an enormous vertical resolution of 1 pm or better.

The exponential dependence of the tunneling current on the tip sample distance can be arrived at from the solution to the one-dimensional problem of an electron incident at a rectangular potential barrier [152]. By solving the Schrödinger equation for regions outside and inside the barrier one calculates the transmission coefficient T (the ratio between the incoming and transmitted electron wave), which is proportional to the tunneling current I , to be equal to $e^{-2\kappa d}$, where κ is the decay constant. However, this simple result is often

¹⁵This section is written based on Refs. [152, 151, 153].

¹⁶Can also be a semiconductor or materials with conductivity lower than conventional metals, e.g., the samples measured in this thesis.

¹⁷One can have constant DOS and difference in work function (e.g. metal grown on metal) that will give a change in tunneling current that is not of topographic origin

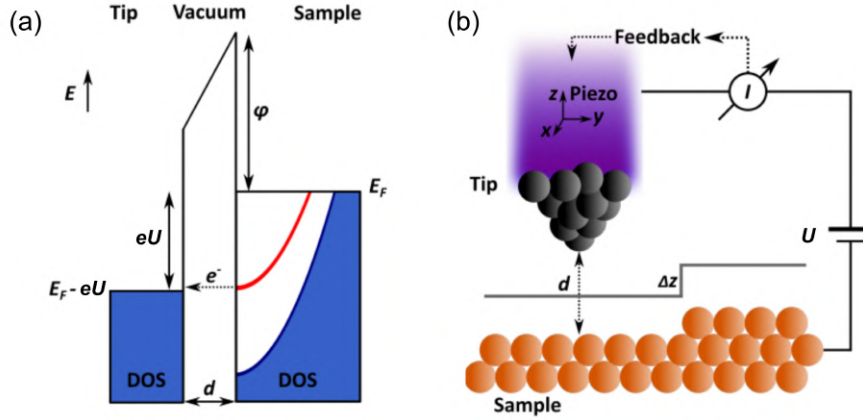


Figure A.1.1: Scanning tunneling microscopy. (a) Schematic representation of electron tunneling from the sample state (red) to tip states under a negative bias voltage. (b) Schematic representation of the constant-current mode operation of an STM. Image taken from Ref. [151].

unable to capture subtleties of an STM image. Importantly, any influence of the STM tip or details of the tunnel barrier has been neglected in this simple model. To obtain a better understanding of STM experiments one resorts to Bardeen's model [154] which can describe the tunneling current in three dimensions. This model was later extended by Tersoff, Hamann [155] and Chen [156] for easy application to most STM experiments and is still used today.

Using time dependent perturbation theory Bardeen's formalism calculates the probability of an electron in state ψ_μ of the sample (S) to populate states of the tip (T) ψ_μ and vice-versa, which directly relates to the tunneling current from sample to tip and tip to sample. By applying a bias voltage we can shift the Fermi energies of the tip (E_F^T) and sample (E_F^S) with respect to each other and thereby allowing for a net tunneling current to flow. The expression obtained for tunneling current given below is arrived at after assuming that the electrons do not interact with each other during the tunneling process nor do they lose energy, i.e., only elastic tunneling can take place.

$$I = I_{T \rightarrow S} - I_{S \rightarrow T} \quad (\text{A.5})$$

$$I = \frac{4\pi e}{\hbar} \sum_{\mu\nu} [f(E_\mu^S - E_F^S) - f(E_\nu^T - E_F^T)] |M_{\mu\nu}|^2 \delta(E_\nu^T - E_\mu^S - eU) \quad (\text{A.6})$$

where f denotes the Fermi-Dirac distribution and the delta function ensures elastic tunneling. $M_{\mu\nu}$ is the tunnel matrix element which describes the coupling between tip and sample states, i.e., the tunneling probability of electrons is determined by the overlap of the sample and tip wavefunctions. All elements of this matrix need to be calculated following the expression:

$$M_{\mu\nu} = -\frac{\hbar^2}{2m} \int \left(\psi_\mu^* \nabla \psi_\nu - \psi_\nu \nabla \psi_\mu^* \right) \cdot d\mathbf{S} \quad (\text{A.7})$$

Theoretically, this is the essence of Bardeen's approach. He showed that one can calculate the tunnel matrix elements by simply performing the above integral over an arbitrary separation surface \mathbf{S} within the vacuum barrier, implying that the system on one side of the barrier does not change the other significantly.

Nevertheless the above task is still demanding. Hence to simplify the problem at hand Tersoff and Hamann assumed a spherically symmetric s wavefunction to describe the tip apex: since the tunneling current shows an exponential dependence on the distance from the sample it should be reasonable to assume that it is dominated by contribution from the outermost atom of the tip and the simplest atomic orbital is the s -wave. The ansatz for the sample (Bloch wave) and tip (s -wave) wavefunctions used are:

$$\psi_S \propto \sum_G e^{-\sqrt{\kappa^2 + |\mathbf{k}_\parallel + \mathbf{G}_\parallel|^2} d} e^{i(\mathbf{k}_\parallel + \mathbf{G}_\parallel) \cdot \mathbf{x}}, \quad (\text{A.8})$$

$$\psi_T \propto \frac{\kappa R}{\kappa |\mathbf{r} - \mathbf{r}_0|} e^{-\kappa |\mathbf{r} - \mathbf{r}_0|} \quad (\text{A.9})$$

where $\kappa^2 = 2m\phi/\hbar^2$, \mathbf{k}_\parallel is the parallel component of the three dimensional Bloch vector, \mathbf{G}_\parallel is the reciprocal lattice vector, d is the distance perpendicular to the surface, \mathbf{x} is a vector parallel to the surface and $|\mathbf{r} - \mathbf{r}_0|$ is the radial distance from the center \mathbf{r}_0 of the outermost tip atom, R being the radius.

Using these wavefunctions the tunnel matrix element can be calculated. The expression for tunneling current, given below, depends on ρ_S and ρ_T which are the energy dependent local density of states (LDOS) for the sample and tip, respectively.

$$I \propto \int_{E_F}^{E_F + eU} \rho_T(E - eU) \rho_S(E, \mathbf{r}_0) |M(E, U, d)|^2 dE \quad (\text{A.10})$$

An appropriate choice of tunnel matrix element $M(E, U, z)$ was found in the one-dimensional, semiclassical Wentzel-Kramers-Brillouin (WKB) approximation [157] (another model for the tunneling current between two electrodes separated by a barrier), expressed as:

$$|M(E, U, d)|^2 \cong \exp\left(-2d \sqrt{\frac{2m}{\hbar^2} \left(\phi + \frac{eU}{2} - (E - E_\parallel)\right)}\right). \quad (\text{A.11})$$

Note that Eqs. A.10 and A.11 show that the tunneling current depends exponentially on the applied bias voltage (U) and the energy of electrons parallel to the surface (E_\parallel). The former implies that at positive bias voltages one mostly probes the occupied states of the

sample at energy eU , tunneling into lower lying states is exponentially suppressed. On the other hand for negative bias voltages, the exponential decay of the tunneling current means that majority of the current is contributed by states corresponding to the Fermi energy of the sample irrespective of the bias. For the E_{\parallel} dependence of tunneling current, since $E_{\parallel} = \hbar^2 k_{\parallel}^2 / 2m$, this implies that the states at $k_{\parallel}=0$, i.e., at $\bar{\Gamma}$ point of the surface Brillouin zone, have the largest contribution to the tunneling current while states away from the $\bar{\Gamma}$ point are exponentially damped. This k_{\parallel} -dependence of the tunneling current is also obtained in the extension of the Tersoff-Harmann model for arbitrary tip-orbitals [156].

We also highlight the fact that the tunneling current is expected to have a dominant contribution from surface states, in comparison to any bulk state, since the STM probes the electronic states near the surface whose wavefunction overlaps with the tip-apex-wavefunction. While the Bloch states from the bulk still exist near the surface and decay exponentially into vacuum, the wavefunction of the surface state rises exponentially as one approaches the surface: they are confined to the surface and decay exponentially both into the bulk and vacuum, as depicted in Fig. A.1.2(b). It is intuitively clear that the surface state wavefunction will have a larger overlap with the tip wavefunction in comparison to the delocalized bulk state, resulting in a larger weight to the tunneling current. This becomes relevant for the surface state of topological insulators such as Bi_2Se_3 which exists within the bulk band gap. The tunneling current from the TSS is expected to dominate (theoretically) even at energies away from the Dirac point where it is degenerate with the bulk valence or conduction band.

In order to obtain an even simpler and easy to use expression for the tunneling current, we make assumptions of low temperature and low bias voltage. The latter ensures that $|M|$ does not change with significantly with voltage, simplifying the expression for tunneling current as:

$$I \propto \int_{E_F}^{E_F+eU} \rho_T(E - eU) \rho_S(E, \mathbf{r}_0) dE \quad (\text{A.12})$$

This expression is generally used to interpret an STM image. It shows that the tunneling current measured on the surface includes all states between Fermi energy and that shifted by the bias voltage, i.e., it is proportional to the integrated LDOS of the sample, measured at the center of curvature of the tip apex, \mathbf{r}_0 . If the LDOS of the tip¹⁸ is assumed to be constant and taken out of the integral, the tunneling current is proportional to the LDOS of the sample measured at \mathbf{r}_0 . This means that a constant current STM image reflects the contours of constant LDOS of the sample. A pictorial representation of the above equation is shown in Fig. A.1.3.

¹⁸For the purposes of interpretation of a real experiment one must not forget that the tunneling current is a convolution of the sample and tip density of states.

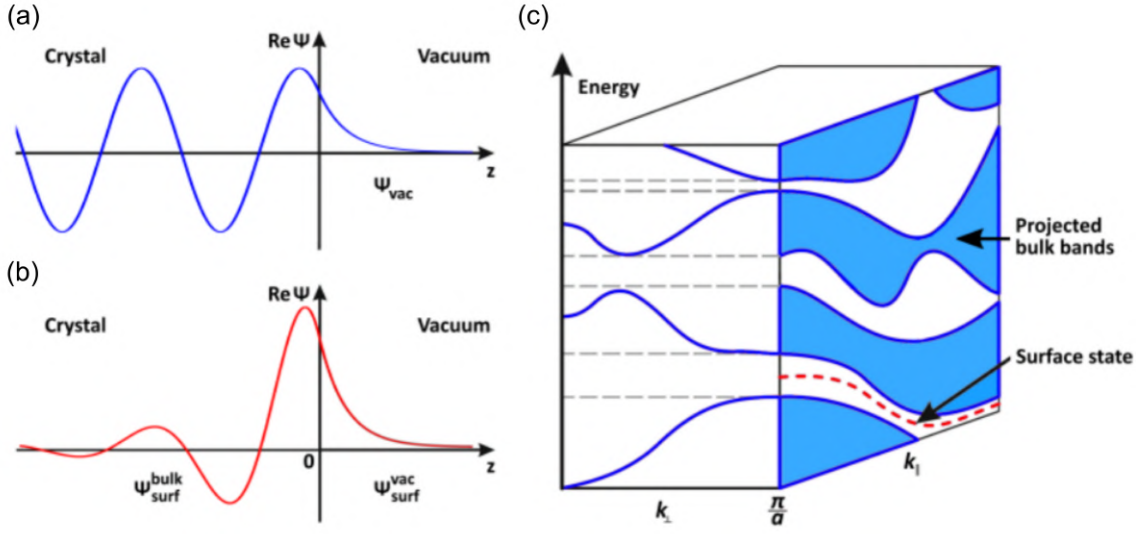


Figure A.1.2: Surface and bulk states. (a,b) Real part of a one-dimensional bulk and surface state wave function, respectively. Both decay exponentially into the vacuum. Additionally, the surface state is damped out inside the bulk of the crystal. (c) The surface state (red dashed line) is located in the gap of the bulk bands (blue) projected along k_{\perp} onto the k_{\parallel} plane at $k_{\perp} = \pi/a$. Image, text and concept from Refs. [151, 158].

A.2 Scanning tunneling spectroscopy

We can directly probe the local density states as a function of energy by measuring dI/dU or the differential conductance. This is readily seen by differentiating Eq. A.12 (assuming the tip density of states and the tunnel matrix to be constant in the measured energy interval):

$$\frac{dI}{dU} \propto \rho_T \cdot \rho_S(E_F + eU, \mathbf{r}_0) \quad (\text{A.13})$$

The differential conductance (dI/dU) data can be acquired for a single position (STS point spectrum) or for all positions (x, y) in a given image window which will give a 3D data set, illustrated in Fig. A.1.3.

The differential conductance is usually measured at a constant tip-sample distance at a particular position on the sample. The data is acquired by means of a lock-in amplifier where a small AC voltage (U_{mod}) at a modulation frequency of ω_{mod} is used to modulate the applied bias-voltage (U_0) as: $U_0 + U_{\text{mod}} \cos(\omega_{\text{mod}}t)$. This introduces a modulation in the tunneling current I_{mod} (depicted in Fig. A.2.4(a)). By expanding the current in a Taylor series one can see that I_{mod} is proportional to dI/dU :

$$I(U) = I(U_0) + \frac{dI}{dU} U_{\text{mod}} \cos(\omega_{\text{mod}}t) \quad (\text{A.14})$$

$$= I(U_0) + I_{\text{mod}} \cos(\omega_{\text{mod}}t) \quad (\text{A.15})$$

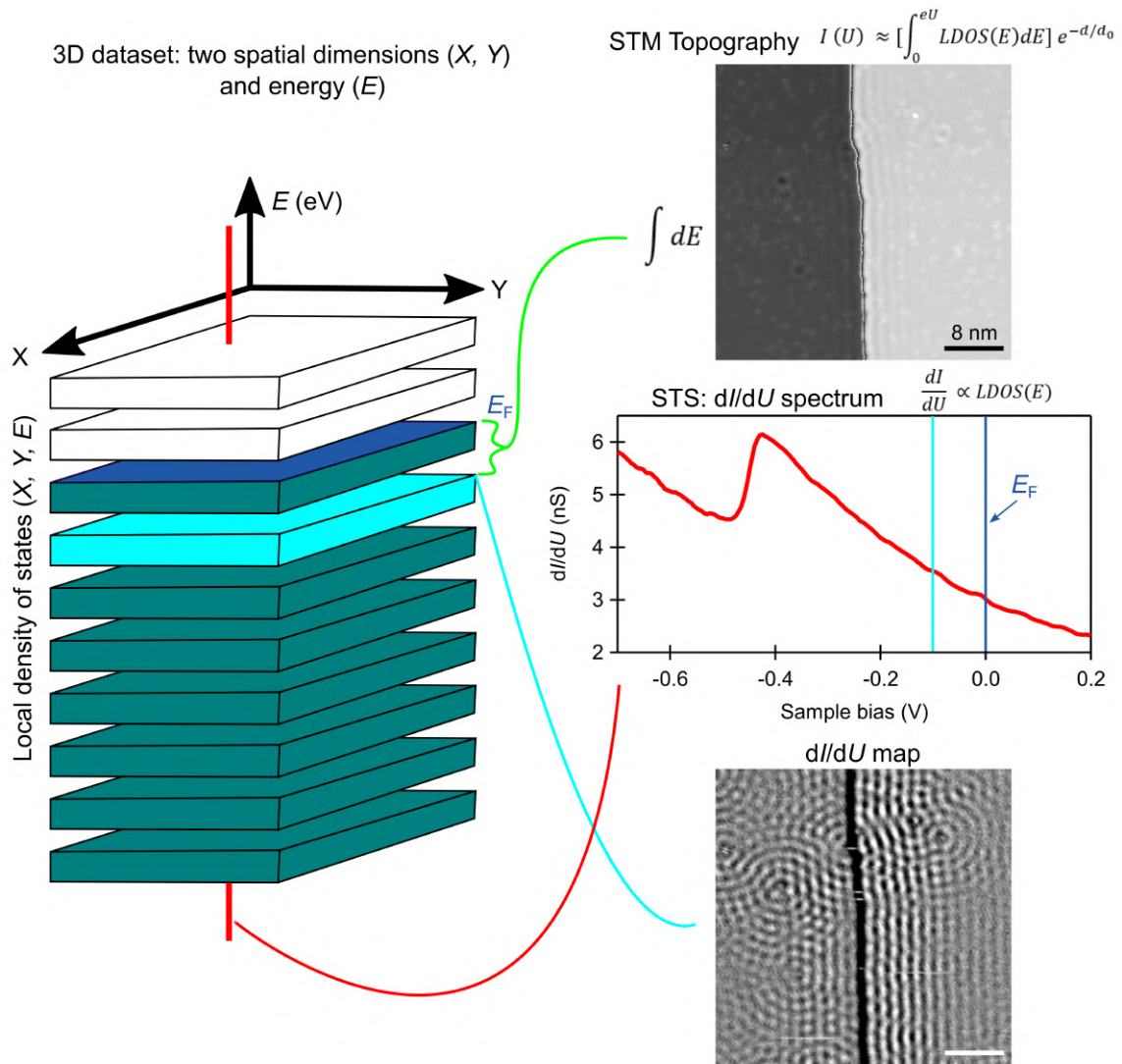


Figure A.1.3: Traditional STM/STS measurements. Schematic representation of the two measured quantities: tunneling current (I) and differential conductance (dI/dU) in relation to the local density of states of the sample. Data acquired on the Cu(111) surface is used to demonstrate the different traditional measurements of STM topography, STS spectrum and STS spatial map. Concept from Ref. [159].

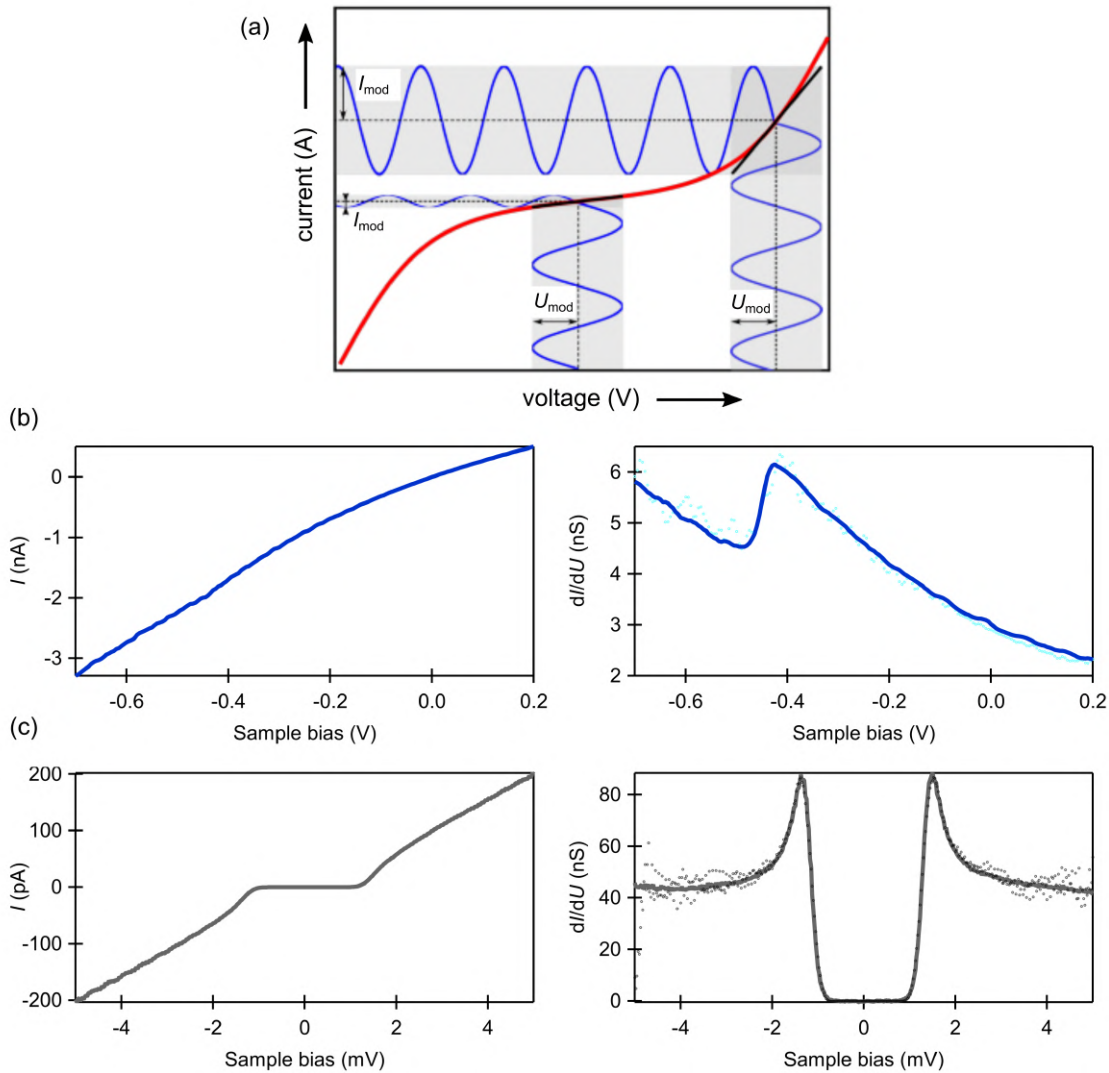


Figure A.2.4: Scanning tunneling spectroscopy. (a) Illustration of the principle of acquiring differential conductance spectrum using a lock-in amplifier. U_{mod} is the AC modulation voltage which results in the modulation of the output current signal I_{mod} . $I_{\text{mod}}/U_{\text{mod}} = dI/dU$ or the slope of the $I(U)$ spectrum. Image from Ref. [151]. (b,c) Spectra taken on the Cu(111) surface and a SC Nb film, respectively. The $I(U)$ characteristics and the corresponding dI/dU plot is shown. The dI/dU trace is obtained by differentiating $I(U)$ curves (open circles) and that recorded using a lock-in (solid line).

In Fig. A.2.4(b,c) $I(U)$ curves together with the simultaneously acquired dI/dU curves by means of a lock-in are shown. The dI/dU curves can also be obtained via numerical differentiation of the $I(U)$ curves [also illustrated in Fig. A.2.4(b,c)]. The former, using the lock-in technique is usually preferred due to its advanced noise filtering capabilities. However, under rare circumstances the latter may become a better choice. For example, in case of any instability in the tunnel junction a dI/dU -lock-in-spectrum is marred by sudden jumps in the tunneling current. To avoid such jumps in the data one needs to measure faster than the timescale between two successive jumps/disruptions in the measurement. This is possible in case of measuring $I(U)$ spectra where a single spectrum between 2 mV and -2 mV with a stepsize of 5 μ V can be acquired in 100 ms. In comparison, a lock-in spectrum of same bias range and resolution takes 160 s. This method of data acquisition was used for acquiring spectra on the surface of CPSBS in Chapter 3. It is important to note that in this method one must acquire $I(U)$ -spectra on the order of 100 and average them. This is followed by numerical differentiation and smoothing to obtain a dI/dU curve that has a signal-to-noise ratio that is comparable to the lock-in-spectrum.

A.2.1 Normalization

Equation A.13 which is used to understand the measured dI/dU spectrum is applicable only if the tunnel matrix element can be assumed to be constant. Otherwise the equation needs to be rewritten as:

$$\frac{dI}{dU} \propto \rho_S(eU)M(eU, eU, d) + e \int_0^{eU} \rho_S(E) \frac{d}{d(eU)} [M(E, eU, d)] dE \quad (\text{A.16})$$

where E_F has been set to zero. Hence our dI/dU spectrum may not always be directly proportional to the LDOS of the sample but may also have an unwanted contribution from $M(E, U, d)$. One way to suppress this contribution is to normalize the dI/dU -spectrum by I/U , which results in the following expression [160]:

$$\frac{\frac{dI}{dU}}{I/U} = \frac{\rho_S(eU) + \int_0^{eU} \frac{\rho_S(E)}{M(eU, eU, d)} \frac{d}{d(eU)} [M(E, eU, d)] dE}{\frac{1}{eU} \int_0^{eU} \rho_S(E) \frac{M(E, eU, d)}{M(eU, eU, d)} dE} \quad (\text{A.17})$$

Since $M(E, eU, d)$ and $M(eU, eU, d)$ appear as a ratio, their exponential dependence on U and d are canceled out. Hence the quantity on the left-hand side of the equation is a good measure of the LDOS of the sample.

Another normalization method used in the thesis is to simply divide the dI/dU spectrum with I_0/U_0 , where I_0 is the setpoint current and U_0 is the stabilization bias. This method of normalization can help to qualitatively compare different spectra. Overall no normalization technique is generally applicable. It must be chosen based on the particular experiment and the aspect of the data that one may wish to highlight. For a dI/dU spectrum showing a superconducting gap around the Fermi level, it is normalized by dividing by the average

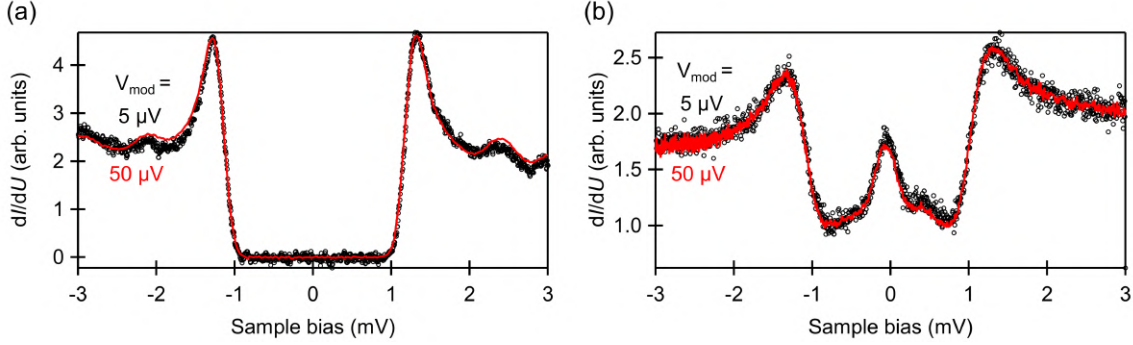


Figure A.3.5: Lower limit of lock-in modulation amplitude. (a, b) SC gap measured on a Nb film (a) and in-gap zero bias peak measured on the proximitized surface of $(\text{Bi}_{1-x}\text{Sb}_x)_2\text{Te}_3$ thin film in the presence of an in-plane magnetic field (b), for different values of lock-in modulation voltage. Data acquired at 0.35 K. Data acquisition parameters: (a) $U = 5$ mV, $I = 200$ pA, $U_{\text{mod}} = 5 \mu\text{V}_p$ (black) and $50 \mu\text{V}_p$ (red); (b) $U = 3$ mV, $I = 120$ pA, $U_{\text{mod}} = 5 \mu\text{V}_p$ (black) and $50 \mu\text{V}_p$ (red).

value of the conductance in the nonsuperconducting/normal state. In some cases a second degree polynomial was fit to the data outside the SC gap and the dI/dU spectrum was normalized by dividing by the fitted polynomial. This was necessary if the normal state tip plus sample DOS was not constant over the interval used for normalization.

A.3 Energy resolution and effective temperature

The proportionality of the differential conductance to the density of states of the sample is obtained only in the $T=0$ K limit (Eq. A.13). In fact, the density of states is convoluted with the derivative of the Fermi function, given as:

$$\frac{df(E)}{dE} = \frac{1}{k_B T} \frac{e^{-\frac{E}{k_B T}}}{(1 + e^{-\frac{E}{k_B T}})^2} \quad (\text{A.18})$$

For $T=0$ K, $\frac{df(E)}{dE}$ is a delta function and Eq. A.13 is recovered. However, for finite temperatures the delta function changes to a Gaussian of width $\approx 3.5k_B T$, broadening our spectral features, and is therefore a factor that limits our energy resolution. For example, a system temperature of 4 K, 0.7 K and 0.35 K imply a thermal energy resolution of 1 meV, 200 μeV and 100 μeV , respectively. It is possible to overcome this thermal resolution limit by making use of a superconducting tip: discussion and example can be found in section 4.6.2.

A second source of broadening is the AC modulation voltage U_{mod} that is added to the bias voltage during acquisition of spectra using the lock-in. As a result the intrinsic spectrum is convoluted with a function of the form $\sqrt{U_{\text{mod}}^2 - U^2}/\pi U_{\text{mod}}^2$, applicable only for

applied voltages which are $\leq U_{\text{mod}}$ [161]. Hence one must choose a modulation voltage that is large enough for good signal strength but also less than a value that can lead to artificial broadening. We have acquired high resolution SC spectra with a typical modulation amplitude of $50 \mu\text{V}$ and have experimentally ascertained that using a modulation voltage lower than this value does not lead to an improvement in the resolution of spectral features, such as the coherence peak in a SC gap or a ZBCP inside the SC gap (see Fig. A.3.5). Hence the resolution of these spectra are not limited by the modulation voltage but must have another origin.

Another factor which can limit our energy resolution is broadening due to 'unknown' electronic noise in our circuit¹⁹. A possible origin can be any form of capacitive crosstalk between the current measurement line and the environment or other cables as a consequence of imperfect shielding of the current cable. Also resistive parts of the circuit, for example the op-amp of the current preamplifier uses a feedback resistor of $1 \text{ G}\Omega$ (for a gain of 10^9), can lead to Johnson/thermal noise as well as low frequency noise. In most cases we are able to get rid of any capacitive noise in the dI/dU signal by carefully aligning the phase of the reference and input signal for the lock-in. Impact of other noise sources on the the dI/dU signal is limited to the bandwidth required by the lock-in for proper averaging times. For our measurements this is typically only 38.9 Hz (an averaging time of $\sim 100 \text{ ms}$ or the time in which the low-pass filter reaches 63.2% of a step response) which adds an rms voltage noise of $26 \mu\text{V}$ or a current noise of 0.03 pA .

The impact of all the above sources of experimental broadening on our dI/dU spectra, in particular the SC spectra, can be captured by an effective broadening term. Experimentally we use the temperature required to fit the SC gap of a well-known superconductor as this effective broadening term and hence call it the effective temperature of our junction. In principle this term takes into account all extrinsic sources of broadening. Such a calibration experiment for our setup can be found in Ref. [58] where the effective temperature was found to be 0.7 K .

A.4 Superconducting density of states

For a temperature and a magnetic field value that is below T_c and H_c , respectively, some materials undergo a thermodynamic phase transition to a new state that is energetically more favorable. The reduction in energy is a consequence of pairing of electrons near the Fermi level which form Cooper pairs. Such pairs, formed of electrons whose momenta are of equal magnitude but opposite direction, result from an attractive interaction between the electrons mediated by the crystal lattice vibrations or phonons. All Cooper pairs have the same net momentum, i.e., $\mathbf{q}=0$, and occupy the same macroscopic quantum state, the ground state, which is well separated from single-electron states by an energy gap. The energy gap protects Cooper pairs from normal scattering processes in the crystal, allowing

¹⁹By far the most important electronic noise source is given by ground loops, which we avoid by our grounding scheme.

them to move without any dissipation. Hence a zero resistance or *super* conductance state is achieved and termed as *superconductivity*.

The microscopic understanding of the phenomenon of Cooper pair formation or the emergence of superconductivity was gained from the theory of Bardeen, Cooper and Schrieffer (BCS theory). The theory successfully predicted the temperature dependence of the energy gap and its relation to the critical temperature T_c among others and is well supported by several experiments. Here we briefly review the BCS formalism. The BCS Hamiltonian [162, 163] in second quantization reads as:

$$H = \sum_{\mathbf{k}\sigma} \xi_{\mathbf{k}} c_{\mathbf{k}\sigma}^\dagger c_{\mathbf{k}\sigma} + \frac{1}{N} \sum_{\mathbf{k}\mathbf{k}'} V_{\mathbf{k}\mathbf{k}'} c_{\mathbf{k}\uparrow}^\dagger c_{-\mathbf{k}\downarrow}^\dagger c_{-\mathbf{k}'\downarrow} c_{\mathbf{k}'\uparrow} \quad (\text{A.19})$$

where $\xi_{\mathbf{k}} = \hbar\mathbf{k}^2/2m$ is the kinetic energy of a free electron and the operators c and c^\dagger annihilate an electron or create an electron of spin state σ , respectively. The second term on the right side of the equation represents all the cooper pairs in the superconducting state that result from the attractive interaction $V_{\mathbf{k}\mathbf{k}'}$. For a solution of this Hamiltonian one employs a mean field approximation since a large number of particles are involved and any fluctuation in the number of Cooper pairs should therefore be small. In this approach the Hamiltonian can be rewritten as:

$$H_{\text{BCS}} = \sum_{\mathbf{k}\sigma} \xi_{\mathbf{k}} c_{\mathbf{k}\sigma}^\dagger c_{\mathbf{k}\sigma} - \sum_{\mathbf{k}} \Delta_{\mathbf{k}}^* c_{-\mathbf{k}\downarrow} c_{\mathbf{k}\uparrow} - \sum_{\mathbf{k}} \Delta_{\mathbf{k}} c_{\mathbf{k}\uparrow}^\dagger c_{-\mathbf{k}\downarrow}^\dagger \quad (\text{A.20})$$

where a new 'gap' operator $\Delta_{\mathbf{k}} = -\frac{1}{N} \sum_{\mathbf{k}'} V_{\mathbf{k}\mathbf{k}'} \langle c_{-\mathbf{k}'\downarrow} c_{\mathbf{k}'\uparrow} \rangle$ and its complex conjugate was introduced and determines the expectation value of a Cooper pair.

In order to diagonalize H_{BCS} , further new fermionic operators are needed, which are linear combinations of electron creation and annihilation operators:

$$\begin{pmatrix} \gamma_{\mathbf{k}\uparrow} \\ \gamma_{-\mathbf{k}\downarrow}^\dagger \end{pmatrix} = \begin{pmatrix} u_{\mathbf{k}}^* & -v_{\mathbf{k}} \\ v_{\mathbf{k}}^* & u_{\mathbf{k}} \end{pmatrix} \begin{pmatrix} c_{\mathbf{k}\uparrow} \\ c_{-\mathbf{k}\downarrow}^\dagger \end{pmatrix} \quad (\text{A.21})$$

where $u_{\mathbf{k}}$ and $v_{\mathbf{k}}$ are complex numbers with the condition that $|u_{\mathbf{k}}|^2 + |v_{\mathbf{k}}|^2 = 1$. The above mapping is called *Bogoliubov transformation*. If we insert the inverse transformation into H_{BCS} and after some math (see Ref. [164]) the diagonalized BCS Hamiltonian reads as:

$$H_{\text{BCS}} = \sum_{\mathbf{k}} \sqrt{\xi_{\mathbf{k}}^2 + |\Delta_{\mathbf{k}}|^2} \left(\gamma_{\mathbf{k}\uparrow}^\dagger \gamma_{\mathbf{k}\uparrow} + \gamma_{-\mathbf{k}\downarrow}^\dagger \gamma_{-\mathbf{k}\downarrow} \right) \quad (\text{A.22})$$

$$H_{\text{BCS}} = \sum_{\mathbf{k}\sigma} E_{\mathbf{k}} \gamma_{\mathbf{k}\sigma}^\dagger \gamma_{\mathbf{k}\sigma} \quad (\text{A.23})$$

$E_{\mathbf{k}}$ represents the eigenvalues of the Hamiltonian, its momentum dependence, $E_{\mathbf{k}} = \pm\sqrt{(\xi_{\mathbf{k}} - \mu)^2 + |\Delta_{\mathbf{k}}|^2}$, gives the dispersion relation, μ being the chemical potential. This

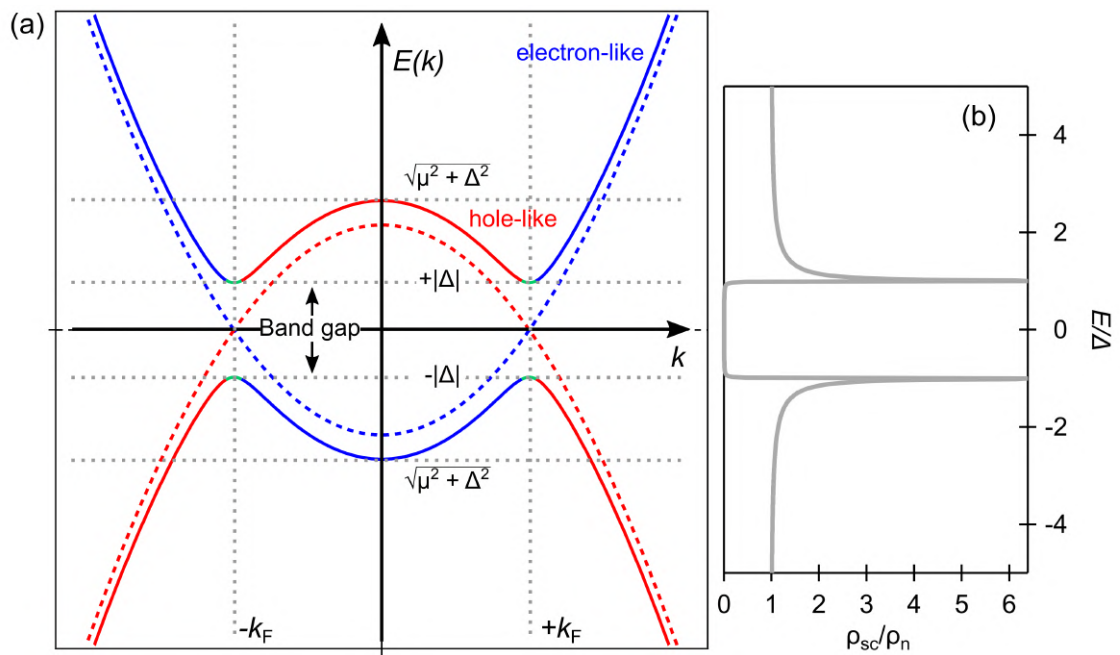


Figure A.4.6: Dispersion relation of the Bogoliubov quasiparticles, $E_{\mathbf{k}} = \pm\sqrt{(\hbar^2 k^2/2m - \mu)^2 + |\Delta_{\mathbf{k}}|^2}$, and the DOS. (a) Solid (dashed) line corresponds to the spectrum for $\Delta > 0$ ($\Delta = 0$). Blue (red) denotes the electron-like (hole-like) branches. Note that only the first quadrant of E vs. k is necessary. The spectrum in the other quadrants is obtained through electron-hole symmetry ($E_{\mathbf{k}} = -E_{-\mathbf{k}}$) and time-reversal symmetry ($E_{\mathbf{k}} = E_{-\mathbf{k}}$). (b) Corresponding to (a), the quasiparticle density of states in the presence of a gap Δ , normalized by the density of states in the normal state.

relation is the single particle excitation spectrum of the BCS Hamiltonian. To see this we include a constant term that was ignored from Eq. A.20 onwards:

$$H_{\text{BCS}} = \underbrace{\sum_{\mathbf{k}\sigma} E_{\mathbf{k}} \gamma_{\mathbf{k}\sigma}^{\dagger} \gamma_{\mathbf{k}\sigma}}_{\text{Bogoliubov quasiparticle dispersion}} + \underbrace{E_{\text{BCS}}}_{\text{condensation energy}} \quad (\text{A.24})$$

At the lowest temperature, in the absence of any quasiparticles, the energy of the system equals only the condensation energy of the Cooper pairs (it must be less than zero for a superconducting state). The other term from which we obtained the $E_{\mathbf{k}}$ relation, describes the dispersion of Bogoliubov quasiparticles, sketched in Fig. A.4.6(a). These quasiparticles are elementary excitations of this system created by the fermionic operators γ and γ^{\dagger} . Following Fig. A.4.6(a), to create a quasiparticle in the superconducting state a minimum energy of Δ is required. Thus $|\Delta_{\mathbf{k}}|$ defines the energy gap of the superconducting state, precisely the magnitude of the gap.

The Bogoliubov quasiparticles are superposition of particles and holes, away from k_{F} they can be electron-like or hole-like. However, right at the Fermi level they are equal superposition of electron and hole. Such an excitation is within the superconducting gap and to get such an excitation additional terms are required that will compete with the $\Delta_{\mathbf{k}}$ term in the Hamiltonian. This is one of the ingredients required to obtain a MZM.

As discussed before in section A.2, in our spectroscopy experiment we will measure the quasiparticle density of states, shown in Fig. A.4.6(b). We can calculate the density of states using the above dispersion relation and by integrating over momentum space. The density of states of the superconductor (ρ_{sc}) reads as:

$$\rho_{\text{sc}}(E, \Delta) = \frac{dN}{dE} \frac{1}{V} = \frac{d}{dE} \frac{1}{V} \left[V \int \frac{d^3k}{(2\pi)^3} \right] = \frac{d}{dE} \frac{1}{V} \left[V \frac{4\pi}{(2\pi)^3} \int \frac{d}{dE} \frac{1}{\frac{dE}{dk}} k^2 \right] \quad (\text{A.25})$$

Differentiating the dispersion relation with respect to k :

$$\frac{dE}{dk} = \frac{\partial E}{\partial \xi} \frac{d\xi}{dk} = \frac{\sqrt{E^2 - \Delta^2}}{E} \frac{k}{m_e} \quad (\text{A.26})$$

By inserting Eq. A.26 in Eq. A.25 and approximating the energy to be for a small range around the Fermi level and writing $(\xi - \mu)^2 = E^2 - \Delta^2$, we obtain:

$$\rho_{\text{sc}}(E, \Delta) = \rho_{\text{n}} \frac{E}{\sqrt{E^2 - \Delta^2}} \quad (\text{A.27})$$

where ρ_{n} is the DOS in the normal state. The SC DOS has a energy gap of 2Δ around the Fermi energy. At the edge of the gap on either side of the Fermi level, i.e., $\pm\Delta$, the DOS diverges. This divergence corresponds to the quasiparticle resonances or the coherence peaks of the SC gap.

A.4.1 Pairing symmetry

In the last section the magnitude of the function $\Delta_{\mathbf{k}}$ has reflected an energy gap in the single particle excitation spectrum. In this section we discuss the symmetry of $\Delta_{\mathbf{k}}$ with respect to the lattice or its momentum space (\mathbf{k}) dependence, referred to as the pairing symmetry. Since a Cooper pair is obtained from the electrons in a crystal which are described by a Hamiltonian that is invariant for the different lattice symmetry operations, the pairing potential for the Cooper pair as well as its wavefunction must also be subject to these symmetries. For such considerations, the possible pairing states can be obtained with the framework of group theory as in the work of A. Ramires in Chapter 3.

Here we attempt to provide a simple illustration of the relation between symmetry of the lattice and $\Delta_{\mathbf{k}}$ using a square lattice. The discussion here is based on Ref. [165]. The first step is to write the electron-electron interaction in terms of the different lattice sites. For a square lattice with δ_x and δ_y as unit vectors in orthogonal \mathbf{x} and \mathbf{y} directions it reads:

$$V(\mathbf{r}_i - \mathbf{r}_j) = \underbrace{U \delta(\mathbf{r}_i - \mathbf{r}_j)}_{\text{on-site interaction}} \quad (\text{A.28})$$

$$+J \left[\delta(\mathbf{r}_i - (\mathbf{r}_j - \delta_x)) + \delta(\mathbf{r}_i - (\mathbf{r}_j + \delta_x)) \right] \quad (\text{A.29})$$

$$+ \underbrace{\delta(\mathbf{r}_i - (\mathbf{r}_j - \delta_y)) + \delta(\mathbf{r}_i - (\mathbf{r}_j + \delta_y))}_{\text{nearest-neighbor interaction}} \quad (\text{A.30})$$

$$+W \left[\delta(\mathbf{r}_i - (\mathbf{r}_j - \delta_x - \delta_y)) + \delta(\mathbf{r}_i - (\mathbf{r}_j + \delta_x - \delta_y)) \right] \quad (\text{A.31})$$

$$+ \underbrace{\delta(\mathbf{r}_i - (\mathbf{r}_j - \delta_x + \delta_y)) + \delta(\mathbf{r}_i - (\mathbf{r}_j + \delta_x + \delta_y))}_{\text{next-nearest-neighbor interaction}}, \quad (\text{A.32})$$

where U is the electron-electron interaction on the same site, J on nearest-neighbor and W on the next-nearest-neighbor sites. The above equation can be Fourier transformed and expressed in terms of square lattice harmonics:

$$V_{\mathbf{k}\mathbf{k}'} = \sum_{i=1}^9 \lambda_i g_i(\mathbf{k}) g_i(\mathbf{k}') \quad (\text{A.33})$$

where $\lambda_1 = 4\pi^2 U$, $\lambda_2 = \lambda_3 = \lambda_6 = \lambda_7 = 2\pi^2 J$, $\lambda_4 = \lambda_5 = \lambda_8 = \lambda_9 = \pi^2 W$, and $g_i(\mathbf{k})$ are given by

$$\begin{aligned} g_1(\mathbf{k}) &= \frac{1}{2\pi}, g_2(\mathbf{k}) = \frac{1}{2\pi} [\cos(k_x) + \cos(k_y)], g_3(\mathbf{k}) = \frac{1}{2\pi} [\cos(k_x) - \cos(k_y)], \\ g_4(\mathbf{k}) &= \frac{1}{2\pi} \cos(k_x) \cos(k_y), g_5(\mathbf{k}) = \frac{1}{2\pi} \sin(k_x) \sin(k_y), g_6(\mathbf{k}) = \frac{1}{2\pi} [\sin(k_x) + \sin(k_y)], \\ g_7(\mathbf{k}) &= \frac{1}{2\pi} [\sin(k_x) - \sin(k_y)], g_8(\mathbf{k}) = \frac{1}{2\pi} \cos(k_x) \sin(k_y), g_9(\mathbf{k}) = \frac{1}{2\pi} \sin(k_x) \cos(k_y) \end{aligned}$$

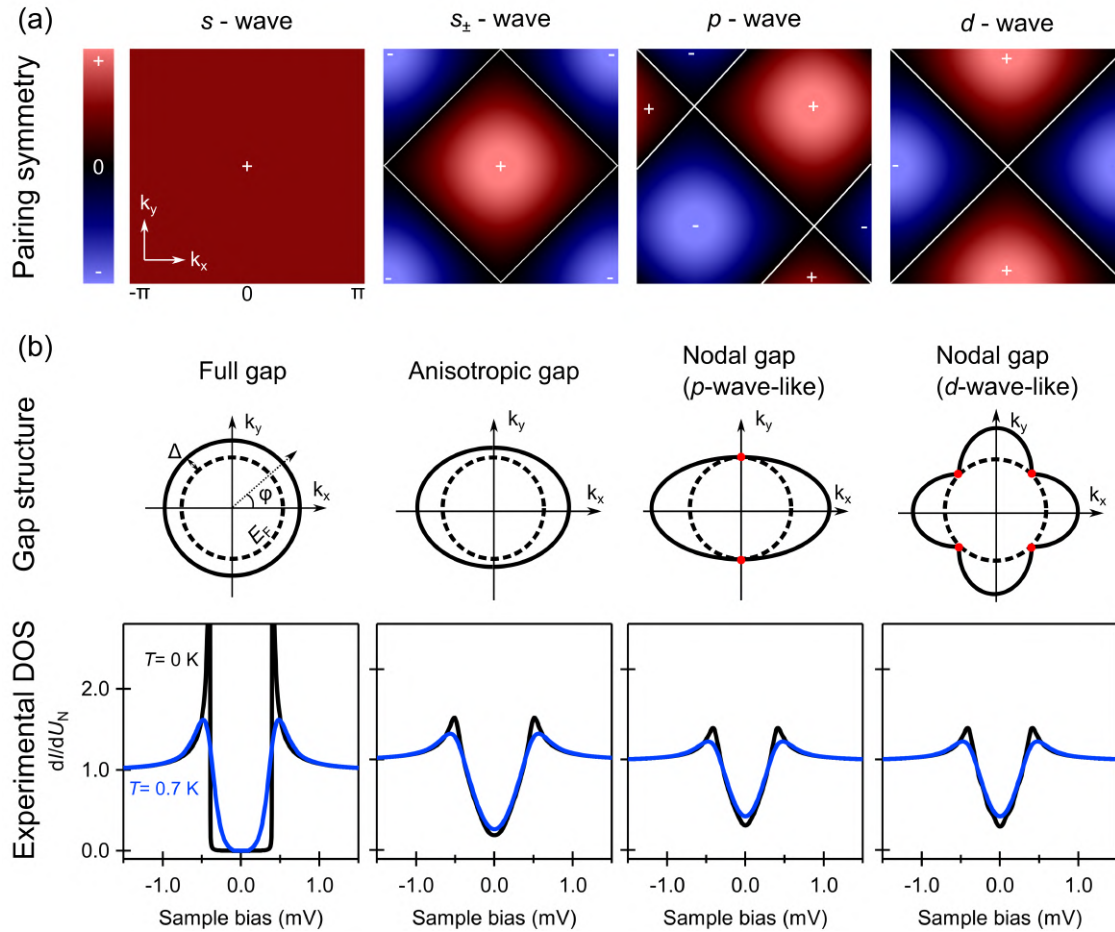


Figure A.4.7: Pairing symmetries and expected DOS in a STS experiment. (a) Different pairing symmetries over the first Brillouin zone. Light red (light blue) corresponds to a positive (negative) sign. While transitioning from the positive to negative the superconducting gap must go to zero, indicated by the white (nodal) lines. (b) Same information as in (a) but now visualized over a 2D isotropic Fermi surface. The positions where the gap goes to zero are indicated with red dots, also called gap nodes. For the different gap structures the corresponding integrated DOS (simulated) for temperatures of 0 K and 0.7 K are shown below.

The nine square lattice harmonics listed here are the few lower orders and not the complete set. These harmonic functions reflect the symmetries of the square lattice considered. Now $V_{\mathbf{k}\mathbf{k}'}$ is related to the gap $\Delta_{\mathbf{k}}$ which then can be similarly expressed in terms of harmonic functions.

Each harmonic corresponds to a gap channel with a symmetry that adheres to the lattice symmetry. Ultimately one of these channels must be selected based on the details of the effective electron-electron interaction. The symmetry of the selected channel is often used to name the gap or pairing itself. For example different spherical harmonic functions (Y_{lm}) are classified by the quantum numbers $l = 0, 1, 2..$ and are named as *s*-wave, *p*-wave, *d*-wave, respectively. Similarly we can check the symmetry to the particular lattice harmonic to name the gap or pairing symmetry. For example, $g_1(\mathbf{k})$ and $g_2(\mathbf{k})$ square harmonics are *s*-wave like (transforming as the identity under all symmetry operations), $g_6(\mathbf{k}) - g_9(\mathbf{k})$ are *p*-wave like (there is sign change for π rotation) and $g_3(\mathbf{k}) - g_5(\mathbf{k})$ are *d*-wave like (there is sign change for $\pi/2$ rotation). Pairing symmetry in terms of these harmonics is visualized in Fig. A.4.7(a). The name or the label is determined so as to be consistent with the spherical isotropic system. However, it is the particular crystal lattice harmonic which defines the symmetry.

Another way of depicting the same information is by plotting the SC gap amplitude over the Fermi surface. This is shown in the second panel of Fig. A.4.7, where we have assumed a 2D isotropic Fermi surface. A full gap or a *s*-wave like gap is isotropic in momentum space, whereas an anisotropic gap has a reduced gap size and a nodal gap has zero gap size for certain positions in momentum space. To relate this information on the gap size over the Fermi surface to the quantity measured in an STS experiment we must integrate over the entire momentum space. We show the simulated STS spectra for the four different gap symmetries in Fig. A.4.7(b) for temperatures of 0 K and 0.7 K. Hence experimentally one can confidently distinguish only between a full gap and any other gap symmetry (provided that the energy scale corresponding to the measurement temperature is much smaller than the SC gap). The nodal *p*-wave like and *d*-wave like gaps (simulated using $\cos \Phi$ and $\cos 2\Phi$ functions, respectively) cannot be differentiated solely based on STS spectra.

It is understood that identifying symmetry of the Cooper pair wavefunction is a central theme in understanding the phenomenon of superconductivity. All superconductors break gauge symmetry below the transition temperature, i.e., each Cooper pair is associated with a fixed phase factor and the relative phase between two pairs is also fixed. Superconductors where only the gauge symmetry is broken are also the simplest, conventional kind. They usually show an energy gap that is isotropic in momentum space or *s*-wave like or follows the crystal symmetry. On the other hand if the gap symmetry is lower than the point group symmetry of the crystal, the superconductor is termed as unconventional, as is the case for the doped Bi_2Se_3 superconductors measured in this thesis. Unconventional superconductors also have an gap function with odd parity and may break other symmetries such as time reversal symmetry.

Experimentally, by measuring the DOS in the STS we only have access to the magnitude of the Cooper pair wavefunction which is proportional to the gap size. By further analyzing

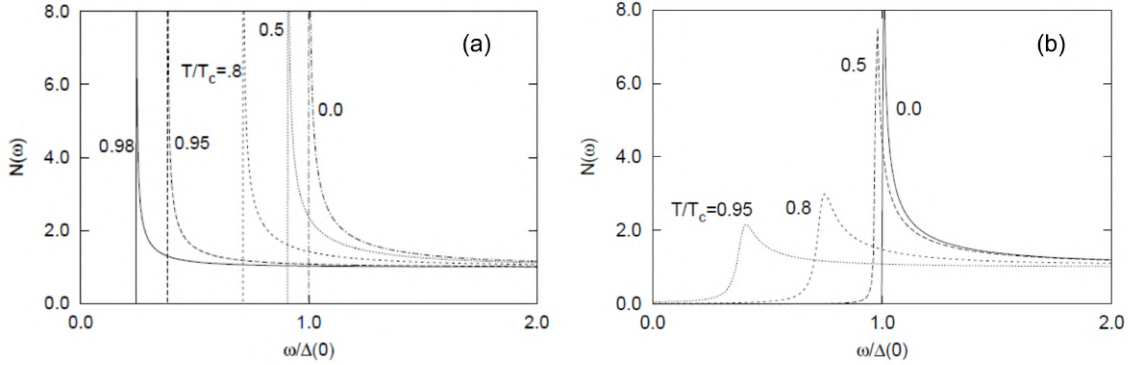


Figure A.4.8: Calculated SC DOS ($N(\omega)$) as a function of energy (scaled by the gap Δ) for Pb, for different temperatures within the BCS theory (a) and Eliashberg theory (b). Finite temperatures only lead to a reduced gap in (a) whereas considerable smearing is observed in (b). Plots taken from Ref. [166].

the STS spectra we can comment on the symmetry of the SC gap. However, since we do not have any access to the phase of the Cooper pair wavefunction we cannot discuss if there is a sign change in the gap function in momentum space. For example, we cannot prove that a twofold symmetric gap structure with two gap nodes is truly p -wave like. SC interference experiments which employ the Josephson effect are better suited for extracting the phase information. Other experiments such as the Knight shift of the nuclear magnetic resonance (NMR) frequency and the muon spin rotation (μ SR) can help to determine the parity or the spin state of the Cooper pairs.

A.4.2 Fitting of superconducting gap spectra

In this thesis the SC gaps measured were fit using the BCS DOS A.26 modified by a Γ term, as was proposed by Dynes [167]:

$$\rho_{\mathbf{k}}(E) = (E - i\Gamma) / \sqrt{(E - i\Gamma)^2 - \Delta_{\mathbf{k}}^2} \quad (\text{A.34})$$

The original proposal by Dynes to include this energy-independent imaginary Γ term was to account for the temperature dependent smearing of the gap edge that is expected for strong-electron-phonon-coupled superconductors, illustrated in Fig. A.4.8. These superconductors cannot be adequately described within the BCS framework which assumes electron-phonon interaction energy as a constant given by the highest possible phonon energy (the Debye frequency). Instead, one has to consider the energy or the frequency dependence of the gap function, as done within the Migdal-Eliashberg theory.

However, such systematic broadening of the gap edge is rarely observed in spectroscopy, even for strongly coupled superconductors. Hence in practice the Γ term of Eq. A.34 is

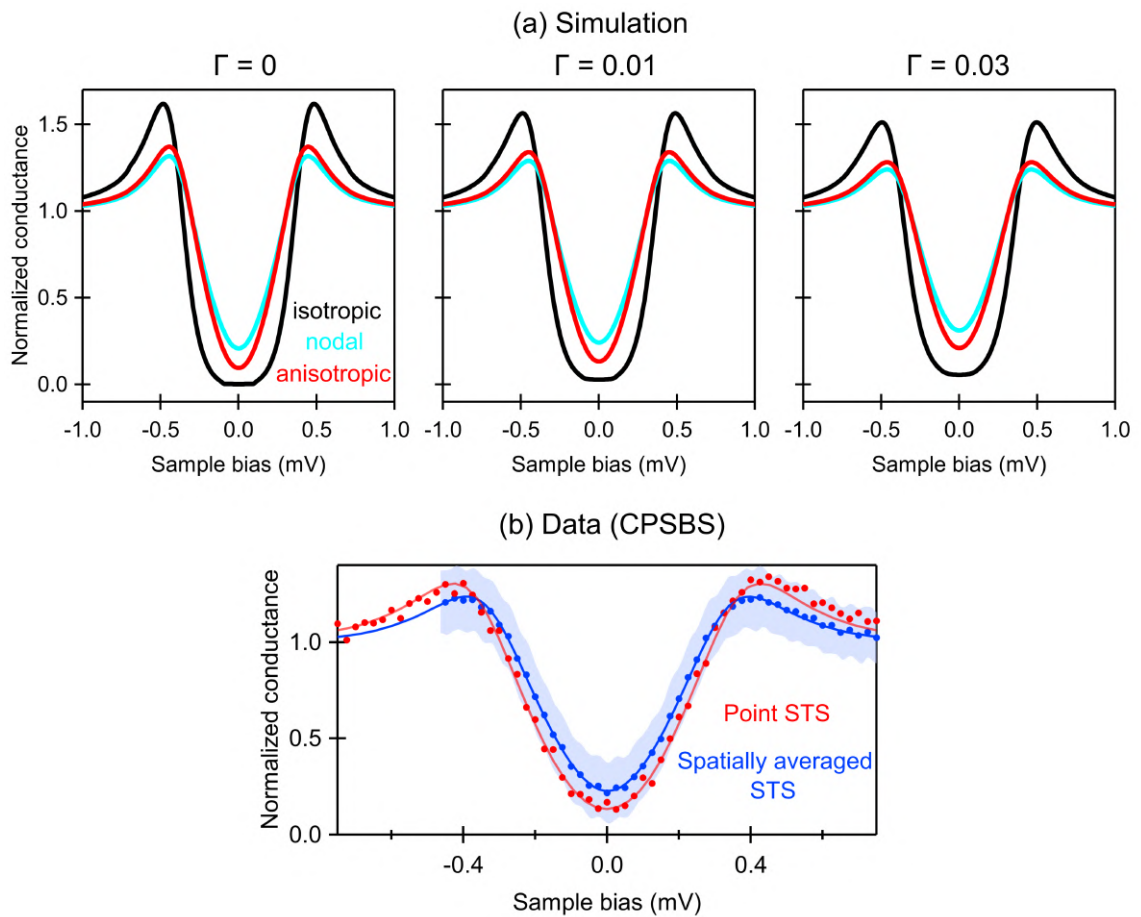


Figure A.4.9: Distinguishing different gap structures. (a) Simulation of the dI/dU spectra for isotropic, nodal and anisotropic gap functions with $\Delta=0.4$ meV, $T=0.7$ K and $\Gamma=0, 0.01$ and 0.03 meV. (b) Point STS (red dots) and spatially averaged STS (blue dots) with their respective anisotropic gap fits (solid lines). The light blue shaded region marks the standard deviation of the data points for the spatially averaged STS.

used to account for other sources of broadening. The unavoidable (extrinsic) sources being the finite temperature of the measurement setup and electronic noise. Broadening from these sources are usually taken care of by convoluting Eq. A.34 with the derivative of the Fermi function for an calibrated effective junction temperature of 0.7 K. Hence the value of Γ obtained from the fit can be treated as intrinsic broadening to the superconducting density of states caused by pair-breaking scattering processes such as inelastic electron-electron or electron-phonon or simply due to the presence of nodes in the gap function²⁰.

We briefly discuss the interpretation of the fit parameter Γ for the superconductor CPSBS, presented in Chapter 3, since it has nodes in its gap function. For such a superconductor even elastic scattering can lead to pair breaking since the Cooper pair maybe scattered to a position in momentum space where a SC gap does not exist. These quasiparticles at the nodes can lead to broadening of the SC gap and must be taken into account while fitting. In Fig. A.4.9(a) we have simulated the dI/dU spectrum considering three different gap structures: isotropic (full gap), nodal (p -wave like) and anisotropic with lifted nodes, for a total gap magnitude of 0.4 meV, at finite temperatures of 0.7 K and for different Γ values. We find that it is always possible to distinguish between the different gap structures in the presence (Γ is finite) and absence (Γ is zero) of quasiparticles given the same total gap magnitude (this value is obtained from the T_c by assuming weak coupling BCS behavior). Following this line of argument we have concluded in Chapter 3 that the point STS measured on the surface of CPSBS is best described by an anisotropic gap function with lifted nodes. While it is logically sound, there is need for caution experimentally. To illustrate this point we have replotted the point STS and its best fit from Chapter 3 (red dots and solid line, respectively) together with a STS (blue dots) that was obtained by averaging over 900 spectra from different spatial locations on the sample in Fig. A.4.9(b). We find that the blue spectrum is more broadened than the red one, indicating spatial inhomogeneity. This places an error bar on the ZBC and coherence peak values which are on the order of the differences expected between the nodal and anisotropic gap. Further, the data acquisition mode in this case²¹ introduced a large error bar for each data point, visualized by the light blue shaded region in Fig. A.4.9(b). Hence it is non trivial to experimentally distinguish different gap structures, requiring system temperatures on the order of 10 mK and data acquisition methods that are optimized to have very low noise conditions.

A.5 Quasiparticle interference

STM and STS lack the momentum-resolution that is offered by techniques such as angle-resolved photoemission spectroscopy (ARPES). For example, in general it cannot be used

²⁰In some cases, based on the fit, it is hard to distinguishing whether the broadening should be attributed to the Γ term or a different effective temperature, particularly when both terms can be adequately used to fit the data well.

²¹On the CPSBS sample, data could only be acquired in the $I-U$ mode since the disordered sample surface made the tunnel junction unstable.

to trace the dispersion relation $\varepsilon(k)$ for Bloch electrons in a metal, characterized by the wavevector k and energy ε . This is easily seen if we express the measured LDOS in a STM/STS experiment for a given position in terms of the Bloch wavefunction $\psi_{\mathbf{k}}(\vec{r})$ by

$$\text{LDOS}(E, \vec{r}) \propto \sum_{\mathbf{k}} |\psi_{\mathbf{k}}(\vec{r})|^2 \delta(E - \varepsilon(\vec{k})) \quad (\text{A.35})$$

At any given point in time, for a single location, we sum over the expectation value of all Bloch states for a particular energy and hence it must be the same for all locations in space. However, if there was a disturbance in the LDOS that varied in space and stood stationary in time, the LDOS will also vary spatially! This notion can be precisely achieved when a Bloch state reflects off defects, adatoms, step edges etc., and interferes with itself leading to the formation of a standing wave near the vicinity of the local disorder. The standing wave, whose wavelength is given as $\lambda = 2\pi/\mathbf{q}$, is observed as modulations in the LDOS in a STM experiment. The wavevector \mathbf{q} can be related to the wavevectors of the interfering waves ($\mathbf{k}_1, \mathbf{k}_2$) such that $\mathbf{q} = \mathbf{k}_2 - \mathbf{k}_1$. Further, elastic scattering increases the probability that the two \mathbf{k} vectors lie on the same constant energy contour (CEC) in \mathbf{k} -space.

Experimentally, the spatial variations of LDOS for a given energy are recorded as dI/dU maps, also known as quasiparticle interference (QPI) patterns. By identifying and tracing the energy dependence of the scattering wavevector \mathbf{q} from the Fourier transform of the QPI image, and hence the \mathbf{k} -vectors, one is able to map out the electronic dispersion of bands. In the most simple approximation $\mathbf{q} = 2\mathbf{k}$ where the incident state is backscattered. Although this technique has emerged as a powerful tool for electronic characterization of materials including superconductors [38], there is a catch. The process of assigning meaning to the QPI pattern in terms of scattering from one part of the band structure to another can quickly become complicated if scattering between different bands need to be considered, also some of these scattering processes may not take place due to selection rules or if it leads to a spin flip of the electron [168]. Under such circumstances theoretical simulation is required for interpretation of the map. Such simulations can be done using the T -matrix approach or by computing the a joint density of states (JDOS). The former explicitly takes into account the local potential of the scatterer and calculates the density of states in \mathbf{q} -space, while the latter obtains the QPI pattern based on the CECs of the band structure.

Here we discuss the expected QPI pattern from the Cu(111) surface state and the topological surface state based on their constant energy contours. It is important to note that we are considering the most simple scattering picture: an incident quasiparticle is scattered at a point-like defect that corresponds to an isotropic potential of the form $V(r) = V_0\delta(r - r_0)$. Assuming energy, momentum, spin and particle number conservation, the final electronic state must have the same energy as the initial state and a momentum that is limited by the CEC of the band to which the initial state belongs. Given the nature of the scattering potential, it is most likely that the initial state is simply backscattered. This is indeed the most dominant scattering wavevector that is found for the surface state electrons of Cu(111) crystal. These states have a parabolic dispersion that is free-electron

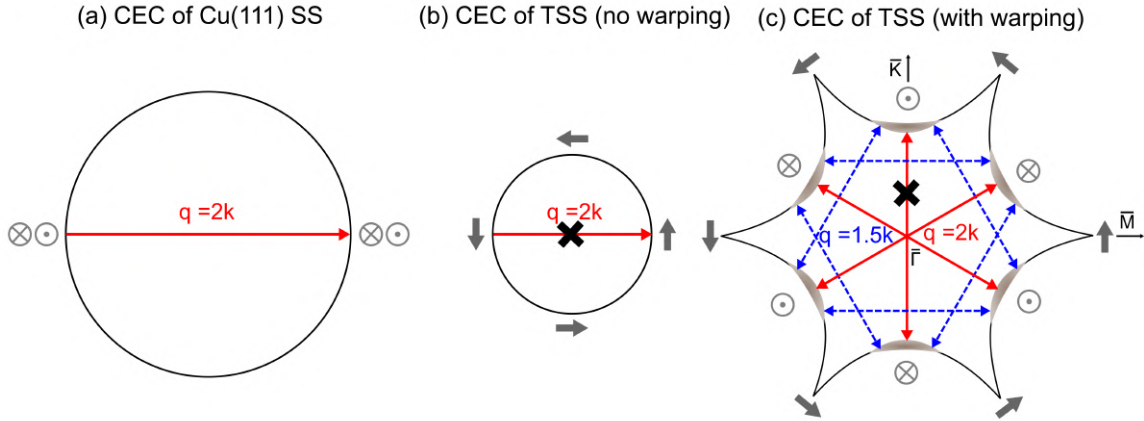


Figure A.5.10: Constant energy contours for the Cu(111) SS and the TSS of TI materials. The spin orientation of the electronic state is marked for each case. The solid circle (cross) indicates that the spin is out of plane along $+\hat{z}$ ($-\hat{z}$) and the arrows show the spin to be in the xy plane. Note that the $\bar{\Gamma}$ M points in (c) lie on the mirror symmetry lines and the system has threefold rotational symmetry.

like, $E(k) = \hbar^2 k^2 / 2m_{\text{eff}}$ with an effective mass $m_{\text{eff}} = 0.4m_e$. A constant energy cut of the band [depicted in Fig. A.5.10(a)] is a circle, hence an initial state with momentum \mathbf{k} is backscattered to $-\mathbf{k}$ which gives the scattering wavevector $\mathbf{q} = 2\mathbf{k}$. Since every state on the CEC can be backscattered and the scattering potential is isotropic we obtain a QPI pattern which is circular in the Fourier space and of radius \mathbf{q} [169]. The weak spin-orbit coupling in Cu leaves the surface band spin degenerate and hence spin of the quasiparticle is conserved for all scattering processes.

The scattering process for the TSS of materials such as Bi_2Se_3 and Bi_2Te_3 is however not as simple as the surface state of noble metals. This is in particular due to its dispersion and spin configuration. Close to the Dirac point the dispersion is linear and a CEC is a circle [depicted in Fig. A.5.10(b)]. However the spins of the surface state electrons are aligned in the plane of the surface and perpendicular to the momentum vector giving rise to an in-plane helical spin texture. As a consequence electrons are not allowed to backscatter since electrons with opposite momenta also have opposite spin and backscattering would require a spin-flip. This means that the strongest scattering wavevector, as found for the free electron like surface states of noble metals, is eliminated in this case. However, oblique scattering is still allowed [170], and the expected QPI pattern is a disc of radius $\mathbf{q} < 2\mathbf{k}$ instead of a ring of $\mathbf{q} = 2\mathbf{k}$. Experimentally, the topological protection against backscattering has been demonstrated for Bi_2Se_3 and Bi_2Te_3 [171–175] although there exists a report that has observed the $\mathbf{q} = 2\mathbf{k}$ ring on Mn doped Bi_2Se_3 [176] suggesting that the protection is not complete.

At energies far away from the Dirac point the surface state becomes hexagonally warped [177, 61], likely due to the hybridization between the surface and bulk states. The warping

enters the Hamiltonian as a cubic term [62, 170],

$$H(\vec{k}) = v(\vec{k} \times \vec{\sigma}) \cdot \hat{z} + \lambda k^3 \cos 3\phi_{\vec{k}} \sigma^z. \quad (\text{A.36})$$

where the first term describes the isotropic 2D Dirac state. The azimuthal angle of \vec{k} is $\phi_{\vec{k}} = \tan^{-1}(k_y/k_x)$, where the $\overline{\Gamma\text{K}}$ direction is taken as \hat{x} axis. Warping transforms the circular energy contour into a hexagon and further into a snowflake shape at even higher energy [see Fig. A.5.10(b)]. It further leads to a spin texture that bends in and out of plane. At the $\overline{\Gamma\text{M}}$ points (tips of the CEC), which lie on mirror symmetry lines, the warping term vanishes since σ^z is odd under mirror operation and the spins lie in plane while at the $\overline{\Gamma\text{K}}$ points (curved regions of the CEC) the spins lie out-of-plane with staggered signs [see Fig. A.5.10(b)]. Scattering on this CEC can be understood by considering that points of extremal curvature, namely the valleys and tips, correspond to high density of states which can give rise to strong nesting conditions and at the same time the spin orientation also plays a role. Scattering is found to be absent for backscattered states in the valleys and tips, represented by $\mathbf{q} = 2\mathbf{k}$, since it requires a spin-flip. Instead, scattering is dominated by wavevectors $\mathbf{q} \simeq 1.5\mathbf{k}$, which connect points between two valleys with the same sign of spin. The absence of any other scattering wavevector can also be argued by taking into account the degree of spin overlap. This simplified picture of the scattering process has helped to explain the QPI patterns observed in STM experiments on TI materials where QPI peaks along $\overline{\Gamma\text{K}}$ direction are strongly suppressed while those along $\overline{\Gamma\text{M}}$ are found to be intense.

A.6 Landau quantization

²²In the presence of a uniform external magnetic field \mathbf{B} , charged particles such as electrons move in cyclotron orbits (a circular path) induced by the Lorentz force. Their equation of motion in a magnetic field given by

$$\hbar \frac{d\mathbf{k}}{dt} = -e\mathbf{v} \times \mathbf{B} \quad (\text{A.37})$$

shows that the wavevector \mathbf{k} is confined to an orbit in a plane that is normal to \mathbf{B} . Further, rewriting the velocity of motion \mathbf{v} in terms of position \mathbf{r} we find that \mathbf{r} and \mathbf{k} are in the same plane (normal to each other and both to \mathbf{B}) and related as

$$k = \frac{eB}{\hbar} r = \frac{1}{\ell^2} r \quad (\text{A.38})$$

where $\ell = \sqrt{\frac{\hbar}{eB}}$ is the magnetic length.

²²References for this section include [178, 179].

Thereafter, imposing the Bohr-Sommerfeld quantization condition for Bloch electrons in a magnetic field, as was suggested by Onsager [180], one finds that the orbit of the electron is quantized in such a way that the magnetic flux threading the orbit is also quantized as

$$\Phi_n(\mathbf{r}) = BS_n(\mathbf{r}) = (n + \gamma) \frac{2\pi\hbar}{e} = \Phi_0(n + \gamma) \quad (\text{A.39})$$

where $\Phi_0 = \frac{h}{e}$ is a quantum unit of magnetic flux and n is an integer. The area of the electron orbit $S_n(\mathbf{r})$ in real space can be further related reciprocal-space area $S_n(\mathbf{k})$ through

$$S_n(\mathbf{k}) = \frac{1}{B\ell^4} BS_n(\mathbf{r}) = \frac{e^2 B}{\hbar^2} \Phi_n(\mathbf{r}) = \frac{2\pi e B}{\hbar} (n + \gamma) \quad (\text{A.40})$$

which implies that $S_n(\mathbf{k})$ is also quantized.

The quantity γ that we have used in the above equations is quantum correction term. As function of energy E and magnetic field B it is expressed as:

$$\gamma(E, B) = \gamma_M + \gamma_B = \frac{1}{2} - \frac{\Gamma(E)}{2\pi}$$

where the first term, referred to as the Maslov term, equals $1/2$ and can be thought of as the zero-point correction of the harmonic oscillator. The second term is the Berry phase contribution, a term obtained from the work of Roth and others [181–183]. They found that Γ relates to the Berry phase that a Bloch electron acquires during its cyclotron motion. The Berry phase is given as

$$\Gamma = i \oint_C d\mathbf{k} \cdot \langle u_{\mathbf{k}} | \nabla_{\mathbf{k}} u_{\mathbf{k}} \rangle$$

in terms of the Bloch function $u_{\mathbf{k}}(\mathbf{r})$, and is calculated along the cyclotron orbit C . For Schrödinger electrons the Berry phase is obtained as zero, while it is π for Dirac electrons in graphene and the TSS of TI materials. This implies that a special scenario arises for Dirac electrons in terms of the area of the cyclotron orbit in k -space since the term γ goes to zero instead of the usual value of $1/2$.

To get a further insight into the above relations, we imagine the area of the cyclotron orbit to be the end faces of a cylindrical tube, this tube will intersect a 3D spherical Fermi surface for a specific energy value. For a magnetic field in the z direction [see Fig. A.6.11(a)] we can obtain the value of this energy by using Eq. A.40 where $S_n(\mathbf{k}) = \pi k_n^2$ and energy (E) and \mathbf{k}_n are related by a parabolic dispersion; $\gamma=1/2$. Hence the energy at \mathbf{k}_z of the tube is given as

$$E(n, k_z) = \hbar \frac{eB}{m_{\text{eff}}} \left(n + \frac{1}{2} \right) + \frac{\hbar^2}{2m_{\text{eff}}} k_z^2 \quad (\text{A.41})$$

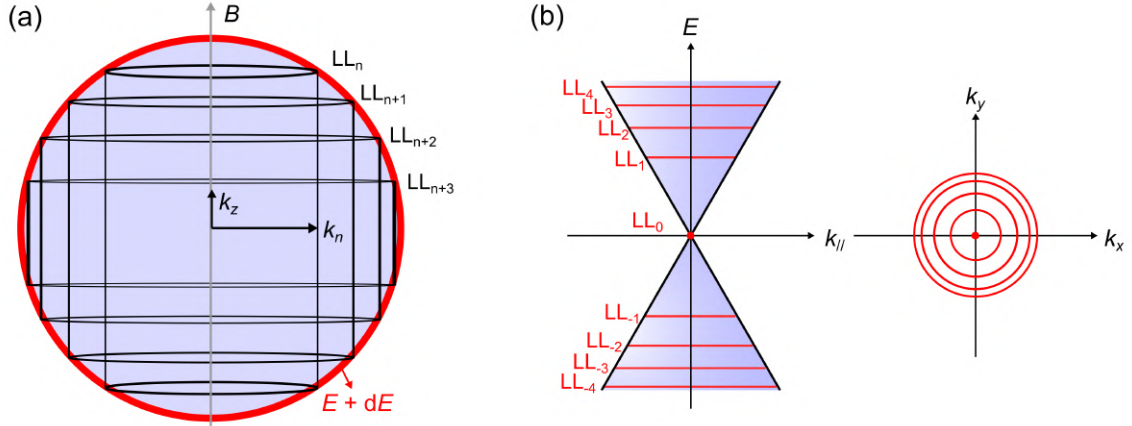


Figure A.6.11: Landau levels in 3D parabolic band and 2D linear band. (a) Intersection of Landau tubes with the 3D Fermi surface in k -space. The magnetic field direction is along z axis. (b) Landau levels for a 2D state with Dirac dispersion. Each circle represents a Landau level.

The electrons can occupy only these discrete energy values, also known as Landau levels (LLs). For a particular magnetic field, the LLs correspond to all the tubes that can intersect the Fermi surface [see Fig. A.6.11(a)]. With increasing magnetic field, the radius of each tube increases and hence the energy of the n th LL shifts. The area of the part of the tube that lies between the constant energy contours E and $E + dE$ gives the number of states contained in each LL.

By setting $k_z = 0$ in Eq. A.41 one can also obtain the LLs for a parabolic 2D state. However a more interesting case, as pointed before, is presented by the 2D linear state (Dirac dispersion). The energy of LLs of this state can be obtained similar to the parabolic case but by taking the linear dispersion instead and a Berry phase of π . The energy of the n -th LL is given as

$$E(n) = E_D + \text{sgn}(n)v_F\sqrt{2eB\hbar|n|} \quad (\text{A.42})$$

which encodes the unique signature of Dirac electrons, i.e., the energy of the LLs varies as $\sqrt{|n|B}$ and not nB (obtained for Schrödinger electrons), meaning that the energy difference between the LLs are not same and decreases with increasing n . Another feature which helps to identify the Dirac electrons is the nature of the zeroth LL since it stays independent of the magnetic field. We demonstrate these aspects by using a spectroscopy dataset taken on the surface of $(\text{Bi}_{1-x}\text{Sb}_x)_2\text{Te}_3$ thin film [Fig. A.6.12(a-c)]. The peaks in the LDOS spectrum can be attributed to the LLs and their positions give the energy E_n of each LL. In Fig. A.6.12(c) we find the energy of the LLs to vary linearly as a function of the scaling variable \sqrt{nB} , as expected for a Dirac dispersion. However, a more interesting observation is the deviation of the zeroth LL from this straight line, which suggests that the band acquires a finite mass term (m_{eff}). This deviation from an ideal Dirac dispersion can be

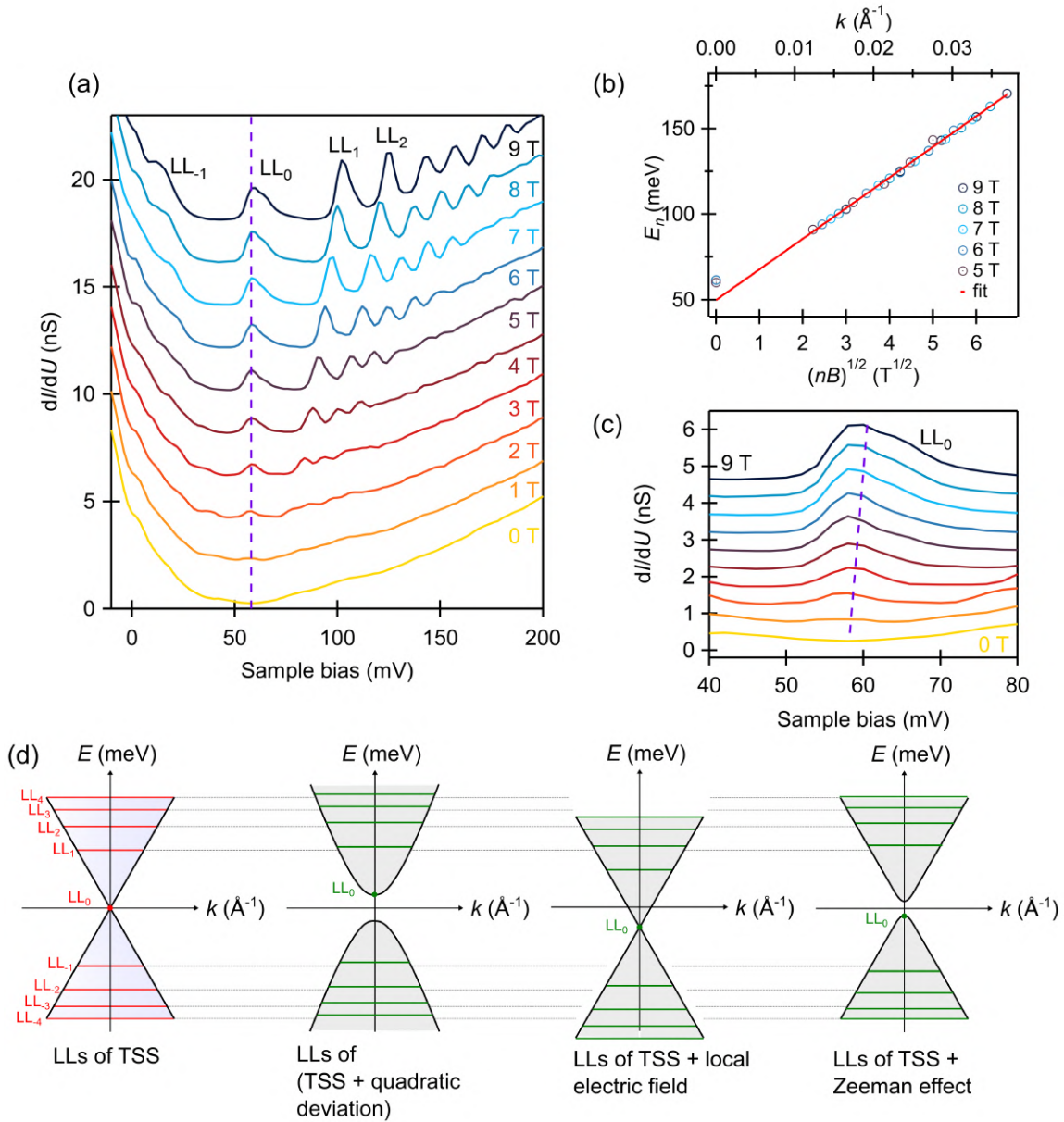


Figure A.6.12: Factors responsible for modifying the LL energies of the TSS. (a) dI/dU spectra acquired on the surface of $(\text{Bi}_{1-x}\text{Sb}_x)_2\text{Te}_3$ thin film, showing peaks that can be associated with LL formation. The spectra are offset vertically for clarity. The applied magnetic field is indicated for each spectrum. The dashed violet line helps to trace the zeroth LL expected at the Dirac point. (Data from J. Brede.) (b) Scaling analysis of the energy of the LLs from (a). The zeroth LL deviates from the linear relation. (c) Visualization of the variation in position of the zeroth LL as a function of magnetic field. (d) Schematic depiction of the LLs for the TSS under the influence of different factors.

approximated by considering a quadratic term in the dispersion relation. Naturally, this modifies E_n values by a term that is proportional to the magnetic field ($E \propto \frac{\mu_B B}{m_{\text{eff}}}$), and the effect is prominent for E_0 .

A closer look at the zeroth LL as a function of magnetic field [panel (c)] shows that the energy varies around the mean value of 61 meV and a single linear term is not enough to describe the variation. This leads us to consider other factors which can influence the energy positions of the LLs, namely the presence of a local electric field and the Zeeman term [see schematic depiction in panel (d)]. We discuss these factors based on Refs. [184–187]. A local electric field can arise from potential variations due to structural and charge inhomogeneities or can be simply due to the STM tip [185] which is biased with respect to the sample. The primary task is to identify the source of this potential variation and then be able to model it accordingly. For example in Ref. [184], a case of well defined potential variation occurs due to 1D structural buckling on the surface of Bi_2Te_3 with a periodicity of 100 nm. The energy of the zeroth LLs was found to be shifted by as much a 12 meV while traversing the structural stripes. The higher energy levels either showed a smaller or no offset in energy as a function of position. They understood the behaviour of the LLs based on the spatial extent of the LL wavefunction: for higher indices the larger spread of the wavefunction meant that it became immune to potential variations whose length scale was smaller. On the other hand the potential landscape was more complicated on the surface of Bi_2Se_3 , as presented in Ref. [186] and had to be extracted by tracing the spatial variation in energy of the zeroth LL. Hence only after careful experimental characterization followed by modelling can the consequence of the spatial potential variation on the LLs of the TSS be extracted.

If it is possible to independently eliminate the effect of m_{eff} and potential variation, one may observe the genuine Zeeman shift of the LLs which occurs due to the coupling of the electron spin with the magnetic field. Since the TSS lacks spin degeneracy, the Zeeman effect only leads to an energetic shift of the LLs except for the zeroth LL which splits. The Zeeman energy term varies linearly with magnetic field being equal to $\frac{1}{2}g_s\mu_B B$, where g_s is the electron g -factor of the TSS. The Zeeman effect is most pronounced for the zeroth LL and decreases rapidly with increasing LL index. Investigating the Zeeman effect on LLs is best done with spin polarized STM as this should help to visualize the spin-magnetization distribution of the of the cyclotron orbit of the LL.

For the dataset presented in Fig. A.6.12(a), a simple linear fit for E_n against \sqrt{nB} gives values of Dirac point (DP) energy as 49 ± 0.8 meV and a Fermi velocity (v_F) of $5 \pm 0.05 \times 10^5$ m/s. The latter is higher than that reported in Ref. [188]. Note that we can improve the quality of the fit by including the additional terms discussed above, which yields $E_{\text{DP}} = 60 \pm 0.6$ meV, $v_F = (3.5 \pm 0.1) \times 10^5$ m/s, $m_{\text{eff}} = 0.20 \pm 0.2$ and a g_s of 10. However, we stress again that careful experiments are required to segregate the different sources which shift the LL energies. It possible that two terms shift the levels in opposite directions and thereby will lead to an effective cancellation. Detailed experiments were not done for the LL dataset presented here.

In this thesis we observed LLs only the surface of $\text{Sr}_x\text{Bi}_2\text{Se}_3$ and in particular near E_F

and were attributed to higher indices. This enhancement of the LL peaks near E_F has been observed in other TIs [184] as well as graphene [189] and Bi(111) thin films [190]. The explanation that is commonly accepted is that the quasiparticle lifetime becomes longer near E_F which can be due to electron-electron interactions [191, 192] or a decrease in electron-phonon coupling. Estimates of such lifetime for zero field give ~ 20 fs/eV [189], which is expected to increase in the presence of magnetic field from stronger electron-electron interactions.

LL peaks in spectroscopy should also show an enhancement with increasing magnetic field and a smaller LL-index n . This is understood with the help of the magnetic length $\ell = \sqrt{\frac{\hbar}{eB}}$. Twice the magnetic length forms the diameter of the cyclotron orbit in real space (this also gives the spatial extent of the LL wave function). For higher magnetic fields where the cyclotron orbit becomes less than or equal to the mean free path of the electrons in the system, it means that the electron has a lesser probability of being scattered. Similar argument is applicable for lower LL-indices since the width of the orbit is $\propto \ell\sqrt{2|n|}$ for a Dirac system.

We did not observe any LLs on the surface of n -type Bi_2Se_3 crystals, $\text{Cu}_x\text{Bi}_2\text{Se}_3$ and most $\text{Sr}_x\text{Bi}_2\text{Se}_3$ pieces that were measured as a part of this thesis. A possible explanation could be that the strong electric field that exists between the STM tip and sample causes a widening of the cyclotron orbit [185] which may ultimately break the orbit through scattering effects. Another possibility, entirely unrelated to the latter case, is that various scattering channels exist for the TSS (including inelastic electron-phonon processes) due to impurity bands which can arise from the large amount of native and dopant induced defects that are present in these samples. These bands may exist near the surface state and maybe lead to broadening and even total suppression of the LL peaks through scattering effects. It is important to note that these impurity bands as well as a large amount of bulk carriers are not expected for the TI thin films where LLs of the TSS are observed consistently and reproducibly.

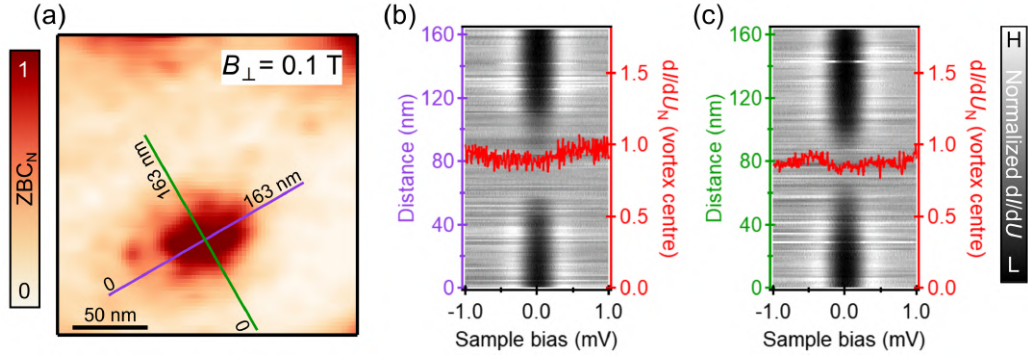


Figure B.1.13: (a) Normalized ZBC map at $B_{\perp}=0.1$ T showing a single isolated vortex. Data was acquired as a STS-grid in the I - V mode for 30 by 30 pixels, covering an area of 200 by 200 nm². The image shown here is obtained after interpolation and smoothing. (b) Normalized dI/dU spectra along the purple line (long axis) in (a). Each horizontal row is a dI/dU spectrum vs sample bias. The color scale represents the dI/dU intensity and the vertical axis shows the distance along the purple line in (a). The red dI/dU spectrum superimposed on the map is taken at the center of the vortex and highlights the absence of any vortex bound states. (c) A similar map as done in (b) for the green line (short axis) in (a). The superconducting gap disappears over a longer distance along the long axis of the vortex in comparison to the short axis, as expected. Stabilization parameters: $U = 1$ mV, $I = 50$ pA (100 sweeps) for (a); $U = 3$ mV, $I = 50$ pA (200 sweeps) for (b) and $U = 3$ mV, $I = 50$ pA (200 sweeps) for (c).

B.1 Additional data on CPSBS and PSBS

Absence of vortex bound states

No vortex core states were observed for a single isolated vortex in CPSBS, as shown in Fig. B.1.13. This is expected for a dirty superconductor [134]. We estimate the mean free path (l) in the sample to be 1.2 nm using the relation $l = \hbar k_F / \rho_0 n e^2$ (the relation holds for a spherical Fermi surface and values for residual resistivity (ρ_0) and carrier density (n) are taken from Ref. [57]). The mean free path in CPSBS is an order of magnitude smaller than the average in-plane coherence length (ξ_{GL}) of 25 nm indicating that the sample is in the dirty limit.

Superconducting stripe pattern

In this section we discuss the signatures of superconductivity observed on the surface of the second sample (S-II). We did not observe a vortex lattice on this sample unlike for S-I, which was discussed in the main text. Instead, we found superconducting regions, roughly 100 nm in width, separated by non-superconducting regions. Moreover, the superconducting areas extended in one direction in a stripe fashion, as seen in the normalized ZBC map of Fig. B.1.14(a). Following the lineprofile from Fig. B.1.14(a) the largest gaps

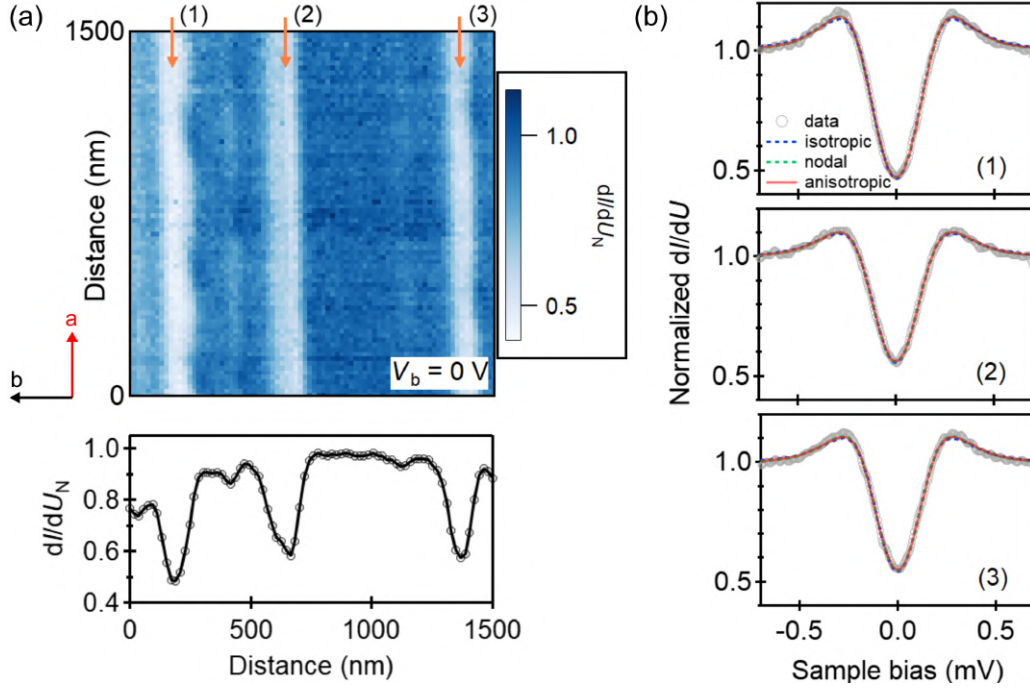


Figure B.1.14: (a) Normalized ZBC map over a field-of-view of 1500 by 1500 nm², taken with a resolution of 80 by 80 pixels. STS grid was obtained in the I - V mode with stabilization parameters $U = 1.5$ mV and $I = 100$ pA. A vertically averaged lineprofile of the map showing a significant suppression in ZBC for three regions, is given below. (b) Normalized conductance spectra for an energy range around zero-bias (gray open circles) is shown for regions marked (1), (2) and (3) in (a), respectively. The gray traces are obtained by averaging 80 spectra in the respective regions along a vertical line. The spectra show a superconducting gap. They are fit for three different gap functions: isotropic (blue dashed), nodal (green dashed) and anisotropic (red), as described in the main text.

	T_{eff} (K)	Γ (meV)	Δ_k (meV)	Δ_0 (meV)	Δ_1 (meV)
Trace 1					
isotropic	0.7 *	0.029	0.15		
nodal	0.7 *	0.005	0.20	0	0.20
anisotropic	0.7 *	0.01	0.20	0.02	0.18
Trace 2					
isotropic	0.7 *	0.038	0.14		
nodal	0.7 *	0.016	0.19	0	0.19
anisotropic	0.7 *	0.021	0.19	0.02	0.17
Trace 3					
isotropic	0.7 *	0.030	0.13		
nodal	0.7 *	0.01	0.18	0	0.18
anisotropic	0.7 *	0.015	0.18	0.02	0.16

Table 3: Fitting parameters for trace 1, 2 and 3 from Fig. B.1.14(b). The parameter T_{eff} is held fixed in each case, indicated by the symbol *. The error bars obtained from the fitting routine are on the order of a few μeV .

are identified around 190, 660 and 1367 nm with very small gaps about 417 and 1120 nm. These superconducting stripes were found to be oriented perpendicular to the structural one-dimensional stripe. Strangely the latter was not observed in this particular area. Its orientation for the sample was determined from a non-superconducting region. To understand if there is a correlation between appearance of superconductivity and the absence of the structural stripe more statistics is required.

In Fig. B.1.14(b) spectra from the three superconducting stripe regions of panel (a) are shown. We show fits to different gap functions, as done for the superconducting gap spectrum of the vortex region in the main text, with fitting parameter values given in Table 3. Fits to isotropic and nodal gap look good and are qualitatively similar. The gap size obtained from the fits are 38% and 50% of the bulk gap value, respectively. Hence the superconducting state observed here is not fully developed. Further, proximity of the superconducting region to normal conducting regions can lead to an inverse proximity effect and consequently a small gap. Hence, based on the gap size one cannot ascertain the gap structure that is realized. Therefore we analyze the values obtained for the Γ parameter used in the fit.

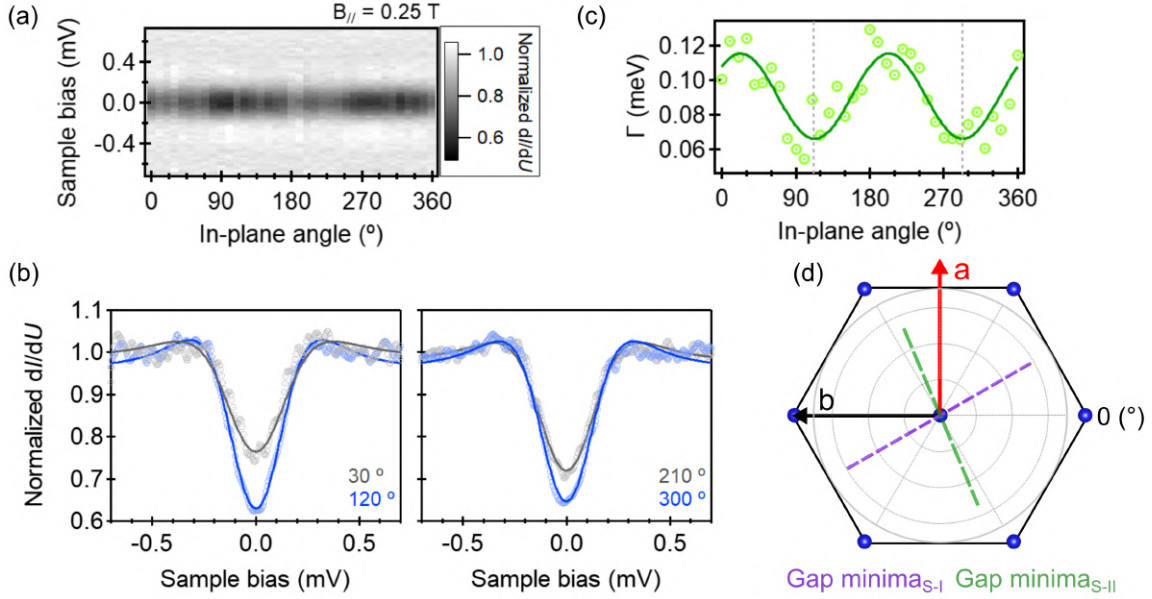


Figure B.1.15: (a) Waterfall plot showing the superconducting gap measured in region (1) of Fig. B.1.14(a), in the presence of an in-plane field of 0.25 T. Orientation of the field is given by the in-plane angle, measured from the horizontal axis. The error bar for the in-plane field alignment is between 5 - 10°. (b) Superconducting gaps from (a) with the corresponding fits are shown for 30, 120, 210 and 300°. The superconducting gaps are fit using Γ as the only fitting parameter; $T_{\text{eff}}=0.7$ K and $\Delta=0.14$ meV. (c) A twofold oscillation in Γ is observed. Data is fit (green line) with a cosine function of the form $f(x) = y_0 + A\cos^2(\theta + \Phi)$, to obtain minima at 113° and 293°. (d) Position of minima in the superconducting gap structure obtained for S-I (purple dashed line) and S-II (green dashed line) with respect to the top Se lattice and the monoclinic a and b axes.

The Γ term was originally introduced by Dynes *et al.* [167] to take into account a finite quasiparticle (QP) lifetime from recombination processes. However, such effects are negligible in both weak and strong coupling superconductors. Instead, for a real experiment the Γ term is used to account for broadening from extrinsic and intrinsic sources. In principle, we have calibrated our experimental setup and accounted for extrinsic sources of broadening in the effective junction temperature parameter. Hence, the Γ value obtained from the fit should reflect intrinsic sources only. In this case inelastic scattering process which lead to pair breaking and QPs due to nodes or anisotropy of the gap function can be considered as intrinsic sources. Γ values of the order of 10 μeV is expected for superconductors having a nodal gap [193], making the obtained Γ values of 29-38 μeV for an isotropic gap larger than expectation. Reasonable Γ values of 5-16 μeV are achieved for the case of a nodal gap. Note that the gaps can be fit equally well with an anisotropic gap function which returns similar Δ values as for the nodal case, but with slightly larger Γ values, as expected.

In order to obtain conclusive evidence for the presence of nodes in the gap and the possibility of the nodes being lifted, we measured the response of the gap in the presence of an in-plane magnetic field (B_{\parallel}) of 0.25 T. The field is further rotated in the ab -plane of the crystal [Fig. B.1.15(a)]. The azimuthal angle of B_{\parallel} with respect to the monoclinic crystal axes for the sample is given in Fig. B.1.15(d).

Despite the absence of any in-plane vortices (area being too small for a flux tube), we observe a twofold variation in the gap spectra with the direction of B_{\parallel} [Fig. B.1.15(a)]. Spectra for select symmetric angles are shown in Fig. B.1.15(b) to demonstrate the variation in gap size and symmetry with respect to the angle of B_{\parallel} .

The influence B_{\parallel} on the measured superconducting gap can be understood based on the Volovik and Zeeman effects. The former effect has been discussed for nodal superconductors [74]. The presence of an in-plane field leads to an induced supercurrent running perpendicular to the field direction. The supercurrent with velocity \mathbf{v}_s leads to a Doppler shift in the energy (ε) of a quasiparticle with momentum \mathbf{k} as $\varepsilon(\mathbf{k}) \rightarrow \varepsilon(\mathbf{k}) - \hbar\mathbf{k}\cdot\mathbf{v}_s$. This effect leads to the generation of maximum number of quasiparticles when the field is oriented perpendicular to a gap node/minima as compared to any other direction, leading to a maximum smearing of the gap edge for an integrated DOS measurement. The Zeeman depairing effect has similar consequences on the gap. In this case the Zeeman energy scale for $B_{\parallel}=0.25$ T is $29 \mu\text{eV}$, comparable to the minimal gap magnitude from the anisotropic fit.

The consequences of the Volovik and Zeeman effect on the gap is extracted from the data by fitting the spectra in Fig. B.1.15(a) using Γ as the only fitting parameter while keeping T_{eff} and Δ constant. This allows us to directly see the change in the amount of quasiparticles as a function of the field direction. The quality of the fit is shown in Fig. B.1.15(b) for select spectra and the Γ values for all spectra are plotted in Fig. B.1.15(c). We observe a twofold symmetry in Γ with respect to the field direction with an anisotropy of 45%. The smallest value Γ or the least amount of quasiparticles are expected when the field points in the direction of the gap node/minima which occurs around 113° and 293° , based on a cosine fit to the data points. Identical results are obtained irrespective of the gap function used for the fit. Lastly, we identify the orientation of the gap node/minima with respect to the crystallographic axes in Fig. B.1.15(d). The gap nodes/minima are rotated away from the mirror plane by 23° . Since they are not mirror symmetry protected it is reasonable to assume that even in this case the nodes are lifted or in other words we conclude an anisotropic gap structure for S-II. We also point out that the position of the gap minima in S-I (deduced from the vortex anisotropy) and in S-II (deduced from in-plane field anisotropy) are not the same, although they are both rotated away from the mirror plane by 60° and 23° , respectively.

Doppler shifted LDOS in a magnetic field

In the last section we explained that the differential conductance (dI/dU) for a nodal superconductor in the presence of an in-plane magnetic field B_{\parallel} , depends on the orientation

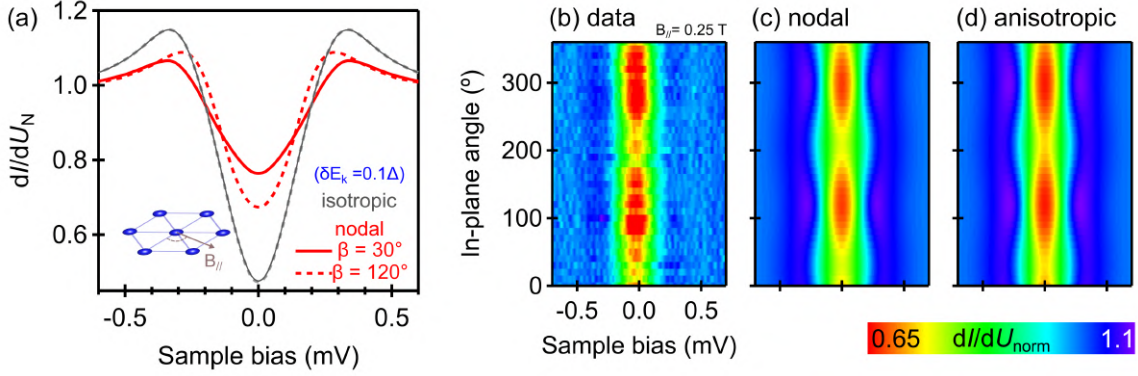


Figure B.1.16: (a) Simulated curves for the SC LDOS for $T_{\text{eff}}=0.7$ K, $\delta E_k=0.1\Delta$ for isotropic (gray traces) and nodal (red traces) gap functions. (b) Normalized conductance as a function of the in-plane angle of a $B_{||}$ field of 0.25 T. (c-d) Simulation of the normalized conductance for different gap functions, i.e., nodal (c) and anisotropic (d).

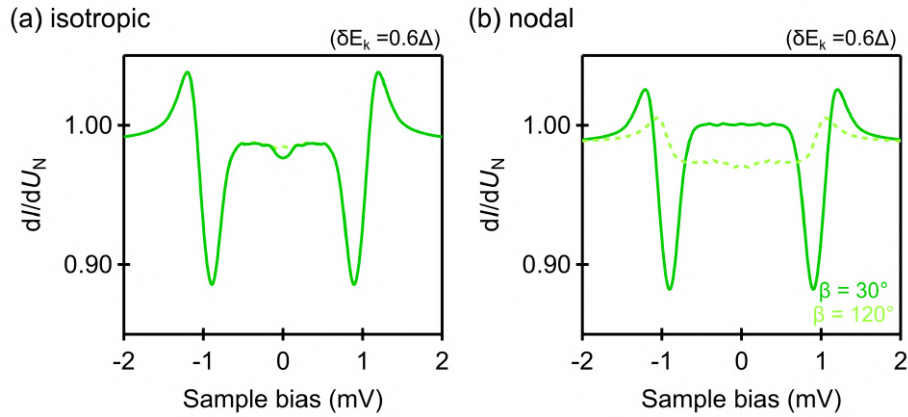


Figure B.1.17: Simulated spectra for the LDOS for $T_{\text{eff}}=0.7$ K, $\delta E_k=0.6\Delta$, for isotropic (gray traces) and nodal (red traces) gap functions.

of B_{\parallel} with respect to the nodes in the gap. The variation in the dI/dU spectra due to the Volovik effect was accounted for by the broadening parameter Γ . Here, we modify the BCS DOS to explicitly incorporate this effect [194–196]. Note that the approach outlined in Refs. [194, 195] is applied for an Abrikosov vortex lattice i.e., where the inter-vortex distance is much larger than the vortex size, in the presence of a magnetic field which can be both out-of-plane or in-plane. While there are no vortices to be observed in the superconducting stripe region, one can still consider the supercurrent running along the edge of the stripe in analogy to the circulating supercurrents outside the vortex core. The origin and consequences of the supercurrent are discussed below.

An external magnetic field is excluded from the bulk of a superconductor except for a layer of thickness of the London penetration depth λ , owing to the Meissner effect. This is possible due to the flow of a supercurrent (moving superconducting fluid) in the same length scale as λ which generates a magnetic field in a direction opposite to the external field. Associated with this supercurrent is a position dependent supercurrent density $\mathbf{j}_s(\mathbf{r})$ which equates to the product of the electron-pair density $\rho_s(\mathbf{r})$ and the superfluid velocity $\mathbf{v}_s(\mathbf{r})$. A non-zero superfluid velocity results in a 'Galilean boost' or a 'Doppler shift' in the energy of a quasiparticle in the laboratory frame of reference, previously referred to as the Volovik effect. The energy scale of this shift is given as $\delta E_k = \hbar \mathbf{k} \cdot \mathbf{v}_s$. By including this term in the BCS DOS we modify it as:

$$N_{\mathbf{k}}(E) = |Re[(E - \hbar \mathbf{k} \mathbf{v}_s) / \sqrt{(E - \hbar \mathbf{k} \mathbf{v}_s)^2 - \Delta_{\mathbf{k}}^2}]|. \quad (\text{B.43})$$

Using Refs. [194, 195], $\delta E_k = \hbar \mathbf{k} \mathbf{v}_s = \frac{v\Delta}{\rho} \sin(\phi - \beta)$, where v defines the energy in units of the gap magnitude Δ ; ρ is a length scale in units of the inter-vortex distance, where a value of 0.1 would mean a length of the order of the vortex size; ϕ refers to the angular dependence of SC gap as in the nodal case and β is the angle between the applied in-plane magnetic field and the horizontal axis. For a nodal gap function $\Delta_{\mathbf{k}} \equiv \Delta_0 \cos(\phi)$, a maxima in δE_k occurs for $\phi = \pi/2$ and $\beta = 0$.

In Fig. B.1.16(a) we show simulated curves for Doppler shift energy scale that is 10% of the SC gap (Δ), for isotropic (gray traces) and nodal (red traces) gap functions. A clear difference can be seen between the red traces where the magnetic field is orientated along the antinodes (solid line) and nodes (dashed lines). Hence the data [Fig. B.1.16(b)] that was obtained in the SC stripe region as a function of in-plane field can be well described by the DOS in Eq. B.43 assuming a nodal gap function [Fig. B.1.16(c)]. Better agreement is obtained for an anisotropic gap [Fig. B.1.16(d)].

Using δE_k that is 10% of the SC gap (by fitting a single experimental spectra and optimizing parameters) and k_F of 0.18 \AA^{-1} (ARPES data [103]) we obtain a superfluid velocity (\mathbf{v}_s) of 14 m/s. This value is only $\sim 9\%$ of the superfluid velocity measured 160 nm away from the vortex core in NbSe₂ [196]. Moreover it is orders of magnitude smaller than the value estimated from the applied field value (B) and London penetration depth (λ) of

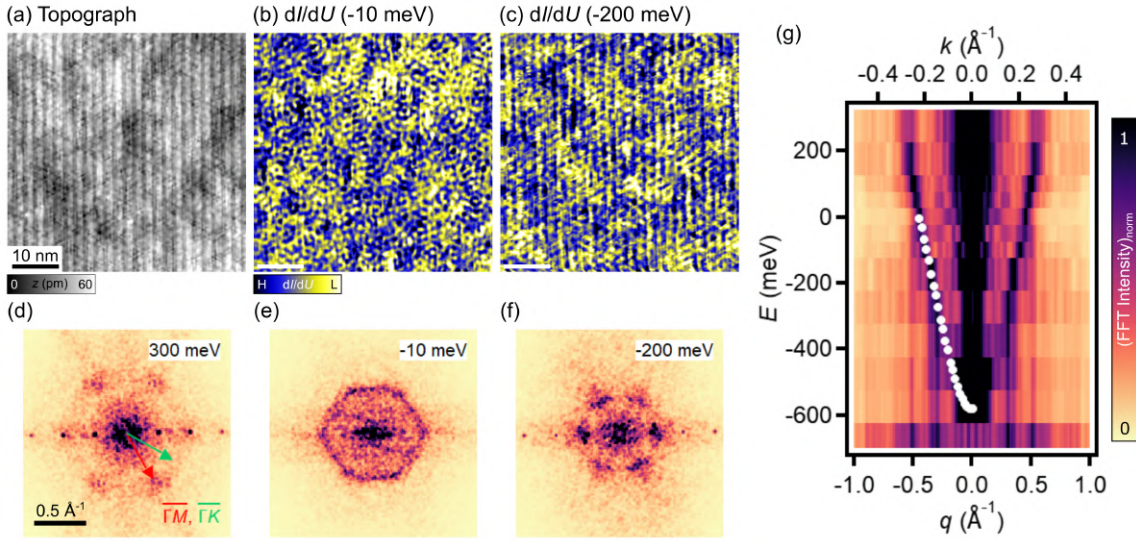


Figure B.1.18: (a) STM topograph on the cleaved surface of PSBS. (b,c) Differential conductance images of the same area as (a) at sample bias of -10 mV (b) and -200 mV (c), showing an intense QPI pattern. Setpoint: 1 nA (a,b); 2 nA (c). (d-f) Fourier transform of differential conductance images at indicated bias voltages. A six-fold symmetric pattern is obtained in the \mathbf{q} -space for all energies with intensity along the $\overline{\Gamma M}$ direction. (g) Linecut along the $\overline{\Gamma M}$ direction for energies given by the vertical scale. The corresponding \mathbf{k} vector is shown on the top axis (for $\mathbf{q}=2\mathbf{k}$). The FFT intensity is normalized to intensity of the \mathbf{q} -vector of interest at E_F . The observed dispersion agrees well with the ARPES data [198] (overlaid white dots) for 1 QL Bi_2Se_3 on top of the PbSe layer upon cleaving the PSBS crystal.

doped Bi_2Se_3 using the relation $\mathbf{v}_s = eB\lambda/2m_e$; which approximates the field strength to be constant and equal to the applied field on the top surface layer [197]. To further examine if such a value is reasonable for the system of CPSBS and in particular the SC stripe region, we need to consider an explicit distribution of the field in the sample.

A stronger effect on the LDOS via the Doppler shift in quasiparticle energies can be observed when the energy scale of the shift is on the order of the superconducting energy gap. The expected shape of the spectra for isotropic and nodal gap structure that is Doppler shifted by 60% of the gap energy is shown in Fig. B.1.17(a,b). Experiments to this end were done on a thin film of Bi_2Te_3 grown on NbSe_2 [197].

Unexpected QPI pattern on PSBS and CPSBS

We performed QPI experiments on the cleaved surfaces of PSBS and CPSBS where standing waves or interference patterns arise due to the elastic scattering of surface states at sub-surface defects and Cu adatoms. Such interference patterns in real space is Fourier transformed to identify characteristic scattering wavevectors which are related to the con-

stant energy contours of the band structure [169, 38] in the most simple approximation (discussion in Appendix A.5). QPI data could be obtained on the $m = 1$ and 2 surfaces as well as the non-superconducting regions of CPSBS. No twofold anisotropy was observed in the scattering patterns in Fourier space for all examined surfaces. This lends support to our claim in the main text that the observed vortex anisotropy does not originate from an anisotropy of the Fermi surface. In the remainder of this section and the following subsections we discuss the QPI data obtained on PSBS, CPSBS and $m=2$ surface in detail.

For an area of $50 \text{ by } 50 \text{ nm}^2$ [Fig. B.1.18(a)] typical dI/dU maps taken at indicated bias voltages are shown in Fig. B.1.18(b) and (c) for the $m=1$ surface on PSBS. Fast Fourier transform (FFT) of dI/dU maps for three selected bias voltages are shown in Fig. B.1.18(d), (e) and (f), respectively. We observe a sixfold symmetric pattern in the Fourier space with intensity along the $\overline{\Gamma M}$ direction for large positive and negative bias. Closer to the Fermi level this pattern transforms into a closed hexagon with intensity peaks showing up along $\overline{\Gamma K}$ direction as well [Fig. B.1.18(e)]. Above 300 meV and below -300 meV the QPI intensity is faint (data not presented).

We further analyze the QPI pattern by taking linecuts of the FFT images along one of the $\overline{\Gamma M}$ direction (averaged over $\pm 1 \text{ \AA}^{-1}$) for a bias range between -600 to 300 mV, resulting in Fig. B.1.18(g). This allows to easily trace scattering vector \mathbf{q} as a function of energy. The corresponding \mathbf{k} -vector is derived from the simple scaling relation $\mathbf{q}=2\mathbf{k}$ which is valid for scattering from \mathbf{k} to $-\mathbf{k}$ of a circular Fermi contour. Despite this crude approximation, the agreement between the obtained dispersion from QPI patterns and ARPES data [white dots in Fig. B.1.18(g)] for $m=1$ surface, is excellent, supporting our simple model. However, contrary to the circular QPI patterns from circular Fermi surfaces on noble metal surfaces [199, 200, 169, 201, 202], we observe the aforementioned hexagonal QPI. Similar QPI patterns are commonly observed on the surface of bulk TIs such as Bi_2Se_3 [176] and Bi_2Te_3 [174, 172, 203], at energies away from the Dirac point, where origin of the QPI-symmetry is explained considering the hexagonal warping of the TI surface state [62, 174, 172, 204]. The hexagonal deformation of the Fermi surface makes contribution from scattering wavevectors that connect regions of high density of states on the constant energy contour to be dominant [204]. Among them, vectors that lead to direct backscattering are strongly suppressed due to the topological protection/spin texture of the surface state, leaving only scattering vectors which connect the isoenergy surface along $\overline{\Gamma M}$ direction (see Appendix A.5 for a sketch). Indeed, a weak hexagonal distortion of the surface state for $m=1$ can be found in the ARPES data [102]. While this can explain why some scattering vectors may become stronger in intensity, it cannot explain the absence of scattering vectors along the $\overline{\Gamma K}$ direction since the band is expected to be spin degenerate.

Another explanation for the observed hexagonal QPI pattern may be found in the structure of the scatterer, which defines the symmetry of the scattering potential [176], as well as the density of scatterers which defines the extent of disorder or scattering rate in the system [205]. For the $m=1$ surface the majority scatters are triangular shaped defects. The triangular shape affects scattering processes in such a way that scattering along $\overline{\Gamma K}$ is suppressed relative to $\overline{\Gamma M}$. A large defect density further adds to this tendency [205].

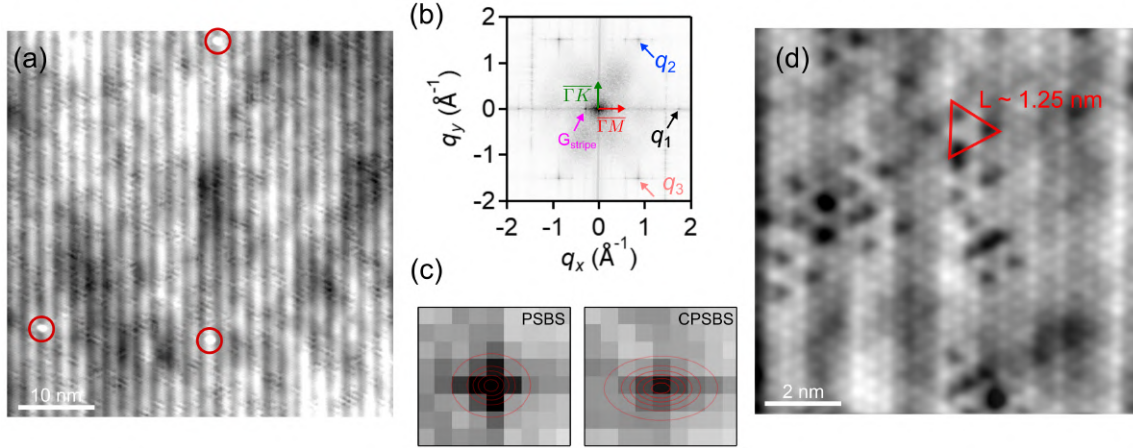


Figure B.1.19: (a) An atomically resolved 50 by 50 nm STM topograph on the cleaved surface of PSBS. The prominent one-dimensional strip along with a large density ($1.2 \times 10^{20} \text{ cm}^{-3}$) of triangular defects and a small amount of adatoms (red circles) are observed. (b) Fourier transform of the image in (a). The three sets of Bragg spots are indicated as q_1 , q_2 and q_3 , respectively. $\overline{\Gamma K}$ and $\overline{\Gamma M}$ directions as well as spots corresponding to the stripe are also identified. (c) Zoom of the stripe spots from the FFT of atomic resolution images taken on PSBS and CPSBS with the 2D Gauss fits. The spots correspond to \mathbf{q} -vectors of 0.28 \AA^{-1} and 0.29 \AA^{-1} , respectively. (d) Atomically resolved image showing the typical defect found in 1 QL Bi_2Se_3 on PbSe. One defect is highlighted by the red triangle.

Note that only scattering processes of wavelength smaller than the defect size is affected by its shape. For the $m=1$ surface the defects are roughly 1.25 nm [see Fig. B.1.19(d)]. Wavelengths smaller than this value amounts to \mathbf{q} values larger than 0.5 \AA^{-1} , observed for QPI patterns at positive sample bias. Hence the shape of the defect is relevant only for QPI patterns at positive energies.

We exclude the possibility that the one-dimensional stripe observed on $m=1$ surface [see Fig. B.1.19(a)] can give rise to the observed QPI pattern, owing to its reduced symmetry. Moreover, the stripe corrugation is found to not change significantly as a function of energy (see Fig. B.1.20), hence it is only a constant background to the observed QPI modulation.

Ultimately, theoretical support is required to compute the joint density of states and the spin-dependent scattering probability based on the ARPES data to understand the contribution of different \mathbf{q} -vectors to the scattering pattern. In the following subsections we discuss some specific aspects which are related to the QPI data.

High symmetry directions, defect density and size

The high symmetry directions, namely $\overline{\Gamma M}$ and $\overline{\Gamma K}$, are identified from the Fourier transform of an atomically resolved STM topograph [Fig. B.1.19(a,b)]. Additionally, three sets of Bragg peaks (q_1 , q_2 and q_3) and two spots (G_{stripe}) corresponding to the one-dimensional

stripe are identified in the Fourier image. We have calibrated this image by forcing all six Bragg spots to lie on the corners of a hexagon of length $2\pi/(\sqrt{3}/2a)$, where a is the in-plane lattice constant of the Se layer (0.417 nm). Using the calibrated FFT image the maxima corresponding to the stripe and Bragg spots were fitted by 2D Gaussian peaks to extract the \mathbf{q} -vectors. G_{stripe} was found to be 0.28 \AA^{-1} , which translates to a real space periodicity (b) of 2.18 nm. This gives a ratio of the lattice vectors a/b as 0.192, differing from the literature ratio by 1% only. A zoom of the stripe spots on the PSBS and CPSBS (NSC) surfaces with the respective 2D Gauss fits are shown in Fig. B.1.19(c). The stripe spots on CPSBS are less intense due to the disorder on the surface. The horizontal distortion of the spot is an artifact.

The triangular defects in Fig. B.1.19(a) are more clearly seen in the zoom image in Fig. B.1.19(d). The major triangular defect is indicated by the red triangle, whose length corresponds to approximately 3 atomic lengths, i.e., 1.25 nm. This defect has not been seen in STM studies of bulk Bi_2Se_3 crystals [146] and occurs exclusively in PSBS. As discussed in Ref. [146], the lateral size of the defect on the surface can be used to infer the depth of the defect with respect to the top layer. The observed defect in this case is somewhat larger than three atomic sites meaning that it can be a substitution defect in the Bi(4A), Se(5B) or PbSe layer. The defect that is considered in the PbSe layer is a Bi atom sitting on a Pb site, i.e., a Bi_{Pb} antisite defect. First-principles calculations [206] have shown that a high density of Bi_{Pb} antisite defects strongly shifts the PbSe bands down in energy thereby helping to expose the Bi_2Se_3 derived bands around the Γ point. These defects modify the chemical formula of the material to $(\text{Bi}_x\text{Pb}_{1-x}\text{Se})_5(\text{Bi}_2\text{Se}_3)_6$ with $x=0.38$ being the optimum value based on defection formation energy calculations. From Fig. B.1.19(d) we find atleast 12 triangular defects in the area of 100 nm^2 corresponding to a defect density of $1.2 \times 10^{20} \text{ cm}^{-3}$ (from another image it is found to be $2 \times 10^{20} \text{ cm}^{-3}$). These numbers are then used to find the number of defects (n_{def}) expected for a unit cell area of 0.89 nm^2 . For the formula unit, x value = $n_{\text{def}}/5 = 0.1/5 = 0.02$. This number is 20 times lower than the concentration expected from the calculations. Therefore it possibly not a Bi_{Pb} antisite defect. The proper identification with the help of *ab initio* simulations will be done in future.

Stripe corrugation

In Fig. B.1.20 we note the reduced stripe corrugation from the $m=1$ to the $m=2$ surface, the average value being $11 \pm 0.4 \text{ pm}$ and $3.6 \pm 0.7 \text{ pm}$, respectively. While the apparent corrugation did not show any significant dependence on the sample bias for the $m=1$ surface, the apparent corrugation was found to be reduced by 50% at positive bias for $m=2$ surface.

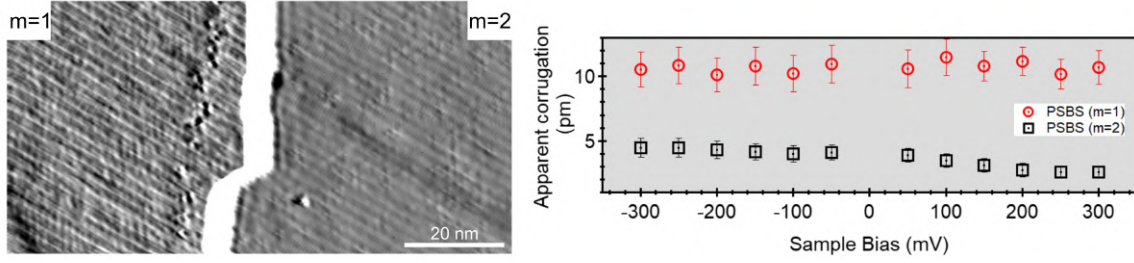


Figure B.1.20: Apparent corrugation of the one-dimensional stripe on the $m=1$ and $m=2$ surfaces. Left panel shows a differentiated STM topograph image for a step edge between $m=1$ and $m=2$ surface.

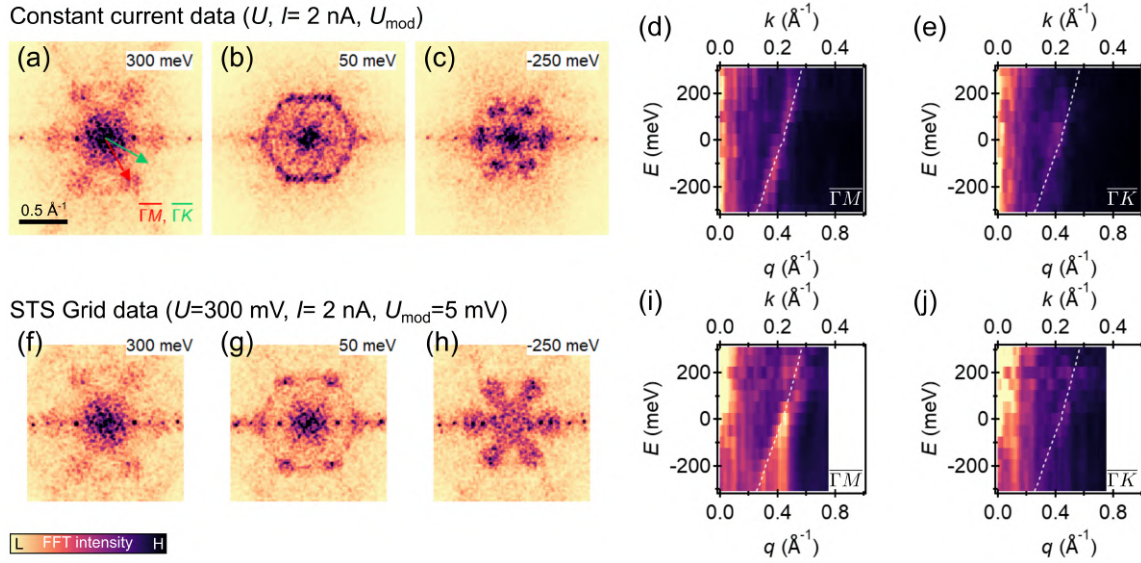


Figure B.1.21: (a-c, f-h) Fourier transform of dI/dU maps for indicated bias voltages using different measurement techniques, namely constant current lock-in mapping (a-c) and STS grids (f-h). The resulting energy dispersion in \mathbf{q} -space is shown in (d, e) and (i, j) for the two techniques, respectively. White dashed line corresponds to ARPES data [198] on the $m=1$ surface. Constant current data was acquired with a setpoint current of 2 nA, lock-in parameters: $f = 6.67$ kHz and U_{mod} of 5, 30 and 50 mV. STS grid was obtained under stabilization parameters of $U = 300$ mV, $I = 2$ nA and lock-in parameters: $f = 6.67$ kHz and $U_{\text{mod}} = 5$ mV_p.

Data acquisition mode

QPI data can be acquired in three different modes, namely constant height, constant current and spectroscopy grid (STS grid). It is not possible to take QPI data in the constant height mode where the tip height is stabilized only at the first image point, on $m=1$ and 2 surfaces, due to the 1D-stripe which causes a variation in the actual tip sample distance following its own modulation. The exponential dependence of the tunneling current on the tip sample distance results in the stripe pattern dominating over any QPI signal. We can overcome this challenge by using the constant current mode where the tip height is stabilized to the same current value at each point. The current value at a single point is a convolution of the integrated density of states and the transmission function (dependent on the tip-sample distance) of the tunnel junction. This means at a point in-between the stripe where the density of states is lower the tip is brought closer to the sample by the feedback circuit to keep the current unchanged. As a result the dI/dU or QPI signal in-between the stripe is no longer exponentially attenuated. However, the dI/dU signal still contains the stripe modulation through the transmission function. By the additional trick of using the feedback settings with a shorter reaction time it is possible to filter out the stripe frequency from the dI/dU map.

A complementary data acquisition mode is the STS-grid. In a STS-grid the tip height is stabilized at each pixel to the same bias value for all energy maps, unlike the constant current map, where the bias is tied to the map energy. However, since the 1D-stripe is largely independent of bias, it should influence the constant current and STS-grid maps in the same way.

Dispersing features identified in the constant current Fourier images [Fig. B.1.21(a-e)], in particular the $\overline{\Gamma M}$ direction, are reproduced in the STS grid data [Fig. B.1.21(f-j)] on the same sample with same tip. The surface state dispersion along $\overline{\Gamma M}$ agrees well with the ARPES data (white dashed line). Intensity along $\overline{\Gamma K}$ only appears near the Fermi level as a strong feature in the constant current map and a faint one in the STS-grid. There are two possible explanations. It can have a trivial source since length of the associated \mathbf{q} -vector in real space is roughly equal to the size of the defects or it originates from states that have a larger tunneling decay constant as compared to the states which give rise to intensity along $\overline{\Gamma M}$.

Note that a slightly larger \mathbf{q} -vector length (difference of 0.04 \AA^{-1} or $\sim 10\%$) is obtained in STS grid data [Fig. B.1.21(f-h)] as compared to the constant current [Fig. B.1.21(a-c)] data. This could be a result of piezoelectric creep during the long acquisition time for the STS grid. However, by comparing the distance between two defects in the topograph image from the STS grid and constant current, measured as 35 nm and 35.4 nm, respectively, we found the grid data to be compressed by only by 1%.

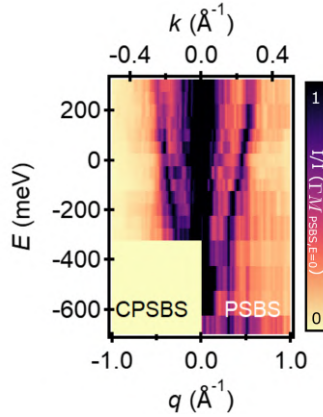


Figure B.1.22: Comparison of the dispersion on the surface of PSBS (right) with that on the non-superconducting surface of CPSBS (left). The QPI intensity for PSBS and CPSBS is normalized to the intensity of the \mathbf{q} -vector of interest for PSBS at E_F . Data was acquired in the constant current mode with a setpoint current of 2 nA. For a given bias the QPI map on PSBS and CPSBS have the same lock-in modulation voltage. Lock-in parameters: $f = 6.67$ kHz and U_{mod} of 5, 30 and 50 mV.

QPI on CPSBS

The single parabolic band on the $m=1$ surface observed using ARPES [198] and QPI analysis (Fig. B.1.18), persists on the cleaved non-superconducting surface of CPSBS (see Fig. B.1.22).

Suppressed QPI intensity with increasing Bi_2Se_3 QLs

- $m=1$ to $m=2$

In Fig. B.1.23 we show QPI maps acquired simultaneously on the $m=1$ and $m=2$ surface by scanning across a step edge of QL height. Such step edges can be found by cleaving a sample which consists of 3 Bi_2Se_3 QLs encapsulated by PbSe layers. QPI data on the two surfaces are separately Fourier transformed to obtain the energy dispersion in \mathbf{q} -space [Fig. B.1.23(e)]. On the $m=1$ surface the \mathbf{q} -vector length is similar to what was discussed in Fig. B.1.18 and also compares well with the ARPES data (white dots) [198]. On the other hand QPI pattern on the $m=2$ surface is observed only for bias voltages ~ -100 meV and above, where two separate \mathbf{q} -vectors are identified (indicated by green and blue arrows). The outer (larger) \mathbf{q} -vector most likely corresponds to scattering involving the surface state and the inner (smaller) \mathbf{q} -vector originates from the conduction band. The observation that scattering from the surface state on the $m=2$ surface can be observed only in the presence of a second band could be an indication of the topological character of the former. For a topological band while scattering is forbidden from \mathbf{k} to $-\mathbf{k}$ due to the opposite spin

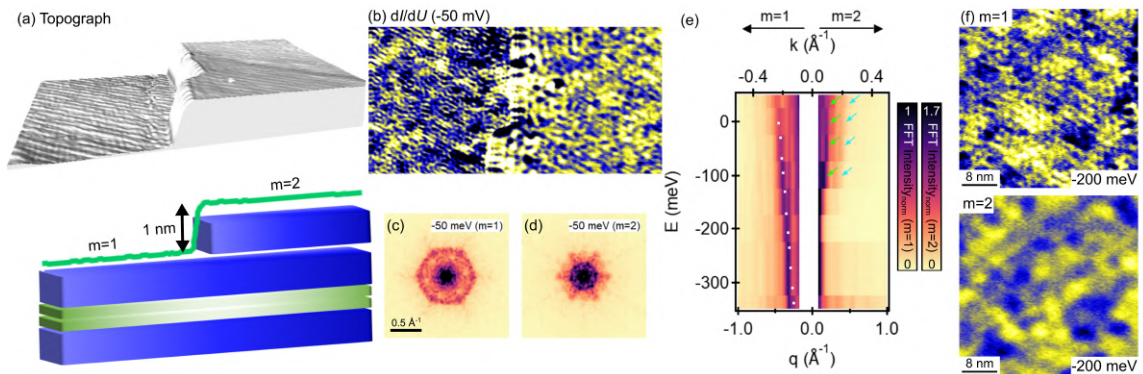


Figure B.1.23: (a) A 3D rendered STM topograph image (50 nm by 100 nm) showing a step edge between a $m=1$ and $m=2$ surface. The cartoon of Bi_2Se_3 and PbSe blocks sketches the scenario of a QL step height. The green trace is the lineprofile of the topograph. (b) QPI map simultaneously acquired on the two different surfaces across the step edge at -50 meV. (c, d) Fourier transform of part of the image (b) corresponding to the $m=1$ surface (c) and $m=2$ surface (d). Both images have been sixfold symmetrized. (e) Energy dispersion for $m=1$ surface (left part) and $m=2$ surface (right part). The corresponding \mathbf{k} value is obtained from the scaling relation $\mathbf{q}=2\mathbf{k}$. White dots correspond to ARPES data [198] on $m=1$ surface. For the $m=2$ surface, features are indicated with green and blue arrows. (f) QPI map taken at a bias voltage of -200 meV on the $m=1$ (upper panel) and $m=2$ (lower panel) surfaces. Setpoint: 500 pA.

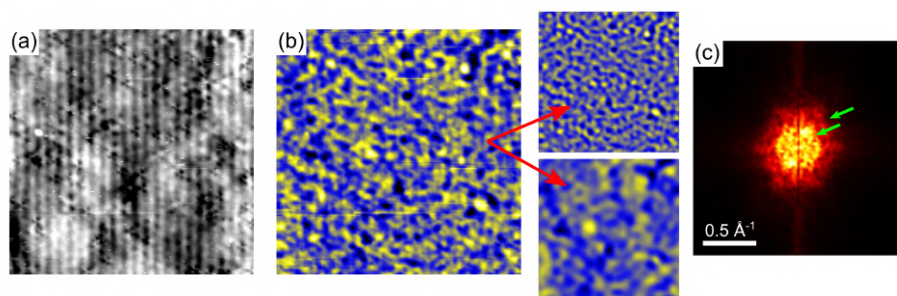


Figure B.1.24: (a) Topograph on the $m=2$ surface over a 50 by 50 nm² area. (b) QPI map in the same field of view as (a) at -50 meV. A small (upper right image) and a large (lower right image) QPI wavelength is extracted. (c) Unsymmetrized Fourier-space image of (b) with two \mathbf{q} -vectors (green arrows) corresponding to the two different QPI wavelengths.

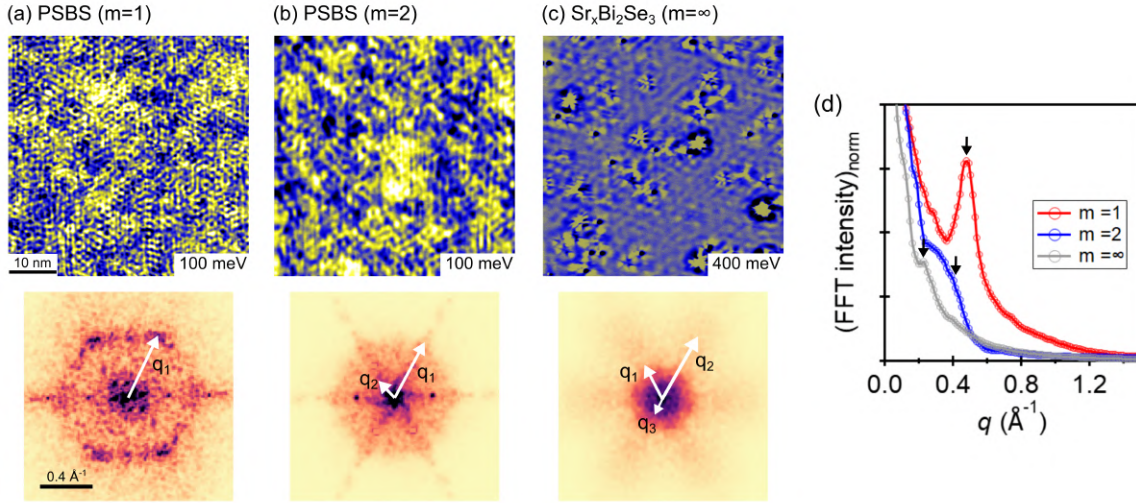


Figure B.1.25: (a-c) QPI maps and corresponding Fourier images on $m=1$ (a), $m=2$ (b) and $m=\infty$ (c) surfaces at indicated sample bias. All visible \mathbf{q} -vectors are indicated. Fourier maps for the $m=2$ and $m=\infty$ have been sixfold symmetrized and the latter is rotated as well. (d) Azimuthally averaged radial profiles of the Fourier signal for the three surfaces. Each curve is normalized between 0 and 1. Black arrows point to the position of the \mathbf{q}_1 in each case. Setpoint: 2 nA (a,b); 20 nA (c). $U_{\text{mod}} = 50$ mV (a), 30 mV (b) and 20 mV (c).

configuration, the presence of a second band may dilute the \mathbf{k} values to $\mathbf{k}+\Delta\mathbf{k}$, acting in a manner similar to disorder [205] and hence lifting the strict topological protection. The absence of QPI on the $m=2$ surface at -200 meV is highlighted in Fig. B.1.23(f), where only a bias-independent large modulation is observed, likely due to charge in-homogeneity.

We additionally show Fig. B.1.24 to convince the reader that two separate wavelengths can be identified from the raw QPI data in real space for the $m=2$ surface at -50 meV; corresponding \mathbf{q} -vectors are seen in the *unsymmetrized* Fourier space image.

- $m=1$ to $m=\infty$

In Fig. B.1.25 we trace the QPI intensity by further increasing the number to Bi_2Se_3 QLs to ∞ . Here we compare QPI maps and their Fourier maps for $m=1$, $m=2$ and $m=\infty$ surfaces, for indicated bias voltages which correspond to a similar energy level above the band bottom as for $m=1$. \mathbf{q} -vectors are indicated in each case with \mathbf{q}_1 originating from the surface state. For $m=\infty$ \mathbf{q}_2 corresponds to scattering involving bulk states and its shape can be explained following Refs. [203, 207]; \mathbf{q}_3 relates to the scattering potential of the defects and does not change with energy.

In Fig. B.1.25(d) we compare intensity of the \mathbf{q}_1 vector (black arrows) for the three

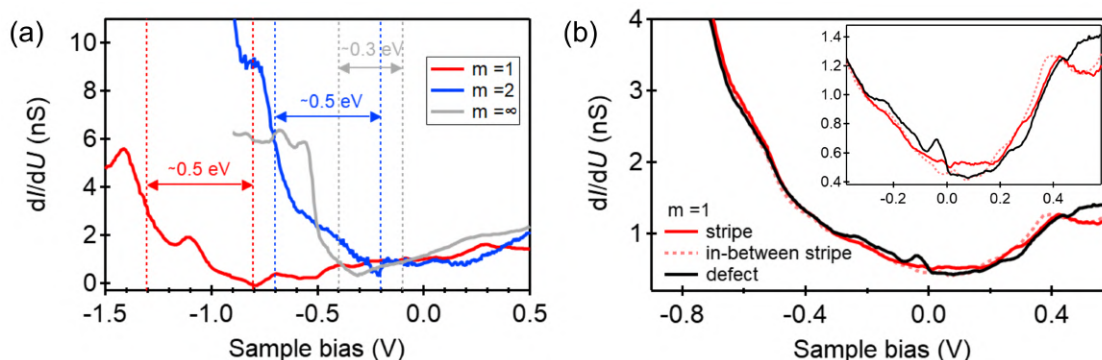


Figure B.1.26: (a) Point-spectra obtained on the $m=1$ (red trace), 2 (blue trace) and ∞ (gray trace) surfaces. (b) Point-spectra taken on the $m=1$ surface for positions corresponding to the stripe (red solid line), in-between the stripe (dashed light red line) and on a defect (black line). The inset is a zoom-in around the Fermi level. Stabilization parameters: $U = 500$ mV, $I = 0.5$ nA (red), $U = 600$ mV, $I = 0.5$ nA (blue), $U = -900$ mV, $I = 2$ nA (gray) for (a); $U = 600$ mV, $I = 0.5$ nA for (b).

surfaces. Each curve has been normalized between 0 and 1. It is readily seen that by increasing the number of Bi_2Se_3 QLs there is a strong suppression in the QPI intensity. We attribute this to the increase in topological character of the surface state, which suppresses the most intense scattering vector that also happens to correspond to direct backscattering.

STS on surfaces corresponding to $m=1, 2$ and ∞

Point-spectra on the $m=1$ (red trace) and $m=2$ (blue trace) surfaces show a bandgap of ~ 0.5 eV (Fig. B.1.26) between the conduction and valence band, consistent with the ARPES data [102]. The bottom of the conduction band and top of the valence band are indicated with dashed lines in each case, identified either from the sudden or a rapid rise in the dI/dU signal.

Upon increasing the number of QLs the bandgap in the material is expected to reduce. A reduced bandgap of ~ 0.3 eV is observed on the $m=\infty$ (gray trace) surface which corresponds to a bulk Bi_2Se_3 crystal. Finite density of states within the bandgap for the blue and gray traces originate from the surface states.

The red trace shown in Fig. B.1.26(a) for the $m=1$ surface is the only spectrum that relates to the APRES data nicely. Other spectra on the $m=1$ surface [see Fig. B.1.26(b)], taken on a different sample with a different tip, only match above -0.2 V. The common and reproducible feature for all spectra is a step around 0.4 V. Some minor differences are observed for the spectra taken on the stripe and that in-between, as seen in Fig. B.1.26(b). Spectrum on the defect shows a peak around -0.03 V.

Bibliography

- ¹M. Sato and Y. Ando, “Topological superconductors: a review”, *Reports on Progress in Physics* **80**, 076501 (2017) (cit. on pp. 3, 4).
- ²Y. Ando, “Topological insulator materials”, *J. Phys. Soc. Jpn.* **82**, 102001 (2013) (cit. on p. 3).
- ³X.-L. Qi and S.-C. Zhang, “Topological insulators and superconductors”, *Rev. Mod. Phys.* **83**, 1057–1110 (2011) (cit. on p. 3).
- ⁴E. Majorana, “Teoria simmetrica dell’elettrone e del positrone”, *Il Nuovo Cimento* (1924-1942) **14**, 171 (2008) (cit. on p. 3).
- ⁵C. Beenakker, “Search for Majorana fermions in superconductors”, *Annual Review of Condensed Matter Physics* **4**, 113–136 (2013) (cit. on p. 3).
- ⁶J. Alicea, “New directions in the pursuit of Majorana fermions in solid state systems”, *Reports on Progress in Physics* **75**, 076501 (2012) (cit. on p. 3).
- ⁷L. Fu and E. Berg, “Odd-parity topological superconductors: theory and application to $\text{Cu}_x\text{Bi}_2\text{Se}_3$ ”, *Phys. Rev. Lett.* **105**, 097001 (2010) (cit. on pp. 3, 4, 13, 14, 116).
- ⁸W. P. Halperin, J. M. Parpia, and J. A. Sauls, “Superfluid helium-3 in confined quarters”, *Physics Today* **71**, 30–36 (2018) (cit. on p. 4).
- ⁹G. Xu, B. Lian, P. Tang, X.-L. Qi, and S.-C. Zhang, “Topological superconductivity on the surface of Fe-based superconductors”, *Phys. Rev. Lett.* **117**, 047001 (2016) (cit. on p. 4).
- ¹⁰P. Zhang, K. Yaji, T. Hashimoto, Y. Ota, T. Kondo, K. Okazaki, Z. Wang, J. Wen, G. D. Gu, H. Ding, and S. Shin, “Observation of topological superconductivity on the surface of an iron-based superconductor”, *Science* **360**, 182–186 (2018) (cit. on p. 4).
- ¹¹L. Jiao, S. Howard, S. Ran, Z. Wang, J. O. Rodriguez, M. Sigrist, Z. Wang, N. P. Butch, and V. Madhavan, “Chiral superconductivity in heavy-fermion metal UTe_2 ”, *Nature* **579**, 523–527 (2020) (cit. on p. 4).
- ¹²L. Fu and C. L. Kane, “Superconducting proximity effect and Majorana fermions at the surface of a topological insulator”, *Phys. Rev. Lett.* **100**, 096407 (2008) (cit. on pp. 4, 7, 89, 90, 103).
- ¹³M.-X. Wang, C. Liu, J.-P. Xu, F. Yang, L. Miao, M.-Y. Yao, C. L. Gao, C. Shen, X. Ma, X. Chen, Z.-A. Xu, Y. Liu, S.-C. Zhang, D. Qian, J.-F. Jia, and Q.-K. Xue, “The coexistence of superconductivity and topological order in the Bi_2Se_3 thin films”, *Science* **336**, 52–55 (2012) (cit. on pp. 4, 89, 118).

- ¹⁴X.-L. Qi, T. L. Hughes, and S.-C. Zhang, “Chiral topological superconductor from the quantum Hall state”, *Phys. Rev. B* **82**, 184516 (2010) (cit. on p. 4).
- ¹⁵J. D. Sau, R. M. Lutchyn, S. Tewari, and S. Das Sarma, “Generic new platform for topological quantum computation using semiconductor heterostructures”, *Phys. Rev. Lett.* **104**, 040502 (2010) (cit. on p. 4).
- ¹⁶R. M. Lutchyn, E. P. A. M. Bakkers, L. P. Kouwenhoven, P. Krogstrup, C. M. Marcus, and Y. Oreg, “Majorana zero modes in superconductor-semiconductor heterostructures”, *Nature Reviews Materials* **3**, 52–68 (2018) (cit. on p. 4).
- ¹⁷V. Mourik, K. Zuo, S. M. Frolov, S. R. Plissard, E. P. A. M. Bakkers, and L. P. Kouwenhoven, “Signatures of Majorana fermions in hybrid superconductor-semiconductor nanowire devices”, *Science* **336**, 1003–1007 (2012) (cit. on p. 4).
- ¹⁸A. Das, Y. Ronen, Y. Most, Y. Oreg, M. Heiblum, and H. Shtrikman, “Zero-bias peaks and splitting in an Al-InAs nanowire topological superconductor as a signature of Majorana fermions”, *Nature Physics* **8**, 887–895 (2012) (cit. on p. 4).
- ¹⁹G. C. Ménard, S. Guissart, C. Brun, R. T. Leriche, M. Trif, F. Debontridder, D. Demaille, D. Roditchev, P. Simon, and T. Cren, “Two-dimensional topological superconductivity in Pb/Co/Si(111)”, *Nat. Commun.* **8**, 2040 (2017) (cit. on pp. 4, 7, 111).
- ²⁰S. Kezilebieke, M. N. Huda, V. Vano, M. Aapro, S. C. Ganguli, O. J. Silveira, S. Glodzik, A. S. Foster, T. Ojanen, and P. Liljeroth, “Topological superconductivity in a van der Waals heterostructure”, *Nature* **588**, 424–428 (2020) (cit. on p. 4).
- ²¹S. Kezilebieke, V. Vano, M. N. Huda, M. Aapro, S. C. Ganguli, P. Liljeroth, and J. L. Lado, “Moiré-enabled topological superconductivity”, *Nano Letters* **22**, PMID: 34978831, 328–333 (2022) (cit. on p. 4).
- ²²S. Nadj-Perge, I. K. Drozdov, J. Li, H. Chen, S. Jeon, J. Seo, A. H. MacDonald, B. A. Bernevig, and A. Yazdani, “Observation of Majorana fermions in ferromagnetic atomic chains on a superconductor”, *Science* **346**, 602–607 (2014) (cit. on p. 4).
- ²³L. Schneider, P. Beck, J. Neuhaus-Steinmetz, L. Rózsa, T. Posske, J. Wiebe, and R. Wiesendanger, “Precursors of Majorana modes and their length-dependent energy oscillations probed at both ends of atomic Shiba chains”, *Nature Nanotechnology* **17**, 384–389 (2022) (cit. on p. 5).
- ²⁴L. Schneider, P. Beck, T. Posske, D. Crawford, E. Mascot, S. Rachel, R. Wiesendanger, and J. Wiebe, “Topological Shiba bands in artificial spin chains on superconductors”, *Nature Physics* **17**, 943–948 (2021) (cit. on p. 5).
- ²⁵F. Wilczek, “Majorana returns”, *Nature Physics* **5**, 614–618 (2009) (cit. on p. 5).
- ²⁶S. Sasaki, M. Kriener, K. Segawa, K. Yada, Y. Tanaka, M. Sato, and Y. Ando, “Topological superconductivity in $\text{Cu}_x\text{Bi}_2\text{Se}_3$ ”, *Phys. Rev. Lett.* **107**, 217001 (2011) (cit. on pp. 5, 6, 115).

- ²⁷T. V. Bay, T. Naka, Y. K. Huang, H. Luigjes, M. S. Golden, and A. de Visser, “Superconductivity in the doped topological insulator $\text{Cu}_x\text{Bi}_2\text{Se}_3$ under high pressure”, *Phys. Rev. Lett.* **108**, 057001 (2012) (cit. on p. 5).
- ²⁸K. Matano, M. Kriener, K. Segawa, Y. Ando, and G.-q. Zheng, “Spin-rotation symmetry breaking in the superconducting state of $\text{Cu}_x\text{Bi}_2\text{Se}_3$ ”, *Nature Phys.* **12**, 852–854 (2016) (cit. on pp. 5, 15).
- ²⁹N. Levy, T. Zhang, J. Ha, F. Sharifi, A. A. Talin, Y. Kuk, and J. A. Stroscio, “Experimental evidence for *s*-wave pairing symmetry in superconducting $\text{Cu}_x\text{Bi}_2\text{Se}_3$ single crystals using a scanning tunneling microscope”, *Phys. Rev. Lett.* **110**, 117001 (2013) (cit. on pp. 5, 6, 16, 115).
- ³⁰H. Peng, D. De, B. Lv, F. Wei, and C.-W. Chu, “Absence of zero-energy surface bound states in $\text{Cu}_x\text{Bi}_2\text{Se}_3$ studied via andreev reflection spectroscopy”, *Phys. Rev. B* **88**, 024515 (2013) (cit. on p. 5).
- ³¹A. Yamakage, K. Yada, M. Sato, and Y. Tanaka, “Theory of tunneling conductance and surface-state transition in superconducting topological insulators”, *Phys. Rev. B* **85**, 180509 (2012) (cit. on p. 6).
- ³²R. Tao, Y.-J. Yan, X. Liu, Z.-W. Wang, Y. Ando, Q.-H. Wang, T. Zhang, and D.-L. Feng, “Direct visualization of the nematic superconductivity in $\text{Cu}_x\text{Bi}_2\text{Se}_3$ ”, *Phys. Rev. X* **8**, 041024 (2018) (cit. on pp. 6, 16, 18, 21, 23, 24, 26, 27, 115, 118).
- ³³E. Lahoud, E. Maniv, M. S. Petrushevsky, M. Naamneh, A. Ribak, S. Wiedmann, L. Petaccia, Z. Salman, K. B. Chashka, Y. Dagan, and A. Kanigel, “Evolution of the Fermi surface of a doped topological insulator with carrier concentration”, *Phys. Rev. B* **88**, 195107 (2013) (cit. on pp. 6, 10, 11).
- ³⁴L. Fu, “Odd-parity topological superconductor with nematic order: application to $\text{Cu}_x\text{Bi}_2\text{Se}_3$ ”, *Phys. Rev. B* **90**, 100509 (2014) (cit. on pp. 6, 14–16, 20, 28, 109).
- ³⁵B. Jäck, Y. Xie, J. Li, S. Jeon, B. A. Bernevig, and A. Yazdani, “Observation of a Majorana zero mode in a topologically protected edge channel”, *Science* **364**, 1255–1259 (2019) (cit. on pp. 6, 90).
- ³⁶M. Chen, X. Chen, H. Yang, Z. Du, and H.-H. Wen, “Superconductivity with twofold symmetry in $\text{Bi}_2\text{Te}_3/\text{FeTe}_{0.55}\text{Se}_{0.45}$ heterostructures”, *Science Advances* **4**, eaat1084 (2018) (cit. on p. 6).
- ³⁷C.-L. Song, Y.-L. Wang, P. Cheng, Y.-P. Jiang, W. Li, T. Zhang, Z. Li, K. He, L. Wang, J.-F. Jia, H.-H. Hung, C. Wu, X. Ma, X. Chen, and Q.-K. Xue, “Direct observation of nodes and twofold symmetry in FeSe superconductor”, *Science* **332**, 1410–1413 (2011) (cit. on p. 6).
- ³⁸J. E. Hoffman, K. McElroy, D.-H. Lee, K. M. Lang, H. Eisaki, S. Uchida, and J. C. Davis, “Imaging quasiparticle interference in $\text{Bi}_2\text{Sr}_2\text{CaCu}_2\text{O}_{8+\delta}$ ”, *Science* **297**, 1148–1151 (2002) (cit. on pp. 6, 140, 156).

- ³⁹M. P. Allan, A. W. Rost, A. P. Mackenzie, Y. Xie, J. C. Davis, K. Kihou, C. H. Lee, A. Iyo, H. Eisaki, and T.-M. Chuang, “Anisotropic energy gaps of iron-based superconductivity from intraband quasiparticle interference in LiFeAs”, *Science* **336**, 563–567 (2012) (cit. on p. 6).
- ⁴⁰X. Liu, R. Tao, M. Ren, W. Chen, Q. Yao, T. Wolf, Y. Yan, T. Zhang, and D. Feng, “Evidence of nematic order and nodal superconducting gap along [110] direction in RbFe₂As₂”, *Nature Communications* **10**, 1039 (2019) (cit. on p. 6).
- ⁴¹S. Urazhdin, D. Bilc, S. H. Tessmer, S. D. Mahanti, T. Kyratsi, and M. G. Kanatzidis, “Scanning tunneling microscopy of defect states in the semiconductor Bi₂Se₃”, *Phys. Rev. B* **66**, 161306 (2002) (cit. on p. 6).
- ⁴²J. Dai, D. West, X. Wang, Y. Wang, D. Kwok, S.-W. Cheong, S. B. Zhang, and W. Wu, “Toward the intrinsic limit of the topological insulator Bi₂Se₃”, *Phys. Rev. Lett.* **117**, 106401 (2016) (cit. on pp. 6, 26).
- ⁴³C. X. Trang, N. Shimamura, K. Nakayama, S. Souma, K. Sugawara, I. Watanabe, K. Yamauchi, T. Oguchi, K. Segawa, T. Takahashi, Y. Ando, and T. Sato, “Conversion of a conventional superconductor into a topological superconductor by topological proximity effect”, *Nat. Commun.* **11**, 159 (2020) (cit. on pp. 7, 90–93, 95, 97, 104, 110).
- ⁴⁴P. Hosur, P. Ghaemi, R. S. K. Mong, and A. Vishwanath, “Majorana modes at the ends of superconductor vortices in doped topological insulators”, *Phys. Rev. Lett.* **107**, 097001 (2011) (cit. on pp. 7, 103, 116).
- ⁴⁵G. C. Ménard, A. Mesaros, C. Brun, F. Debontridder, D. Roditchev, P. Simon, and T. Cren, “Isolated pairs of majorana zero modes in a disordered superconducting lead monolayer”, *Nat. Commun.* **10**, 2587 (2019) (cit. on pp. 7, 103, 111).
- ⁴⁶Y. S. Hor, A. J. Williams, J. G. Checkelsky, P. Roushan, J. Seo, Q. Xu, H. W. Zandbergen, A. Yazdani, N. P. Ong, and R. J. Cava, “Superconductivity in Cu_xBi₂Se₃ and its implications for pairing in the undoped topological insulator”, *Phys. Rev. Lett.* **104**, 057001 (2010) (cit. on pp. 9, 16, 29).
- ⁴⁷M. Kriener, K. Segawa, Z. Ren, S. Sasaki, S. Wada, S. Kuwabata, and Y. Ando, “Electrochemical synthesis and superconducting phase diagram of Cu_xBi₂Se₃”, *Phys. Rev. B* **84**, 054513 (2011) (cit. on pp. 9, 16, 116).
- ⁴⁸L. A. Wray, S. Xu, Y. Xia, D. Qian, A. V. Fedorov, H. Lin, A. Bansil, L. Fu, Y. S. Hor, R. J. Cava, and M. Z. Hasan, “Spin-orbital ground states of superconducting doped topological insulators: A Majorana platform”, *Phys. Rev. B* **83**, 224516 (2011) (cit. on pp. 9, 11, 12).
- ⁴⁹K. Sobczak, P. Strak, P. Kempisty, A. Wolos, A. Hruban, A. Materna, and J. Borysiuk, “Electronic and structural properties of Bi₂Se₃ : Cu”, *Phys. Rev. Mater.* **2**, 044203 (2018) (cit. on p. 9).

-
- ⁵⁰I. Martin, D. Podolsky, and S. A. Kivelson, “Enhancement of superconductivity by local inhomogeneities”, *Phys. Rev. B* **72**, 060502 (2005) (cit. on p. 9).
- ⁵¹I. S. Burmistrov, I. V. Gornyi, and A. D. Mirlin, “Enhancement of the critical temperature of superconductors by Anderson localization”, *Phys. Rev. Lett.* **108**, 017002 (2012) (cit. on p. 9).
- ⁵²K. Zhao, H. Lin, X. Xiao, W. Huang, W. Yao, M. Yan, Y. Xing, Q. Zhang, Z.-X. Li, S. Hoshino, J. Wang, S. Zhou, L. Gu, M. S. Bahramy, H. Yao, N. Nagaosa, Q.-K. Xue, K. T. Law, X. Chen, and S.-H. Ji, “Disorder-induced multifractal superconductivity in monolayer niobium dichalcogenides”, *Nature Physics* **15**, 904–910 (2019) (cit. on p. 9).
- ⁵³Shruti, V. K. Maurya, P. Neha, P. Srivastava, and S. Patnaik, “Superconductivity by Sr intercalation in the layered topological insulator Bi_2Se_3 ”, *Phys. Rev. B* **92**, 020506 (2015) (cit. on pp. 9, 10).
- ⁵⁴Y. Qiu, K. N. Sanders, J. Dai, J. E. Medvedeva, W. Wu, P. Ghaemi, T. Vojta, and Y. S. Hor, “Time reversal symmetry breaking superconductivity in topological materials”, [10.48550/ARXIV.1512.03519](https://arxiv.org/abs/1512.03519) (2015) (cit. on p. 9).
- ⁵⁵S. Sasaki, K. Segawa, and Y. Ando, “Superconductor derived from a topological insulator heterostructure”, *Phys. Rev. B* **90**, 220504 (2014) (cit. on p. 10).
- ⁵⁶H. Zhang, C.-X. Liu, X.-L. Qi, X. Dai, Z. Fang, and S.-C. Zhang, “Topological insulators in Bi_2Se_3 , Bi_2Te_3 and Sb_2Te_3 with a single Dirac cone on the surface”, *Nature Physics* **5**, 438–442 (2009) (cit. on pp. 10–12).
- ⁵⁷L. Andersen, A. Ramires, Z. Wang, T. Lorenz, and Y. Ando, “Generalized Anderson’s theorem for superconductors derived from topological insulators”, *Sci. Adv.* **6**, eaay6502 (2020) (cit. on pp. 10, 47, 118, 148).
- ⁵⁸M. Bagchi, J. Brede, and Y. Ando, “Observability of superconductivity in Sr-doped Bi_2Se_3 at the surface using scanning tunneling microscope”, *Phys. Rev. Materials* **6**, 034201 (2022) (cit. on pp. 10, 26, 97, 130).
- ⁵⁹A. Almoalem, I. Silber, S. Sandik, M. Lotem, A. Ribak, Y. Nitzav, A. Y. Kuntsevich, O. A. Sobolevskiy, Y. G. Selivanov, V. A. Prudkoglyad, M. Shi, L. Petaccia, M. Goldstein, Y. Dagan, and A. Kanigel, “Link between superconductivity and a Lifshitz transition in intercalated Bi_2Se_3 ”, *Phys. Rev. B* **103**, 174518 (2021) (cit. on p. 10).
- ⁶⁰D. A. Khokhlov, R. S. Akzyanov, and A. L. Rakhmanov, “Theory of nematic superconductivity in doped topological insulators (brief review)”, *JETP Letters* **116**, 522–536 (2022) (cit. on pp. 12, 15).
- ⁶¹K. Kuroda, M. Arita, K. Miyamoto, M. Ye, J. Jiang, A. Kimura, E. E. Krasovskii, E. V. Chulkov, H. Iwasawa, T. Okuda, K. Shimada, Y. Ueda, H. Namatame, and M. Taniguchi, “Hexagonally deformed Fermi surface of the 3D topological insulator Bi_2Se_3 ”, *Phys. Rev. Lett.* **105**, 076802 (2010) (cit. on pp. 12, 141).

- ⁶²L. Fu, “Hexagonal warping effects in the surface states of the topological insulator Bi_2Te_3 ”, *Phys. Rev. Lett.* **103**, 266801 (2009) (cit. on pp. 13, 142, 156).
- ⁶³R. S. Akzyanov, D. A. Khokhlov, and A. L. Rakhmanov, “Nematic superconductivity in topological insulators induced by hexagonal warping”, *Phys. Rev. B* **102**, 094511 (2020) (cit. on pp. 13–15).
- ⁶⁴X. Wan and S. Y. Savrasov, “Turning a band insulator into an exotic superconductor”, *Nature Communications* **5**, 4144 (2014) (cit. on p. 14).
- ⁶⁵J. Wang, K. Ran, S. Li, Z. Ma, S. Bao, Z. Cai, Y. Zhang, K. Nakajima, S. Ohira-Kawamura, P. Cermak, A. Schneidewind, S. Y. Savrasov, X. Wan, and J. Wen, “Evidence for singular-phonon-induced nematic superconductivity in a topological superconductor candidate $\text{Sr}_{0.1}\text{Bi}_2\text{Se}_3$ ”, *Nature Communications* **10**, 2802 (2019) (cit. on p. 14).
- ⁶⁶S. Yonezawa, “Nematic superconductivity in doped Bi_2Se_3 topological superconductors”, *Condens. Matter* **4**, 2 (2019) (cit. on p. 15).
- ⁶⁷S. Yonezawa, K. Tajiri, S. Nakata, Y. Nagai, Z. Wang, K. Segawa, Y. Ando, and Y. Maeno, “Thermodynamic evidence for nematic superconductivity in $\text{Cu}_x\text{Bi}_2\text{Se}_3$ ”, *Nature Phys.* **13**, 123–126 (2017) (cit. on p. 15).
- ⁶⁸T. Kawai, C. G. Wang, Y. Kandori, Y. Honoki, K. Matano, T. Kambe, and G.-q. Zheng, “Direction and symmetry transition of the vector order parameter in topological superconductors $\text{Cu}_x\text{Bi}_2\text{Se}_3$ ”, *Nat. Commun.* **11**, 235 (2020) (cit. on pp. 15, 16, 113).
- ⁶⁹J. W. F. Venderbos, V. Kozii, and L. Fu, “Odd-parity superconductors with two-component order parameters: nematic and chiral, full gap, and Majorana node”, *Phys. Rev. B* **94**, 180504 (2016) (cit. on p. 15).
- ⁷⁰P. T. How and S.-K. Yip, “Signatures of nematic superconductivity in doped Bi_2Se_3 under applied stress”, *Phys. Rev. B* **100**, 134508 (2019) (cit. on p. 15).
- ⁷¹A. Y. Kuntsevich, M. A. Bryzgalov, V. A. Prudkoglyad, V. P. Martovitskii, Y. G. Selivanov, and E. G. Chizhevskii, “Structural distortion behind the nematic superconductivity in $\text{Sr}_x\text{Bi}_2\text{Se}_3$ ”, *New J. Phys.* **20**, 103022 (2018) (cit. on pp. 15, 116).
- ⁷²M. P. Smylie, Z. Islam, G. D. Gu, J. Schneeloch, R. D. Zhong, S. Rosenkranz, W. - . Kwok, and U. Welp, “Multimodal synchrotron x-ray diffraction across the superconducting transition of $\text{Sr}_{0.1}\text{Bi}_2\text{Se}_3$ ”, *arXiv*, 10 . 48550 / *arXiv* . 2207 . 13221 (2022) (cit. on p. 15).
- ⁷³G. E. Blonder, M. Tinkham, and T. M. Klapwijk, “Transition from metallic to tunneling regimes in superconducting microconstrictions: excess current, charge imbalance, and supercurrent conversion”, *Phys. Rev. B* **25**, 4515–4532 (1982) (cit. on p. 20).
- ⁷⁴Y. Matsuda, K. Izawa, and I. Vekhter, “Nodal structure of unconventional superconductors probed by angle resolved thermal transport measurements”, *J. Phys.: Condens. Matter* **18**, R705–R752 (2006) (cit. on pp. 21, 152).

- ⁷⁵W. J. Tomasch, “Geometrical resonance in the tunneling characteristics of superconducting Pb”, *Phys. Rev. Lett.* **15**, 672–675 (1965) (cit. on p. 23).
- ⁷⁶O. Neshor and G. Koren, “Observation of Tomasch oscillations and tunneling-like behavior in oxygen-deficient edge junctions”, *Applied physics letters* **74**, 3392–3394 (1999) (cit. on p. 23).
- ⁷⁷T. Wolfram, “Tomasch oscillations in the density of states of superconducting films”, *Phys. Rev.* **170**, 481–490 (1968) (cit. on p. 23).
- ⁷⁸E. L. Wolf, *Principles of Electron Tunneling Spectroscopy* (Oxford University Press, Nov. 2011) (cit. on p. 23).
- ⁷⁹W. L. McMillan and P. W. Anderson, “Theory of geometrical resonances in the tunneling characteristics of thick films of superconductors”, *Phys. Rev. Lett.* **16**, 85–87 (1966) (cit. on p. 23).
- ⁸⁰B. J. Lawson, G. Li, F. Yu, T. Asaba, C. Tinsman, T. Gao, W. Wang, Y. S. Hor, and L. Li, “Quantum oscillations in $\text{Cu}_x\text{Bi}_2\text{Se}_3$ in high magnetic fields”, *Phys. Rev. B* **90**, 195141 (2014) (cit. on p. 24).
- ⁸¹J. Lee, K. Fujita, K. McElroy, J. A. Slezak, M. Wang, Y. Aiura, H. Bando, M. Ishikado, T. Masui, J.-X. Zhu, A. V. Balatsky, H. Eisaki, S. Uchida, and J. C. Davis, “Interplay of electron-lattice interactions and superconductivity in $\text{Bi}_2\text{Sr}_2\text{CaCu}_2\text{O}_{8+\delta}$ ”, *Nature* **442**, 546–550 (2006) (cit. on p. 24).
- ⁸²C.-L. Song and J. E. Hoffman, “Pairing insights in iron-based superconductors from scanning tunneling microscopy”, *Current Opinion in Solid State and Materials Science* **17**, 39–48 (2013) (cit. on p. 24).
- ⁸³H. Kim, Y. Choi, C. Lewandowski, A. Thomson, Y. Zhang, R. Polski, K. Watanabe, T. Taniguchi, J. Alicea, and S. Nadj-Perge, “Evidence for unconventional superconductivity in twisted trilayer graphene”, *Nature* **606**, 494–500 (2022) (cit. on p. 24).
- ⁸⁴C. Mann, D. West, I. Miotkowski, Y. P. Chen, S. Zhang, and C.-K. Shih, “Observation of Coulomb repulsion between Cu intercalants in $\text{Cu}_x\text{Bi}_2\text{Se}_3$ ”, *Phys. Rev. B* **89**, 155312 (2014) (cit. on pp. 25, 26).
- ⁸⁵M. Jurczyk, M. Sikora, M. Chrobak, and L. Jurczyk, “Studies of surface states in Bi_2Se_3 induced by the BiSe substitution in the crystal subsurface structure”, *Applied Surface Science* **528**, 146978 (2020) (cit. on p. 26).
- ⁸⁶Y. S. Hor, A. Richardella, P. Roushan, Y. Xia, J. G. Checkelsky, A. Yazdani, M. Z. Hasan, N. P. Ong, and R. J. Cava, “*p*-type Bi_2Se_3 for topological insulator and low-temperature thermoelectric applications”, *Phys. Rev. B* **79**, 195208 (2009) (cit. on p. 26).
- ⁸⁷C. Mann, D. West, I. Miotkowski, Y. P. Chen, S. Zhang, and C.-K. Shih, “Mapping the 3D surface potential in Bi_2Se_3 ”, *Nature Communications* **4**, 2277 (2013) (cit. on p. 26).

- ⁸⁸L. Seixas, L. B. Abdalla, T. M. Schmidt, A. Fazzio, and R. H. Miwa, “Topological states ruled by stacking faults in Bi_2Se_3 and Bi_2Te_3 ”, *Journal of Applied Physics* **113**, 023705 (2013) (cit. on p. 26).
- ⁸⁹S. V. Eremeev, M. G. Vergniory, T. V. Menshchikova, A. A. Shaposhnikov, and E. V. Chulkov, “The effect of van der Waal’s gap expansions on the surface electronic structure of layered topological insulators”, *New Journal of Physics* **14**, 113030 (2012) (cit. on p. 26).
- ⁹⁰Y. Pan, A. M. Nikitin, G. K. Araizi, Y. K. Huang, Y. Matsushita, T. Naka, and A. de Visser, “Rotational symmetry breaking in the topological superconductor $\text{Sr}_x\text{Bi}_2\text{Se}_3$ probed by upper-critical field experiments”, *Sci. Rep.* **6**, 28632 (2016) (cit. on p. 29).
- ⁹¹K. Willa, R. Willa, K. W. Song, G. D. Gu, J. A. Schneeloch, R. Zhong, A. E. Koshelev, W.-K. Kwok, and U. Welp, “Nanocalorimetric evidence for nematic superconductivity in the doped topological insulator $\text{Sr}_{0.1}\text{Bi}_2\text{Se}_3$ ”, *Phys. Rev. B* **98**, 184509 (2018) (cit. on p. 29).
- ⁹²Y. Sun, S. Kittaka, T. Sakakibara, K. Machida, J. Wang, J. Wen, X. Xing, Z. Shi, and T. Tamegai, “Quasiparticle evidence for the nematic state above T_c in $\text{Sr}_x\text{Bi}_2\text{Se}_3$ ”, *Phys. Rev. Lett.* **123**, 027002 (2019) (cit. on p. 29).
- ⁹³I. Kostylev, S. Yonezawa, Z. Wang, Y. Ando, and Y. Maeno, “Uniaxial-strain control of nematic superconductivity in $\text{Sr}_x\text{Bi}_2\text{Se}_3$ ”, *Nat. Commun.* **11**, 4152 (2020) (cit. on p. 29).
- ⁹⁴Z. Li, M. Wang, D. Zhang, N. Feng, W. Jiang, C. Han, W. Chen, M. Ye, C. Gao, J. Jia, J. Li, S. Qiao, D. Qian, B. Xu, H. Tian, and B. Gao, “Possible structural origin of superconductivity in Sr-doped Bi_2Se_3 ”, *Phys. Rev. Materials* **2**, 014201 (2018) (cit. on p. 31).
- ⁹⁵T. Fröhlich, Z. Wang, M. Bagchi, A. Stunault, Y. Ando, and M. Braden, “Crystal structure and distortion of superconducting $\text{Cu}_x\text{Bi}_2\text{Se}_3$ ”, *Phys. Rev. Materials* **4**, 054802 (2020) (cit. on p. 31).
- ⁹⁶P. Solinas, A. Amoretti, and F. Giazotto, “Sauter-Schwinger effect in a Bardeen-Cooper-Schrieffer superconductor”, *Phys. Rev. Lett.* **126**, 117001 (2021) (cit. on pp. 32, 33).
- ⁹⁷G. Du, J. Shao, X. Yang, Z. Du, D. Fang, J. Wang, K. Ran, J. Wen, C. Zhang, H. Yang, Y. Zhang, and H.-H. Wen, “Drive the Dirac electrons into Cooper pairs in $\text{Sr}_x\text{Bi}_2\text{Se}_3$ ”, *Nat. Commun.* **8**, 14466 (2017) (cit. on pp. 31, 33).
- ⁹⁸R. Kumar, A. Vasdev, S. Das, S. Howlader, K. S. Jat, P. Neha, S. Patnaik, and G. Sheet, “The pressure-enhanced superconducting phase of $\text{Sr}_x\text{Bi}_2\text{Se}_3$ probed by hard point contact spectroscopy”, *Sci. Rep.* **11**, 4090 (2021) (cit. on pp. 31, 33).
- ⁹⁹S. Wilfert, P. Sessi, Z. Wang, H. Schmidt, M. C. Martínez-Velarte, S. H. Lee, Y. S. Hor, A. F. Otte, Y. Ando, W. Wu, and M. Bode, “Scanning tunneling spectroscopy investigations of superconducting-doped topological insulators: experimental pitfalls and results”, *Phys. Rev. B* **98**, 085133 (2018) (cit. on p. 31).

- ¹⁰⁰M. Eltschka, B. Jäck, M. Assig, O. V. Kondrashov, M. A. Skvortsov, M. Etzkorn, C. R. Ast, and K. Kern, “Superconducting scanning tunneling microscopy tips in a magnetic field: geometry-controlled order of the phase transition”, *Appl. Phys. Lett.* **107**, 122601 (2015) (cit. on p. 33).
- ¹⁰¹L. Andersen, Z. Wang, T. Lorenz, and Y. Ando, “Nematic superconductivity in $\text{Cu}_{1.5}(\text{PbSe})_5(\text{Bi}_2\text{Se}_3)_6$ ”, *Phys. Rev. B* **98**, 220512 (2018) (cit. on pp. 47, 48).
- ¹⁰²K. Nakayama, K. Eto, Y. Tanaka, T. Sato, S. Souma, T. Takahashi, K. Segawa, and Y. Ando, “Manipulation of topological states and the bulk band gap using natural heterostructures of a topological insulator”, *Phys. Rev. Lett.* **109**, 236804 (2012) (cit. on pp. 48, 156, 164).
- ¹⁰³K. Nakayama, H. Kimizuka, Y. Tanaka, T. Sato, S. Souma, T. Takahashi, S. Sasaki, K. Segawa, and Y. Ando, “Observation of two-dimensional bulk electronic states in the superconducting topological insulator heterostructure $\text{Cu}_x(\text{PbSe})_5(\text{Bi}_2\text{Se}_3)_6$: implications for unconventional superconductivity”, *Phys. Rev. B* **92**, 100508 (2015) (cit. on pp. 48, 154).
- ¹⁰⁴Y. Zhang, K. He, C.-Z. Chang, C.-L. Song, L.-L. Wang, X. Chen, J.-F. Jia, Z. Fang, X. Dai, W.-Y. Shan, S.-Q. Shen, Q. Niu, X.-L. Qi, S.-C. Zhang, X.-C. Ma, and Q.-K. Xue, “Crossover of the three-dimensional topological insulator Bi_2Se_3 to the two-dimensional limit”, *Nature Physics* **6**, 584–588 (2010) (cit. on p. 48).
- ¹⁰⁵K. Park, J. J. Heremans, V. W. Scarola, and D. Minic, “Robustness of topologically protected surface states in layering of Bi_2Te_3 thin films”, *Phys. Rev. Lett.* **105**, 186801 (2010) (cit. on p. 48).
- ¹⁰⁶Y.-Y. Li, G. Wang, X.-G. Zhu, M.-H. Liu, C. Ye, X. Chen, Y.-Y. Wang, K. He, L.-L. Wang, X.-C. Ma, H.-J. Zhang, X. Dai, Z. Fang, X.-C. Xie, Y. Liu, X.-L. Qi, J.-F. Jia, S.-C. Zhang, and Q.-K. Xue, “Intrinsic topological insulator Bi_2Te_3 thin films on Si and their thickness limit”, *Advanced Materials* **22**, 4002–4007 (2010) (cit. on p. 48).
- ¹⁰⁷J.-P. Xu, C. Liu, M.-X. Wang, J. Ge, Z.-L. Liu, X. Yang, Y. Chen, Y. Liu, Z.-A. Xu, C.-L. Gao, D. Qian, F.-C. Zhang, and J.-F. Jia, “Artificial topological superconductor by the proximity effect”, *Phys. Rev. Lett.* **112**, 217001 (2014) (cit. on p. 89).
- ¹⁰⁸J.-P. Xu, M.-X. Wang, Z. L. Liu, J.-F. Ge, X. Yang, C. Liu, Z. A. Xu, D. Guan, C. L. Gao, D. Qian, Y. Liu, Q.-H. Wang, F.-C. Zhang, Q.-K. Xue, and J.-F. Jia, “Experimental detection of a Majorana mode in the core of a magnetic vortex inside a topological insulator-superconductor $\text{Bi}_2\text{Te}_3/\text{NbSe}_2$ heterostructure”, *Phys. Rev. Lett.* **114**, 017001 (2015) (cit. on p. 89).
- ¹⁰⁹Y. Zang, F. Küster, J. Zhang, D. Liu, B. Pal, H. Deniz, P. Sessi, M. J. Gilbert, and S. S. P. Parkin, “Competing energy scales in topological superconducting heterostructures”, *Nano Lett.* **21**, 2758–2765 (2021) (cit. on p. 89).

- ¹¹⁰H. Kim, Y. Nagai, L. Rózsa, D. Schreyer, and R. Wiesendanger, “Anisotropic non-split zero-energy vortex bound states in a conventional superconductor”, *Applied Physics Reviews* **8**, 031417 (2021) (cit. on p. 89).
- ¹¹¹T. Shoman, A. Takayama, T. Sato, S. Souma, T. Takahashi, T. Oguchi, K. Segawa, and Y. Ando, “Topological proximity effect in a topological insulator hybrid”, *Nat. Commun.* **6**, 6547 (2015) (cit. on p. 90).
- ¹¹²I. K. Drozdov, A. Alexandradinata, S. Jeon, S. Nadj-Perge, H. Ji, R. J. Cava, B. Andrei Bernevig, and A. Yazdani, “One-dimensional topological edge states of bismuth bilayers”, *Nature Physics* **10**, 664–669 (2014) (cit. on p. 90).
- ¹¹³T. Hirahara, G. Bihlmayer, Y. Sakamoto, M. Yamada, H. Miyazaki, S.-i. Kimura, S. Blügel, and S. Hasegawa, “Interfacing 2D and 3D topological insulators: Bi(111) bilayer on Bi₂Te₃”, *Phys. Rev. Lett.* **107**, 166801 (2011) (cit. on p. 90).
- ¹¹⁴Z. F. Wang, M.-Y. Yao, W. Ming, L. Miao, F. Zhu, C. Liu, C. L. Gao, D. Qian, J.-F. Jia, and F. Liu, “Creation of helical Dirac fermions by interfacing two gapped systems of ordinary fermions”, *Nat. Commun.* **4**, 1384 (2013) (cit. on p. 90).
- ¹¹⁵F. Pielmeier, G. Landolt, B. Slomski, S. Muff, J. Berwanger, A. Eich, A. A. Khajetoorians, J. Wiebe, Z. S. Aliev, M. B. Babanly, R. Wiesendanger, J. Osterwalder, E. V. Chulkov, F. J. Giessibl, and J. H. Dil, “Response of the topological surface state to surface disorder in TlBiSe₂”, *New J. Phys.* **17**, 023067 (2015) (cit. on pp. 93, 111).
- ¹¹⁶K. Kuroda, M. Ye, E. F. Schwier, M. Nurmamat, K. Shirai, M. Nakatake, S. Ueda, K. Miyamoto, T. Okuda, H. Namatame, M. Taniguchi, Y. Ueda, and A. Kimura, “Experimental verification of the surface termination in the topological insulator TlBiSe₂ using core-level photoelectron spectroscopy and scanning tunneling microscopy”, *Phys. Rev. B* **88**, 245308 (2013) (cit. on p. 93).
- ¹¹⁷K. Kuroda, M. Ye, A. Kimura, S. V. Ereemeev, E. E. Krasovskii, E. V. Chulkov, Y. Ueda, K. Miyamoto, T. Okuda, K. Shimada, H. Namatame, and M. Taniguchi, “Experimental realization of a three-dimensional topological insulator phase in ternary chalcogenide TlBiSe₂”, *Phys. Rev. Lett.* **105**, 146801 (2010) (cit. on p. 93).
- ¹¹⁸Y. L. Chen, Z. K. Liu, J. G. Analytis, J.-H. Chu, H. J. Zhang, B. H. Yan, S.-K. Mo, R. G. Moore, D. H. Lu, I. R. Fisher, S. C. Zhang, Z. Hussain, and Z.-X. Shen, “Single Dirac cone topological surface state and unusual thermoelectric property of compounds from a new topological insulator family”, *Phys. Rev. Lett.* **105**, 266401 (2010) (cit. on p. 93).
- ¹¹⁹D. Eom, S. Qin, M.-Y. Chou, and C. K. Shih, “Persistent superconductivity in ultrathin Pb films: a scanning tunneling spectroscopy study”, *Phys. Rev. Lett.* **96**, 027005 (2006) (cit. on p. 93).
- ¹²⁰M. M. Oezer, J. R. Thompson, and H. H. Weitering, “Hard superconductivity of a soft metal in the quantum regime”, *Nature Phys* **2**, 173–176 (2006) (cit. on pp. 93, 98, 101, 110, 111).

-
- ¹²¹T. Nishio, T. An, A. Nomura, K. Miyachi, T. Eguchi, H. Sakata, S. Lin, N. Hayashi, N. Nakai, M. Machida, and Y. Hasegawa, “Superconducting Pb island nanostructures studied by scanning tunneling microscopy and spectroscopy”, *Phys. Rev. Lett.* **101**, 167001 (2008) (cit. on p. 93).
- ¹²²S. Qin, J. Kim, Q. Niu, and C.-K. Shih, “Superconductivity at the two-dimensional limit”, *Science* **324**, 1314–1317 (2009) (cit. on pp. 93, 98).
- ¹²³T. Zhang, P. Cheng, W.-J. Li, Y.-J. Sun, G. Wang, X.-G. Zhu, K. He, L. Wang, X. Ma, X. Chen, Y. Wang, Y. Liu, H.-Q. Lin, J.-F. Jia, and Q.-K. Xue, “Superconductivity in one-atomic-layer metal films grown on Si(111)”, *Nature Phys* **6**, 104–108 (2010) (cit. on p. 93).
- ¹²⁴S.-H. Ji, T. Zhang, Y.-S. Fu, X. Chen, X.-C. Ma, J. Li, W.-H. Duan, J.-F. Jia, and Q.-K. Xue, “High-resolution scanning tunneling spectroscopy of magnetic impurity induced bound states in the superconducting gap of Pb thin films”, *Phys. Rev. Lett.* **100**, 226801 (2008) (cit. on pp. 97, 101).
- ¹²⁵R. K. W. Buckel, *Supraleitung* (Wiley, Weinheim, 2004) (cit. on p. 97).
- ¹²⁶R. F. Gasparovic, B. N. Taylor, and R. E. Eck, “Temperature dependence of the superconducting energy gap of Pb”, *Solid State Communications* **4**, 59–63 (1966) (cit. on p. 98).
- ¹²⁷M. Tinkham, *Introduction to superconductivity* (Courier Corporation, 2004) (cit. on p. 98).
- ¹²⁸M. R. Eskildsen, M. Kugler, S. Tanaka, J. Jun, S. M. Kazakov, J. Karpinski, and Ø. Fischer, “Vortex imaging in the π band of Magnesium Diboride”, *Phys. Rev. Lett.* **89**, 187003 (2002) (cit. on p. 101).
- ¹²⁹Y. X. Ning, C. L. Song, Y. L. Wang, X. Chen, J. F. Jia, Q. K. Xue, and X. C. Ma, “Vortex properties of two-dimensional superconducting Pb films”, *J. Phys.: Condens. Matter* **22**, 065701 (2010) (cit. on pp. 101, 103, 110, 111).
- ¹³⁰N. Hayashi, T. Isoshima, M. Ichioka, and K. Machida, “Low-lying quasiparticle excitations around a vortex core in quantum limit”, *Phys. Rev. Lett.* **80**, 2921–2924 (1998) (cit. on p. 102).
- ¹³¹C. Caroli, P. De Gennes, and J. Matricon, “Bound fermion states on a vortex line in a type II superconductor”, *Physics Letters* **9**, 307–309 (1964) (cit. on p. 102).
- ¹³²L. Kong, S. Zhu, M. Papaj, H. Chen, L. Cao, H. Isobe, Y. Xing, W. Liu, D. Wang, P. Fan, Y. Sun, S. Du, J. Schneeloch, R. Zhong, G. Gu, L. Fu, H.-J. Gao, and H. Ding, “Half-integer level shift of vortex bound states in an iron-based superconductor”, *Nature Physics* **15**, 1181–1187 (2019) (cit. on pp. 102, 103).
- ¹³³T. Machida, Y. Sun, S. Pyon, S. Takeda, Y. Kohsaka, T. Hanaguri, T. Sasagawa, and T. Tamegai, “Zero-energy vortex bound state in the superconducting topological surface state of Fe(Se, Te)”, *Nature Materials* **18**, 811–815 (2019) (cit. on p. 102).

- ¹³⁴C. Renner, A. D. Kent, P. Niedermann, Ø. Fischer, and F. Lévy, “Scanning tunneling spectroscopy of a vortex core from the clean to the dirty limit”, *Phys. Rev. Lett.* **67**, 1650–1652 (1991) (cit. on pp. 103, 148).
- ¹³⁵H. Nam, H. Chen, T. Liu, J. Kim, C. Zhang, J. Yong, T. R. Lemberger, P. A. Kratz, J. R. Kirtley, K. Moler, P. W. Adams, A. H. MacDonald, and C.-K. Shih, “Ultrathin two-dimensional superconductivity with strong spin-orbit coupling”, *Proceedings of the National Academy of Sciences* **113**, 10513–10517 (2016) (cit. on pp. 105, 110, 111).
- ¹³⁶K. J. Franke, G. Schulze, and J. I. Pascual, “Competition of superconducting phenomena and Kondo screening at the nanoscale”, *Science* **332**, 940–944 (2011) (cit. on p. 108).
- ¹³⁷B. W. Heinrich, L. Braun, J. I. Pascual, and K. J. Franke, “Protection of excited spin states by a superconducting energy gap”, *Nature Phys* **9**, 765–768 (2013) (cit. on p. 108).
- ¹³⁸H. Huang, C. Padurariu, J. Senkpiel, R. Drost, A. L. Yeyati, J. C. Cuevas, B. Kubala, J. Ankerhold, K. Kern, and C. R. Ast, “Tunnelling dynamics between superconducting bound states at the atomic limit”, *Nature Physics* **16**, 1227–1231 (2020) (cit. on p. 108).
- ¹³⁹L. Serrier-Garcia, J. C. Cuevas, T. Cren, C. Brun, V. Cherkez, F. Debontridder, D. Fokin, F. S. Bergeret, and D. Roditchev, “Scanning tunneling spectroscopy study of the proximity effect in a disordered two-dimensional metal”, *Phys. Rev. Lett.* **110**, 157003 (2013) (cit. on p. 110).
- ¹⁴⁰V. S. Stolyarov, S. Pons, S. Vlaic, S. V. Remizov, D. S. Shapiro, C. Brun, S. I. Bozhko, T. Cren, T. V. Menshchikova, E. V. Chulkov, W. V. Pogosov, Y. E. Lozovik, and D. Roditchev, “Superconducting long-range proximity effect through the atomically flat interface of a Bi_2Te_3 topological insulator”, *J. Phys. Chem. Lett.* **12**, 9068–9075 (2021) (cit. on p. 110).
- ¹⁴¹C. Brun, T. Cren, and D. Roditchev, “Review of 2D superconductivity: the ultimate case of epitaxial monolayers”, *Superconductor Science and Technology* **30**, 013003 (2017) (cit. on p. 110).
- ¹⁴²G. Schubert, H. Fehske, L. Fritz, and M. Vojta, “Fate of topological-insulator surface states under strong disorder”, *Phys. Rev. B* **85**, 201105 (2012) (cit. on p. 111).
- ¹⁴³Y.-L. Wang, Y. Xu, Y.-P. Jiang, J.-W. Liu, C.-Z. Chang, M. Chen, Z. Li, C.-L. Song, L.-L. Wang, K. He, X. Chen, W.-H. Duan, Q.-K. Xue, and X.-C. Ma, “Structural defects and electronic properties of the Cu-doped topological insulator Bi_2Se_3 ”, *Phys. Rev. B* **84**, 075335 (2011) (cit. on p. 116).
- ¹⁴⁴T. Shirasawa, M. Sugiki, T. Hirahara, M. Aitani, T. Shirai, S. Hasegawa, and T. Takahashi, “Structure and transport properties of Cu-doped Bi_2Se_3 films”, *Phys. Rev. B* **89**, 195311 (2014) (cit. on p. 116).
- ¹⁴⁵M. Wang, D. Zhang, W. Jiang, Z. Li, C. Han, J. Jia, J. Li, S. Qiao, D. Qian, H. Tian, and B. Gao, “Growth and structural characterisation of Sr-doped Bi_2Se_3 thin films”, *Scientific Reports* **8**, 2192 (2018) (cit. on p. 116).

-
- ¹⁴⁶Y.-R. Lin, M. Bagchi, S. Soubatch, T.-L. Lee, J. Brede, F. C. Bocquet, C. Kumpf, Y. Ando, and F. S. Tautz, “Vertical position of Sr dopants in the $\text{Sr}_x\text{Bi}_2\text{Se}_3$ superconductor”, *Phys. Rev. B* **104**, 054506 (2021) (cit. on pp. 116, 158).
- ¹⁴⁷W. Zhang, D. West, S. H. Lee, Y. Qiu, C.-Z. Chang, J. S. Moodera, Y. S. Hor, S. Zhang, and W. Wu, “Electronic fingerprints of Cr and V dopants in the topological insulator Sb_2Te_3 ”, *Phys. Rev. B* **98**, 115165 (2018) (cit. on p. 117).
- ¹⁴⁸N. Fukui, T. Hirahara, T. Shirasawa, T. Takahashi, K. Kobayashi, and S. Hasegawa, “Surface relaxation of topological insulators: Influence on the electronic structure”, *Phys. Rev. B* **85**, 115426 (2012) (cit. on p. 118).
- ¹⁴⁹S. Just, F. Lüpke, V. Cherepanov, F. S. Tautz, and B. Voigtländer, “Parasitic conduction channels in topological insulator thin films”, *Phys. Rev. B* **101**, 245413 (2020) (cit. on p. 118).
- ¹⁵⁰J. Schwenk, S. Kim, J. Berwanger, F. Ghahari, D. Walkup, M. R. Slot, S. T. Le, W. G. Cullen, S. R. Blankenship, S. Vranjkovic, H. J. Hug, Y. Kuk, F. J. Giessibl, and J. A. Stroscio, “Achieving μeV tunneling resolution in an *in-operando* scanning tunneling microscopy, atomic force microscopy, and magnetotransport system for quantum materials research”, *Review of Scientific Instruments* **91**, 071101 (2020) (cit. on p. 119).
- ¹⁵¹M. R. Slot, “Patterning atomic flatland:electronic lattices crafted atom by atom”, PhD thesis (Universiteit Utrecht, July 10, 2019) (cit. on pp. 121, 122, 125, 127).
- ¹⁵²S. Heinze, “First-principles theory of scanning tunneling microscopy applied to transition-metal surfaces”, PhD thesis (Universitaet Hamburg, Aug. 16, 2000) (cit. on p. 121).
- ¹⁵³J. Brede, “Spin-polarized scanning tunneling microscopy and spectroscopy of phthalocyanine molecules on surfaces” (2011) (cit. on p. 121).
- ¹⁵⁴J. Bardeen, “Tunnelling from a many-particle point of view”, *Phys. Rev. Lett.* **6**, 57–59 (1961) (cit. on p. 122).
- ¹⁵⁵J. Tersoff and D. R. Hamann, “Theory and application for the scanning tunneling microscope”, *Phys. Rev. Lett.* **50**, 1998–2001 (1983) (cit. on p. 122).
- ¹⁵⁶C. J. Chen, “Origin of atomic resolution on metal surfaces in scanning tunneling microscopy”, *Phys. Rev. Lett.* **65**, 448–451 (1990) (cit. on pp. 122, 124).
- ¹⁵⁷V. A. Ukraintsev, “Data evaluation technique for electron-tunneling spectroscopy”, *Phys. Rev. B* **53**, 11176–11185 (1996) (cit. on p. 123).
- ¹⁵⁸B. Voigtländer, *Scanning probe microscopy* (Springer Berlin Heidelberg, 2015) (cit. on p. 125).
- ¹⁵⁹J. Hoffman, “A search for alternative electronic order in the high temperature superconductor $\text{Bi}_2\text{Sr}_2\text{CaCu}_2\text{O}_{8+\delta}$ by scanning tunneling microscopy”, PhD thesis (University of California, Berkeley, 2003) (cit. on p. 126).

- ¹⁶⁰R. Feenstra, J. A. Stroscio, and A. Fein, “Tunneling spectroscopy of the Si(111) 2×1 surface”, *Surface Science* **181**, 295–306 (1987) (cit. on p. 128).
- ¹⁶¹M. Gruber, A. Weismann, and R. Berndt, “The kondo resonance line shape in scanning tunnelling spectroscopy: instrumental aspects”, *Journal of Physics: Condensed Matter* **30**, 424001 (2018) (cit. on p. 130).
- ¹⁶²J. Bardeen, L. N. Cooper, and J. R. Schrieffer, “Theory of superconductivity”, *Phys. Rev.* **108**, 1175–1204 (1957) (cit. on p. 131).
- ¹⁶³J. Bardeen, L. N. Cooper, and J. R. Schrieffer, “Microscopic theory of superconductivity”, *Phys. Rev.* **106**, 162–164 (1957) (cit. on p. 131).
- ¹⁶⁴C. Timm, “Theory of superconductivity”, Feb. 25, 2022 (cit. on p. 131).
- ¹⁶⁵S. Chi, “Scanning tunneling microscopy study of superconducting pairing symmetry: application to lifeas”, PhD thesis (University of British Columbia, Oct. 1, 2014) (cit. on p. 134).
- ¹⁶⁶F. Marsiglio and J. Carbotte, “Electron-phonon superconductivity”, Feb. 1, 2008 (cit. on p. 137).
- ¹⁶⁷R. C. Dynes, V. Narayanamurti, and J. P. Garno, “Direct measurement of quasiparticle-lifetime broadening in a strong-coupled superconductor”, *Phys. Rev. Lett.* **41**, 1509–1512 (1978) (cit. on pp. 137, 151).
- ¹⁶⁸J. I. Pascual, G. Bihlmayer, Y. M. Koroteev, H.-P. Rust, G. Ceballos, M. Hansmann, K. Horn, E. V. Chulkov, S. Blügel, P. M. Echenique, and P. Hofmann, “Role of spin in quasiparticle interference”, *Phys. Rev. Lett.* **93**, 196802 (2004) (cit. on p. 140).
- ¹⁶⁹L. Petersen, P. T. Sprunger, P. Hofmann, E. Lægsgaard, B. G. Briner, M. Doering, H.-P. Rust, A. M. Bradshaw, F. Besenbacher, and E. W. Plummer, “Direct imaging of the two-dimensional Fermi contour: Fourier-transform STM”, *Phys. Rev. B* **57**, R6858–R6861 (1998) (cit. on pp. 141, 156).
- ¹⁷⁰W.-C. Lee, C. Wu, D. P. Arovas, and S.-C. Zhang, “Quasiparticle interference on the surface of the topological insulator Bi₂Te₃”, *Phys. Rev. B* **80**, 245439 (2009) (cit. on pp. 141, 142).
- ¹⁷¹T. Hanaguri, K. Igarashi, M. Kawamura, H. Takagi, and T. Sasagawa, “Momentum-resolved Landau-level spectroscopy of Dirac surface state in Bi₂Se₃”, *Phys. Rev. B* **82**, 081305 (2010) (cit. on p. 141).
- ¹⁷²Z. Alpichshev, J. G. Analytis, J.-H. Chu, I. R. Fisher, Y. L. Chen, Z. X. Shen, A. Fang, and A. Kapitulnik, “STM Imaging of electronic waves on the surface of Bi₂Te₃: topologically protected surface states and hexagonal warping effects”, *Phys. Rev. Lett.* **104**, 016401 (2010) (cit. on pp. 141, 156).

- ¹⁷³I. Lee, C. K. Kim, J. Lee, S. J. L. Billinge, R. Zhong, J. A. Schneeloch, T. Liu, T. Valla, J. M. Tranquada, G. Gu, and J. C. S. Davis, “Imaging Dirac-mass disorder from magnetic dopant atoms in the ferromagnetic topological insulator $\text{Cr}_x(\text{Bi}_{0.1}\text{Sb}_{0.9})_{2-x}$ ”, *Proceedings of the National Academy of Sciences* **112**, 1316–1321 (2015) (cit. on p. 141).
- ¹⁷⁴T. Zhang, P. Cheng, X. Chen, J.-F. Jia, X. Ma, K. He, L. Wang, H. Zhang, X. Dai, Z. Fang, X. Xie, and Q.-K. Xue, “Experimental demonstration of topological surface states protected by time-reversal symmetry”, *Phys. Rev. Lett.* **103**, 266803 (2009) (cit. on pp. 141, 156).
- ¹⁷⁵S. Kim, S. Yoshizawa, Y. Ishida, K. Eto, K. Segawa, Y. Ando, S. Shin, and F. Komori, “Robust protection from backscattering in the topological insulator $\text{Bi}_{1.5}\text{Sb}_{0.5}\text{Te}_{1.7}\text{Se}_{1.3}$ ”, *Phys. Rev. Lett.* **112**, 136802 (2014) (cit. on p. 141).
- ¹⁷⁶H. Beidenkopf, P. Roushan, J. Seo, L. Gorman, I. Drozdov, Y. S. Hor, R. J. Cava, and A. Yazdani, “Spatial fluctuations of helical Dirac fermions on the surface of topological insulators”, *Nature Phys.* **7**, 939–943 (2011) (cit. on pp. 141, 156).
- ¹⁷⁷Y. L. Chen, J. G. Analytis, J.-H. Chu, Z. K. Liu, S.-K. Mo, X. L. Qi, H. J. Zhang, D. H. Lu, X. Dai, Z. Fang, S. C. Zhang, I. R. Fisher, Z. Hussain, and Z.-X. Shen, “Experimental realization of a three-dimensional topological insulator, Bi_2Te_3 ”, *Science* **325**, 178–181 (2009) (cit. on p. 141).
- ¹⁷⁸M. S. Suzuki and I. S. Suzuki, “Lecture note on de Haas van Alphen effect solid state physics”, June 1, 2015 (cit. on p. 142).
- ¹⁷⁹J. N. Fuchs, F. Piéchon, M. O. Goerbig, and G. Montambaux, “Topological Berry phase and semiclassical quantization of cyclotron orbits for two dimensional electrons in coupled band models”, *The European Physical Journal B* **77**, 351–362 (2010) (cit. on p. 142).
- ¹⁸⁰L. Onsager, “Interpretation of the de Haas-van Alphen effect”, *The London, Edinburgh, and Dublin Philosophical Magazine and Journal of Science* **43**, 1006–1008 (1952) (cit. on p. 143).
- ¹⁸¹L. M. Roth, “Semiclassical theory of magnetic energy levels and magnetic susceptibility of Bloch electrons”, *Phys. Rev.* **145**, 434–448 (1966) (cit. on p. 143).
- ¹⁸²Y. Gao and Q. Niu, “Zero-field magnetic response functions in Landau levels”, *Proceedings of the National Academy of Sciences* **114**, 7295–7300 (2017) (cit. on p. 143).
- ¹⁸³M. Wilkinson and R. J. Kay, “Semiclassical limits of the spectrum of Harper’s equation”, *Phys. Rev. Lett.* **76**, 1896–1899 (1996) (cit. on p. 143).
- ¹⁸⁴Y. Okada, W. Zhou, C. Dhital, D. Walkup, Y. Ran, Z. Wang, S. D. Wilson, and V. Madhavan, “Visualizing Landau levels of Dirac electrons in a one-dimensional potential”, *Phys. Rev. Lett.* **109**, 166407 (2012) (cit. on pp. 146, 147).

- ¹⁸⁵P. Schwab and M. Dzierzawa, “Landau levels in a topological insulator”, *Phys. Rev. B* **85**, 155403 (2012) (cit. on pp. 146, 147).
- ¹⁸⁶Y.-S. Fu, T. Hanaguri, K. Igarashi, M. Kawamura, M. S. Bahramy, and T. Sasagawa, “Observation of Zeeman effect in topological surface state with distinct material dependence”, *Nat. Commun.* **7**, 10829 (2016) (cit. on p. 146).
- ¹⁸⁷Y.-S. Fu, M. Kawamura, K. Igarashi, H. Takagi, T. Hanaguri, and T. Sasagawa, “Imaging the two-component nature of Dirac-Landau levels in the topological surface state of Bi_2Se_3 ”, *Nature Physics* **10**, 815–819 (2014) (cit. on p. 146).
- ¹⁸⁸K. L. Scipioni, Z. Wang, Y. Maximenko, F. Katmis, C. Steiner, and V. Madhavan, “Role of defects in the carrier-tunable topological-insulator $(\text{Bi}_{1-x}\text{Sb}_x)_2\text{Te}_3$ thin films”, *Phys. Rev. B* **97**, 125150 (2018) (cit. on p. 146).
- ¹⁸⁹G. Li, A. Luican, and E. Y. Andrei, “Scanning tunneling spectroscopy of graphene on graphite”, *Phys. Rev. Lett.* **102**, 176804 (2009) (cit. on p. 147).
- ¹⁹⁰H. Du, X. Sun, X. Liu, X. Wu, J. Wang, M. Tian, A. Zhao, Y. Luo, J. Yang, B. Wang, and J. G. Hou, “Surface Landau levels and spin states in bismuth (111) ultrathin films”, *Nat. Commun.* **7**, 10814 (2016) (cit. on p. 147).
- ¹⁹¹J. González, F. Guinea, and M. A. H. Vozmediano, “Unconventional quasiparticle lifetime in graphite”, *Phys. Rev. Lett.* **77**, 3589–3592 (1996) (cit. on p. 147).
- ¹⁹²M. Müller, L. Fritz, and S. Sachdev, “Quantum-critical relativistic magnetotransport in graphene”, *Phys. Rev. B* **78**, 115406 (2008) (cit. on p. 147).
- ¹⁹³H. Boschker, E. Fillis-Tsirakis, C. Richter, D. Zhang, J. Smet, and L. Kuerten, “Microscopic origin of the Dynes parameter Γ of the LaAlO_3 - SrTiO_3 interface superconductor”, *Phys. Rev. B* **102**, 134506 (2020) (cit. on p. 151).
- ¹⁹⁴E. Schachinger and J. Carbotte, “Vortex state Doppler shift on local density of states”, *Physica C: Superconductivity* **341-348**, 1689–1690 (2000) (cit. on p. 154).
- ¹⁹⁵I. Vekhter, P. J. Hirschfeld, J. P. Carbotte, and E. J. Nicol, “Anisotropic thermodynamics of d -wave superconductors in the vortex state”, *Phys. Rev. B* **59**, R9023–R9026 (1999) (cit. on p. 154).
- ¹⁹⁶X. Liu, Y. X. Chong, R. Sharma, and J. C. S. Davis, “Atomic-scale visualization of electronic fluid flow”, *Nat. Mater.* **20**, 1480–1484 (2021) (cit. on p. 154).
- ¹⁹⁷Z. Zhu, M. Papaj, X.-A. Nie, H.-K. Xu, Y.-S. Gu, X. Yang, D. Guan, S. Wang, Y. Li, C. Liu, J. Luo, Z.-A. Xu, H. Zheng, L. Fu, and J.-F. Jia, “Discovery of segmented Fermi surface induced by Cooper pair momentum”, *Science* **374**, 1381–1385 (2021) (cit. on p. 155).
- ¹⁹⁸K. Nakayama, S. Souma, C. X. Trang, D. Takane, C. Chen, J. Avila, T. Takahashi, S. Sasaki, K. Segawa, M. C. Asensio, Y. Ando, and T. Sato, “Nanomosaic of topological Dirac states on the surface of $\text{Pb}_5\text{Bi}_{24}\text{Se}_{41}$ observed by nano-ARPES”, *Nano Lett.* **19**, 3737–3742 (2019) (cit. on pp. 155, 159, 161, 162).

-
- ¹⁹⁹P. T. Sprunger, L. Petersen, E. W. Plummer, E. Lægsgaard, and F. Besenbacher, “Giant Friedel oscillations on the beryllium(0001) surface”, *Science* **275**, 1764–1767 (1997) (cit. on p. 156).
- ²⁰⁰P. Hofmann, B. G. Briner, M. Doering, H.-P. Rust, E. W. Plummer, and A. M. Bradshaw, “Anisotropic two-dimensional Friedel oscillations”, *Phys. Rev. Lett.* **79**, 265–268 (1997) (cit. on p. 156).
- ²⁰¹L. Petersen, P. Laitenberger, E. Lægsgaard, and F. Besenbacher, “Screening waves from steps and defects on Cu(111) and Au(111) imaged with STM: Contribution from bulk electrons”, *Phys. Rev. B* **58**, 7361–7366 (1998) (cit. on p. 156).
- ²⁰²K. Schouteden, P. Lievens, and C. Van Haesendonck, “Fourier-transform scanning tunneling microscopy investigation of the energy versus wave vector dispersion of electrons at the Au(111) surface”, *Phys. Rev. B* **79**, 195409 (2009) (cit. on p. 156).
- ²⁰³P. Sessi, M. M. Otrokov, T. Bathon, M. G. Vergniory, S. S. Tsirkin, K. A. Kokh, O. E. Tereshchenko, E. V. Chulkov, and M. Bode, “Visualizing spin-dependent bulk scattering and breakdown of the linear dispersion relation in Bi_2Te_3 ”, *Phys. Rev. B* **88**, 161407 (2013) (cit. on pp. 156, 163).
- ²⁰⁴J. Wang, W. Li, P. Cheng, C. Song, T. Zhang, P. Deng, X. Chen, X. Ma, K. He, J.-F. Jia, Q.-K. Xue, and B.-F. Zhu, “Power-law decay of standing waves on the surface of topological insulators”, *Phys. Rev. B* **84**, 235447 (2011) (cit. on p. 156).
- ²⁰⁵V. S. Stolyarov, V. A. Sheina, D. A. Khokhlov, S. Vlaic, S. Pons, H. Aubin, R. S. Akzhanov, A. S. Vasenko, T. V. Menshchikova, E. V. Chulkov, A. A. Golubov, T. Cren, and D. Roditchev, “Disorder-promoted splitting in quasiparticle interference at nesting vectors”, *J. Phys. Chem. Lett.* **12**, 3127–3134 (2021) (cit. on pp. 156, 163).
- ²⁰⁶H. Momida, G. Bihlmayer, S. Blügel, K. Segawa, Y. Ando, and T. Oguchi, “Topological interface states in the natural heterostructure $(\text{PbSe})_5(\text{Bi}_2\text{Se}_3)_6$ with Bi_{Pb} defects”, *Phys. Rev. B* **97**, 035113 (2018) (cit. on p. 158).
- ²⁰⁷L. Simon, C. Bena, F. Vonau, M. Cranney, and D. Aubeil, “Fourier-transform scanning tunnelling spectroscopy: the possibility to obtain constant-energy maps and band dispersion using a local measurement”, *Journal of Physics D: Applied Physics* **44**, 464010 (2011) (cit. on p. 163).

Acknowledgment

I am grateful to Prof. Yoichi Ando and Dr. Jens Brede for supervising this thesis and in particular for their time. I acknowledge funding from the CRC1238 B06 project of Prof. Ando during the period between June, 2018 - March, 2023.

I thank Prof. Thomas Michely for the evaluating this thesis and for his support during the last few months.

And I thank my parents for their patience and love, always.

Publications

- M. Bagchi, L. Pitz-Paal, C.P. Grams, O. Breunig, N. Borgwardt, Z. Wang, Y. Ando, M. Grüninger, and J. Hemberger. "Large positive magnetoconductivity at microwave frequencies in the compensated topological insulator BiSbTeSe₂", Phys. Rev. B 99, 161121(R) (2019).
- T. Fröhlich, Z. Wang, M. Bagchi, A. Stunault, Y. Ando, and M. Braden, "Crystal structure and distortion of superconducting Cu_xBi₂Se₃", Phys. Rev. Mater. 4, 054802 (2020).
- Y. R. Lin, M. Bagchi, S. Soubatch, T.-L. Lee, J. Brede, F. C. Bocquet, C. Kumpf, Y. Ando, and F. S. Tautz, "Vertical position of Sr dopants in the Sr_xBi₂Se₃ superconductor", Phys. Rev. B 104, 054506 (2021) (two first authors).
- M. Bagchi, J. Brede, and Y. Ando, "Observability of superconductivity in Sr-doped Bi₂Se₃ at the surface using scanning tunneling microscope", Phys. Rev. Mater. 6, 034201 (2022).
- M. Bagchi, J. Brede, Aline Ramires, and Y. Ando, "Rotation of gap nodes in the topological superconductor Cu_x(PbSe)₅(Bi₂Se₃)₆", *submitted*.
- M. Bagchi, J. Brede, G. Bihlmayer, P. Rössmann, S. Blügel, and Y. Ando, "Unexpected QPI pattern on the surface of (PbSe)₅(Bi₂Se₃)₆", *in preparation*.
- J. Brede, M. Bagchi, A. Greichgauer, A. A. Taskin, A. Uday, A. Bliesener, G. Lippertz, R. Yazdanpanah, and Y. Ando, "Giant chemical potential variations in ultra-thin (Bi_{1-x}Sb_x)₂Se₃ films probed by STM", *in preparation*.
- J. Brede, M. Bagchi, A. Greichgauer, A. A. Taskin, A. Uday, A. Bliesener, G. Lippertz, R. Yazdanpanah, P. Rössmann, S. Blügel, and Y. Ando, "Superconducting proximity effect in (Bi_{1-x}Sb_x)₂Se₃ films probed by STM", *in preparation*.

Erklärung zur Dissertation
gemäß der Promotionsordnung vom 12. März 2020

Diese Erklärung muss in der Dissertation enthalten sein.
(This version must be included in the doctoral thesis)

„Hiermit versichere ich an Eides statt, dass ich die vorliegende Dissertation selbstständig und ohne die Benutzung anderer als der angegebenen Hilfsmittel und Literatur angefertigt habe. Alle Stellen, die wörtlich oder sinngemäß aus veröffentlichten und nicht veröffentlichten Werken dem Wortlaut oder dem Sinn nach entnommen wurden, sind als solche kenntlich gemacht. Ich versichere an Eides statt, dass diese Dissertation noch keiner anderen Fakultät oder Universität zur Prüfung vorgelegen hat; dass sie - abgesehen von unten angegebenen Teilpublikationen und eingebundenen Artikeln und Manuskripten - noch nicht veröffentlicht worden ist sowie, dass ich eine Veröffentlichung der Dissertation vor Abschluss der Promotion nicht ohne Genehmigung des Promotionsausschusses vornehmen werde. Die Bestimmungen dieser Ordnung sind mir bekannt. Darüber hinaus erkläre ich hiermit, dass ich die Ordnung zur Sicherung guter wissenschaftlicher Praxis und zum Umgang mit wissenschaftlichem Fehlverhalten der Universität zu Köln gelesen und sie bei der Durchführung der Dissertation zugrundeliegenden Arbeiten und der schriftlich verfassten Dissertation beachtet habe und verpflichte mich hiermit, die dort genannten Vorgaben bei allen wissenschaftlichen Tätigkeiten zu beachten und umzusetzen. Ich versichere, dass die eingereichte elektronische Fassung der eingereichten Druckfassung vollständig entspricht.“

Teilpublikationen:

- M. Bagchi, J. Brede, and Y. Ando, "*Observability of superconductivity in Sr-doped Bi_2Se_3 at the surface using scanning tunneling microscope*", Phys. Rev. Mater. 6, 034201 (2022).
- M. Bagchi, J. Brede, Aline Ramires, and Y. Ando, "*Rotation of gap nodes in the topological superconductor $\text{Cu}_x(\text{PbSe})_5(\text{Bi}_2\text{Se}_3)_6$* ", submitted.

Datum, Name und Unterschrift

10. 01. 2023

Mahasweta Bagchi

Mahasweta Bagchi

